Deformation behaviour of Cu-Cr in-situ Composite

Thesis submitted for the degree of

Doctor of Philosophy

at the University of Leicester

Kok Loong Lee

Materials Research Group
Engineering Department
University of Leicester

February 2004

Deformation behaviour of Cu-Cr in-situ Composite

Kok Loong Lee

Abstract

With the increasing requirements for higher strength materials with high electrical conductivity, a lot of interest has been paid to develop Cu-based composites in the last 25 years. These composites have superior tensile strength, combined with good electrical conductivity, to that exhibited by pure Cu and conventional Cu alloys. To date, much of the research carried out on this composite has focused on the mechanical and electrical properties of the as-processed material. However, there is a basic lack of understanding of the way in which the properties may change or degrade during service. Without this knowledge, these composites cannot be fully and safely exploited. Thus the objective of this study was to investigate the thermo-mechanical behaviour of a Cu-Cr composite, and the nature and extent of any damage mechanisms occurring within the composite over a wide range of experimental conditions.

Neutron diffraction was used to investigate the deformation behaviour of the individual phases in the composite and their interaction through elastic and plastic loading at room temperature. For the composite, a fairly good agreement was observed in the phase strains predicted by the Eshelby theory and measured by neutron diffraction. In-situ tensile tests in the SEM were also performed to study the damage mechanism of the composite.

Tensile and creep tests were carried out in air and in vacuum over a wide range of temperatures. To provide data for comparison with the composite material, pure Cu specimens were tested whenever possible. Creep resistance increases significantly with the introduction of Cr fibres into Cu. The higher creep rate of the composite in air than in vacuum is due to the gradual decrease of the cross-sectional area of the matrix due to increasing thickness of the oxide layer. Damage characteristics and distributions were found to be similar during tensile and creep testing.

Especially dedicated to my family and Geoff…….

Acknowledgements

I would like to thank the following for being instrumental in the writing of this thesis, in one way or another

1. My former supervisor Anne Whitehouse for her advice and guidance for the duration of this research.
2. Professor Alan Ponter for taking over the role of supervisor when Anne left the department and careful revision of my thesis.
3. Geoff O' Connor deserves a great deal of thanks for his time and patience in setting up the difficult experiments especially on the vacuum creep tests. The late evenings were always greatly appreciated. His encouragement and motivation have benefited me in countless ways throughout the duration of this project. Without him, all this would have been virtually impossible.
4. Parents and sister, for being so supportive throughout my stay in England and always ensuring that my only concern was my studies.
5. Professor Phil Withers of Manchester Materials Science Centre, for many discussions concerning the interpretation of the neutron results and providing the facilities to carry out the in-situ SEM tensile test.
6. Professor Sun Ig Hong of Chungnam National University, for the provision of the TEM facilities.
7. Members of the materials group, for support and friendship, in particular Mohamed and Ludwig.
8. Badminton friends, for their support and friendship, particularly Clive, Phil, Gafar, Nazar, and Ali.

9. Kevin Roberts of Cambridge University for carrying out the swaging of the composite.

10. Last, and definitely not least, Claudia for her understanding, patience and support throughout the duration of this research.

Kok Loong Lee

February 2004

Papers published from this thesis

Chapter 5

- Elevated temperature tensile properties and failure of a copper-chromium in-situ composite, *Journal of Materials Science, 2003, vol. 38, pp. 3437-3447.*

Chapter 6

- Neutron diffraction study of the deformation processed copper chromium composites, *Materials Science and Engineering A*, 2003, vol. A348, pp. 208-213.

Chapter 7

- Creep behaviour of an in-situ copper-chromium composite, *Metallurgical and Materials Transactions A*, 2004, vol. 35A, pp. 695-705.

- Effect of oxidation on the creep behaviour of an in-situ copper-chromium composite, *Composites Part A: Applied Science and Manufacturing*, 2003, vol. 34, pp. 1235-1244.

Contents

Chapter 1

Introduction

I have yet to see any problem, however complicated, which, when you looked at it the right way, did not become still more complicated

-Paul Anderson, New Scientist

Copper is an industrially important non-ferrous metal on account of its high thermal and electrical conductivity, good corrosion resistance and mechanical workability. Improvement in the strength of Cu can be achieved by making a solid solution, a fine dispersion of a second phase in the matrix and fibre reinforcement. Recently, attention has focused on deformation of Cu-based composites [1-7]. Cu-based composites are attractive materials for high strength and high conductivity applications. These composites, comprised of Cu with element X (where X is a bcc metal immiscible in Cu such as Nb, Cr, Fe, Mo or V) can be formed by mechanical working (swaging, extrusion, rolling or drawing) of ductile two phase mixtures prepared by using liquid phase sintering, casting or powder metallurgy techniques [1-3]. The fibrous X metal can bear the higher fraction of load while the surrounding Cu matrix gives good conductivity and ductility.

Among the several Cu-X composites [1-7] that have been studied, Cu-Cr composites have a desirable combination of attributes. Compared to many other Cu-X composites, Cu-Cr composites offer lower cost (the cost of Cr is roughly one-tenth that of Nb), lower solubility of the X element in the Cu matrix, and higher elastic modulus; these attributes make Cu-Cr composites a promising material for many potential applications, particularly at elevated temperatures such as rocket engine

combustion chamber systems. The most significant difference between Cu-Cr in-situ composite and dilute Cu-Cr alloy is the existence of Cr ribbons as the in-situ reinforcing element. To realise the full potential of Cu-Cr composites, more research is needed to improve the current understanding of their behaviour. The primary emphasis in this study, then, is on areas which have received comparatively little discussion in the past. These include:

- **The deformation behaviour of the individual phases in the Cu-10vol.% Cr composites and their interaction through elastic and plastic loading at room temperature and monitoring the in-situ tensile fracture mechanism of the individual phase inside the scanning electron microscope.**
- **Investigation of the creep behaviour of the composite in air and in vacuum at temperatures from 200-650°C.**
- **Evaluating the damage and failure processes by means of detailed microstructural analysis.**

The early chapters of this thesis review the important features of the composites and techniques which are used in the subsequent experiments. In **Chapter 2** a brief introduction of composite theories is given which include the concept of load transfer, internal stresses and stress relaxation. An overview of some approaches used for modelling load transfer in composites are also briefly explained with particular emphasis on the Eshelby model, which is used in chapter six. Finally, the available literature on creep of pure Cu and metal matrix composites is also briefly reviewed.

In **Chapter Three**, the current state of understanding of in-situ metal matrix composites is reviewed. The important findings related to the deformation behaviour of Cu-based composites are discussed.

Chapter Four gives a brief description of the general experimental techniques used to evaluate the properties of this composite, which include x-ray diffraction, tensile and resistivity measurements, creep, scanning electron microscopy (SEM) and transmission electron microscopy (TEM). More specialised techniques such as neutron diffraction and in-situ tensile testing in a scanning electron microscope are found in chapter six.

The production method used to produce this composite is discussed in **Chapter 5.** This is followed by characterisation of the composite microstructure by using SEM and TEM. The texture of the composite is also examined by using the x-ray diffraction technique. This chapter concludes with the characterisation of the behaviour of the composite with hardness, resistivity and both cold and hot tensile tests.

Neutron diffraction is the technique which is often used to determine the internal strain in the composite during the application of an external load. In **Chapter Six,** production of neutrons, the fundamental concept of the diffraction technique and an experimental in-situ neutron diffraction loading experiment at room temperature are described briefly. A comparison is made between the obtained neutron data and the Eshelby model predictions. In-situ tensile tests in a scanning electron microscope used to study the damage mechanism of the composite will also be discussed here.

At elevated temperature, failure of components can occur by creep. Therefore, it would be important to carry out creep tests at an extensive range of high temperatures both in air and in vacuum to obtain a fuller picture of the composites behaviour. All the creep data are presented in **Chapter Seven**, which is followed by a brief literature survey of the state of the research in this area.

Finally, **Chapter Eight** gives a summary of the work carried out in this study and suggestions are made of a number of possible extensions arising out of this research.

References

1 W.A. Spitzig, A.R. Pelton and F.C. Laabs, Characterization of the strength and microstructure of heavily cold worked Cu-Nb composites. Acta Metallurgica, 1987. 35(10): 2427-2442.

2 C.L. Trybus and W.A. Spitzig, Characterization of the strength and microstructural evolution of a heavily cold rolled Cu-20% Nb composite. Acta Metallurgica, 1989. 37(7): 1971-1981.

3 W.A. Spitzig, L.S. Chumbley, J.D. Verhoeven, Y.S. Go and H.L. Downing, Effect of temperature on the strength and conductivity of a deformation processed Cu-20%Fe composite. Journal of Materials Science, 1992. 27(8): 2005-2011.

4 W.A. Spitzig and S.B. Biner, Comparison of strengthening in wire-drawn or rolled Cu-20% Nb with a dislocation accumulation model. Journal of Materials Science, 1993. 28(17): 4623-4629.

5 C. Biselli and D.G. Morris, Microstructure and strength of Cu-Fe in situ composites obtained from prealloyed Cu-Fe powders. Acta Metallurgica et Materialia, 1994. 42(1): 163-176.

6 D. Raabe, Simulation of the resistivity of heavily cold worked Cu-20 wt.% Nb wires. Computational Materials Science, 1995. 3(3): 402-412.

7 Y. Jin, K. Adachi, T. Takeuchi and H.G. Suzuki, Correlation between the cold-working and aging treatments in a Cu-15 wt pct Cr in situ composite. Metallurgical and Materials Transactions A-Physical Metallurgy and Materials Science, 1998. 29(8): 2195-2203.

Chapter 2

Mechanical response of conventional MMC

2.1 Introduction

The aim of this chapter is to give a brief introduction of composite theories which include the concept of load transfer, internal stresses and stress relaxation. These fundamental concepts are important in order to understand the mechanical response and hence optimising the performance of a composite.

There is an extensive body of literature on the creep of pure Cu, and some work has been carried out on the creep behaviour of dispersion-strengthened (DS) Cu alloys, but very little information is available on the creep and/or effect of oxidation on the behaviour of Cu-based composites. The available creep data on Cu-based composites is reviewed during the discussion of the creep results of Cu-10vol.% Cr composites (Chapter 7). Therefore, the available literature on creep of pure Cu and metal matrix composites is briefly reviewed here instead.

2.2 Internal stress response of an MMC

2.2.1 Load transfer

In order to understand the mechanical behaviour of a composite, and hence optimise its performance, it is essential to understand the concept of load sharing between the matrix and the reinforcing phase. Load transfer can be described as the process by which the applied load is shared between the matrix and the reinforcing phase of the composite. The stress varies sharply from point to point (especially with short fibres or particles as reinforcement), but the proportion of the applied load

carried by each phase can be obtained from volume averaging the load within each of them. At equilibrium, the external load is equal to the volume-averaged loads borne by the constituents. This leads to the condition

$$\sigma_f v_f + \sigma_m v_m = \sigma_A \qquad (2.1)$$

where v_f is the volume fraction of reinforcement, v_m is the volume fraction of the matrix, σ_m and σ_f are the mean stress in the matrix and reinforcement respectively, σ_A is the applied stress. Thus, for a simple two-phase composite under a given applied load, a certain proportion of the load will be taken by the reinforcement and the remainder by the matrix.

Most engineering use of materials is limited to the elastic regime. If the response of the composite remains elastic, the fraction of the load carried by the reinforcement will be independent of the applied load, and it is an important feature of the material. If a large fraction of the total applied load is carried by the reinforcement, more stress must be applied in order to obtain large-scale yielding in the matrix, and hence the composite is stronger than the unreinforced metal (figure 2.1). The main function of the reinforcement in the MMCs is to carry most of the applied load. The main functions of the matrix are to bind the reinforcement together and to transmit and distribute the external load to the individual reinforcement particles/fibres.

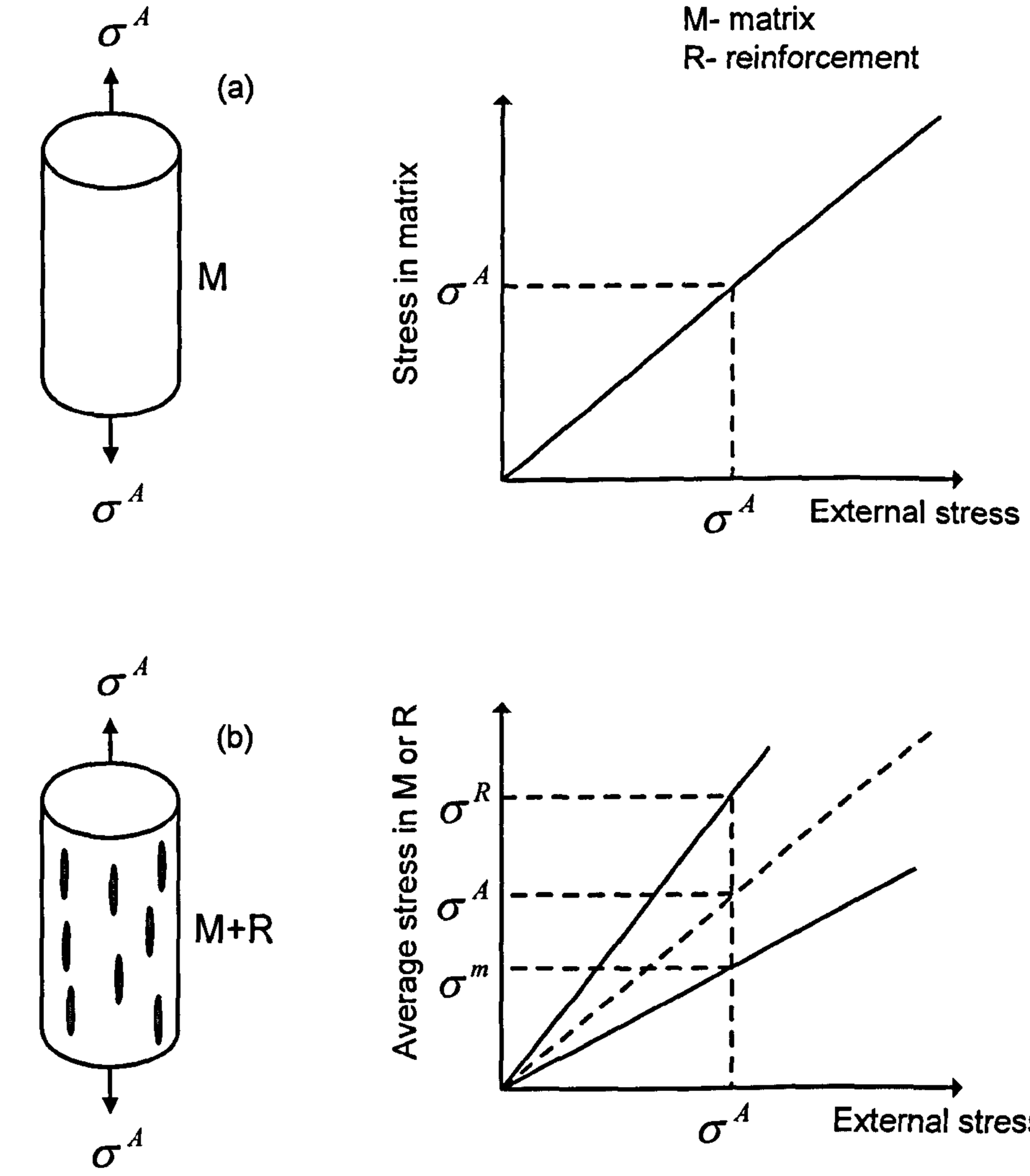

Figure 2.1 A schematic diagram showing the stress distribution of an applied external stress in (a) unreinforced and (b) a composite

The degree of load transfer from the matrix to the reinforcement will depend upon many factors such as the relative stiffnesses of the phases, volume fraction of the reinforcement, the aspect ratio of the reinforcement, the strength of the interfacial bond, and whether the deformation of the composite is purely elastic or contains some degree of plasticity.

2.2.2 Internal stresses

Internal stresses in composites are generated by mechanical loading or thermal loading. These stresses arise due to the different properties of the reinforcement and the matrix [2]. The causes of internal stresses and its importance are explained below.

2.2.3 Internal stress mechanism

The main causes of internal stress generation are thermal mismatch, stiffness mismatch and plastic flow [2]. In metal matrix composites, thermal residual stresses arise due to the manufacturing processes or from changes in working temperature [2]. These stresses are caused by the mismatch of the thermal expansion coefficients between the matrix and the reinforcement, and are important both to the mechanisms of load transfer and to the damage mechanisms that occurs in MMCs [1]. The normal situation for MMCs is that the thermal expansion of the reinforcements is smaller and the elastic stiffness greater than those of the matrix. This means that cooling (e.g. manufacturing) will lead to tensile stresses in the matrix and corresponding compression stresses in the reinforcement. Research has shown that these thermal residual stresses have undesirable effects, such as promoting cavitation and reducing the initial yield stress, relative to its value if there were no internal stress [1, 2].

Plastic flow will occur locally when the stresses generated in the matrix satisfy a yield criterion during loading. This will change the original shape of the hole containing the reinforcement. Therefore, if stress relaxation processes do not occur, the reinforcement must respond by elastic deformation, so creating an internal

stress field. This would result in more load being transferred to the reinforcement as the plastic flow in the matrix increases.

2.3 Stress relaxation

2.3.1 The driving force for relaxation

When taking stress relaxation into consideration, it is essential to understand the distinction between relaxation mechanisms and global plastic flow in the matrix. When global plastic deformation occurs, load is transferred to the reinforcement thus reducing the load carried by the matrix. The stress in the matrix is reduced compared to the unreinforced material during global plastic flow in the matrix [1]. In doing so, it increases the free energy of the system as the misfit increases. This process is unlikely to continue indefinitely because relaxation mechanisms will act to reduce the high stresses in the reinforcement [1]. Stress relaxation mechanisms act to reduce the reinforcement stresses, and hence reduce the overall free energy of the composite. It is the reduction in free energy which is the driving force for stress relaxation, and not simply the reduction of local matrix stresses [1].

Stress relaxation can occur only if it will reduce the free energy of the system and only if a mechanism is available to act [1]. The relaxation mechanisms that operate will depend on the reinforcement size and aspect ratio, the temperature, matrix ductility, and the relative strength of the interfacial bond [1]. Mechanisms of stress relaxation can be classified into two types, those that reduce the reinforcement stress by microstructural modification, and those that introduce micro-damage into the composite [3].

2.3.2 Microstructural modification

(a) Dislocations

Thermally generated misfit strains which were initially present near the matrix reinforcement interface can be accommodated by relaxation due to punching out and movement of dislocations as shown in figure 2.2. This reduces the strain in the region around the reinforcement (i.e., it reduces the misfit).

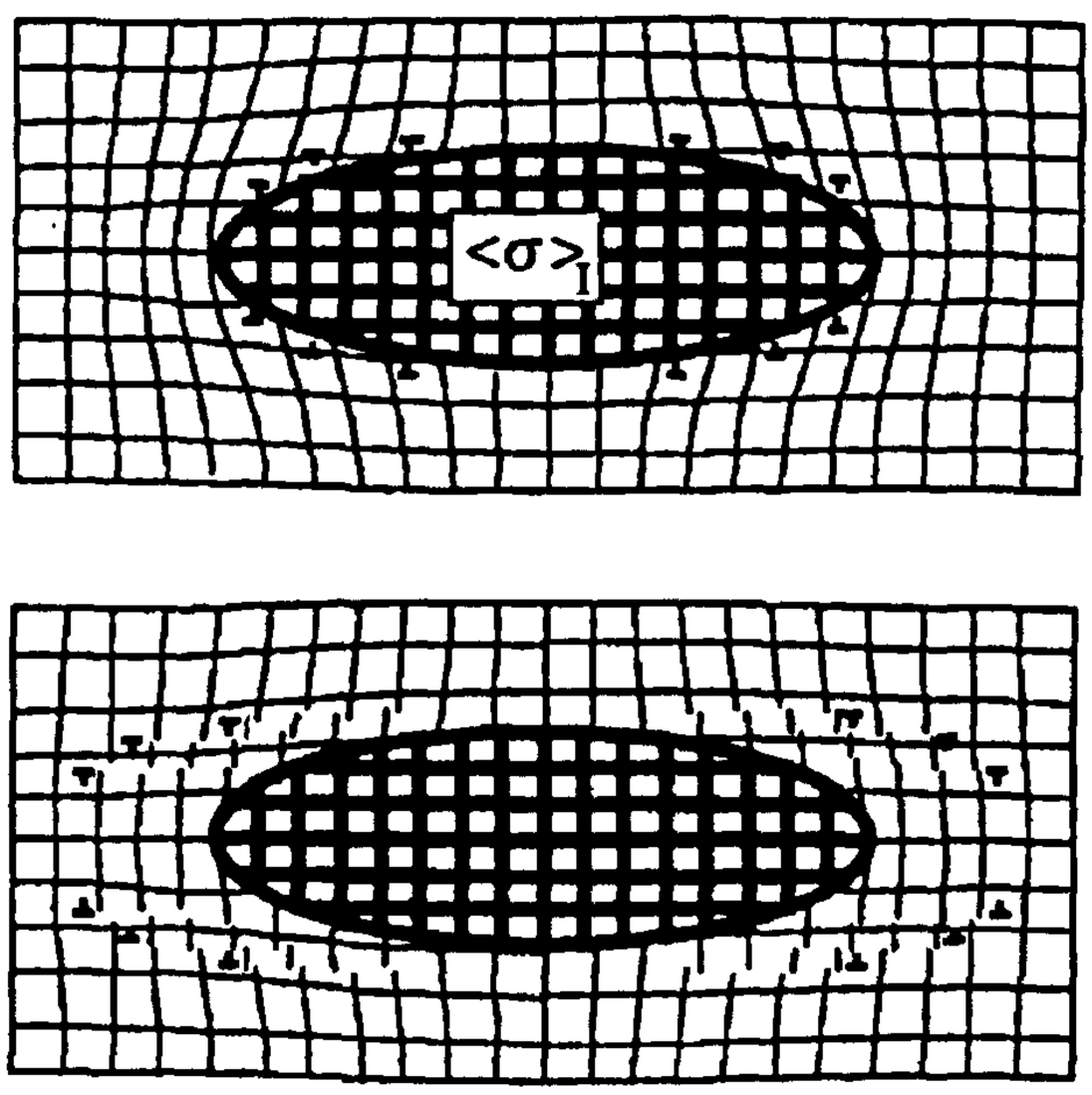

Figure 2.2 Thermally generated misfit strains are relaxed by punching out the dislocations originally present at the matrix/reinforcement interface. This reduces the strain around the reinforcement

Reproduced from reference [3]

(b) Diffusional

The matrix stress distribution generated around the reinforcement is not uniform. This results in stress gradients near the reinforcement that promote diffusion from regions of compressive stress to regions of tensile stress [4-6]. The diffusion path will depend on the temperature. Volume diffusion will dominate at high temperatures. At lower temperatures, a lower energy diffusion path such as

dislocation core, grain boundaries, or matrix/ reinforcement interface will be preferred. All diffusion processes are limited at high strain rates and low temperatures because diffusion is too slow to respond in the available time [1].

(c) Recrystallisation

The inclusion misfit strain at high temperatures can be relaxed by the recrystallisation process. Recrystallisation is likely to be enhanced by the increased dislocation density in the areas of the reinforcement. Microstructural effects such as thermomechanical history [7] and the presence of an oxide dispersion phase in the matrix which will hinder grain boundary migration [8] can also affect the extent of recrystallization. Recrystallization will decrease the hardness of the matrix by reducing dislocation density. As with diffusional relaxation, recrystallization will only be significant at high temperatures.

2.3.3 Micro-damage processes

The following stress relaxation mechanisms are those which cause damage to the microstructure of the composite, and hence influence failure mechanisms. Therefore, it is essential to understand which micro-damage mechanisms are operating in a system and the microstructural factors which influence these.

(a) Reinforcement fracture

For discontinuously reinforced composites, it is not common for stress relaxation to occur due to reinforcement fracture. Reinforcement fracture is only important in cases of high aspect ratio and low volume fraction depending on the magnitude of the stresses developed in the inclusion [1]. For fairly long fibres, a

condition for reinforcement fracture can be calculated using the Shear Lag model [9]. This model assumes that the mechanism of load transfer to the reinforcement during straining is solely due to shear stresses at the matrix reinforcement interface. However, for lower fibre aspect ratios, the tensile transfer at the fibre ends cannot be ignored since it makes a significant contribution to load partitioning.

Reinforcement cracking tends to dominate in composites with low ductility matrices and high interfacial bond strengths. Lloyd et al. [10] investigating Al-SiC composites with different sizes of SiC particulates, found that particle cracking only became a significant damage mechanism when the particle diameter was larger than 20 μm. The fractured particle size distributions were the highest at larger particle size than the mean of the total particle distribution. Larger particles are more prone to crack since they have a higher probability of containing a critical flaw. In general, it has been established that reinforcement cracking is preferred by high aspect ratio, high bond strength and large particle size.

(b) Cavitation and debonding

The interface between the matrix and reinforcement plays a critical role in determining the properties of metal matrix composites [3]. The fundamental failure mechanisms of composites usually happen near the interface between matrix and reinforcement. A well-bonded interface facilitates the efficient load transfer and distribution of load from the matrix to the reinforcing phase, which leads to improved MMC strength. Conversely, load transfer becomes less effective for a weakly bonded interface and therefore limiting the amount of strengthening that can take place. The two main interface failure mechanisms are cavitation and debonding. In particulate or short fibre reinforced MMCs with strong interface bond, ductile

failure occurs by the nucleation, growth, and coalescence of cavitation near the reinforcements or/and within the matrix [11]. For a weakly bonded interface, the reinforcements tend to debond from the matrix in a brittle manner when the local stress (or strain energy release rate) exceeds the interface bond strength [11].

Two main void nucleation modes have been frequently observed in discontinuously reinforced metal matrix composites (figure 2.3)[12]: particle cracking [13-14] and particle metal/interface debonding [15]. This is shown by matching areas of both halves of a fracture surface as shown in figure 2.3. The main factors that influence the mode of nucleation are the interfacial bond strength and the size of the reinforcement. A change from interfacial decohesion to particle cracking has been observed on increasing the interfacial strength [16].

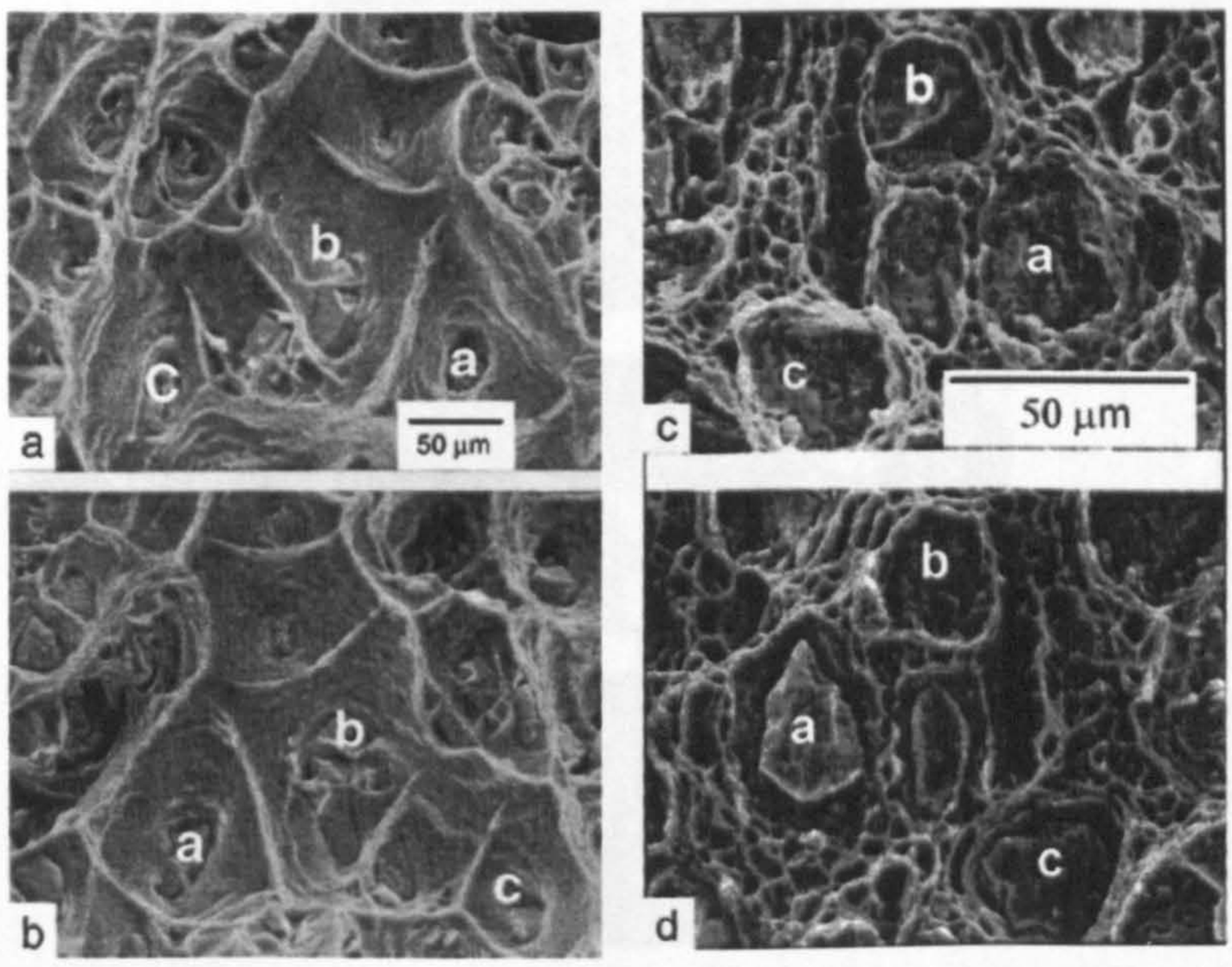

Figure 2.3 Micrographs of matching fracture surfaces of SiC particle reinforced aluminium matrix composites showing (a, b) particle fracture in 1070 aluminium matrix; (c, d) interface debonding in 5050 aluminium matrix
Reproduced from reference [12]

For short fibre reinforcements, failure modes are normally due to formation and coalescence of microvoids within the matrix; nucleation and growth of these

voids ultimately cause interfacial debonding. Voids are generally nucleated in the immediate vicinity of the reinforcement, which is caused by the high triaxial stress state and the increased level of matrix work hardening [17]. TEM work performed by Nutt et al. [17] on deformed microstructure beneath tensile fracture surfaces of Al-SiC composites found that voids of 20-30 nm in diameter were nucleated on the fibre end corner and to have grown toward the centre as well as away from the fibre end (figure 2.4).

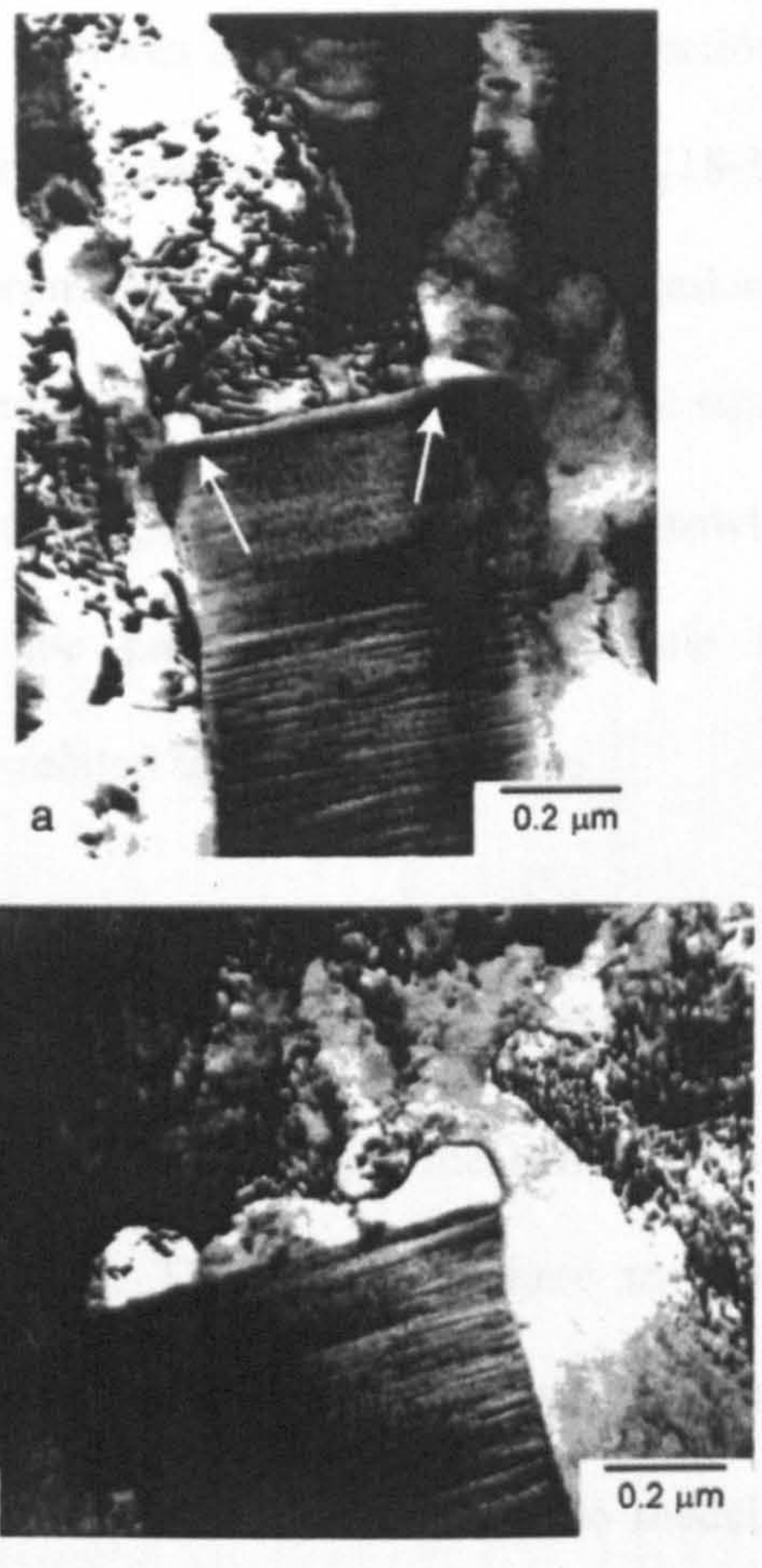

Figure 2.4 Void initiation in tensile fracture specimen of Al-SiC composite (a) void nucleation at corners of the fibre end (shown by arrows) with intense strain in the matrix and (b) void coalescence at the fibre end where voids have initiated at corners and grown toward the centre of the fibre end

Reproduced from reference [17]

It was observed that voids nucleated at the fibre/matrix interface. The growth and coalescence of multiple voids at fibre ends normally resulted in single equiaxed voids that were approximately the same diameter as the fibre. The nucleation of voids is a fairly stable event, needing a considerable plastic strain and does not instantly lead to sudden failure of the composite [18].

The stress state needed for cavitation will depend on the exact nature of the void nucleation event. For a weakly bonded interface, hemispherical voids are most likely formed at the ends of fibres along the loading direction, while voids tend to grow from the matrix for a strongly bonded interface [18-19]. Fisher et al. [20] suggested major reasons promoting the formation of cavitations, such as high matrix flow stress, large reinforcement size, large imposed plastic strain, particle clustering, and small grain size. Knowledge of void nucleation, growth and coalescence in composites is vital for the prediction of their tensile behaviour and creep deformation since they are related to composite failure.

2.4 Modelling internal stresses in composites

Several methods of modelling the mechanical properties of two-phase materials have been proposed. The following three methods describe the three widely used models for calculating the internal stresses (strains) in MMCs. The Eshelby method is described in detail as it is used to model the behaviour of the composite studied.

2.4.1 The Shear Lag model

The shear lag model was first developed by Cox [9] to explain the load transfer in long fibre composites. In this model, it is assumed that the reinforcement

axial stress arises from load transfer across the interface of shear stresses which are generated in the matrix zone close to the fibre and there is no load transfer over the fibre ends. For fibres of finite length and, in the case of particles, unit aspect ratio, the load transfer at the fibre ends cannot be ignored because it makes an important contribution to load partitioning.

Nardone et al. [21] and Clyne [22] have modified the shear lag model to give a more representative description for small aspect ratio reinforcements by taking into account the stress transfer at the ends of the fibres. One such variation assumes the stress at the short fibre ends to be estimated as the average of the maximum stresses possible in the fibre and matrix since the actual value falls between these two. Although this modification gives a more sensible description of the true stress state in the composite, it is not better than Eshelby's method or finite element analyses in predicting the stress in low aspect ratio systems [23].

2.4.2 The Eshelby model

In the 1950's, J.D. Eshelby proposed a technique which was based upon a series of equations that give rise to the stress in an inclusion under a number of different conditions [24]. This technique is based upon a single ellipsoidal inclusion with any aspect ratio, being embedded in a continuous (infinite) matrix. Clyne and Withers have written an excellent review of the principal, uses and limitations of these models [3].

Eshelby used the case of an ellipsoidal inclusion, where the stress state is uniform at any point inside it. The basis for the analysis is the fact that the inclusion does not fit perfectly into the hole in the matrix where it sits. Consider an infinite solid body with stiffness C_M that is initially stress free as shown in figure 2.5a. All

subsequent strains will be measured from this state. Assuming that the inclusion undergoes a shape change such that, if it were a separate body, it will acquire a uniform strain ε^T with no surface traction or stress. ε^T is also known as the transformation strain. This strain might be acquired through a phase transformation, or by a combination of a temperature change and a different thermal expansion coefficient in the inclusion. Because the inclusion is bonded to the matrix, when the transformation occurs the whole body develops some complicated strain field ε^C relative to its original shape before the transformation. By using Hooke's Law, the stress in the matrix, σ_M, is given by

$$\sigma_M = C_M \varepsilon^C \qquad (2.2)$$

but within the inclusion the transformation strain does not contribute to the stress, so the inclusion stress is given by

$$\sigma_I = C_M (\varepsilon^C - \varepsilon^T) \qquad (2.3)$$

where C_M is the stiffness tensor of the matrix material.

The main result of Eshelby was to show that within an ellipsoidal inclusion the strain ε^C is uniform and is related to the transformation strain by

$$\varepsilon^C = S\, \varepsilon^T \qquad (2.4)$$

S is called the Eshelby tensor, and it depends only on the inclusion aspect ratio and the Poisson's ratio of the material. The strain field outside the inclusion (in the matrix) is highly non-uniform because the original stress free transformation takes place inside but not outside the inclusion. However, this part of the solution can be normally ignored.

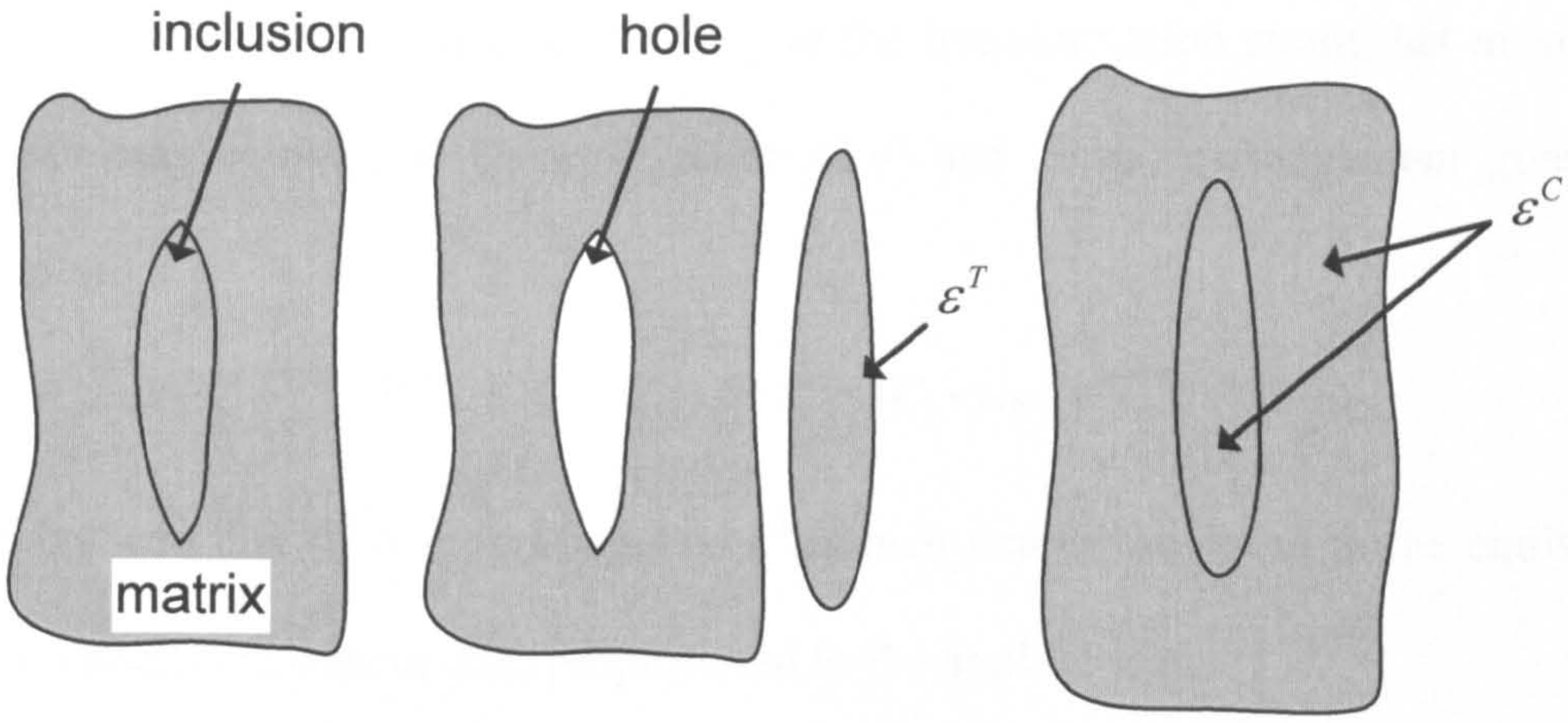

Figure 2.5 Schematic illustration of Eshelby's inclusion problem: (a) Stress free state (b) Inclusion undergoes a stress free transformation strain ε^T and (c) Joining the inclusion and matrix together produces the strain state ε^C in both the inclusion and the matrix [3]

From here the situation can be extended to demonstrate an equivalence between the homogeneous problem and an inhomogeneous (real inclusion) of the same shape. Consider two infinite solid bodies of matrix as shown in figure 2.6. One body has a homogeneous inclusion with some transformation strain ε^T (figure 2.6a), while the other body has a real inclusion with a stiffness C_I, but no transformation strain (figure 2.6b). We need to find the transformation strain ε^T that gives the two problems the same stress and strain distributions when both bodies are subjected to an applied strain ε^A at infinity. For the first body (figure 2.6a), the inclusion stress is just equation (2.3) with the applied strain added which gives

$$\sigma_I = C_M(\varepsilon^A + \varepsilon^C - \varepsilon^T) \qquad (2.5)$$

while the second body (figure 2.6b) has no ε^T but a different stiffness, giving a stress of

$$\sigma_I = C_I(\varepsilon^A + \varepsilon^C) \qquad (2.6)$$

Equating equations (2.5) and (2.6) will give the transformation strain that makes the two problems equivalent. Using equation (2.4) and some rearrangement gives the expression

$$-[C_M + (C_I - C_M)\, S]\, \varepsilon^T = (C_I - C_M)\, \varepsilon^A \qquad (2.7)$$

It can be seen that ε^T is proportional to ε^A, which makes the stress in the equivalent inhomogeneity (real inclusion) proportional to the applied strain.

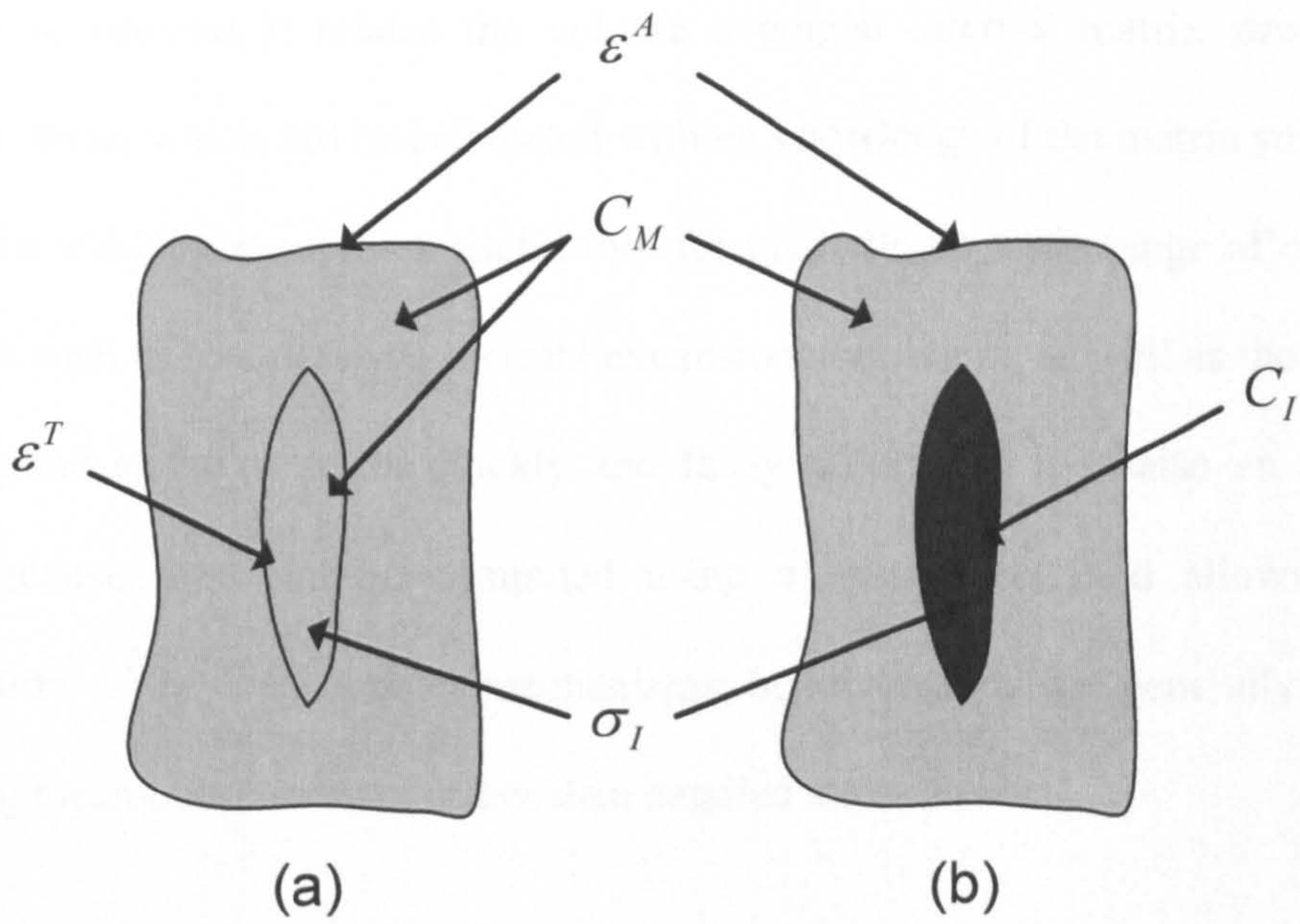

Figure 2.6 Schematic illustration of Eshelby's equivalent inclusion problem. When both bodies are subjected to a far field strain ε^A, the inclusion in (a) with transformation strain ε^T has the same stress σ_I and strain as the real inclusion (b) [3]

Up to now, the outlined theory has only concentrated on a single ellipsoidal inclusion embedded within a matrix. This is not really suitable because most composite systems have between 20 to 35 vol.% reinforcement. The presence of further inclusions will have an effect on the stresses experienced by an individual inclusion. This can be included into the Eshelby approach by using the theory of background stress, which is also known as mean field (phase) stress, first proposed by

Brown et al. [25] for a single inclusion. By modifying this to take the volume fraction of reinforcement into account, the following equation is obtained

$$\sigma_f v_f + \sigma_m v_m = 0 \qquad (2.8)$$

This method treats the inclusion as being randomly distributed in the matrix, ignoring all the interactions between individual inclusions. This random distribution is commonly exhibited by many types of composite system. Therefore, equation (2.8) is very useful, because it relates the volume averaged internal matrix stress to the inclusion stress, which can be calculated without knowledge of the matrix stress field.

The Eshelby model is a useful tool for predicting a wide range of composite properties such as modulus and thermal expansion coefficient, as well as the response to an applied stress or strain quickly and fairly accurately. It is also an attractive model because they can be computed using a spreadsheet, and allows a clear visualisation of the load transfer mechanisms; however, they are generally better at predicting mean phase stresses rather than detailed stress fields.

2.4.3 Finite element analysis

Finite element analysis has become increasingly popular in the study of the mechanical behaviour of composites due to great improvements in computing power and software development. The thermomechanical history, phase geometry and non-uniform local stress and strain fields can be included readily and the dependence of the macroscopic mechanical properties on phase geometries, the amount of load transfer from the matrix to the reinforcement and the constrained matrix deformation can be determined.

Both finite element and boundary element methods have been used to determine the effects of variables such as reinforcement shape, spacing etc., on composites' properties [26-30]. In general, in these analyse, modelling the elastic and plastic properties of the composites needs idealisation of material behaviour and of phase geometry which may not represent the actual morphology or behaviour of the material.

2.5 Creep

2.5.1 Creep of metals

Creep may be defined as the process by which thermally activated flow occurs when a constant stress is applied to a metal for a prolonged period of time. As the deformation mechanisms responsible for creep are thermally activated, for most metals, it is significant only at elevated temperature (T/0.3-0.4 T_m where T_m is the melting temperature of the material in Kelvin). At temperatures above 0.3 T_m, dislocations can climb as well as glide, grains slide over each other at grain boundaries and vacancies diffuse. These cause the phenomenon of material creep.

The curve can conveniently be split up into sections as indicated in figure 2.7. All stages of creep are not necessarily exhibited by a particular material for given experimental testing conditions. In the primary region the specimen usually extends very quickly but slows down as work hardening (strain hardening) sets in and the strain rate decreases. During secondary creep, the deformation continues at a constant rate. In this stage, a balance exists between the rate of work hardening and the rate of softening because of recovery or recrystallization. The secondary creep may be essentially plastic in character, depending on the stress level and temperature. When the stress is sufficiently high and temperature is also high, there

is a tertiary stage in which the creep rate increases until fracture. Tertiary creep is more probably caused by the result of structural changes occurring in the material. Evidence has been found for void formation and extensive crack formation during this stage.

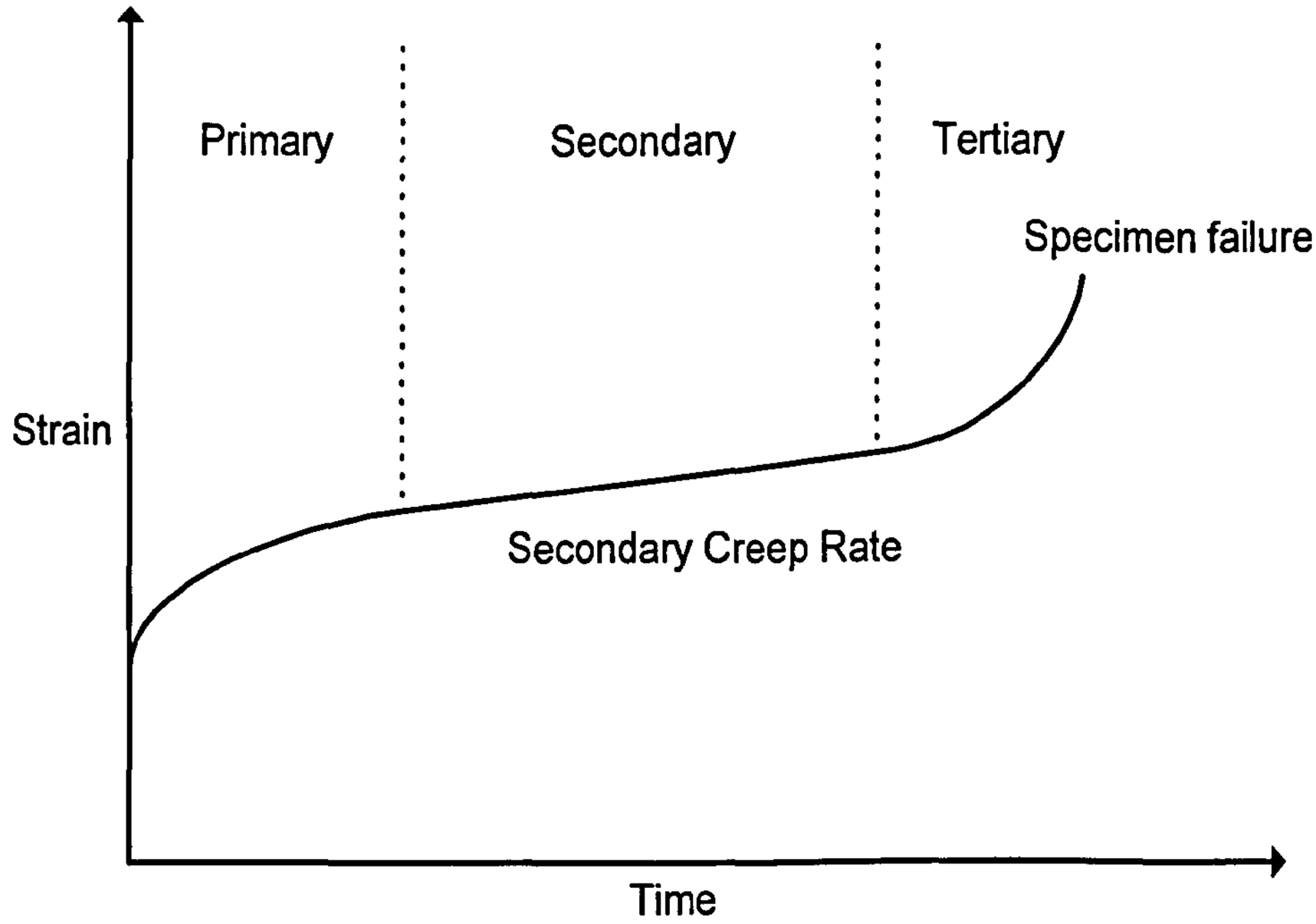

Figure 2.7 Schematic representation of a typical creep deformation curve during testing under a constant applied load

It is well known that the high temperature creep of metallic materials can be described by the power law relationship

$$\dot{\varepsilon}_m = A\sigma^n \exp(\frac{-Q}{RT}) \qquad (2.9)$$

where $\dot{\varepsilon}_m$ is the minimum creep rate, A is a structure dependent parameter, σ is the applied stress, n is the apparent stress exponent, Q is the true activation energy, R is the universal gas constant and T is the absolute temperature. This power law

relationship appears to provide an excellent description of the steady state creep behaviour [31].

The creep of copper has perhaps been studied more than that of any other metals [32-37]. The central interests in these studies are on which mechanisms control creep under specific temperature and stress conditions by comparing values of the stress exponent, n and activation energy, Q based on the power law interpretation [32-37]. The interpretation of rate controlling mechanism(s) during creep is usually based on these two values. Under steady state conditions it is assumed that processes governing work hardening closely match those of recovery and therefore a steady state is attained. For copper and most pure metals deforming in the high stress region, the stress exponent is usually in the range 4-7 [37].

2.5.2 Creep of composites

Composites reinforced with continuous fibres normally constitute an extreme, upper bound, of strength, and the behaviour is viscoelastic with the matrix forming the viscous part, in parallel coupling with the elastic fibres [2]. For composites with short aligned fibres, they have an initial primary creep (viscoelastic) and a steady-state creep rate where sections of the matrix which are not supported by fibres (e.g. between ends of fibres), contribute to creep with a constant creep rate. Composites reinforced with particles have virtually no steady state creep, and these particles cause the early initiation of creep damage (e.g. voids) in the matrix, which leads to a very long tertiary creep. Typical creep curves for metal matrix composites for long continuous fibres, short fibres and particles are shown in figure 2.8.

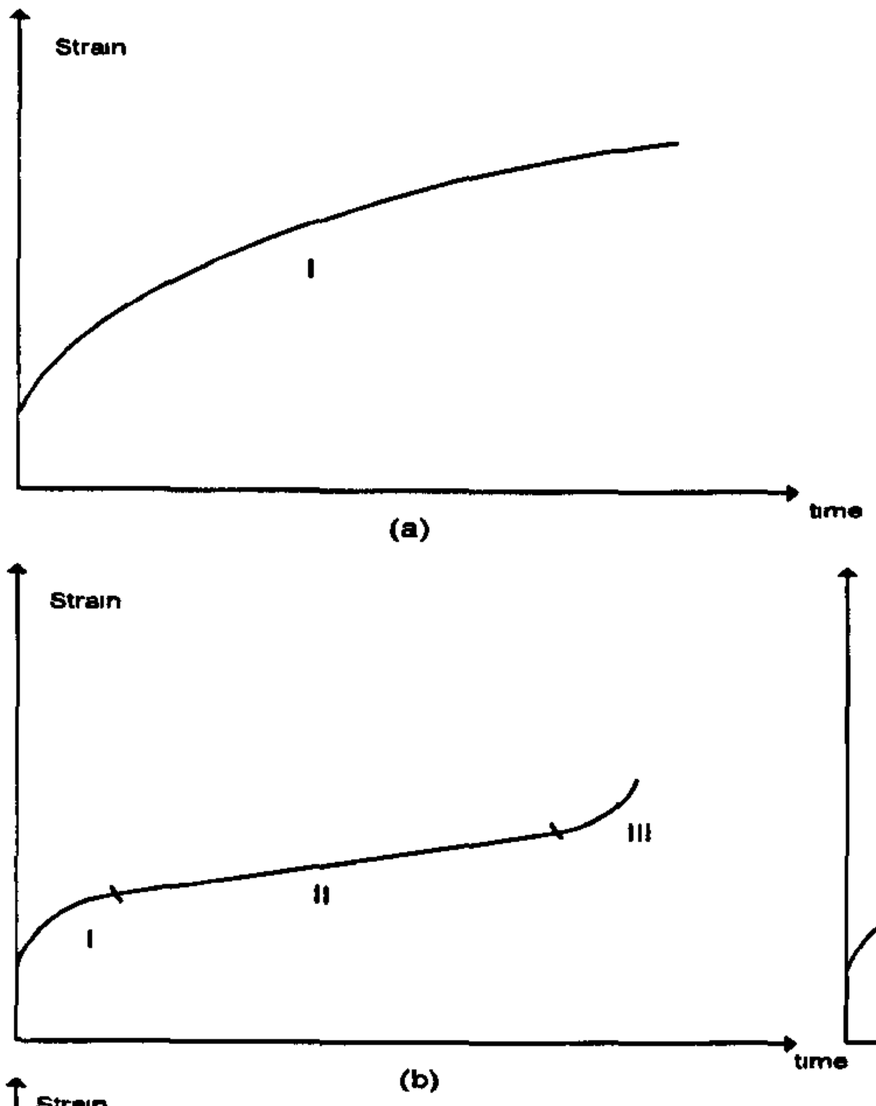

I – Primary creep II – Secondary creep III -Tertiary creep

Figure 2.8 Typical creep curves for metal matrix composites (a) long continuous fibres; (b) short fibres; (c) particles
Reproduced from reference [2]

In recent years, extensive investigations have been carried out to determine the creep properties of discontinuously reinforced aluminium-based composites due to a growing interest in assessing the potential use of these composites for use as materials for high temperature applications [38-48]. The creep behaviour of these composites is unique in two ways. Firstly, the stress dependence of the creep rate, expressed by the value of stress exponent n, is very high (greater than 20), and in some cases, variable [38-48]. Secondly, the temperature dependence of the minimum creep rate, which is measured by the creep activation energy Q, is much higher (greater than 250 kJ/mol) than that for self-diffusion in aluminium.

Nieh et al. [38] reported that the creep behaviour for composites consisting of 6061Al reinforced with SiC particles and whiskers in the temperature range 504 - 644 K. They found that the steady state creep rate in both materials depends strongly on the applied stress and temperature; the stress exponent was very high (n = 21) and the activation energy was about three times as high as the activation energy for self-diffusion in aluminium.

Nardone et al. [44] investigated the effects of stress and temperature on the creep behaviour of SiC whisker reinforced 2124 Al composite and found that the stress exponent changes from 8.4 at 450 K to 21 at 561 K. The measured activation energies increased from 277 kJ/mol in the temperature range of 423 - 477 K to 431 kJ/mol at 547 - 575 K.

The apparent stress exponent values are usually greater than 20 and the apparent activation energy values are often greater than 250 kJ/mol (the activation energy for self diffusion of aluminium is 142 kJ/mol). The concept of threshold stress has been used by many researchers to rationalize the strong stress and temperature dependence of the creep rate for these composites. In this respect, the power law creep equation

$$\dot{\varepsilon}_m = A\sigma^n \exp(\frac{-Q}{RT})$$

can be modified as (2.10)

$$\dot{\varepsilon}_m = A'\left(\frac{\sigma - \sigma_o}{G}\right)^{n_o} \exp(\frac{-Q}{RT})$$

where $\dot{\varepsilon}_m$ is the minimum creep rate, A and A' are structure dependent parameters, σ is the applied stress, σ_o is the threshold stress, G is the temperature dependent shear modulus, n is the apparent stress exponent, n_o is the true stress exponent, Q is

the true activation energy R is the universal gas constant and T is the absolute temperature. Normally, these lower values are often similar in magnitude to those anticipated from the creep of pure metals.

It is well known that on stressing a composite the load will be transferred to the reinforcement, which has the effect of partially unloading the matrix. As a result, the creep life and the creep strength of the matrix are greatly improved by the addition of the reinforcement phase. The creep rate of the matrix metal alone can be several orders of magnitude higher than the creep rate of the MMC.

Park et al. [45] reported that the creep behaviour of powder metallurgy Al - 30 vol.% SiCp/6061 composite and unreinforced 6061 Al alloy under the same testing condition. They found that the creep resistance of the composite is one order of magnitude higher than that of the unreinforced alloy. A similar result was obtained by Peng et al. [46] for whisker reinforced 8009Al composites where the creep rate of the Al – 15 vol.% $Al_{18}B_4O_{33}w$/8009 and Al – 15 vol.%SiCw/8009 composites were about two orders of magnitude lower than that of the unreinforced 8009 Al alloy. Higher creep resistance results from partial load transfer to the reinforcement with a corresponding reduction in the effective stress acting on the matrix.

On the other hand, the absence of creep strengthening was also observed in Al-based composites. Mohamed et al. [47] reported the creep behaviour of powder metallurgy Al - 10 vol.%SiCp/2124 composite and monolithic 2124 Al alloy under the same testing condition. They found that the creep strength of the composite became essentially the same at high strain. The loss of strengthening at high strain rates was due to the debonding of SiC particulates from the 2124 Al matrix. Similar behaviour was also observed by Tjong et al. [48] in the creep properties of powder

metallurgy Al-SiC composites and pure Al at 573 - 673 K. They showed that the incorporation of small SiC particulates (3.5 μm) into Al decreases the creep rate of the Al matrix by about three orders of magnitude while large SiC particulates (10-20 μm) did not provide any strengthening at all as shown in figure 2.9.

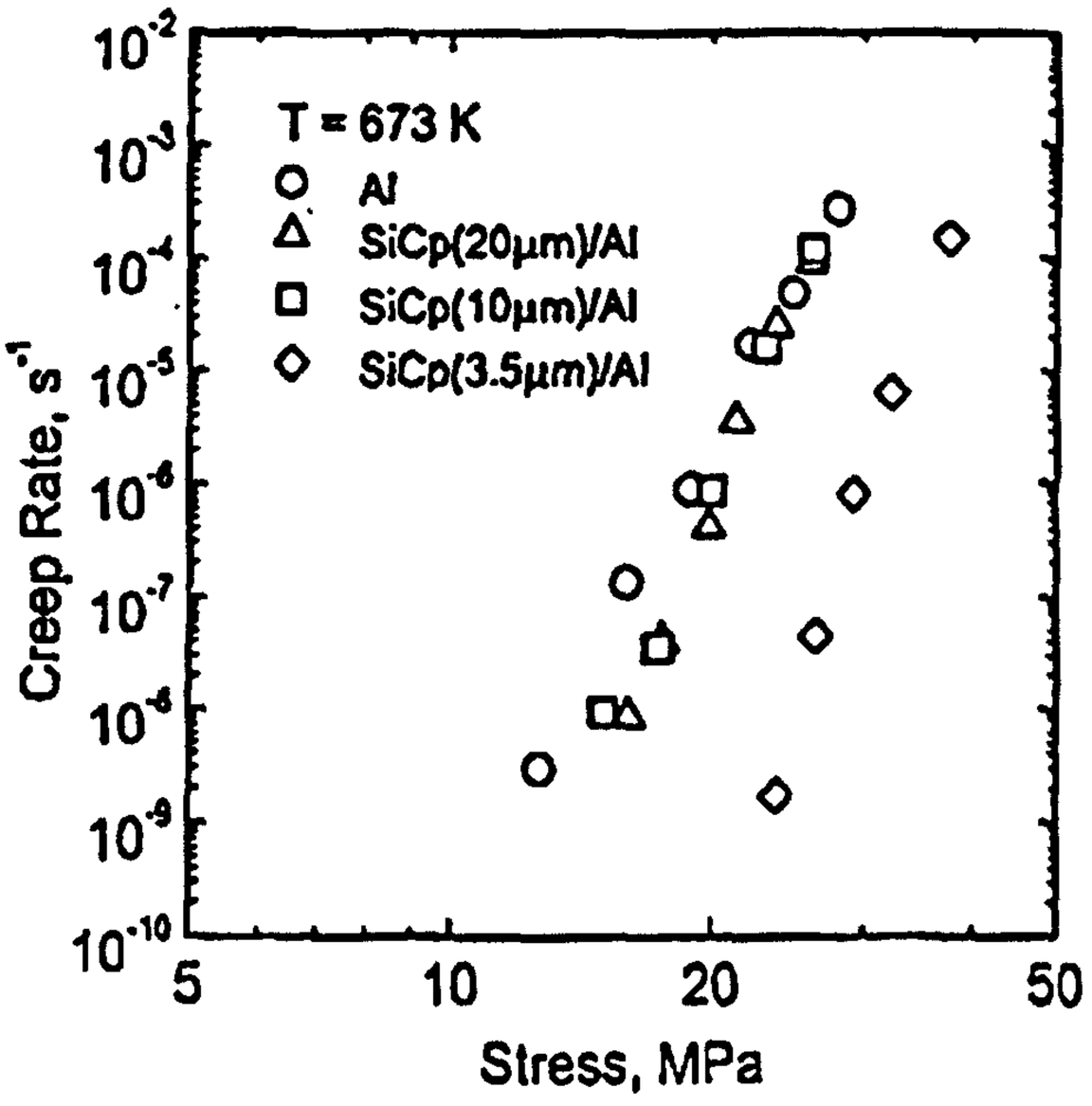

Figure 2.9 Variation minimum creep rate with applied stress for both unreinforced pure Al and Al - 10 vol.%SiCp/2124 composite at 673 K
Reproduced from reference [48]

The creep properties of both reinforced and unreinforced Al are controlled by fine oxide particulates introduced during PM processing of the materials. The large SiC particulates do not improve the creep properties of pure Al because the interparticle spacing for SiC particulates was about two orders of magnitude larger than that for fine oxide particles [48].

Krajewski et. al [49] studied the influence of SiC particulate reinforcement on the creep behaviour of 2080 Al composite at 423 – 623 K. They found that the composites were less creep resistant than monolithic alloys crept at 423 K. These results were in poor correlation with continuum mechanics models for direct

reinforcement strengthening [50-51]. The models predicted that the reinforcing particle improves the creep resistance by reducing the effective stress for creep deformation. However, SiC particulates improved the creep resistance of 2080 Al composite at the higher temperature of 623 K.

References

1 A.F. Whitehouse, Damage and Failure of Discontinuously Reinforced Aluminium Composites During Tensile Deformation, PhD Thesis, University of Cambridge, 1993.

2 H. Lilholt, Aspects of deformation of metal matrix composites. Materials Science & Engineering A-Structural Materials Properties Microstructure & Processing, 1991. A135: 161-171.

3 T.W. Clyne and P.J. Withers, An Introduction To Metal Matrix Composites, Cambridge University Press, (1993).

4 J. Rosler, G. Bao and A.G. Evans, The Effect of Diffusional Relaxation on the Creep Strength of Composites, Acta Metallurgica et Materialia, 1991. 39(11): 2733-2738.

5 R. Monzen, M. Kato and T. Mori, Diffusional Relaxation around Martensitically Transformed Fe-Co Particles in a Cu Matrix, Acta Metallurgica et Materialia, 1989. 37(12): 3177-3182.

6 F.R. Brotzen and A. Seeger, Diffusion near Dislocations, Dislocation Arrays and Tensile Cracks, Acta Metallurgica et Materialia, 1989. 37(11): 2985-2992.

7 Y. Liu, N.Hansen and D.J. Jensen, Recrystallisation microstructure in cold-rolled aluminium composites reinforced by silicon carbide whiskers, Metallurgical Transactions, 1989. 20A: 1743-1753.

8 R.A. Shahani and T.W. Clyne, Recrystallisation in fibrous and particulate MMCs, Materials Science and Engineering A, 1991. A135: 281-285.

9 H.L. Cox, The elasticity and strength of paper and other fibrous. British Journal of Applied Physics, 1952. 3: 72-79.

10 D. Lloyd, Aspects of particle fracture in particulate reinforced MMCs. Acta Metallurgica, 1991. 39: 59-72.

11 J.K. Kim and Y.W. Mai, Effect of interface strength on MMC properties. Comprehensive Composite Materials, edited by T.W. Clyne

12 P.M. Mummery, B. Derby and C.B. Scruby, Acoustic emission from particulate-reinforced metal matrix composites. Acta Metallurgica et Materialia, 1993. 1(5): 1431-1445.

13 C.P. You, A.W. Thompson and I.M. Bernstein IM, Proposed failure mechanism in a discontinuously reinforced aluminium alloy. Scripta Metallurgica, 1987. 21(2): 181-185.

14 D. Lloyd, Aspects of particle fracture in particulate reinforced MMCs. Acta Metallurgica, 1991. 39: 59-72.

15 J.J. Stephens, J.P. Lucas and F.M. Hosking, Cast Al-7 Si composites: effect of particle type and size on mechanical properties. Scripta Metallurgica, 1988. 22(8): 1307-1312.

16 L.M. Tham, M. Gupta and L. Cheng, Effect of limited matrix-reinforcement interfacial reaction on enhancing the mechanical properties of aluminium-

silicon carbide composites. Acta Metallurgica et Materialia, 2001. 49: 3243-3253.

17 S.R. Nutt and A. Needleman, Void nucleation at fibre ends in Al-SiC composites. Scripta Metallurgica, 1987. 21: 705-710.

18 A.F. Whitehouse and T.W. Clyne, Cavity formation during tensile straining of particulate and short fibre MMCs. Acta Metallurgica, 1993. 41(6): 1701-1711.

19 A.F. Whitehouse and T.W. Clyne, Effects of reinforcement content and shape on cavitation and failure in metal-matrix composites. Composites, 1993. 24(3): 256-261.

20 J.R. Fisher and J. Gurland, Void nucleation in spheroidized carbon steels, part 1. Metal Science, 1981. 15: 185-202.

21 V.C. Nardone and K.M. Prewo, On the strength of discontinuous silicon carbide reinforced aluminium composites. Scripta Metallurgica, 1986. 20(1): 43-48.

22 T.W. Clyne, A simple development of the shear lag theory appropriate for composites with a relatively small modulus mismatch. Materials Science & Engineering A-Structural Materials Properties Microstructure & Processing, 1989. A122(2): 183-192.

23 O.B. Pedersen and P.J. Withers, Iterative estimates of internal stresses in short-fibre metal matrix composites. Philosophical Magazine A-Physics of Condensed Matter Defects & Mechanical Properties, 1992. 65(5): 1217-1233.

24 J.D. Eshelby, The Determination Of The Elastic Field Of An Ellipsoidal Inclusion, And Related Problems", Proceeding Royal Society, 1957. A241: 376-396.

25 L.M. Brown and W.M. Stobbs, The Work Hardening of Cu-SiO_2-I. A Model Based On Internal Stresses. Philosphical Magazine, 1971. 23: 1185-1199.

26 N. Shi and R.J. Arsenault, Influence of thermally induced plasticity on the Bauschinger effect of SiC/Al composites. Metallurgical Transactions A-Physical Metallurgy & Materials Science, 1993. 24A(8): 1879-1882.

27 T. Christman, A. Needleman and S. Suresh, An experimental and numerical study of deformation in metal-ceramic composites. Acta Metallurgica, 1989. 37(11): 3029-3050.

28 T. Christman, A. Needleman and S. Suresh, An analysis of the effects of matrix void growth on deformation and ductility in metal-ceramic composites. Acta Metallurgica et Materialia, 1991. 39(10): 2317-2335.

29 M. Dong and S. Schmauder, Modelling of metal matrix composites by a self-consistent embedded cell model. Acta Materialia, 1996. 44(6): 2465-2478.

30 J. Wulf, T. Steinkopff and H.F. Fischmeister, FE-simulation of crack paths in the real microstructure of an Al(6061)/SiC composite. Acta Materialia, 1996. 44(5): 1765-1779.

31 R.W. Evans and B. Wilshire, Introduction to Creep, 1993.

32 H.D. Chandler, Creep of copper in the temperature range 423-623 K. Materials Science & Engineering A-Structural Materials Properties Microstructure & Processing, 1993. A169(1-2): 27-32.

33 R.P. Reed, N.J. Simon and R.P. Walsh, Creep of copper: 4-300 K. Materials Science & Engineering A-Structural Materials Properties Microstructure & Processing, 1991. A147(1): 23-32.

34 E.C. Muehleisen, C.R. Barrett and W.D. Nix, On the high temperature-low stress creep of copper. Scripta Metallurgica, 1970. 4(12): 995-999.

35 M.D. Hanna and G.W. Greenwood, Cavity growth and creep in copper at low stresses. Acta Metallurgica, 1982. 30(3): 719-724.

36 O. Masateru and R. Imamura, A study on the effect of vacuum environments on creep rupture property of a commercial pure copper at elevated temperature. Proceedings of the Japan congress on materials research, 1980. 132-137.

37 T. Main, Creep of copper, Master's thesis, 1995, University of Wales.

38 T.G. Nieh, Creep rupture of a silicon carbide reinforced aluminium composite. Metallurgical Transactions A-Physical Metallurgy & Materials Science, 1984. 15A(10): 39-46.

39 H.M.A. Winand, P.J. Withers and A.F. Whitehouse. Measurement of cavitation damage in isothermally crept Al/SiC composites using small-angle neutron scattering. Physica B, 1997. 234-236: 1022-1023.

40 A.F. Whitehouse, H.M.A. Winand and T.W. Clyne, The effect of processing route and reinforcement geometry on isothermal creep behaviour of particulate and short fibre MMCs. Materials Science & Engineering A-Structural Materials Properties Microstructure & Processing, 1998. A242: 57-69.

41 A.F. Whitehouse and H.M.A. Winand, The tensile creep response of Al-SiC particulate and whisker composites. Scripta Materialia, 1999. 41(8): 817-822.

42 H.M.A. Winand, A.F. Whitehouse and P.J. Withers, An investigation of the isothermal creep response of Al-based composites by neutron diffraction. Materials Science & Engineering A-Structural Materials Properties Microstructure & Processing, 2000. 284(1-2): 103-113.

43 T.L. Dragone and W.D. Nix, Steady state and transient creep properties of an aluminium alloy reinforced with alumina fibers. Acta Metallurgica et Materialia, 1992. 40(10): 2781-2791.

44 V.C. Nardone and J.R. Strife, Analysis of the creep behaviour of silicon carbide whisker reinforced 2124 Al (T4). Metallurgical Transactions A-Physical Metallurgy & Materials Science, 1987. 18A(1): 109-114.

45 K.T. Park and F.A. Mohamed, Creep strengthening in a discontinuous SiC-Al composite. Metallurgical & Materials Transactions A-Physical Metallurgy & Materials Science, 1995. 26A(12): 3119-3129.

46 L.M. Peng, S.J. Zhu, Z.Y. Ma, J. Bi, F.G. Wang, H.R. Chen and D.O. Northwood, High temperature creep deformation of Al/sub 18/B/sub 4/O/sub 33/ whisker-reinforced 8009 Al composite. Materials Science & Engineering A-Structural Materials Properties Microstructure & Processing, 1999. A265(1-2): 63-70.

47 L. Yong and F.A. Mohamed, An investigation of creep behaviour in an SiC-2124 Al composite. Acta Materialia, 1997. 45(11): 4775-4785.

48 S.C. Tjong and Z.Y. Ma, High-temperature creep behaviour of powder-metallurgy aluminium composites reinforced with SiC particles of various sizes. Composites Science & Technology, 1999. 59(7): 1117-1125.

49 P.E. Krajewski, J.E. Allison and Jones, The effect of SiC particle reinforcement on the creep behaviour of 2080 aluminium. Metallurgical &

Materials Transactions A-Physical Metallurgy & Materials Science, 1997. 28A: 611–620.

50 L.C. Davis, J.E. Allison, Micromechanics effects in creep of metal matrix composites. Metallurgical & Materials Transactions A-Physical Metallurgy & Materials Science, 1995. 26A: 3081–3090.

51 G. Bao, J.W. Hutchinson and R.M. McMeeking, Particle reinforcement of ductile matrices against plastic flow and creep, Acta Metall. 1991. 39:1871-1882.

Chapter 3

In-situ Composites

3.1 Introduction

Considerable work is being done on the deformation of two-phase materials. Instead of reviewing all of this literature, this chapter will focus on some of the important findings related to the deformation behaviour of Cu-based composites.

3.2 In-situ composites

Composite materials are produced by combining two or more materials into a new material that may be better suited for a particular application than either of the original materials alone. Although composite material systems are not the solution to every materials design problem, the base applications for which composites are used continue to broaden. Composites have been called "materials of the future" because their properties are superior to those of conventional materials. Basically, composites can be classified into three categories:

I. Reinforcement by long continuous or unbroken fibres or filaments with diameters of around 100 μm. The filaments can consist of smaller diameter fibres spun into a yarn.
II. Reinforcement by whiskers, or chopped fibres with diameters around 1 μm.
III. Reinforcement by particulates, which are approximately equiaxed particles.

The last two are known as discontinuously reinforced while the former is continuously reinforced.

This general concept of a composite material is also applicable for metal matrix composites (MMCs), where a good ductility of the metal matrix is usually

combined with the high strength and stiffness of the reinforcement phase. A good example would be Al reinforced with micron-scale SiC particles. The Al matrix has high fracture toughness and formability but low hardness and stiffness, while the SiC has exceptional hardness and stiffness but poor fracture toughness. Therefore, when this composite is manufactured, it will possess a toughness and formability of Al and the stiffness and wear resistance of SiC [1]. A typical application of Al-SiC composites is the disc brake rotor [1]. The major drawback of this composite includes brittleness, highly anisotropic properties and high cost of manufacture [1].

In view of the mediocre mechanical properties of relatively pure, highly conducting Cu alloys there is interest in developing Cu matrix composite materials for electrical applications [2,3,5]. Ideally, the reinforcing phase should be fibrous to achieve optimal mechanical properties without seriously compromising conductivity. Composites based on metallic reinforcements have the advantages of some conductivity in the second phase as well as having ductile characteristics. During the past 25 years, a new generation of Cu conductive materials (Cu-X) [2-14], which possessed extraordinary mechanical and electrical properties, have been developed within the framework of metal matrix composites. These composites, comprised of Cu (FCC) with element X (where X is a BCC metal immiscible in Cu such as Nb, Cr, Fe, Mo or V) can be formed by mechanical working (swaging, extrusion, rolling or drawing) of ductile two phase mixtures prepared by using liquid phase sintering, casting or powder metallurgy techniques [1].

Deformation processing consists of deforming a precursor billet to a very large deformation, usually a true strain, η, (defined as the natural log of the initial cross sectional area of the specimen over the final cross sectional area after deformation) of greater than around 3 (equivalent to a reduction in area of

approximately 95 %). At these large deformations the X metal deforms into aligned ribbon shaped fibres in the Cu matrix. Figure 3.1 shows the typical transverse cross sections of the Cu-based composite; the ribbon-like morphology of the fibre is clearly evident here [10].

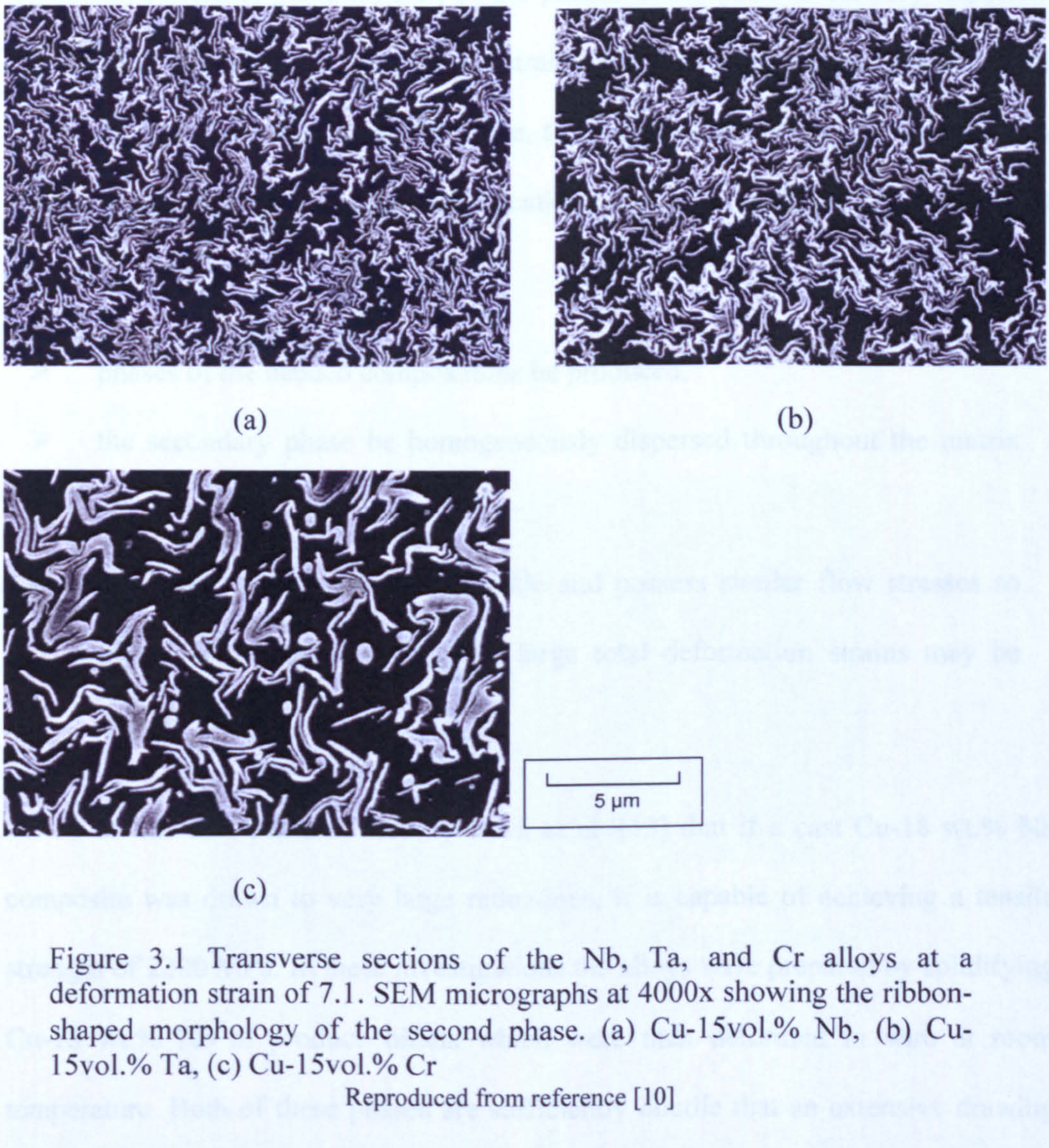

Figure 3.1 Transverse sections of the Nb, Ta, and Cr alloys at a deformation strain of 7.1. SEM micrographs at 4000x showing the ribbon-shaped morphology of the second phase. (a) Cu-15vol.% Nb, (b) Cu-15vol.% Ta, (c) Cu-15vol.% Cr

Reproduced from reference [10]

In these composites, the volume fractions of the secondary phase are relatively low (≤ 20 %) so that it exists as isolated particles in a powder compact or isolated dendrites in a casting. Terminologically, this kind of material is generally referred to as an "in-situ composite" because during deformation processing both

phases equally deform with the result that fibres with very large aspect ratios are formed in a matrix material [1]. The key factor in the formation of these composites depends on the starting materials [11]. The first step in the preparation of these composites is the manufacture of a billet of a two-phase alloy. The initial shape (spherical, dendritic, globular, etc.) of the phases in the billet is not very important because when very large deformation strains are employed, aligned fibres of the secondary phase are produced. Therefore, the initial billet can be manufactured by powder processing technique or solidification. The requirements of the processing are that

- phases of the needed compositions be produced,
- the secondary phase be homogeneously dispersed throughout the matrix phase,
- both phases are sufficiently ductile and possess similar flow stresses so that co-deformation occurs and large total deformation strains may be applied.

It was first demonstrated by Bevk et al. [13] that if a cast Cu-18 wt.% Nb composite was drawn to very large reductions, it is capable of achieving a tensile strength of 2200 MPa. In these investigations the alloys were prepared by solidifying Cu-18 wt.% Nb to produce billets which were then deformed to wire at room temperature. Both of these phases are sufficiently ductile that an extensive drawing of $\eta = 11.5$ may be done without need for annealing. The electrical conductivity of these materials was also found to be excellent, greater than 60 % of the International Annealed Copper Standard (% IACS). The main factor in achieving high strength levels in these in-situ composites was the ability of the fibre phase to be deformed

large amounts without the need for thermal stress relief anneals, as this leads to coarsening of the fine fibres. It is this unique combination of high strength and high electrical conductivity that is of great engineering interests because Cu-based composites are seldom used for their strength alone, and applications whose only requirement is high conductivity are best served by pure Cu.

The remarkable malleability of the Cr phase has been shown in the production of fibres, in spite of the brittle nature of pure Cr at room temperature. This was first studied by Funkenbusch et al. [11,12] in a Cu-17vol.% Cr alloy drawn into wires (figure 3.2). The strength of the composite increased with increasing true drawing strain, reaching 840 MPa at a drawing strain of 6.3, which was higher than that predicted by the rule of mixtures.

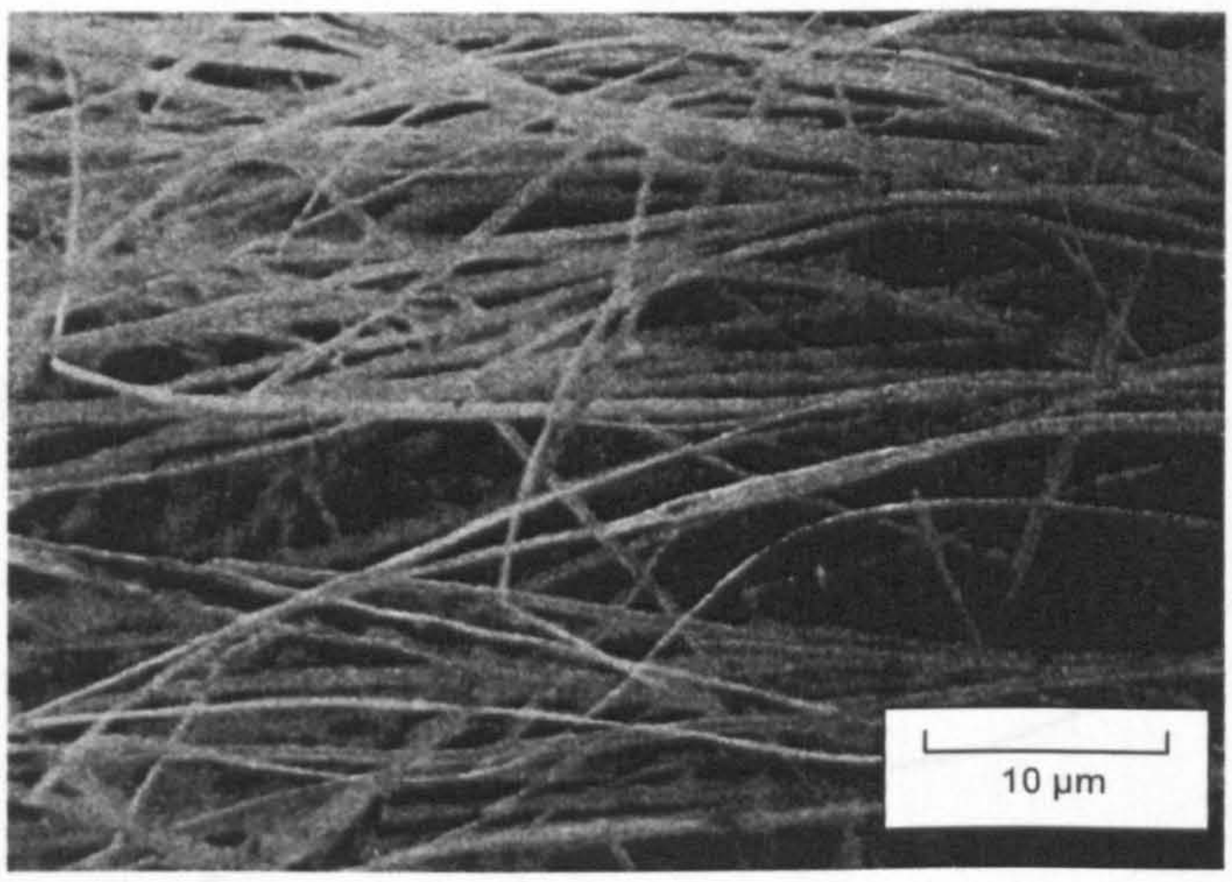

Figure 3.2 Cr fibres extracted from Cu-17vol.% Cr alloy
Reproduced from reference [11]

What is extraordinary is the behaviour of the individual Cr dendrites which, in contrast with the behaviour of bulk Cr at room temperature, show extensive plasticity and are drawn into long fibres [11,12]. This unusual behaviour of Cr in the composite is believed to be due to its initial morphology. Fine and isolated Cr dendrites were produced during the casting of this alloy. If the brittle behaviour of

bulk Cr is due to its inability to accommodate strain incompatibilities arising between neighbouring grains, then isolated, single crystal particles of Cr have to behave in a ductile manner [11,12].

The mechanical properties of Cu-Cr composites are dependent upon the extended solid solubility of Cr at elevated temperature, 0.89 At. % @ 1076.6°C, followed by a reduction in solid solubility as temperature is reduced, essentially 0.0 At. % @ 25°C.

The solubility of Cr in Cu can be calculated by the following equation [15]

$$X \text{ (Cr. in Cu)} = 24480 \exp. (-114880/RT)$$

where R is in Joules/Mole K

The excellent electrical conductivity of this composite is based upon the very low solubility of Cr in Cu at room temperature. The phase diagram of this composite is shown in figure 3.3.

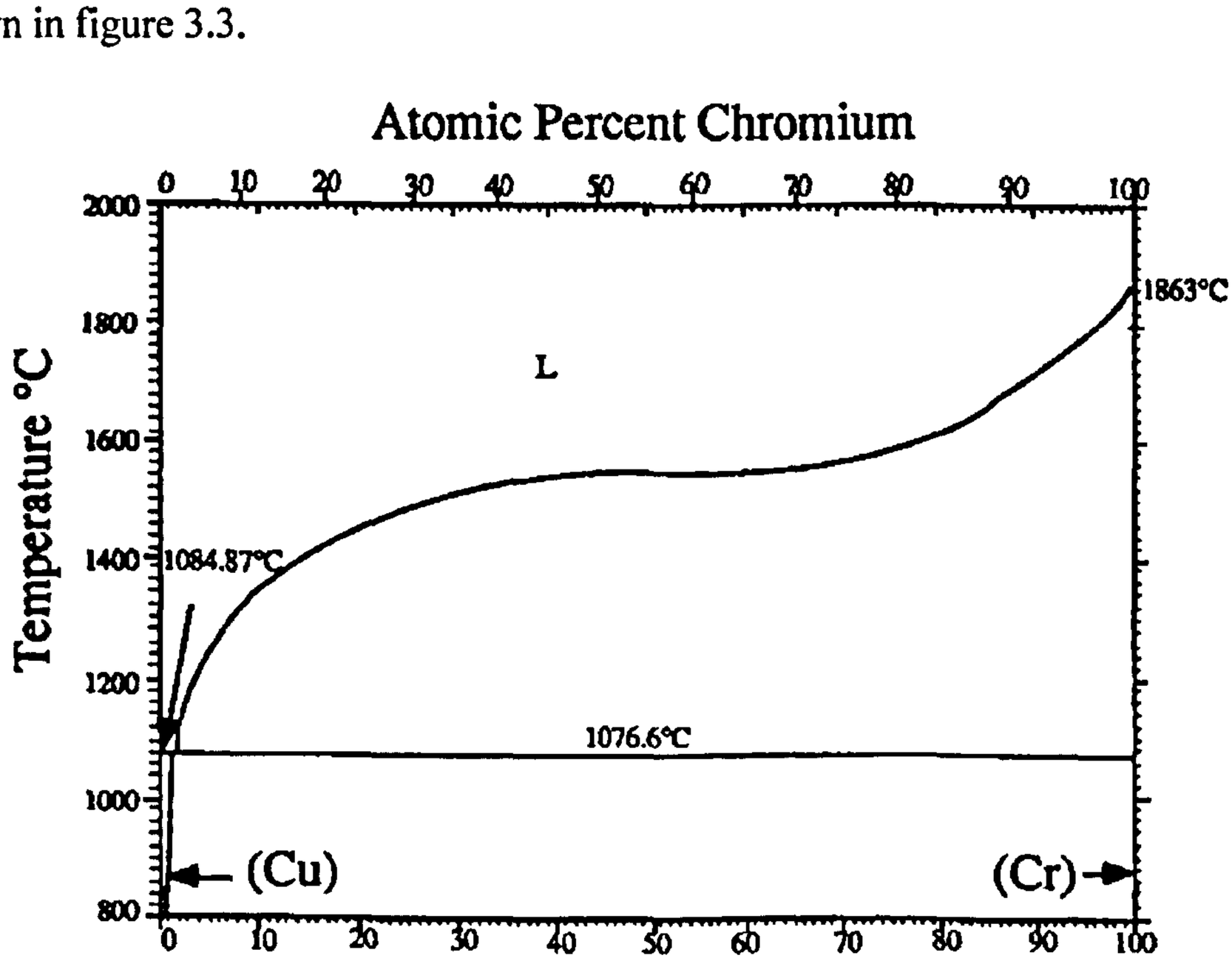

Figure 3.3 Phase diagram for Cu-Cr
Reproduced from reference [15]

3.3 Strengthening models

Many investigations of the mechanical properties of in-situ composites have been carried out and the results were often compared with the rule of mixtures approach. In the rule of mixtures, stresses in the individual phases are added together in proportion to the volume fraction of each phase to give the overall composite stress. The strength of the composites have usually had positive deviations from the rule of mixtures approach and have been found to be dependent on the crystal structure of the two phases involved [13] (figure 3.4).

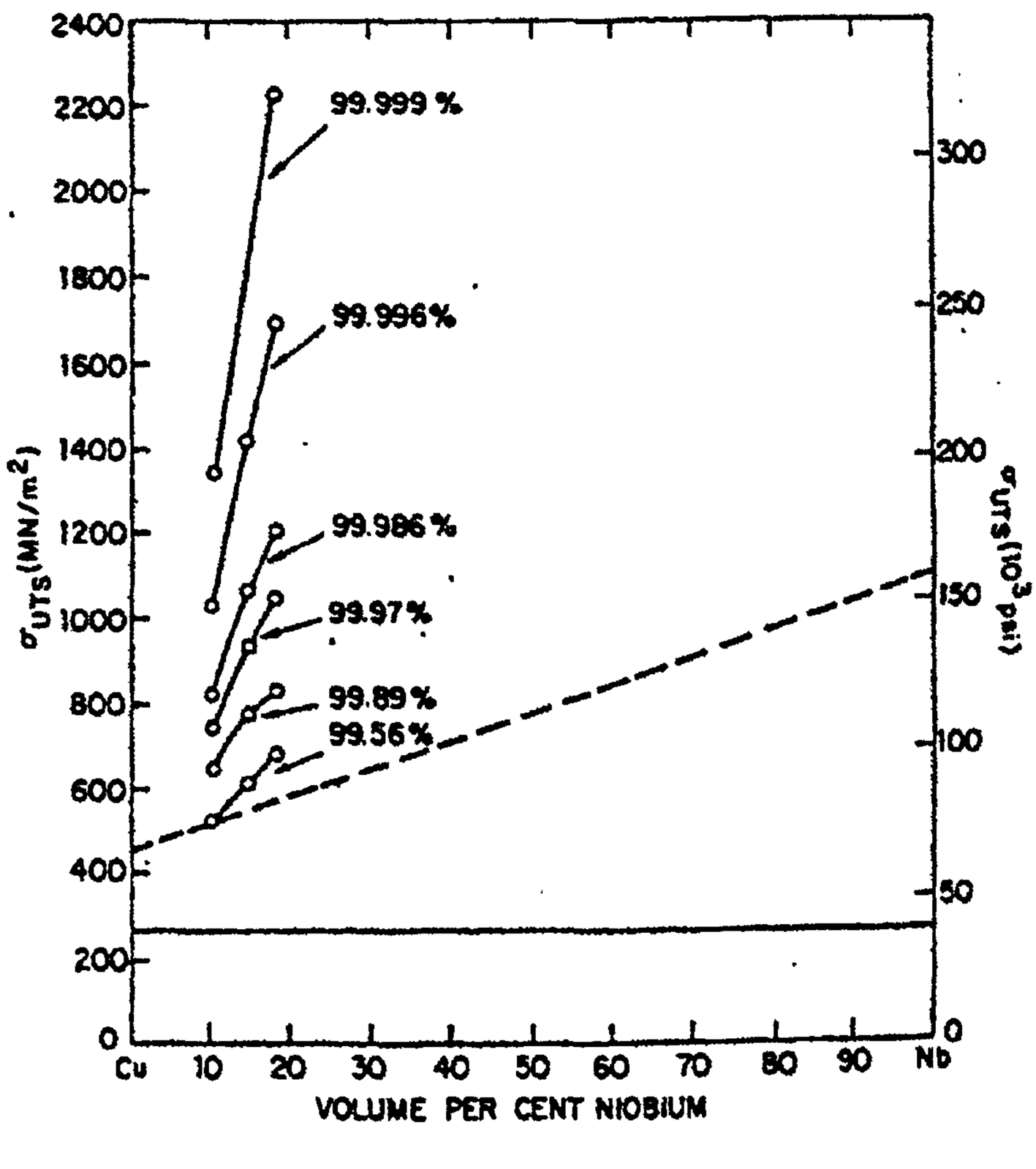

Figure 3.4 The UTS of Cu-Nb composites as a function of niobium concentration at different drawing strains (99.56 - 99.999 % which corresponds to η= 5.2 - 11.5). The solid and dashed line represents the extremes of the rule of mixtures prediction of σ_{UTS}

Reproduced from reference [13]

Research has shown that the result shown above is typical of FCC-BCC combinations and result in a greater relative strengthening compared to FCC-FCC mixtures [1]. The greater strengthening in the former composites is believed to be due to the bcc fibres developing a ribbon like cross section. This ribbon-like fibre morphology is a consequence of the {110} fibre texture that develops during cold working of bcc metals [13,16] (figure 3.5). In FCC-FCC composites, the FCC fibres are free to deform axisymmetrically during cold working and their cross sectional shapes do not change significantly [17].

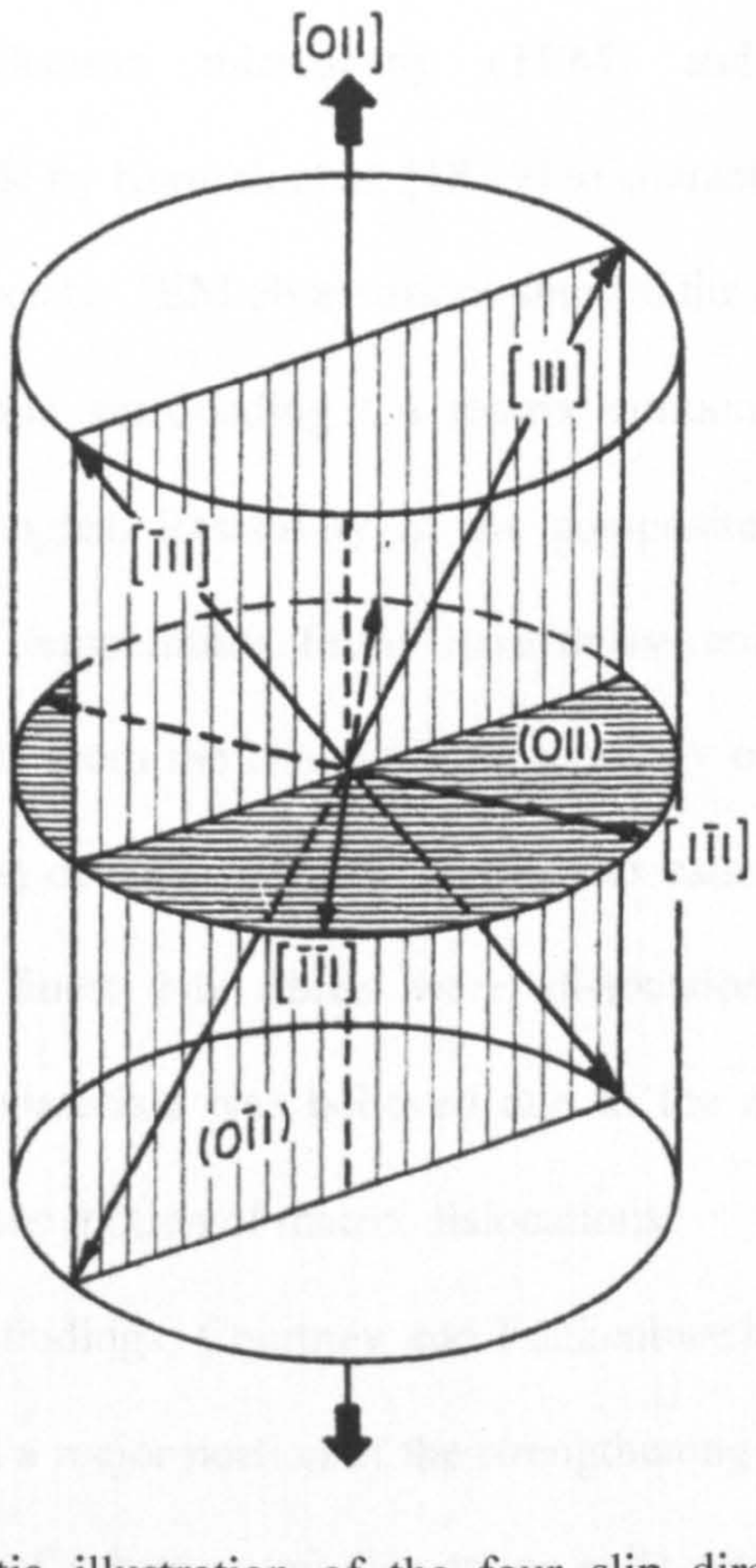

Figure 3.5 Schematic illustration of the four slip directions in a bcc material with a {110} preferred orientation. Only two of the four {111} directions can accommodate extension parallel to the fibre axis, resulting in plane strain deformation rather than axially symmetric flow

Reproduced from reference [13]

The strength of heavily deformed in-situ composites exceeds that predicted by the rule of mixtures, and a fundamental understanding of the strengthening mechanisms involved has been the subject of much discussion. Two distinct models have been proposed in an attempt to explain the anomalous strengthening in in-situ composites upon extensive deformation. There are:

- The dislocation model proposed by Courtney and Funkenbusch [12,20-21].
- The Hall-Petch barrier model proposed by Spitzig, Verhoeven and Chumbley [22-27].

Transmission electron microscopy (TEM) and electrical resistivity measurements were made by Karasek et al. [18,19] to characterise the microstructure of a Cu-Nb in-situ composite. TEM observations showed the Nb fibres to be virtually dislocation-free while the surrounding Cu matrix contained a large number of dislocation cells and tangles. Resistivity of the composites was measured up to 600°C as a function of temperature. From these measurements, and assuming no contribution to resistivity from the change in morphology of the fibres during heat treatment, the dislocation density in the Cu matrix was estimated to be the order of 10^{13} cm^{-2} while the finest Nb fibres were dislocation free. The increased strengthening of these materials was believed due to the effectiveness of the Nb interfaces as barriers to the motion of matrix dislocations.

Based on these findings, Courtney and Funkenbusch [12,20,21] proposed a model which shows that a major portion of the strengthening of in-situ composites is due to the development of substructural dislocation cells within a single phase (e.g., within the Cu of a Cu-Nb composites). The basis of this model is that additional (geometrically necessary) dislocations are generated during deformation of two phases, as compared to single-phase materials due to the greater strain

incompatibility between adjacent grains in a two phase material. The main experimental problem of verification of this theory is the measurement of the dislocation density which should be very low after large prior strain but is imprecisely measured in thin foils of these inhomogeneous two-phase composites.

Spitzig et al. [22-27] have shown that the strength of Cu based in-situ composite is strongly related to the interphase spacing, as described by the Hall-Petch-type relationship. They found that transmission electron microscopy (TEM) and electrical resistivity results disagree with many of the assumptions made by Courtney in their work hardening model. TEM observations showed that the continued strengthening in the Cu-Nb composites was a consequence of deformation induced microstructural changes in both Cu and Nb. The microstructural evolution in the Cu matrix involved a deformation-recovery-recrystallization cycle, thereby, allowing reductions and refinement of the Nb fibres sizes and spacings. Despite the relatively large degree of deformation, the dislocation density in the Cu matrix was found to be only about of 10^{10} to 10^{11} cm^{-2}. Strengthening in these composites was due to the Nb fibres acting as planar barriers to plastic flow between the two phases. Besides this, Spitzig et al. also found that the rate of strengthening with increasing η was significantly reduced in the 5vol.% Nb composite compared to a 20vol.% Nb composite. Therefore, 5vol.% Nb in a deformation processed Cu-Nb composite may be the minimum amount of fibre reinforcement required to raise the strength of the composite. When the composite was subjected to heat treatment, Nb fibres were found to coarsen at 550°C after 2 hours. In the work hardening model, this event was assumed to be insignificant. This research also found that the major change in electrical resistivity measurements resulting from heat treatment was connected to the fibre coarsening and not a decrease in dislocation density. The barrier model is

seen as the better predictor of the strengthening seen in the heavily deformed composite and is widely accepted by most researchers in this field.

3.4 In-situ deformation

X-ray and neutron diffraction have been widely used to measure the internal strain and hence internal stresses in many composite materials, particularly metal matrix composites. The fundamental principle behind the diffraction techniques is if a stress is present, there will be a shift in diffraction peaks because the interplanar d-spacings are different than those in the unstressed state. This change in d-spacing is what is measured, correlated to a strain and finally to a stress. For x-ray diffraction, the stress state measured is the total stress corresponding to the sum of the macro- and microstresses.

The main advantage of using neutrons over X-rays is the high level of penetration into most materials. For example, the 90 % absorption depth of thermal neutrons in aluminium is 288 cm compared with 0.018 cm for $Cu-K\alpha$ X-rays. In x-ray diffraction, electrons are the primary scattering body and the scattering amplitude is proportional to the atomic number. Despite the limited penetration depth of an X-ray beam, this technique is also widely used because of its easy availability compared to neutron sources.

In this section previous research on the measurement of internal stresses using the neutron diffraction technique is discussed. Diffraction measurements of the in-situ deformation have been successful in metal matrix composites but very few studies have been done on metal-metal composites. Therefore, some of the important findings on metal matrix composites will be discussed here as well. Normally, there are two types of stresses which can be measured- residual stresses which can arise

from any manufacturing process, which imparts permanent inhomogeneous deformation into a material and internal stresses generated from the application of an external load during stress measurement.

3.4.1 Residual stresses

Residual stresses may be generated from either thermal or mechanical treatment. However, despite the importance of the residual stresses in composites, most research has been focused on the thermally induced residual stresses in composites due to differences in the coefficients of thermal expansion between matrix and reinforcements. These residual stresses play a significant role in the load bearing processes in metal matrix composites. Research conducted by Arsenault et al. [28] on SiC/Al composite material showed that the yield stress of the composite under uniaxial tension was different from that under uniaxial compression. This asymmetric response was due to the average tensile thermal residual stresses in the matrix.

Experimental work [9] on Cu-Fe composites has found that the yield stress is different during tension and compression testing, that is, there is a strong Bauschinger effect. At low drawing strains this effect was caused by the dislocation substructures in the Cu matrix which produce significant directional internal stresses. At larger drawing strains the Cu grain size, which is determined by the closely spaced Fe fibres, became too small to maintain an internal dislocation substructure and therefore the Bauschinger effect weakened. Internal microstrains are still recorded by the x-ray analysis, probably caused by the local stress and strain incompatibilities between the Cu matrix and the Fe reinforcements.

3.4.2 Stresses generated during external loading

The technique of measuring stress using the neutron diffraction technique within a composite during the application of an external load has been widely used [29-34]. Allen et al. [31] used an in situ neutron diffraction technique to study the strain in Al/SiC whisker and particulate composites under a uniaxial tensile load. Ignoring the initial thermal stress, the axial lattice displacements returned to an approximately strain free state. However, the lattice transverse strains in the matrix were in compression and the SiC reinforcement was in tension.

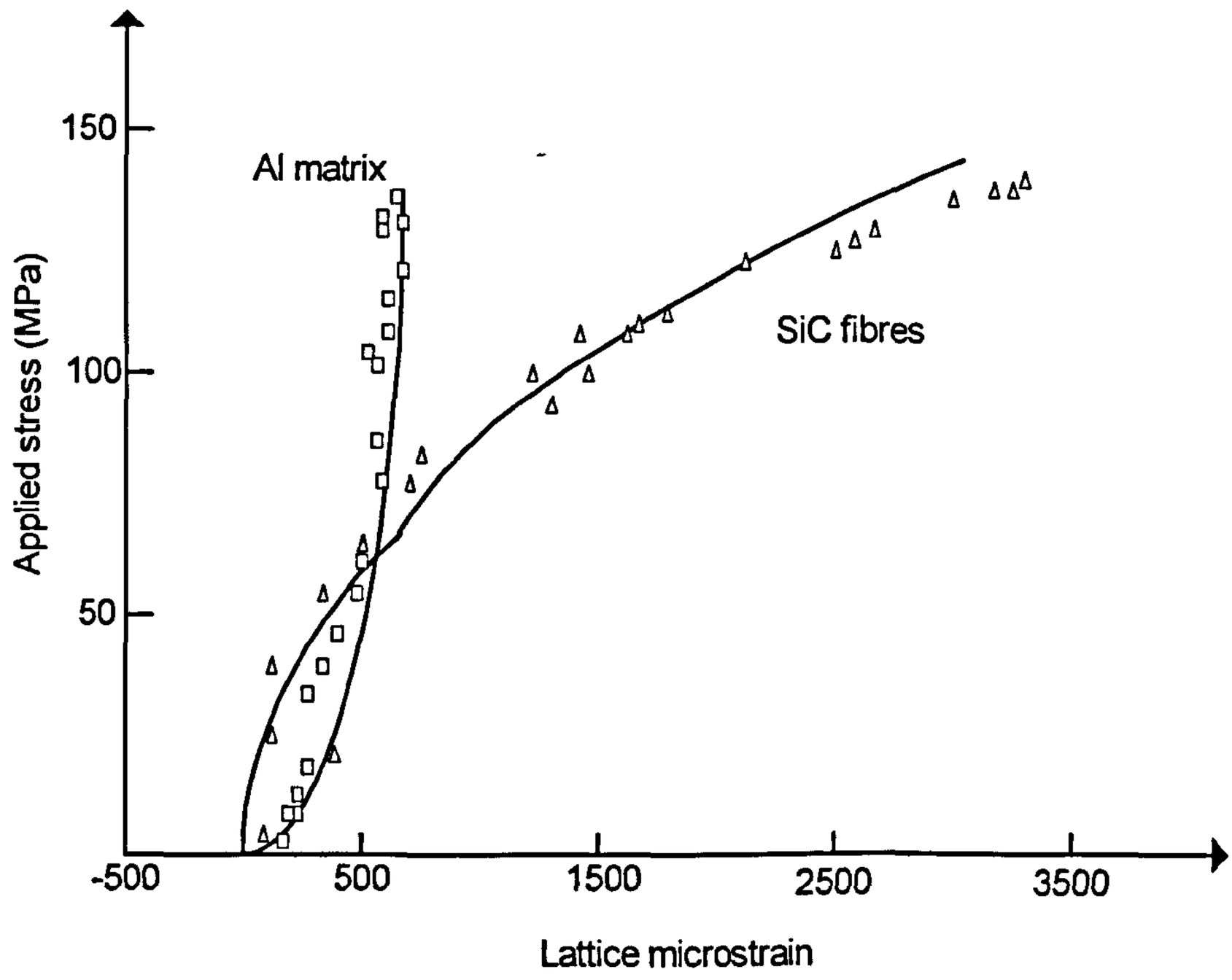

Figure 3.6 Internal strain response of a fibre-reinforced Al/SiCw composite measured by neutron diffraction
Reproduced from reference [32]

A typical behaviour of a short fibre, particulate or whisker reinforced metal matrix composite [32] is shown in figure 3.6. Initially, the elastic strain of the matrix is higher than the reinforcement due to the higher stiffness of the ceramic. As the deformation proceeds and the matrix has begun to deform plastically, the degree of

misfit between the two phases increases, and this will transfer more load progressively to the reinforcement which results in a higher strain in the SiC. Meanwhile, the lattice strain in the matrix does not increase further because the shape change in the matrix is mainly caused by plastic deformation.

3.5 Elevated temperature response

One major problem reported for in-situ Cu-based composites was the loss of strength when exposed to high temperatures [21,35-37]. The massive interphase boundary area within the composites provides a large driving force for energy minimization via phase size coarsening. Therefore, the very fine fibres can easily spheroidize and coarsen rapidly at high temperatures. The effect of temperature up to 600°C on the ultimate tensile strength of Cu-5vol.% Nb composites deformation processed to η's of 4.8, 8.2, and 11.0 was carried out by Verhoeven and co-workers [35]. They found that the strength of Cu-5vol.% Nb composites was superior to that of Cu at all the temperatures but particularly at temperatures up to 300°C. Above 300°C, the strength of Cu-5vol.% Nb composites showed pronounced deterioration, and at 600°C, it was not much better than Cu. The degree of coarsening increased at a given temperature as the degree of deformation processing of the wire increased, that is, as the fibre thickness decreased. A similar conclusion was reached from TEM studies of the Nb fibres from samples annealed at 300°C, 350°C, and 400°C, [21,36] (figure 3.7) which showed that the sharp edges of the fibres had become noticeably rounded at 350°C. It is important to note that all these studies were concentrated at intermediate to high drawing strain composite material and no attempt was made to understand the behaviour of low drawing strain composite.

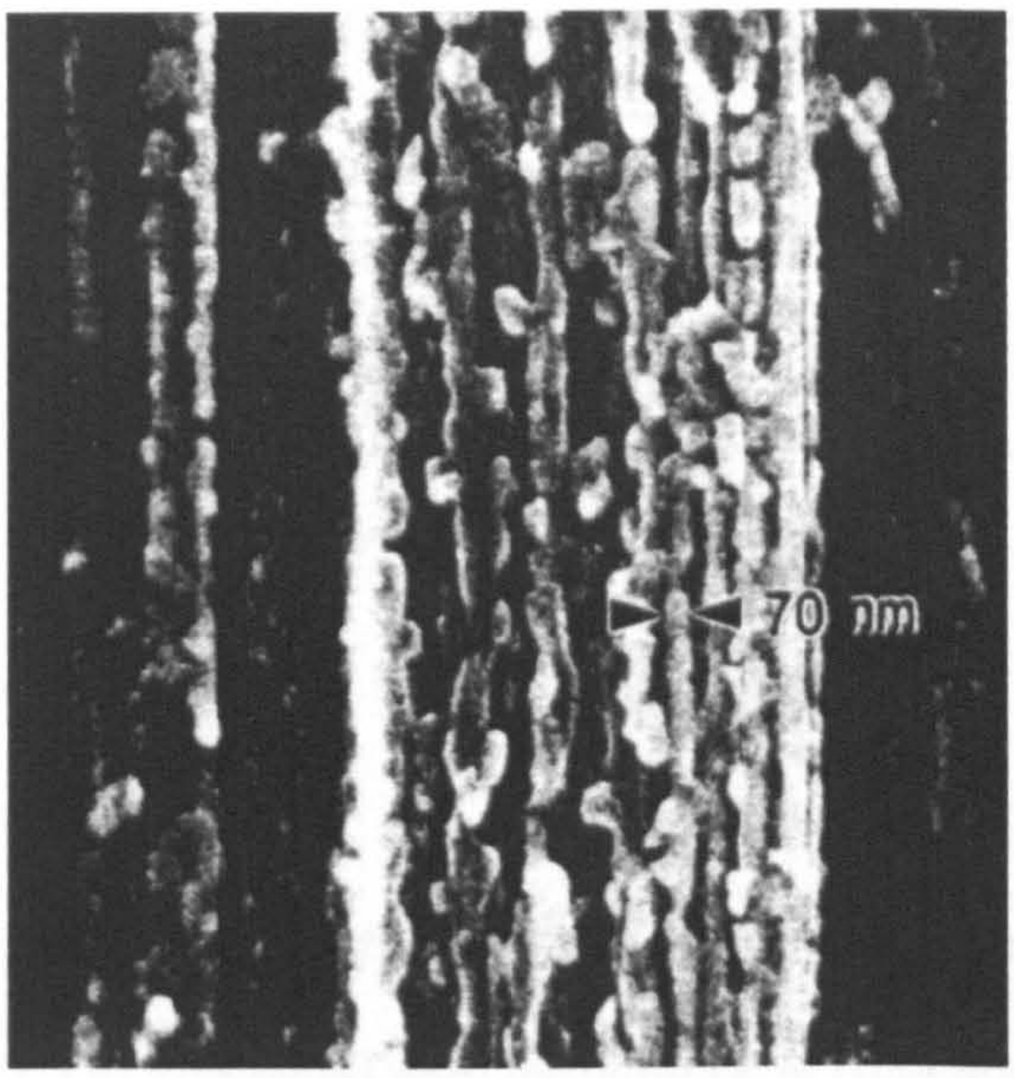

Figure 3.7 A SEM picture of a longitudinal surface of a wire, deep etched to remove the Cu. It is seen that the Nb fibres have coarsened to the extent that they have pinched off at many places

Reproduced from reference [36]

Spitzig et al. [37] investigated the high temperature (22–600˚C) properties of the Cu-20vol.% Fe composites deformation processed from a powder metallurgy compact. They found that the ultimate tensile strengths decreased with increasing temperature but were still far greater than those of similarly processed Cu at temperatures up to 450˚C. At temperatures of 300˚C and 450˚C, the strength of Cu-20vol.% Fe composites was about seven and six times greater, respectively, than that of Cu. However, at 600˚C the strength of Cu-20vol.% Fe composites was only slightly better than that of Cu due to the coarsening of the Fe fibres. Therefore, Cu-20vol.% Fe composites produced by deformation processing of powder metallurgy compacts have mechanical properties far superior to those of similarly processed Cu at room temperature up to 450˚C.

Similar analyse was also carried out by Courtney et al. [38] on the Cu-14.3 vol.% Fe composites formed by the powder metallurgy technique. They showed that the coarsening process actually formed in a few steps at 800˚C. Firstly, a single

ribbon shaped fibre would form into parallel cylinders. These Fe cylinders in turn formed a "string of pearls" edge instability that finally led to formation of spherical Fe particles in the Cu matrix.

Experimental work was also performed by Spitzig et al. [39] on Cu-20vol.% Nb and Cu-20vol.% Ta composites formed by extensive cold drawing to compare the mechanical properties (22–600°C) of both composites. They discovered that the strength of the Cu-20vol.% Ta was greater than Cu-20vol.% Nb at equal temperatures due to the higher modulus and melting temperature of tantalum (E = 186 GPa, T_m = 3000°C) as compared with niobium (E = 105 GPa, T_m = 2470°C). The decrease in strength of the composites up to 300°C was relatively small, but above 300°C the strength dropped drastically, due to the coarsening of the individual niobium and tantalum fibres. Scanning electron microscopy showed that coarsening was observed above 450°C for Cu-20vol.% Nb and 600°C for Cu-20vol.% Ta composites. Therefore, a fibre metal with high elastic modulus and high melting temperature would give a superior composite at elevated temperatures.

3.6 Research objectives

To date, considerable research has been carried out to optimise the mechanical and electrical properties of Cu-Cr composites. However, experimental evidence is lacking on the load partitioning between the two phases under applied loading. In a conventional MMC, deformation in the matrix causes a misfit to be generated between the matrix and the plastically non-deformable reinforcement. However, Cu-Cr composites differ fundamentally from conventional composites in that both phases are able to deform plastically. The aim of this research is to

understand the deformation behaviour of the individual phases in the Cu-Cr composites and their interaction through elastic and plastic loading.

Since the thermal conductivity of Cu-based composites is high, it can be used for future space and energy technologies such as rocket engine combustion chamber systems. These materials require not only high thermal conductivity but also adequate creep resistance to ensure a reliable performance in service. Cu-Cr composites have some potential applications at high temperatures so that it is important to obtain detailed information on the creep behaviour and creep fracture.

References

1 A. M. Russell, L. S. Chumbley and Y. Tian, Deformation Processed Metal-Metal Composites. Advanced Engineering Materials, 2000.1-2:11-22.

2 C.L. Trybus and W.A. Spitzig, Characterization of the strength and microstructural evolution of a heavily cold rolled Cu-20% Nb composite. Acta Metallurgica, 1989. 37(7): 1971-1981.

3 W.A. Spitzig, L.S. Chumbley, J.D. Verhoeven, Y.S. Go and H.L. Downing, Effect of temperature on the strength and conductivity of a deformation processed Cu-20%Fe composite. Journal of Materials Science, 1992. 27(8): 2005-2011.

4 W.A. Spitzig and S.B. Biner, Comparison of strengthening in wire-drawn or rolled Cu-20% Nb with a dislocation accumulation model. Journal of Materials Science, 1993. 28(17): 4623-4629.

5 C. Biselli and D.G. Morris, Microstructure and strength of Cu-Fe in situ composites obtained from prealloyed Cu-Fe powders. Acta Metallurgica et Materialia, 1994. 42(1): 163-176.

6 D. Raabe, Simulation of the resistivity of heavily cold worked Cu-20 wt.% Nb wires. Computational Materials Science, 1995. 3(3): 402-412.

7 Y. Jin, K. Adachi, T. Takeuchi and H.G. Suzuki, Correlation between the cold-working and aging treatments in a Cu-15 wt pct Cr in situ composite. Metallurgical and Materials Transactions A-Physical Metallurgy and Materials Science, 1998. 29(8): 2195-2203.

8 K. Adachi, S. Tsubikawa, T. Takeuchi T and H.G. Suzuki, Strengthening Mechanism of cold-drawn wire of in situ Cu-Cr composite. Journal of the Japan Institute of Metals, 1997. 61(5): 397-403.

9 C. Biselli and D.G. Morris, Microstructure and Strength Of Cu-Fe In-Situ Composites After Very High Drawing Strains, Acta Materialia, 1996. 44(2): 493-504.

10 J.D. Verhoeven, W.A. Spitzig, L.L. Jones, H.L. Downing, C.L. Trybus, E.D. Gibson, L.S. Chumbley, L.G. Fritzemeier and G.D. Schnittgrund, Development of deformation processed copper-refractory metal composite alloys. Journal of Materials Engineering, 1990. 12(2): 127-139.

11 P.D. Funkenbusch, T.H. Courtney and D.G. Kubisch, Fabricability and microstructural development in cold worked metal matrix composites. Scripta Metallurgica, 1984. 18(10): 1099-1104.

12 P.D. Funkenbusch and T.H. Courtney, On the strength of heavily cold worked in situ composites. Acta Metallurgica, 1985. 33(5): 913-922.

13 J. Bevk, J.P. Harbison and J.L. Bell, Anomalous increase in strength of in situ formed Cu-Nb multifilamentary composites. Journal of Applied Physics, 1978. 49(12): 6031-6038.

14 J. Bevk, W.A. Sunder, G. Dublon, and D.E. Cohen DE, In-Situ Composites IV, Ed. F.D. Lempkey, H.E. Cline and M. Mclean, Elsevier Sci. Publ. Co. (1982)

15 T.W. Ellis, Deformation Processed Cu-Cr Alloys, PhD thesis, Iowa State University.

16 K.R. Karasek and J. Bevk, Normal-state resistivity of in situ-formed ultrafine filamentary Cu-Nb composites. Journal of Applied Physics, 1981. 52(3): 1370-1375.

17 G. Frommeyer and G. Wassermann, Microstructure and anomalous mechanical properties of in situ-produced silver-copper composite wires. Acta Metallurgica, 1975. 23(11): 1353-1360.

18 K.R. Karasek and J. Bevk, Dislocation resistivity in in situ formed Cu-Nb multifilamentary composites. Scripta Metallurgica, 1980. 14(4): 431-435.

19 K.R. Karasek and J. Bevk, Normal-state resistivity of in situ-formed ultrafine filamentary Cu-Nb composites. Journal of Applied Physics, 1981. 52(3): 1370-1375.

20 P.D. Funkenbusch, J.K. Lee and T.H. Courtney, Ductile two-phase alloys: prediction of strengthening at high strains. Metallurgical Transactions A-Physical Metallurgy & Materials Science, 1987. 18A(7): 1249-1256.

21 P.D. Funkenbusch and T.H. Courtney, On the role of interphase barrier and substructural strengthening in deformation processed composite materials. Scripta Metallurgica, 1989. 23(10): 1719-1724.

22 J.D. Verhoeven, L.S. Chumbley, F.C. Laabs and W.A. Spitzig, Measurement of filament spacing in deformation processed Cu-Nb alloys. Acta Metallurgica et Materialia, 1991. 39(11): 2825-2834.

23 W.A. Spitzig, J.D. Verhoeven, C.L. Trybus and L.S. Chumbley, Comments on 'On the role of interphase barrier and substructural strengthening in deformation processed composite materials' by P.D Funkenbusch and T.H. Courtney (and discussions). Scripta Metallurgica et Materialia, 1990. 24(6): 1171-1184.

24 L.S. Chumbley, H.L. Downing, W.A. Spitzig and J.D. Verhoeven, Electron-Microscopy Observation of an In Situ Cu-Nb Composite, Materials Science and Engineering A-Structural Materials Properties Microstructure and Processing, 1989. 117: 59-65.

25 W.A. Spitzig and P.D. Krotz, A comparison of the strength and microstructure of heavily cold worked Cu-20% Nb composites formed by different melting procedures. Scripta Metallurgica, 1987. 21(8): 1143-1146.

26 J.D. Verhoeven, W.A. Spitzig, F.A. Schmidt, P.D. Krotz and E.D. Gibson, Processing to optimize the strength of heavily drawn Cu-Nb alloys. Journal of Materials Science, 1989. 24(3): 1015-1020.

27 W.A. Spitzig, H.L. Downing, F.C. Laabs, E.D. Gibson and J.D. Verhoeven, Strength and Electrical Conductivity of a Deformation-Processed Cu-5Pct Nb Composite. Metallurgical Transactions, 1993. 24: 7-13.

28 R.J. Arsenault and M. Taya, Thermal residual stress in metal matrix composite. Acta Metallurgica, 1987. 35(3): 651-659.

29 H.P. Cheskis and R.W. Heckel, in Metal Matrix Composites, ASTM STP 438. 1968. 76.

30 H. P. Cheskis and R.W. Heckel, Metallurgical. Transaction, 1970, 1:1931.

31 A.J. Allen, M. Bourke, S. Dawes, M.T. Hutchings and P.J. Withers, The Analysis of Internal Strains Measured by Neutron Diffraction in Al/SiC MMCs. Acta. Metallurgica, 1992. 40: 2361-2373.

32 P.J. Withers, Measurement of Residual and Applied Stress using Neutron Diffraction. M.T. Hutchings and A.D. Krawitz (editors), Kluwer Academic Publishers, 1992. 205-222.

33 N. Shi and R.J. Arsenault, Analytical evaluation of the thermal residual stresses in SiC/Al composites. JSME International Journal Series I-Solid Mechanics Strength of Materials, 1991. 34(2): 43-55.

34 L.F. Smith, A.D. Krawitz, P. Clarke, S. Saimoto, N. Shi and R.J. Arsenault, Residual stresses in discontinuous metal matrix composites. Materials Science & Engineering A-Structural Materials Properties Microstructure & Processing, 1992. A159(2): 13-15.

35 W.A. Spitzig, H.L. Downing, F.C. Laabs, E.D. Gibson and J.D. Verhoeven, Strength and Electrical Conductivity of a Deformation-Processed Cu-5Pct Nb Composite. Metallurgical Transactions, 1993. 24: 7-13.

36 J.D. Verhoeven, H.L. Downing, L.S. Chumbley and E.D. Gibson, The resistivity and microstructure of heavily drawn Cu-Nb alloys. Journal of Applied Physics, 1989. 65(3): 1293-1301.

37 W.A. Spitzig, L.S. Chumbley, J.D. Verhoeven, Y.S. Go and H.L. Downing, Effect of Temperature on the Strength and Conductivity of Deformation Processed Cu-20%Fe Composite, Journal Of Materials Science, 1992. 27(8): 2005-2011.

38 J.C. Malzhan Kampe, T.H. Courtney and Y. Leng, Shape instabilities of plate-like structures. Experimental observations in heavily cold worked in situ composites, Acta Metallurgica, 1989. 37(7): 1735-1745.

39 P.D. Krotz, W.A. Spitzig and F.C. Laabs, High temperature properties of heavily deformed Cu-20vol.% Nb and Cu-20vol.% Ta composites. Materials Science & Engineering A-Structural Materials Properties Microstructure & Processing, 1989. A110: 37-47.

Chapter 4

Experimental Techniques

By a small sample we may judge the whole piece.

-Miguel de Cervantes, Don Quixote

4.1 Introduction

Following the review of in-situ Cu-based composites in the previous chapter, this chapter will set out to describe the experimental testing procedures which were used to evaluate the properties of Cu-10vol.% Cr composites in this study. These include texture measurements, tensile and resistivity measurements, creep testing and TEM sample preparation. Neutron diffraction experiment and in-situ tensile tests inside the scanning electron microscope are described in Chapter 6.

4.2 Texture measurements

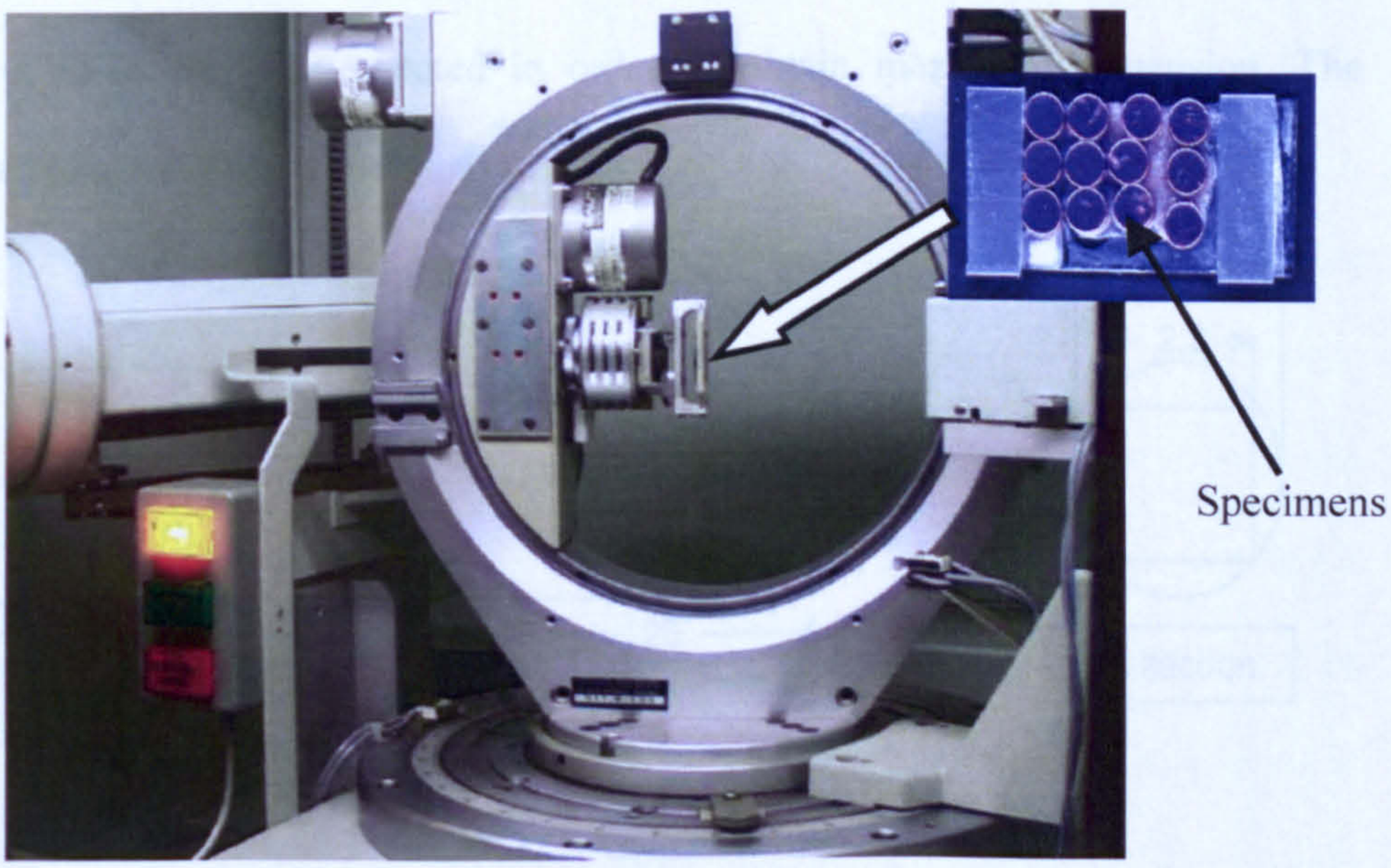

Figure 4.1 Experimental set-up for texture measurement

X-ray diffraction (XRD) was performed on a Siemens D5000 diffractometer using a Huber closed Eularian cradle at the Manchester Materials Science Centre. Cu K_α radiation (λ= 0.1541nm) was used on transverse section of the material (figure 4.1). Since the Cr phase is the minority phase in this composite, 12 transverse specimens were arranged very close to each other to generate more accurate data. Four pole-figures were measured for both the Cu matrix and the Cr phase. The measurements were carried out at 5° intervals in both chi and phi and up to 80° tilt in chi. Data collection time was 2 hours per pole figure and the collected data was corrected for defocusing effects. The data obtained was plotted in a Windows format using a texture software.

4.3 Specimen preparation

The rough surface of the as-processed copper-chromium rod made it difficult to measure the diameter, and failure of the material tended to occur within the grips. To rectify this problem, the specimens were machined to obtain a smooth surface. A square cross-section was selected in order to obtain maximum dimension. The tensile specimen is shown in figure 4.2.

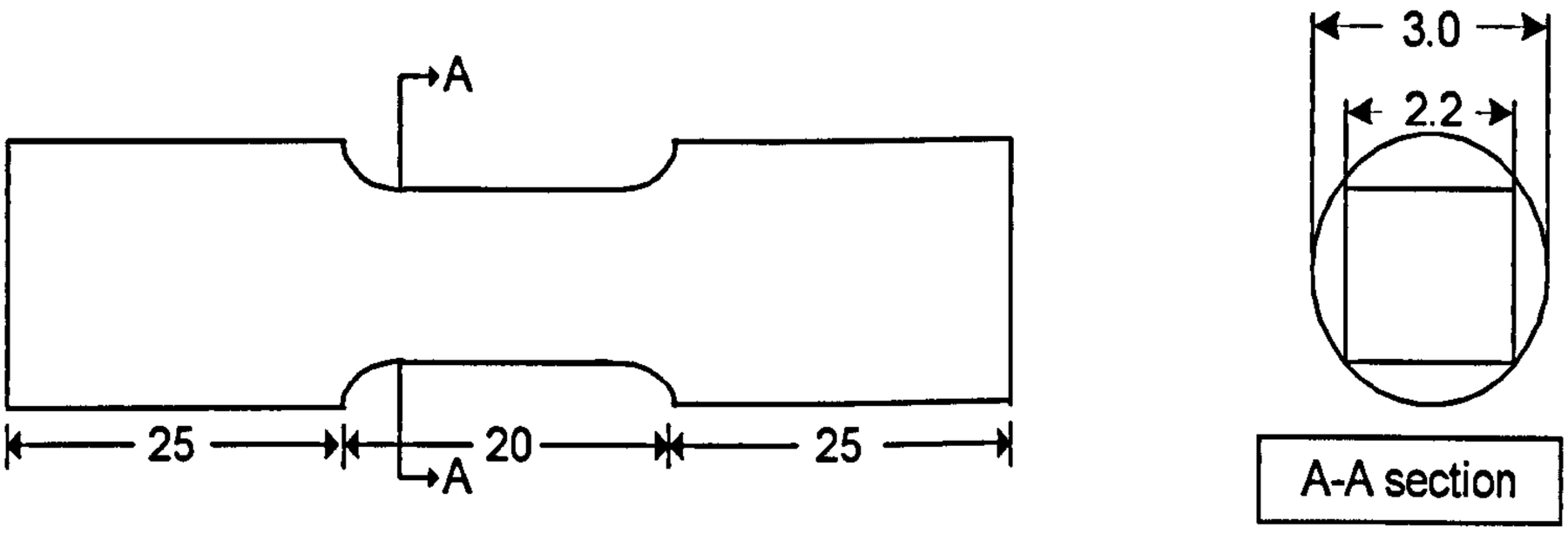

All dimensions are in mm

Figure 4.2 Tensile specimen

4.4 Extensometery

Strain measurement was carried out using a videoextensometer system. There are a few advantages of using this system [1]. Firstly, the videoextensometer system is non-contacting and therefore does not influence the rupture point. It can measure strains up to failure and also the transverse strain. This system also allows automatic detection and measurement of specimen necking and thus determination of true stress.

The videoextensometer system uses a video camera and pixel interpolation to measure the distance between two target areas with a distinct black/white transition. The image, which has been digitised by the CCD-camera (fullimage-camera) is processed by a computer supported videoprocessor in real time.

4.4.1 Principle of operation

Targets were marked by producing straight lines on the specimen using white tippex. It was essential that the targets create as sharp and as great a contrast difference as possible to ensure correct automatic target recognition and tracking. The video extensometer was developed based on the principle *"If it can be Seen, then it can be Measured"*. Reference marks were shown on the computer monitor indicating the selected targets as shown in figure 4.3. With conventional extensometers, it is necessary to fix them at a known gauge length and convert the extension signal received into a strain value. This might create errors as normally it is difficult to verify the exact gauge length once the extensometer is fitted to the specimen. This video extensometer operates as a 'strain meter' by directly calculating the measured extension as a percentage of the original length and only requires the exact initial gauge length to calculate the actual extension.

The video extensometer Windows-based software controls all operations and set-up procedures for the extensometer. In testing, the specimen marked with white tippex was placed in the testing machine. The camera was mounted on a tripod and adjusted so that the computer monitor shows a clear image of the targets and has sufficient field of view to display the specimen over the whole testing range. These targets points were then selected using the computer mouse and the known values entered which results in recalculation of the field of view with the size indicated on the computer monitor. The extensometer can be easily calibrated by placing a known distance piece adjacent to the specimen face or measuring the specimen width/diameter with a micrometer.

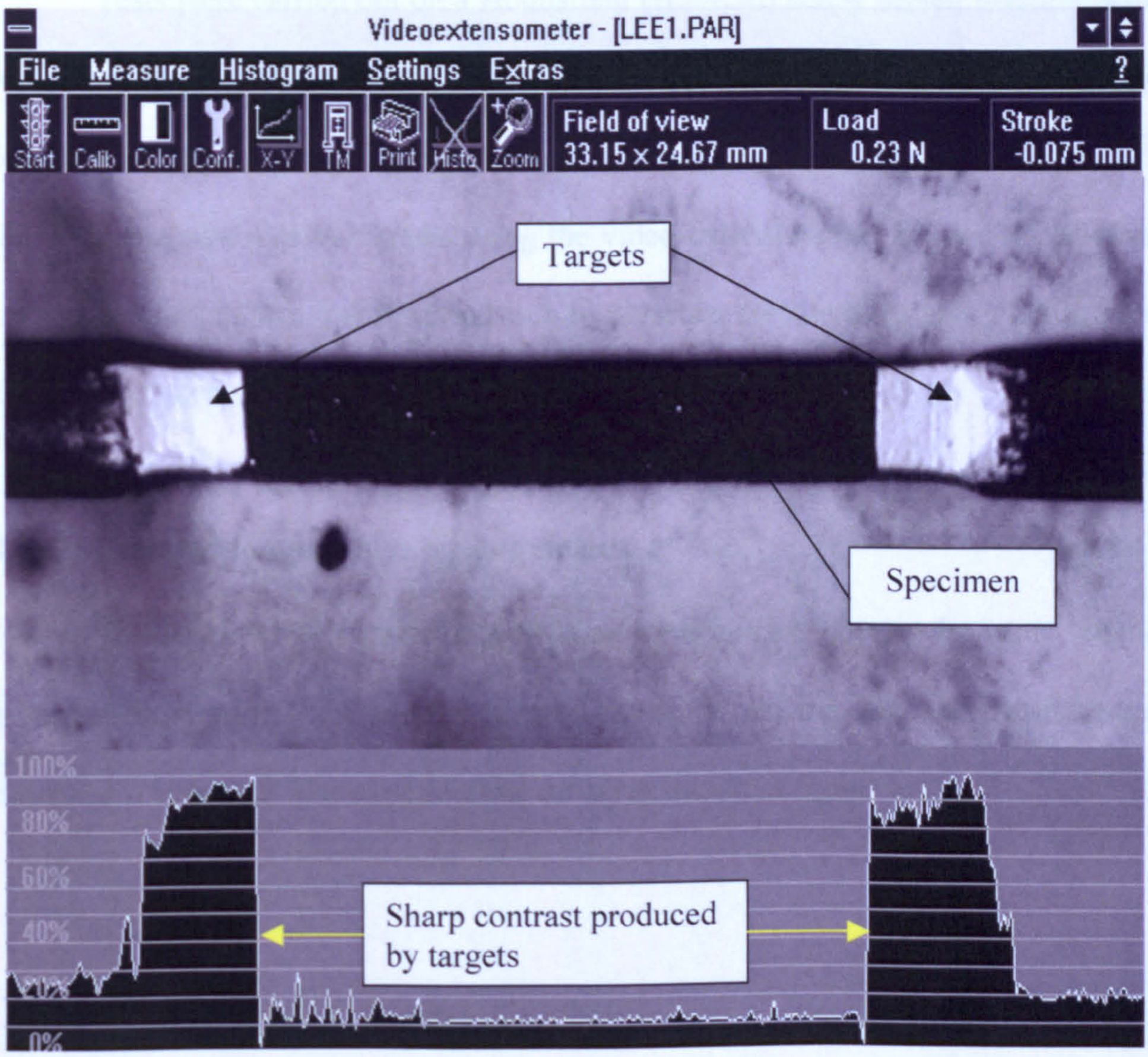

Figure 4.3 Typical screen display during testing

For the conductivity measurements during tensile testing, where the change in the diameter of the specimen was needed, there was an option to select the number of zones between the axial targets over which it was to be measured and whether the mean or minimum value was to be recorded. As a matter of fact, the entire testing process can be observed on the computer monitor by which errors can be almost completely excluded and it was also possible to save each single image (e.g. at the moment of rupture).

4.5 Tensile properties evaluation

4.5.1 Room temperature measurements

Tests were carried out on a Hounsfield (H50KM) screw driven machine with a 5 kN load cell. The crosshead speed was 1 mm min^{-1} and the specimen gauge length was approximately 20 mm. This gave a resulting strain rate of 0.8×10^{-3} s^{-1}. The displacement was monitored using the video extensometer. For each specimen, tensile tests to failure were carried out to measure the ductility and examine the fracture surfaces.

4.5.2 Elevated temperature measurements

Tensile tests at elevated temperature were carried out on the same tensile machine fitted with 3 kW radiant heating elements. All the tests carried out were destructive in nature. The experimental set-up is shown in figure 4.4.

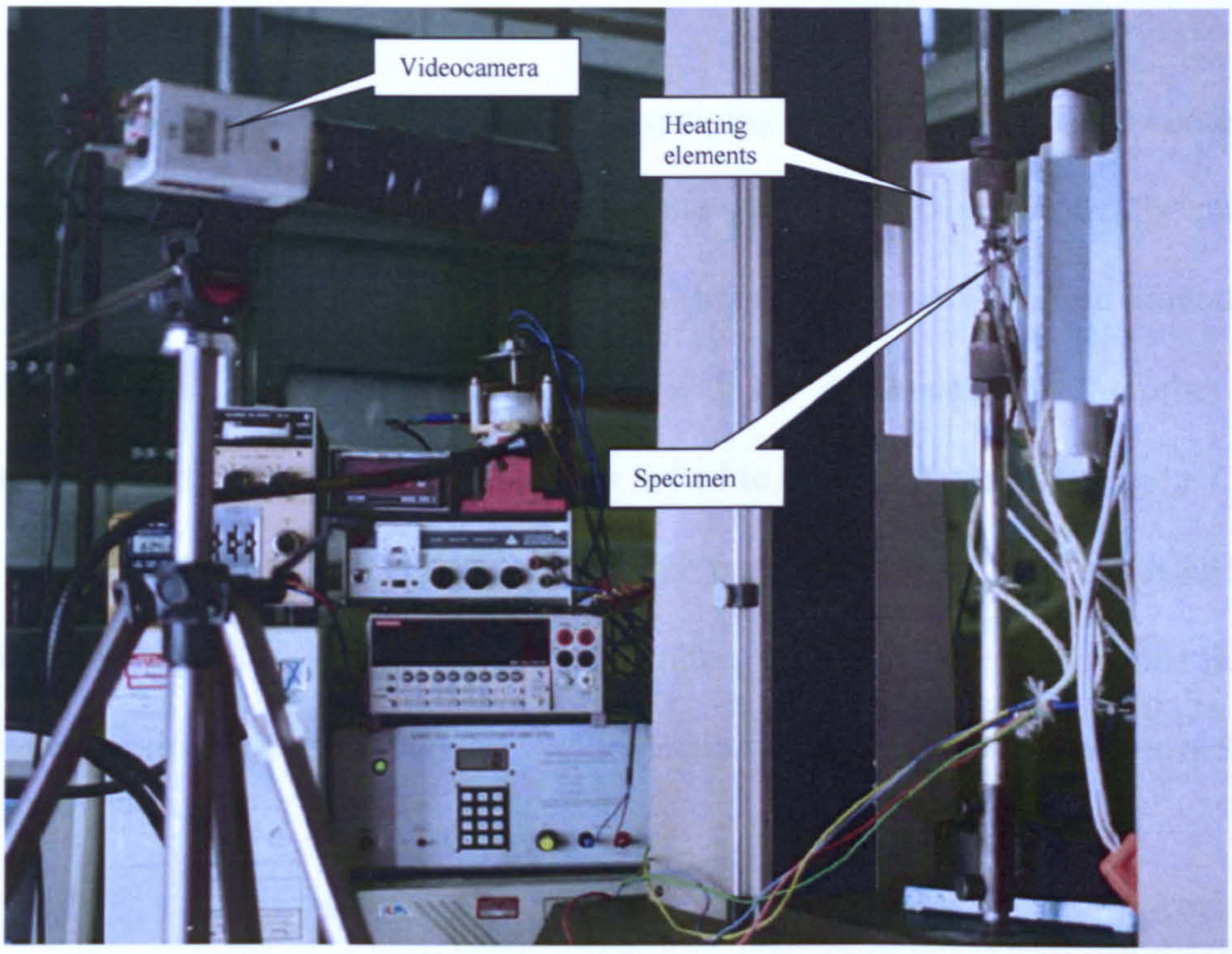

Figure 4.4 Elevated temperature tensile set-up

The specimen temperature was monitored by winding a thermocouple wire around the specimen such that the end was in contact with the specimen, with the other end attached to a digital thermometer. Once the specimen reached the required temperature, it was soaked for approximately 15 minutes so ensure that equilibrium temperature was achieved before starting the test. No load was applied to the specimen while heating up, and the specimen was removed immediately after testing to minimise any creeping effects. Tensile tests were performed at temperatures ranging from 100-600°C. The temperature distribution of the sample is not greater than ± 5°C and test temperature could be controlled to within ± 5°C.

4.5.3 Cold temperature measurements

Cryogenic tests were performed by spraying liquid nitrogen directly onto the specimen. The supply of liquid nitrogen to the specimen was automatically cut-off when the desired temperature is achieved. A thermocouple was attached around the specimen such that the end was in contact with the specimen, with the other end attached to a digital thermometer which is linked to the liquid nitrogen supply. Once the specimen temperature reached –70°C, the supply of liquid nitrogen would be automatically cut-off. If the specimen temperature increases above –70°C, the liquid nitrogen would be sprayed onto the specimen. The accuracy of this method is $\pm 5^{\circ}$ C.

4.6 Electrical resistivity

4.6.1 Resistivity during tensile testing at room temperature

In order to examine the change in resistivity of the composite during tensile deformation, an in-situ conductivity test (four head clamps) was developed, which was based on the four-point technique as shown in figure 4.5. On applying a constant current (I= 0.1A), through the two outer contacts, a voltage drop, V, across the two inner contacts was recorded by the computer.

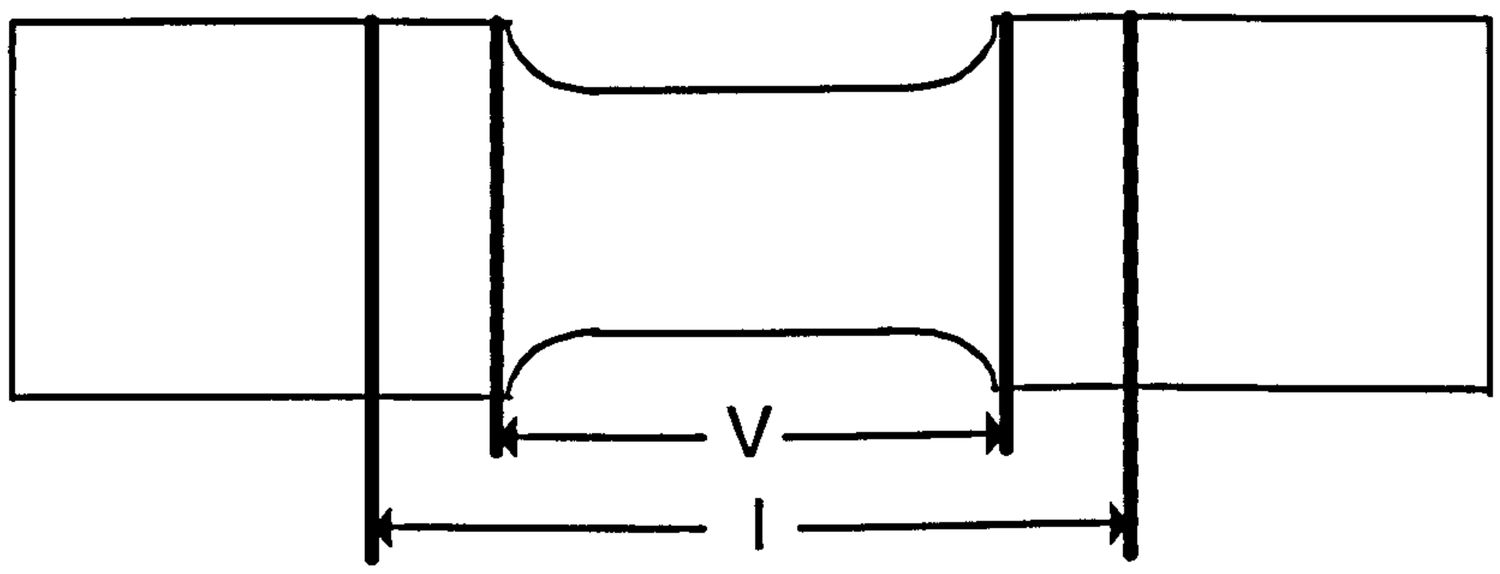

Figure 4.5 Principle of the four-point probe method

The resistivity ρ is given by

$$\rho = \frac{RA}{L}$$

where R ($R = \frac{V}{I}$) is the resistance of the composite, A the cross-section area of the specimen, L length between the voltage drop, both of L and A vary during loading which were measured by a video extensometer.

To determine whether the four head clamps design was accurate enough to measure the resistivity of the composite, it was tested on a pure Cu sample. The conductivity of pure Cu measured at room temperature using these clamps resulted in reproducible conductivity readings that were within 1% IACS (International Annealed Copper Standard) of those quoted in the literature. During tensile testing, both the axial and transverse specimen deformations were monitored using the videoextensometer system. The resistance test procedure was automated over an IEEE-488 bus using a computer as the controller. The changes of electrical resistivity and the tensile strains were taken until fracture. The resistivity was calculated by assuming a constant volume of the deformed sample.

4.7 Creep

Creep tests were performed on the composites in air and vacuum over a temperature range of 200-650°C. For the vacuum testing, a chamber was used with a resulting vacuum at approximately 10^{-5} Pa. All testing was conducted in tension using constant load creep frames with a 10:1 lever arm ratio loading arms. Both specimen and grips were enclosed and resistively heated in a cylindrical furnace. The fully assembled creep rig is shown in figure 4.6.

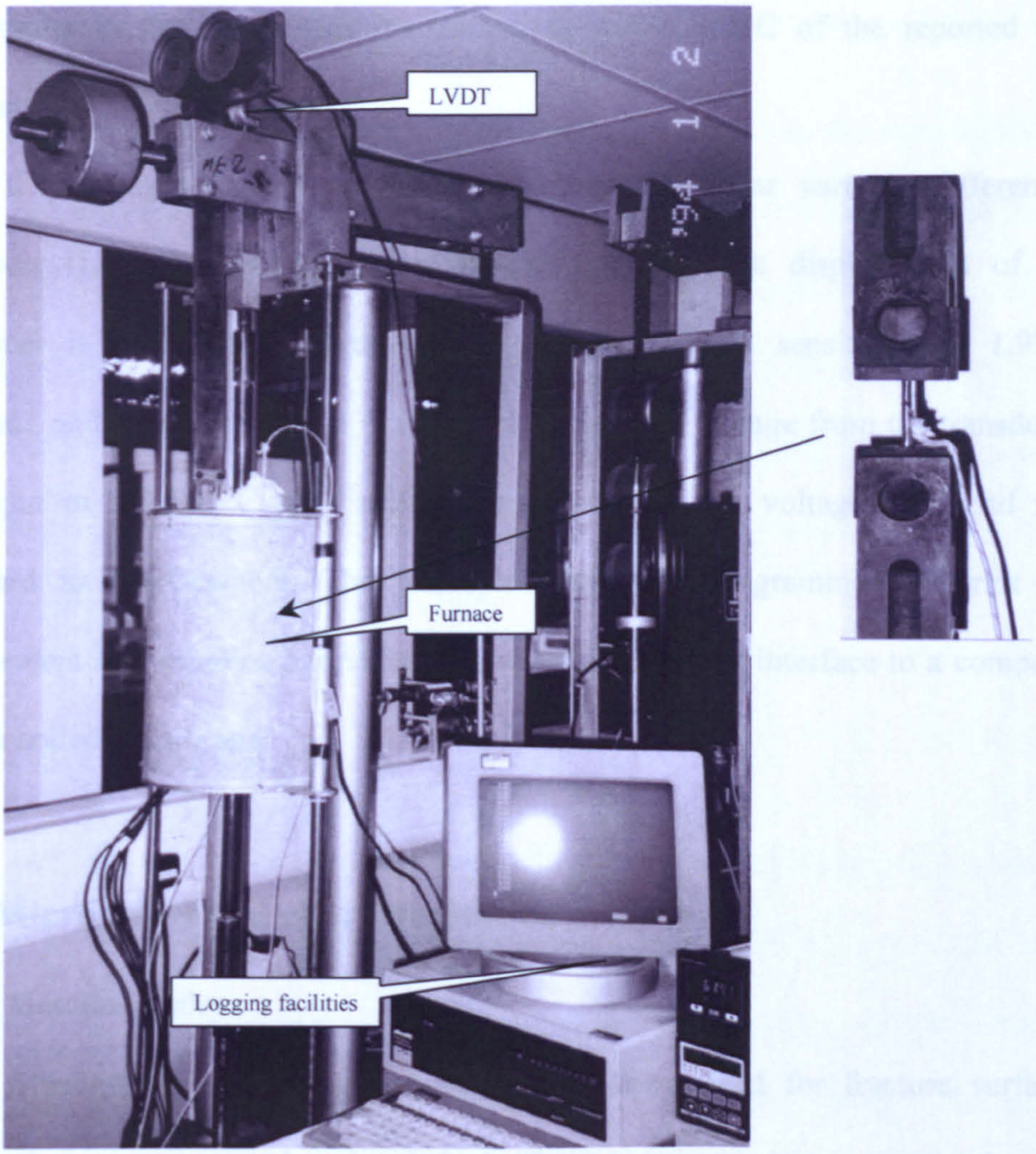

Figure 4.6 Experimental set-up for creep test in air

The temperature of the furnace was controlled by Type-K chromel–alumel thermocouples connected to a Eurotherm high stability controller and thyristor pack. A small fraction of the test load (not more than 10 %) was applied before and during heating of the specimen. This improved the axiality of loading by reducing the displacement of the specimen and load rods due to lateral forces from furnace packing. Specimens were soaked for at least 1 hour or until temperature equilibrium was obtained. The temperature of the specimen was measured with Type-K chromel –alumel thermocouples that were in contact with the specimen gauge area.

Temperature in the gauge was maintained to within ± 2°C of the reported test temperature.

Creep displacements were measured using a linear variable differential transducer (LVDT) attached to the top-loading arm. The displacement of the transducer is proportional to the output voltage, with a sensitivity of 1.9777 volts/mm, and an accuracy of ± 0.001 mm. The output voltage from the transducer was input to a E525 Cypher microprocessor, where the voltage was read and converted to displacement. The microprocessor was programmed to print the displacement at 5 minutes interval which was linked via an interface to a computer for data collection storage.

4.8 Microstructural characterisation

4.8.1 Metallography

After testing, all the specimens, except those used for fracture surfaces examination were mounted and polished. These specimens were examined using Scanning Electron Microscopy and Transmission Electron Microscopy detailed below.

4.8.2 Scanning electron microscopy (SEM)

(a) Specimen preparation

A small section (approximately 2 cm) measured from the fracture surface of the specimen was removed and mounted longitudinally in non-conducting acrylic. Specimens for metallographic examination were prepared by a procedure of grinding, polishing and etching.

(b) Grinding

This stage is needed to remove most of the scratches. The mounted specimen was placed into a clamp and attached to the polishing machine with the specimen facing down onto a grinding wheel. Initially, coarse SiC paper was placed on the wheel and lubricated with water. The clamp was set to rotate in the same direction as the grinding wheel and both were set rotating at 150 rpm. The clamp was pushed down onto the grinding wheel with a pressure of 5 lbs per specimen for 2 minutes. The specimen was then washed with water.

(c) Polishing (Struers method)

The SiC paper was then replaced with a DP Dac polishing cloth. A green lubricant and a 6 micron diamond spray were used to polish the material at a pressure of 10 lbs per specimen. The lubricant and 6 micron diamond were sprayed onto the wheel at regular intervals (20 seconds) for 5 minutes. After that, the sample was washed in detergent. Next, the polishing cloth was replaced with a DP Mol cloth used with a 3 micron diameter spray and red lubricant. The 3 micron diameter spray and red lubricant were sprayed onto the wheel at regular intervals (20 seconds) for 4 minutes. The sample was washed in detergent again before the final polish. The final polish used an OP Chem cloth and an OPS solution. The wheel and clamp were rotated at 150 rpm with a pressure of 2.5 lbs per specimen for 2 minutes. At this stage, the surface of the specimen should be very shiny as to resemble a mirror.

(d) Etching

Before etching, the specimen was washed thoroughly in detergent and rinsed with propanol and dried with a small fan heater. The polished surface was dipped in

a 40% nitric acid in water (HNO_3) for 5 seconds. After etching, the specimen was washed with alcohol and dried.

4.8.3 Transmission electron microscopy (TEM)

Samples were prepared for transmission electron microscopy by first cutting sections from the bulk material (rod form) using a high speed saw. The resulting slices were about 2 mm in thickness. These slices were ground using 400 grit SiC paper to about 0.3 mm thick. Next, these samples were further ground to a thickness of 0.15 mm using 1200 grit SiC paper. Discs of 3 mm in diameter were subsequently cut from this sample. Then, these samples were both spark cut and punched using a mechanical punch. For the crept samples, 3 samples were punched from one fractured specimen.

The TEM samples were prepared by an ion-thinning method. The ion-thinned samples were prepared in a Gatan-600 ion-milling machine at liquid nitrogen temperature with an accelerating voltage of 5 kV, a gun current of 0.5 mA and an incident angle of 8°. TEM observation was carried out on a JEM-2000FXII at the accelerating voltage of 200 kV.

Reference

1 N. Metcalfe, ME-46 Videoextensometer, Polymer 96.

Chapter 5

Materials Characterisation

5.1 Introduction

In this chapter, the fabrication technique of the composite is discussed. This is followed by characterisation of the composite microstructure by using the SEM and TEM. The texture of the composite is also examined by using the x-ray diffraction technique. Finally, the tensile and resistivity results of the composite are presented and discussed.

5.2 Material

5.2.1 Material production

The Cu-10vol.% Cr in situ composite used in this study was produced by vacuum casting at 1600°C by Essex Metallurgical Limited. The final ingot was approximately 14.5 mm in diameter. It was then hot forged at 900°C and swaged at room temperature into 3 mm diameter rod. This process was carried out in the Department of Materials Science and Metallurgy at Cambridge University. Deformation reduction can be expressed in terms of true strain $\eta = \ln \frac{A_i}{A_f}$, where A_i is the initial cross sectional area of the specimen and A_f is the final cross sectional area after deformation. This true strain must be greater than around 3 (equivalent to a reduction in area of approximately 95 %) to achieve any strengthening effect in the composite [1]. In the 3 mm rod, the deformation strain η was 3.15 which was approximately 95.6 % reduction in area.

5.2.2 Microstructure and texture evolution

(a) Microstructures

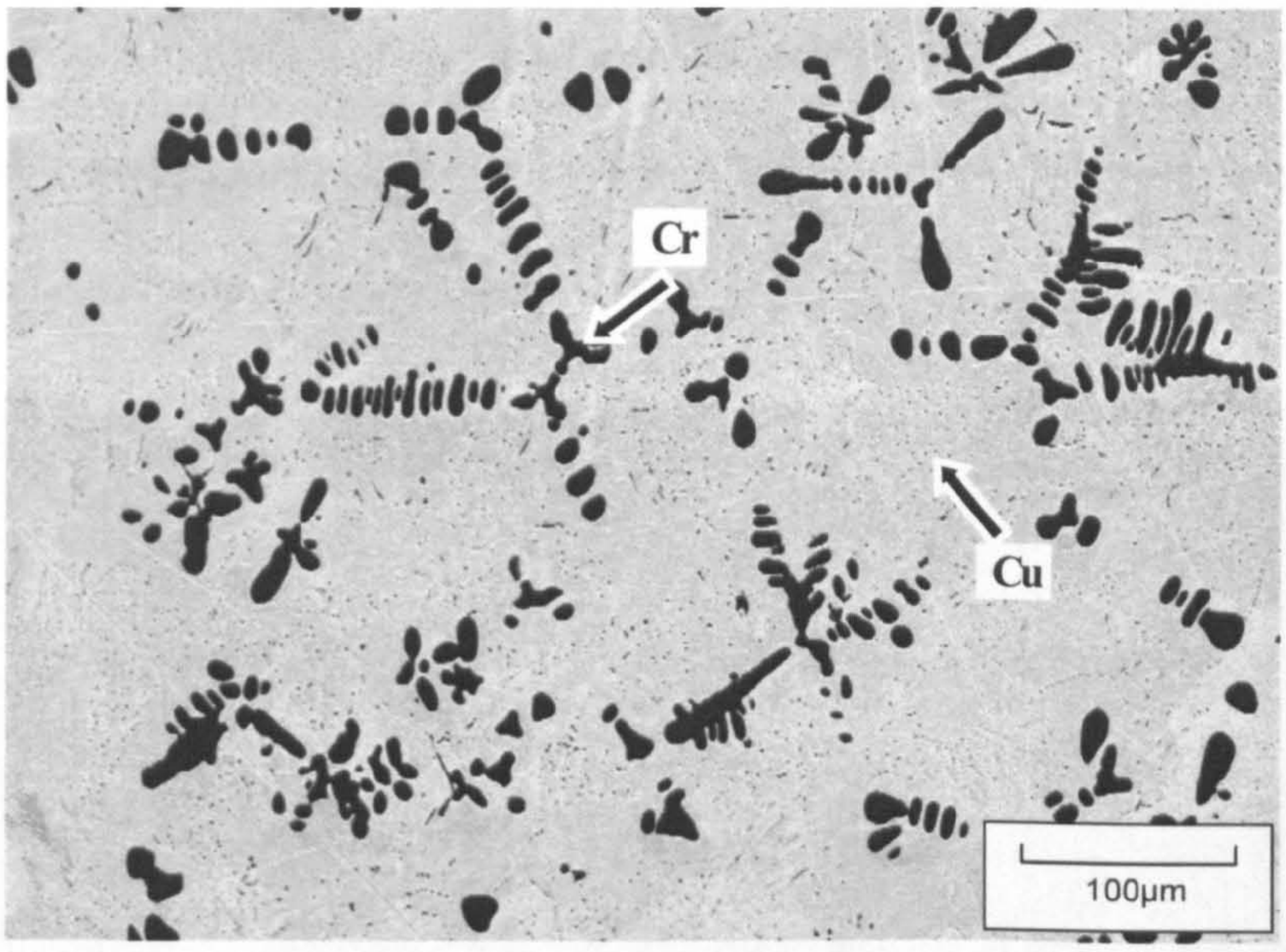

Figure 5.1 SEM image of the as-cast composite, the Cu matrix having being selectively etched away

In the as-cast state, the Cr was in a dendritic form as shown in figure 5.1. The dimension of dendritic Cr (including dendritic arms) varies from 20-100 μm. Because the mass density of Cu is 8.93 gcm^{-3} and that of Cr is 7.14 gcm^{-3} gravitational segregation of the primary dendrites during casting is not a major concern. During subsequent deformation, the Cr dendrites (the finer the dendrite size, the higher the flow stress subsequent to deformation) elongated into fibres parallel to the rod axis in a Cu matrix as shown in figure 5.2. The good interfacial bonding between Cu and Cr makes the large deformation possible without any interfacial failure, which is one of the advantages of in-situ composites.

It can be seen that after deformation, the original morphologies of dendritic Cr could not be distinguished. Some of them have been fully deformed into Cr fibres (A), while others (B) are still in particle form. The mean thickness of the Cr fibres

was 2 μm with an average aspect ratio of 25:1 (dimension parallel to the rod axis: dimension perpendicular to the rod axis) as measured from 10 SEM micrographs. A few fibres with a thickness of about 10 μm and an aspect ratio of 10 were also found in this composite. In this heavily deformed in-situ composite all fibres were aligned parallel to the rod axis.

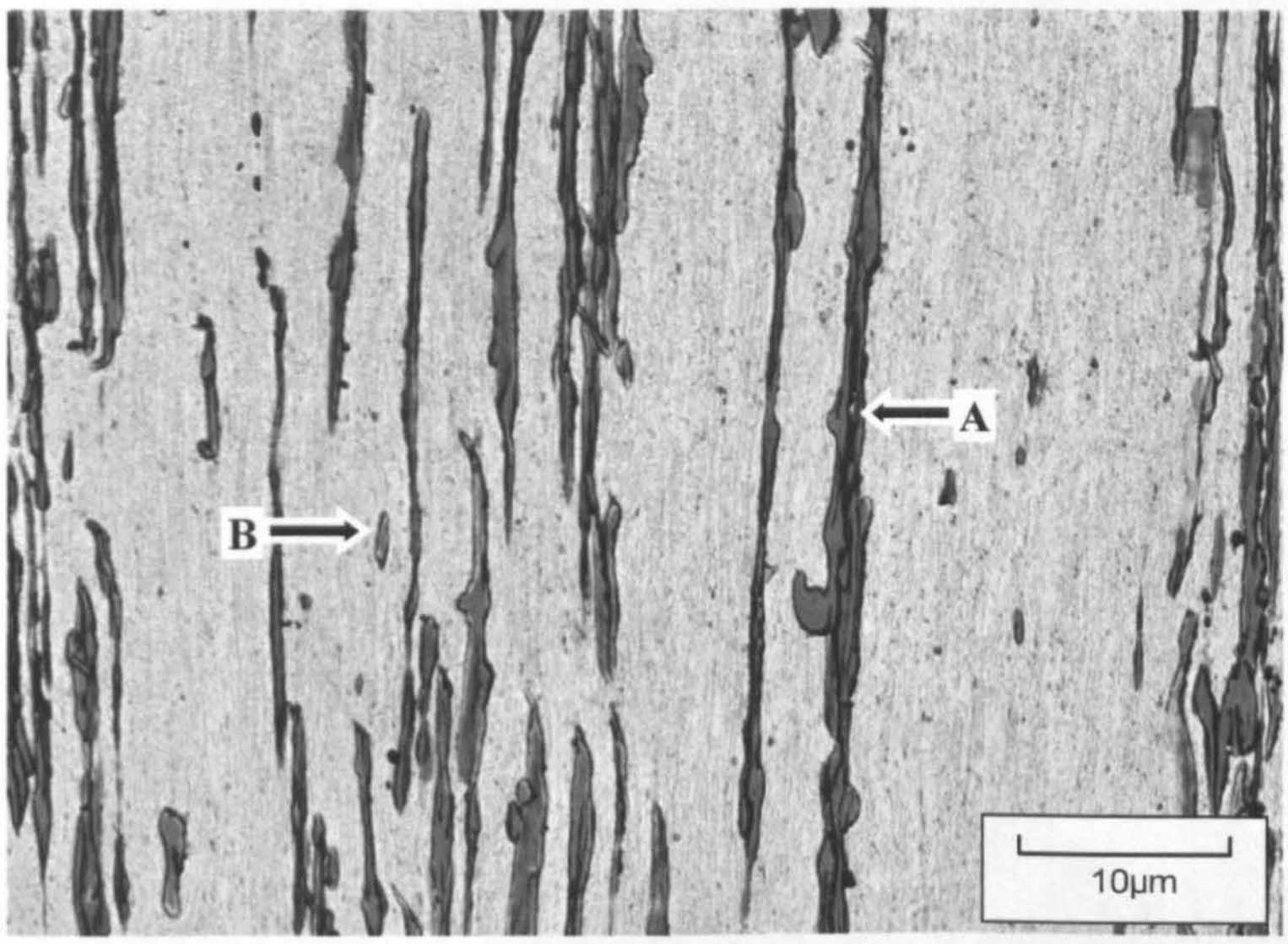

Figure 5.2 Longitudinal cross section of the composite. The Cu matrix appears light grey, and the Cr fibres appear dark grey in this back-scattered SEM micrograph. The Cr fibres lie parallel to the specimen rod axis

A transverse cross section micrograph is shown in figure 5.3. The ribbon-like morphology of the fibres is evident here; that is one of the dimensions is considerably smaller than the other. This tendency becomes quite pronounced at high η values in Cu-X composites, but it is relatively modest in these composites, since their maximum deformation was only $\eta=3.15$. The orientation of individual fibres relative to each other appears random. The ribbon morphology is due to the <110> swaging texture that develops in bcc Cr. Figure 5.4 shows a three dimensional representation of the composite rod composed of separate longitudinal and transverse SEM images.

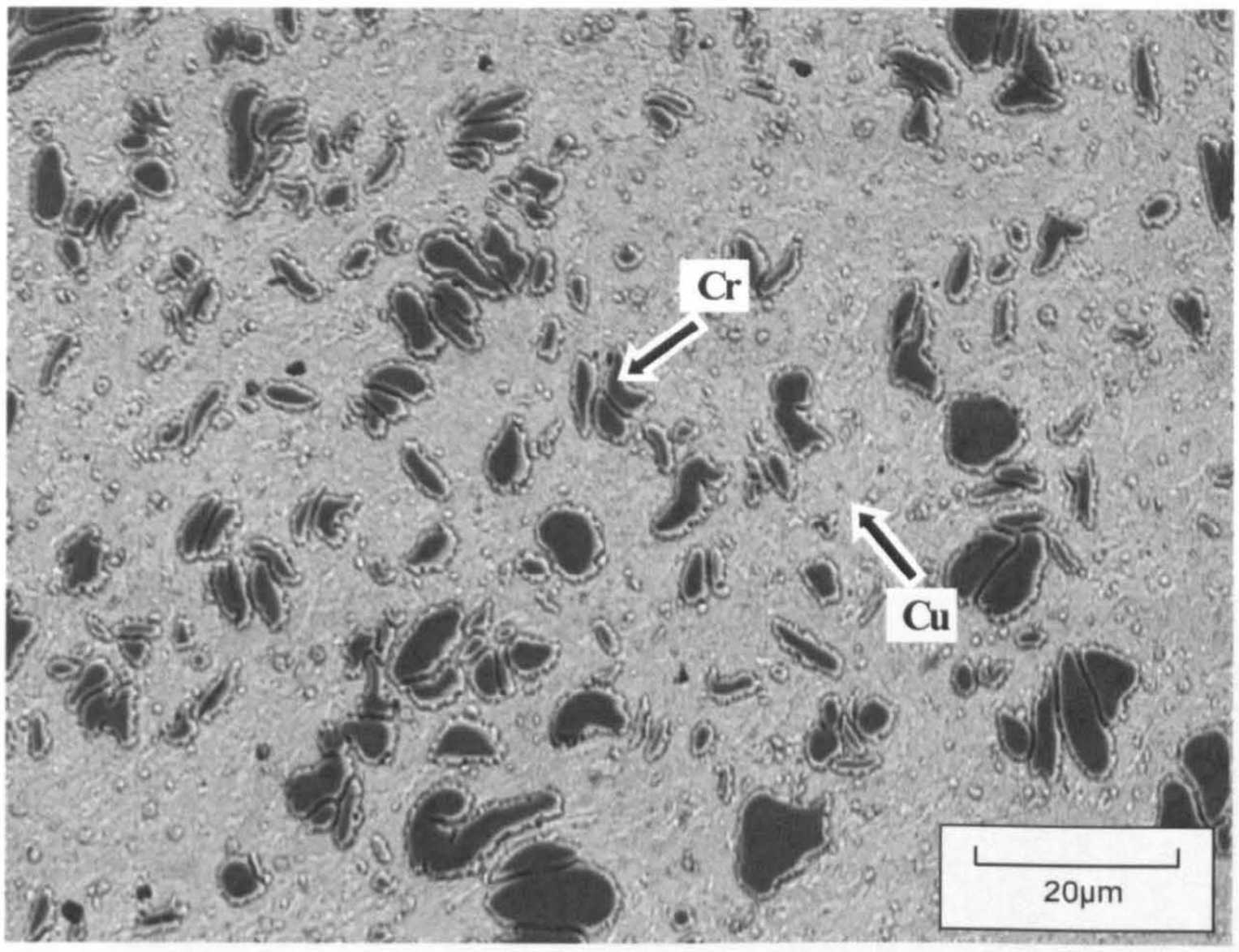

Figure 5.3 Transverse cross section of the composite

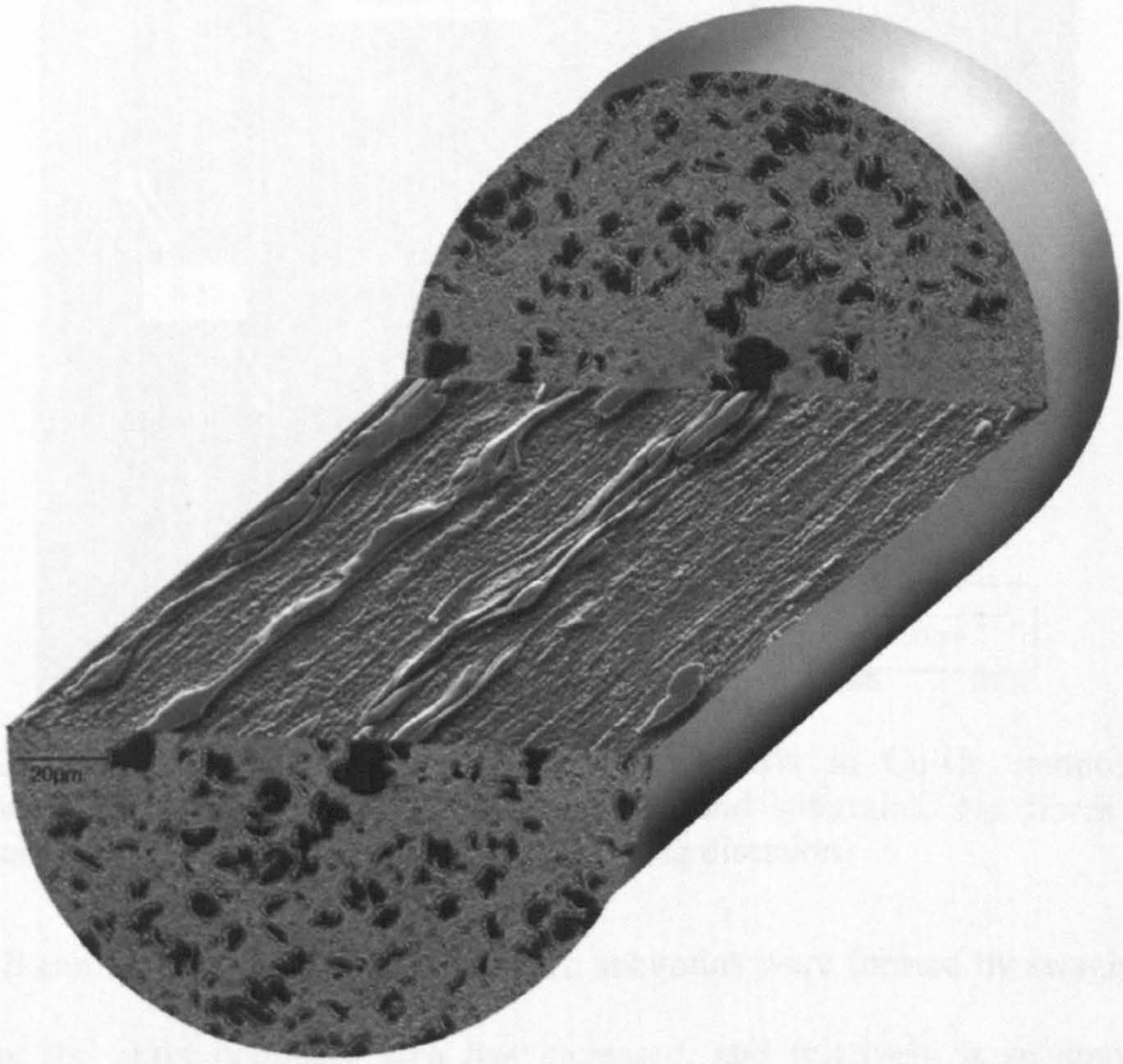

Figure 5.4 Three-dimensional view of the composite microstructure

The microstructure of the composite was also examined in detail using the TEM. Due to the difference in hardness of Cr and Cu, thinning is non-homogeneous. The Cr fibres usually remain thick when the Cu regions are thin enough for TEM experiments. Figure 5.5 shows the TEM image of the Cu matrix taken on the longitudinal section of the composite.

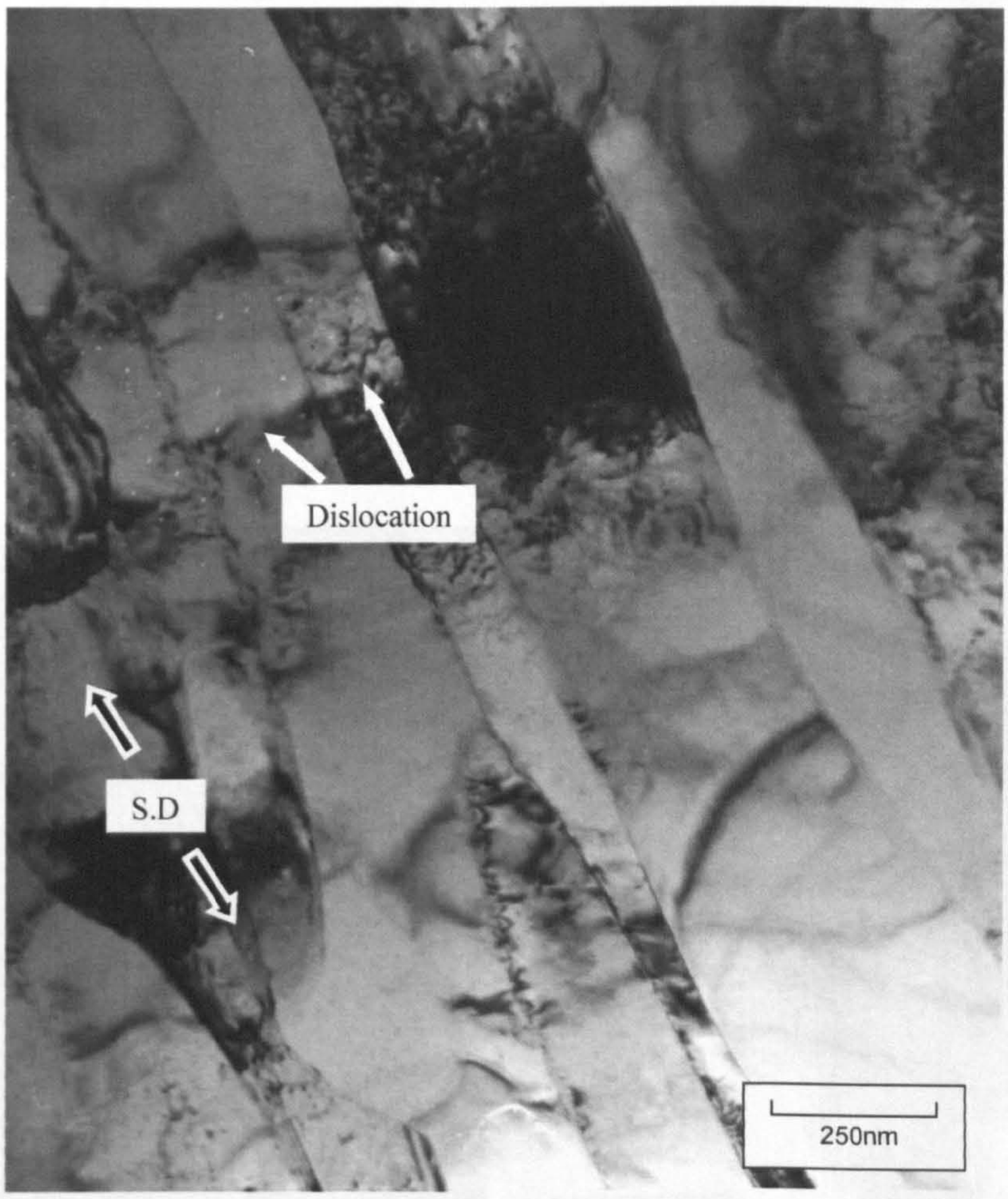

Figure 5.5 Longitudinal section of the Cu matrix in Cu-Cr composites showing the elongated Cu dislocation cells and subgrains. No fibres are present in the above micrograph (S.D: Swaging direction)

It can be seen that the elongated Cu subgrains were formed by swaging and therefore the grain boundary area has increased, and relatively large amount of dislocations were found in the deformed Cu phase. The axis of the banded Cu grains

lies in Cu <111> as confirmed by the selected area diffraction (SAD) pattern. The increase of both boundary area and the relatively high density of dislocations in Cu contribute to the work hardening of the Cu phase. After swaging, both Cu and Cr have been strengthened due to the work hardening (refer to Table 5.1).

The large Cr fibres which are observed using SEM cannot be easily observed in TEM due to preferential thinning (because of the difference in hardness between Cr and Cu) since the process used to make the samples electron transparent may only thin regions which do not contain the large Cr fibres. This is true for low deformation strain since the TEM specimens examined did contain some relatively thick regions which appeared to be large Cr fibres (confirmed by EDX spectrum) as shown in figure 5.6.

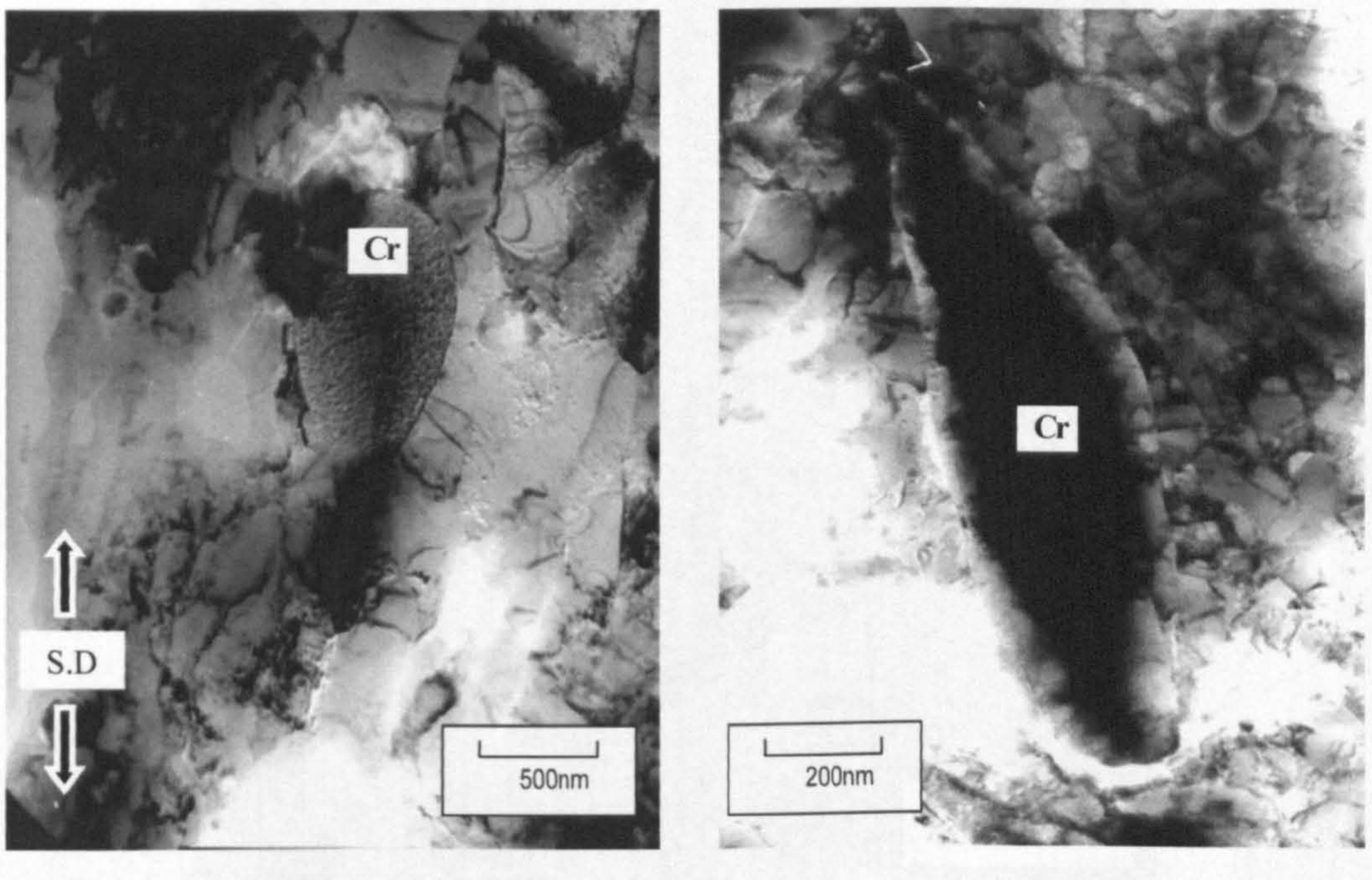

(a) (b)

Figure 5.6 Longitudinal section of the composite showing a (a) partially elongated Cr fibre and (b) fully elongated Cr fibre

Dislocations have been produced in Cr because of the plastic deformation. The black and white speckles in the TEM micrographs are surface artefacts resulting from ion milling of the foils.

In the transverse section, the composite consisted of Cu sub-grains with a more or less rectangular cross section and a relatively high dislocation density as shown in figure 5.7. Dislocations are observed forming cells within grains, although the cell walls are not very coarse. Dislocation cell structures with cell sizes of 0.65 μm are observed in the Cu matrix of the composite.

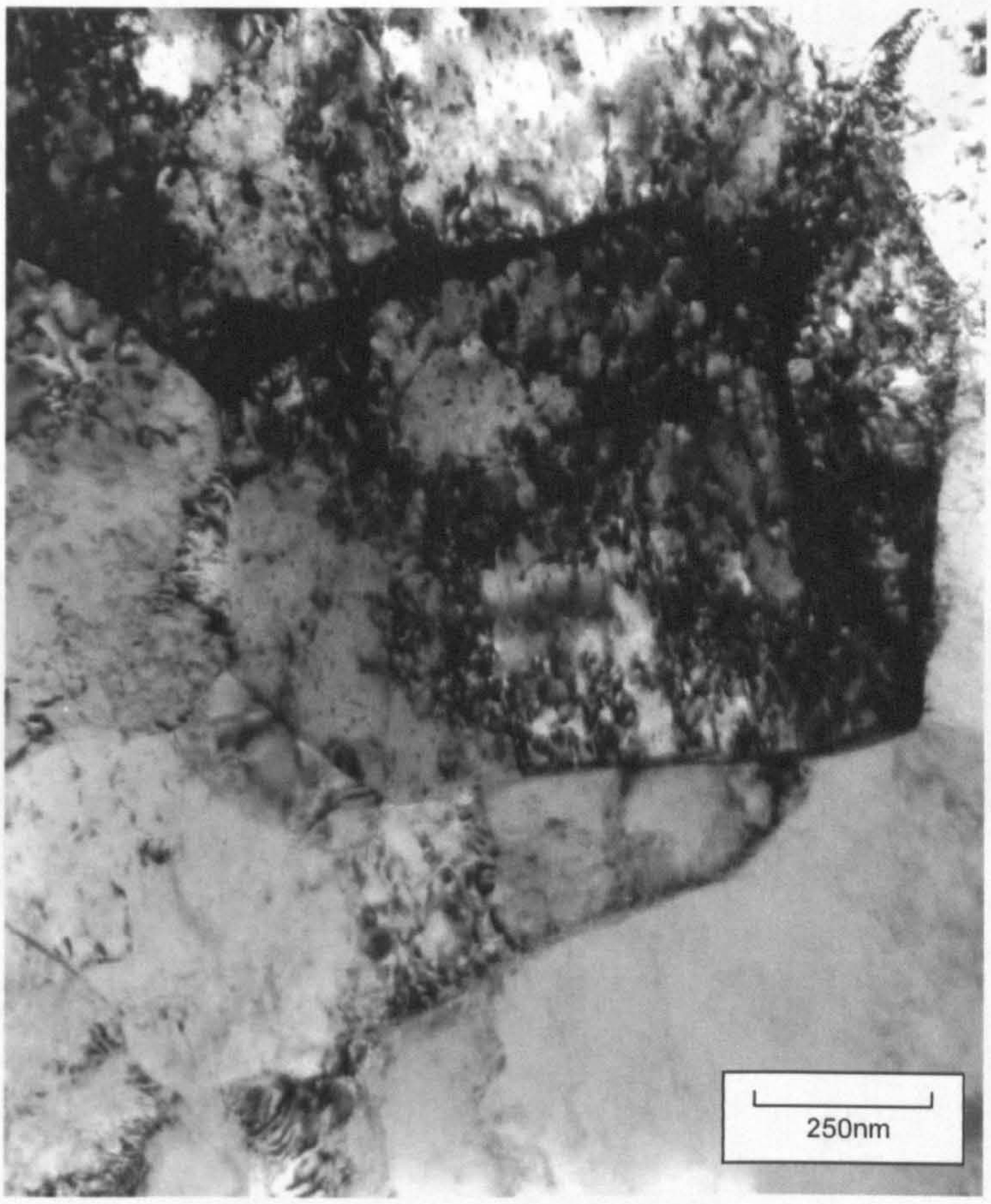

Figure 5.7 Transverse section of the composite showing that the composite consisted of Cu grains with more or less rectangular shape and a relatively high dislocation density

(b) Texture

Texture investigation in deformed composites provide a good means of obtaining information about the deformation behaviour. X-ray diffraction (XRD) analysis of the material at η= 3.15 indicated that the Cr had acquired the <110> fibre texture as shown in figure 5.8.

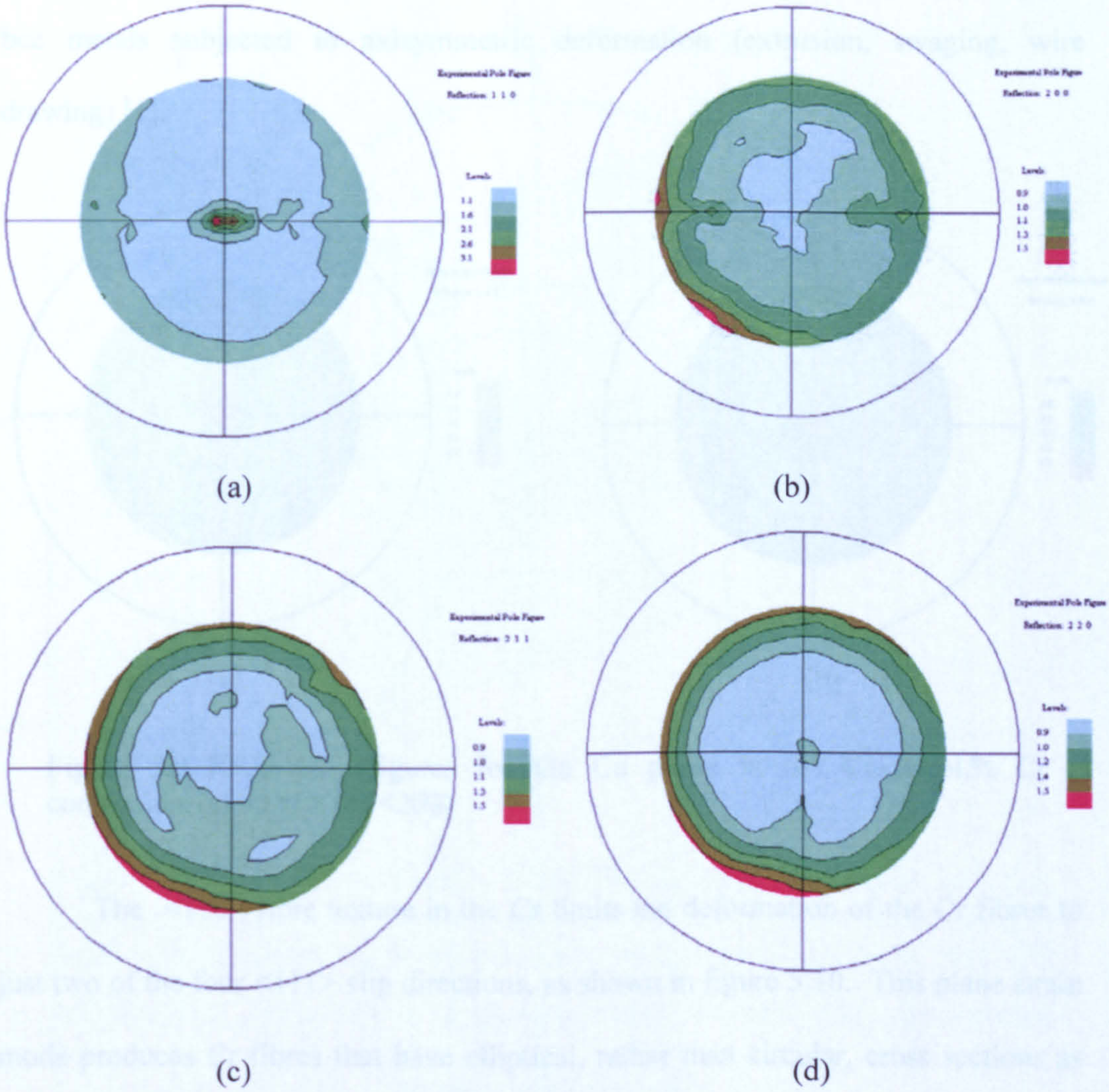

(a) (b)

(c) (d)

Figure 5.8 XRD pole figures for the Cr phase in the Cu-10vol.% Cr composites (a) <110> (b) <200> (c) <211> and (d) <220>

Cr pole figures for the <200>, <211>, and <220> were taken, but the resulting intensities were too near the background level to yield useful results. As

shown in figure 5.8, Cr has a predominant <110> texture while the Cu matrix has both <111> and <200> texture (figure 5.9). These findings are consistent with those of earlier studies of Cu-matrix, bcc fibre composites [1-3]. In a Cu-10vol.% Fe composite, Biselli et al. [2] determined that the Fe fibres assume a strong <110> fibre texture, that is, the <110> direction of individual Fe grains tends to lie parallel to the specimen's cylindrical line. Such <110> fibre texture is typical of single-phase bcc metals subjected to axisymmetric deformation (extrusion, swaging, wire drawing) [1].

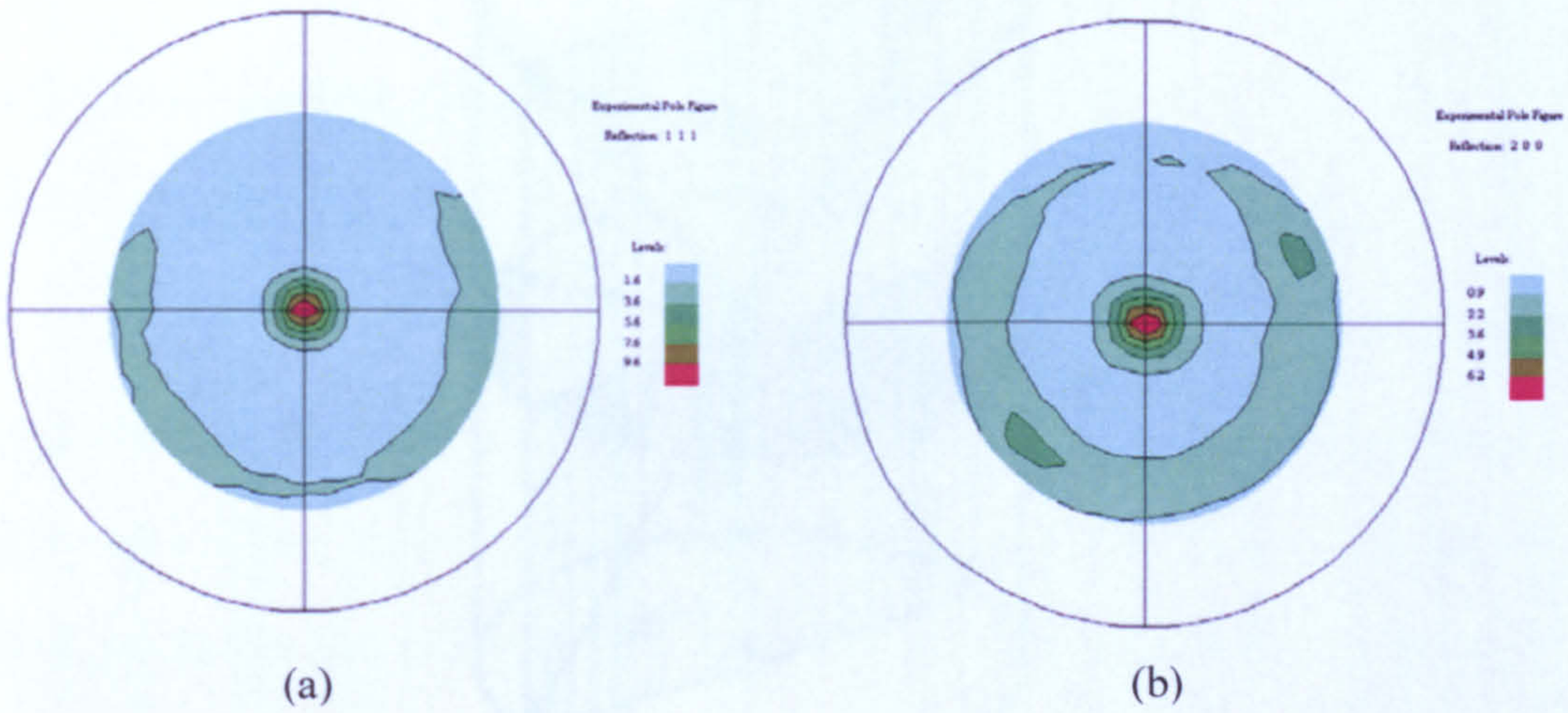

(a) (b)

Figure 5.9 XRD pole figures for the Cu phase in the Cu-10vol.% Cr composites (a) <111> (b) <200>

The <110> fibre texture in the Cr limits the deformation of the Cr fibres to just two of the four <111> slip directions, as shown in figure 5.10. This plane strain mode produces Cr fibres that have elliptical, rather than circular, cross sections as seen in a transverse section (figure 5.3). This tendency becomes quite pronounced at high η values (5-10) in Cu-X composites, but it is relatively modest in these composites, since their maximum deformation was only $\eta = 3.15$. Nevertheless, this plane straining effect results in a larger Cu-Cr interfacial area than would be present

if the Cr deformation were more nearly axisymmetric and the Cr fibres were approximately cylindrical. This larger Cu-Cr interfacial area will lower the effective shear stress at the Cu-Cr interface by distributing the shear force over a larger area, and thus this fibre morphology is less likely to experience matrix-fibre separation than would be the case in a classic composite containing cylindrical fibres.

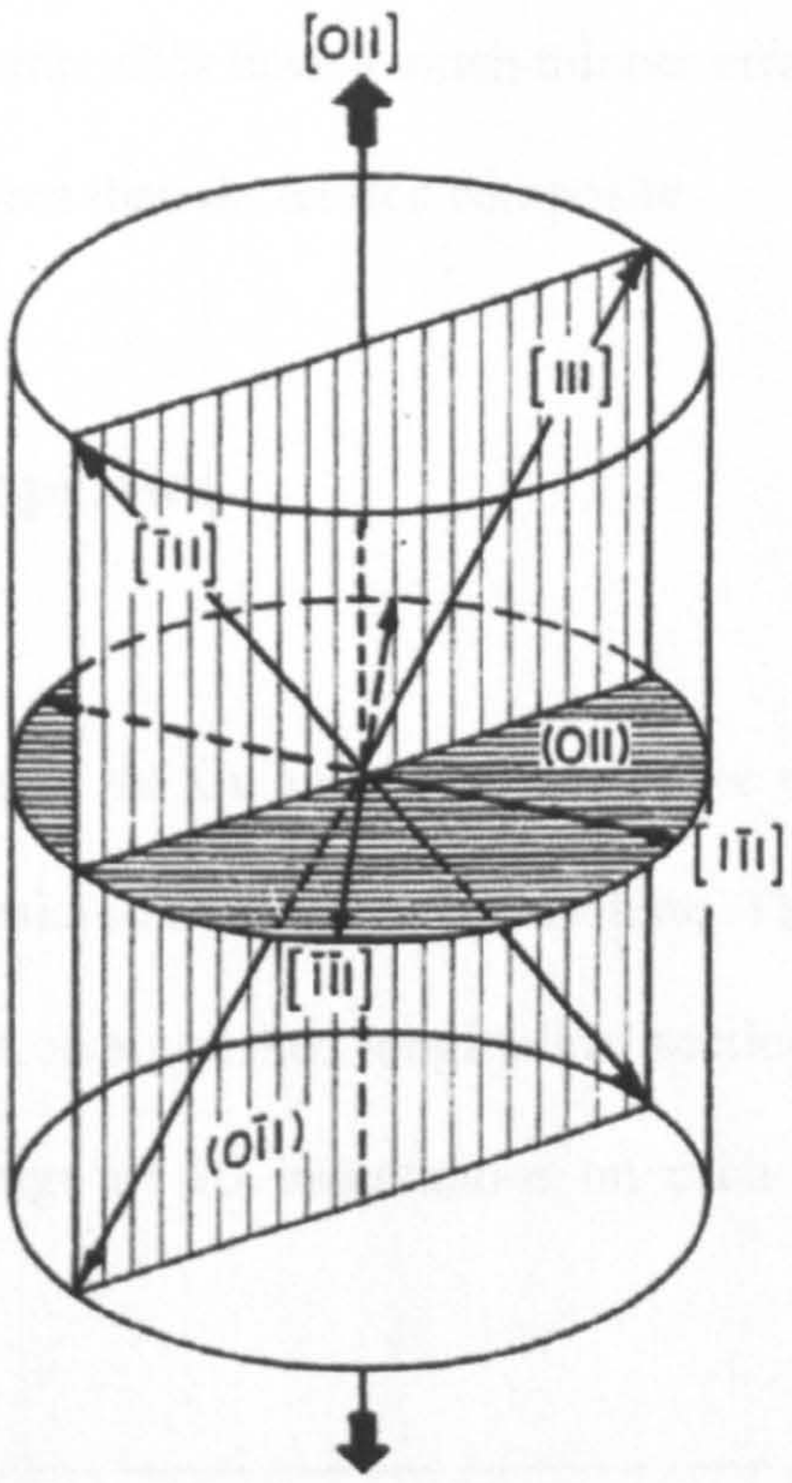

Figure 5.10 In a bcc crystal with a <110> fiber texture, two of the four <111> directions are positioned perpendicular to the rod axis and cannot slip (Schmid factor = 0). Thus, all slip is limited to the remaining two directions, the [111] and the $[\bar{1}11]$, resulting in a plane-straining filament with the unequal dimensions seen in figure 5.3
Reproduced from reference [4]

Beck et al. [4] were among the first to suggest that the strength of the fcc-bcc combination is much higher than fcc-fcc mixtures. The fcc-fcc mixtures strength was observed to increase linearly as deformation progressed, which differs from the

exponential increase in strength observed as true strain of deformation increases in fcc-bcc combination. This higher strengthening in fcc-bcc combination is believed to be a direct result of the filament morphology, which develops during deformation. While the fcc phase is free to deform axisymmetrically, the preference of bcc materials to adopt a <110> texture during drawing results in the curling and folding effect evidence in the Cr fibres shown in figure 5.3. Thus, for an equivalent amount of deformation, fcc-bcc composites have a much thinner effective fibre thickness and a much larger interfacial area than do fcc-fcc composite.

5.3 Mechanical properties

5.3.1 Hardness

The microhardness of the Cu and Cr phases in the composite was measured on a Mitutoyo MVK-G1 microhardness testing machine. The testing was performed under a 98 N load for 10 s on a polished longitudinal section of the composites. The final results are the average of 10 indentations on each specimen. A total of 3 specimens were used.

Phases	**Vickers Hardness (VHN)**		**Equivalent tensile strength for as-swaged (MPa)**
	As-Cast	**As-Swaged**	
Cu	65 (±5)	110 (±8)	350
Cr	185 (±7)	202 (±6)	650

Table 5.1 Hardness of the Cu and Cr phases in the as-cast and as-swaged conditions

Table 5.1 shows the hardness of the Cu and Cr phases in the as-cast and as-swaged conditions. From the hardness result, the equivalent tensile strength was determined from a standard Vickers hardness-tensile strength conversion table [6]. The hardness of the Cu phase increases significantly from 65 to 110 in the average Vickers hardness number (VHN) as the swaging strain increases from 0 to 3.15. This shows the dramatic work hardening of the Cu phase. The hardness of the Cr phase also increases from the as-cast to the as-swaged condition, but the change is much more modest than that of the Cu phase. A similar trend was also reported for Cu-15vol.% Cr-0.2Ti composite [5]. With a further increase in drawing strain, the hardness of the Cu phase continues to increase, but the rate of increase becomes lower [5].

5.3.2 Tensile response

The stress-strain plots obtained at nine testing temperatures are shown in figure 5.11. These plots show that the presence of the Cr fibres increases the room temperature yield strength of the material by 77 % and the ultimate tensile strength of the material by 43 % compared to those of as-swaged pure Cu (99 % purity).

As expected the addition of Cr results in a significant increase in the Young's Modulus and load bearing capacity of the composite at room temperature with a corresponding loss in ductility. The Young's Modulus of the composite may be calculated using the "*Rule of Mixtures*" (ROM) relationship assuming the isostrain loading condition ($E_{composite} = E_f V_f + E_m(1-V_f)$). Here, E_f and E_m are the Young's modulus of fibre and matrix respectively, and V_f is the fibre volume fraction. Substituting $E_f = 280$ GPa, $E_m = 135$ GPa, and $V_f = 0.1$ into this expression

gives a composite modulus of 149 GPa. The slope of the elastic region in figure 5.11 for the composite tested at room temperature is 142 GPa, which is close to the calculated ROM value.

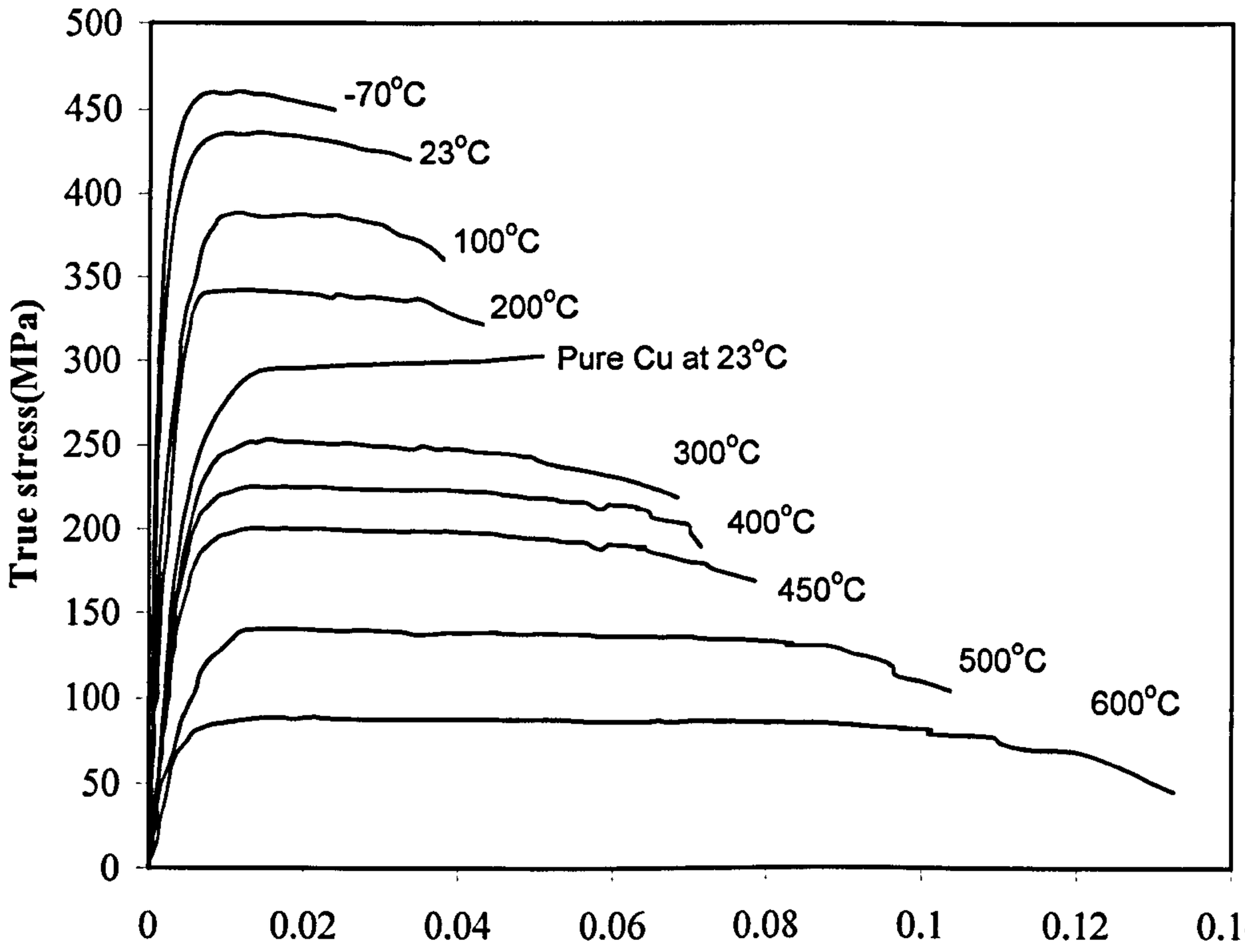

Figure 5.11 Stress/strain response for pure Cu and Cu-Cr composites tested from –70°C to 600°C

Table 5.2 gives a summary of all the tensile properties of the composites tested from –70°C to 600°C. The yield strength and the modulus of the composite decrease with temperature whereas the failure strain increases with temperature. The observed increase in failure strain with an increase in temperature from 22-600°C is as high as 333 %.

Test temperature (° C)	0.2% Yield strength (MPa)	Tensile strength (MPa)	Young's modulus (GPa)	Failure strain
-70	400 (±5)	470 (±7)	160 (±6)	0.02 (±0.01)
22	384 (±7)	430 (±9)	149 (±8)	0.03 (±0.02)
100	333	380	142	0.04
200	326	338	138	0.04
300	226	255	101	0.07
400	206	220	95	0.07
500	121	140	60	0.10
600	82	85	46	0.13

Table 5.2 Summary of mechanical and materials properties of the Cu-Cr composites tested from –70°C to 600°C

The ROM method predicts a room temperature tensile strength of 380 MPa (σ_m= 350 and σ_f= 650 MPa). However simple composite models do not really include the extent of microstructural refinement since the unreinforced materials are unlikely to have the same level of microstructural refinement as for the composite. The ROM value is lower than the 430 MPa measured tensile strength of the composite at 23°C.

Heavily deformed Cu-X composites frequently have strengths higher than ROM predictions for reasons that have been discussed at length elsewhere [1]. Positive deviations from the rule of mixtures occur, with the magnitude increasing with increasing strain [1]. Observed tensile strengths eventually approach the theoretical limit at drawing strain of η= 9-10 and the fibre diameters of tens of nanometers. Dislocation density was found to increase rapidly with strain until the fibre size reaches very small values (tens of nanometers) at which point it decreases sharply and some fibres appeared nearly dislocation free. This behaviour was due to the reduction of interphase spacing with strain and must involve comparatively long range (e.g. dislocation/dislocation) rather than short range (i.e. atomic scale) interactions.

The existing models for strengthening of Cu-X composites are difficult to apply to the composite data of the present study, since tensile strength was measured only at one value of η (= 3.15) at which the interfilamentary spacing is greater that the microstructural scale of the Cu matrix. Therefore, both barrier strengthening models (Spitzig and coworker) [7] and dislocation storage models (Courtney and coworkers) [1] cannot be used to predict the strength of Cu-Cr composites of the present study since the microstructural scale (50-300 nm) of highly deformed composite is much smaller than that (2-5 μm) of the present study.

5.4 Electrical resistivity

Electrical resistivity is a measure of the resistance a particular material presents to a passage of charge carriers or current, under the influence of an electric field. Above temperatures in the vicinity of absolute zero, the resistivity of most metals increases with increasing temperature. As the temperature increases, the amplitude of the atomic vibrations in the crystal lattice increases. Consequently, the probability of collision between conduction electrons and atoms or ions increases, resulting in greater resistance to the flow of current (i.e. greater resistivity).

Within the elastic limit, the effects of deformation on the resistivity of metals are small. Plastic deformation causes the generation of new lattice defects or imperfections, such as vacancies and interstitial atoms, as well as dislocations. Hence, the resistivity increases with deformation. The resistivity of Cu-based composites can be partitioned into the contribution of five scattering mechanisms as follows:

$$\rho_{cu-cr} = \rho_{pho} + \rho_{\text{int}} + \rho_{imp} + \rho_{dis} + \rho_{dam} \qquad (5.1)$$

where ρ_{pho} is the resistivity contribution from phonon scattering, ρ_{dis} is dislocation scattering, ρ_{int} is the interface scattering, ρ_{imp} is the impurity scattering and ρ_{dam} is the resistivity increase due to the damage such as voids and interfacial debonding [8].

The phonon scattering, interface scattering and impurity scattering are not likely to change during deformation of the composite at a constant temperature. Since the dislocation density increases with increasing deformation strain, the resistivity due to dislocation scattering increases with deformation strain. The more rapid increase of resistivity at low strain is more likely to be associated with the resistivity increase due to increasing dislocation density since the microstructural damage due to voids and interfacial debonding would be minimal as there is none at low plastic strains.

The resistivity of the composite tested at room temperature prior to testing was $2.97(\pm 0.02)\,x10^{-8}$ Ωm (resistivity of pure Cu was $1.72(\pm 0.02)\,x10^{-8}$ Ωm). Plastic deformation of the composite changed the resistivity by only approximately 4 % as shown in figure 5.12. Considering that the initial increase of the resistivity can be linked with the increase of dislocations, the increase of resistivity due to damage is thought to be very small before the final fracture process sets in. The small increase in resistivity after the flow stress was saturated indicates that the Cr fibres were behaving in a ductile manner and fracturing or separating from the Cu matrix was not significant as the yield strength ($\sigma_{0.2\%}$ = 384 MPa) was exceeded.

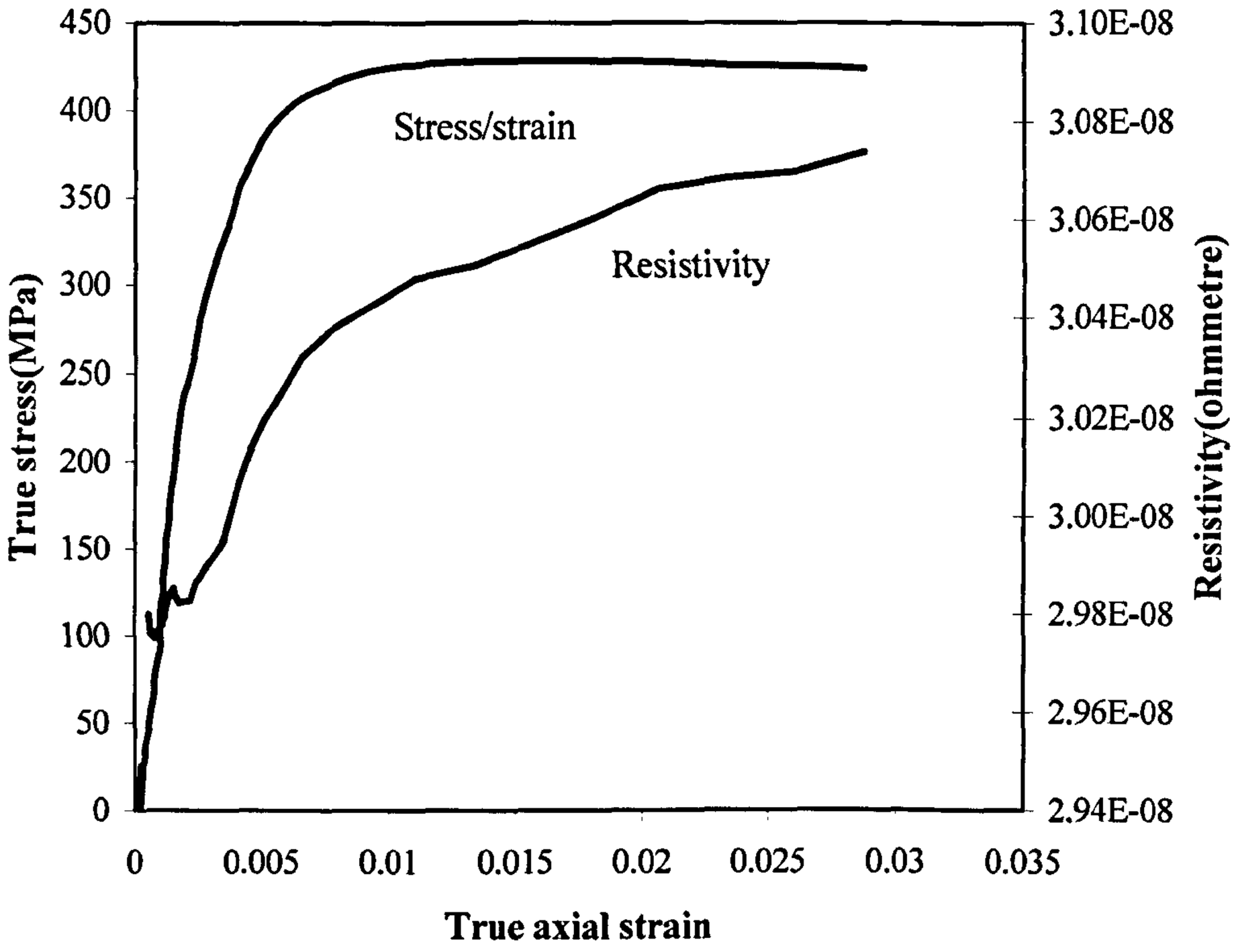

Figure 5.12 Change in resistivity of the composite at room temperature during tensile test

5.5 Microstructural damage

Almost no damage (i.e. cracks and voids) was observed in the composites after swaging, and therefore the subsequent analyses of damage (bulk behaviour) are based on the assumption that all damage observed in the broken tensile test specimens occurred during tensile testing. The fracture surfaces of the test specimens were subsequently examined by SEM to determine the various failure mechanisms that are operative during tensile deformation of the composites.

Selected fractured specimens were also sectioned along their tensile axes and prepared for metallographic examination. In order to characterise the extent of damage as a function of temperature, micrographs were taken of the polished samples at the fracture surface (~ 2 mm from the fracture surface), and far from the

fracture surface (~ 8 mm from the fracture surface) and at an intermediate distance (~ 4 mm from the fracture surface) as shown in figure 5.13.

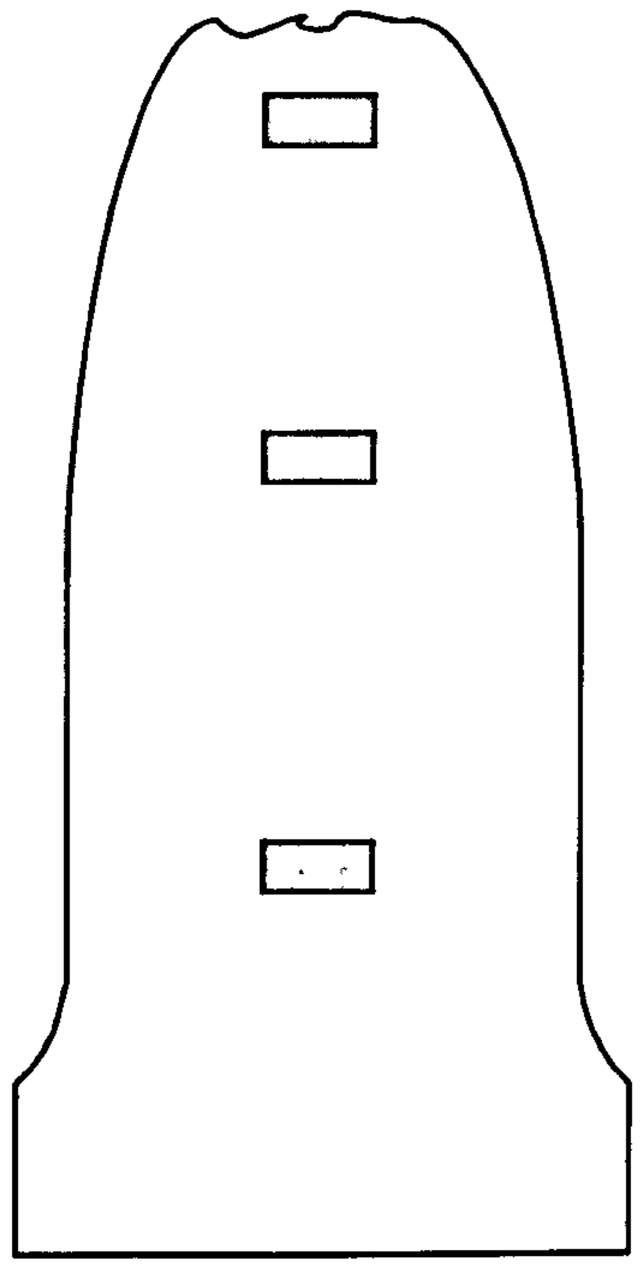

Figure 5.13 Schematic diagram showing the positions on a specimen where the SEM images were taken

5.5.1 Low temperature

Microstructural observation of longitudinal sections of the fractured specimens shows that the damage in the composite was highly localised near the fractured surface as shown in figure 5.14. Damage was seen in the form of reinforcement cracking. Fibre cracking is much more severe and frequent at –70°C, suggesting the ductility of Cr fibres decreases rapidly below room temperature.

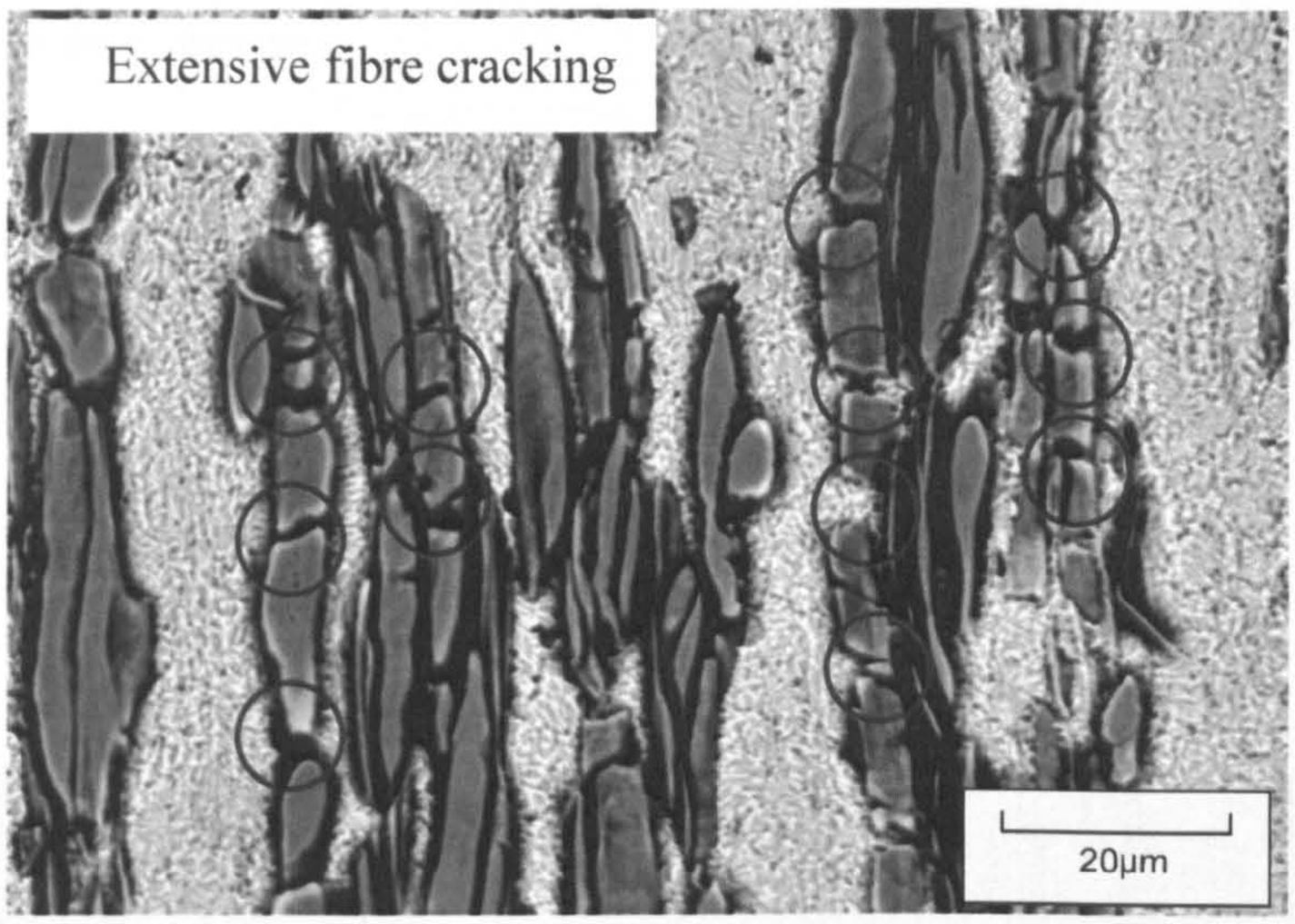

(a)

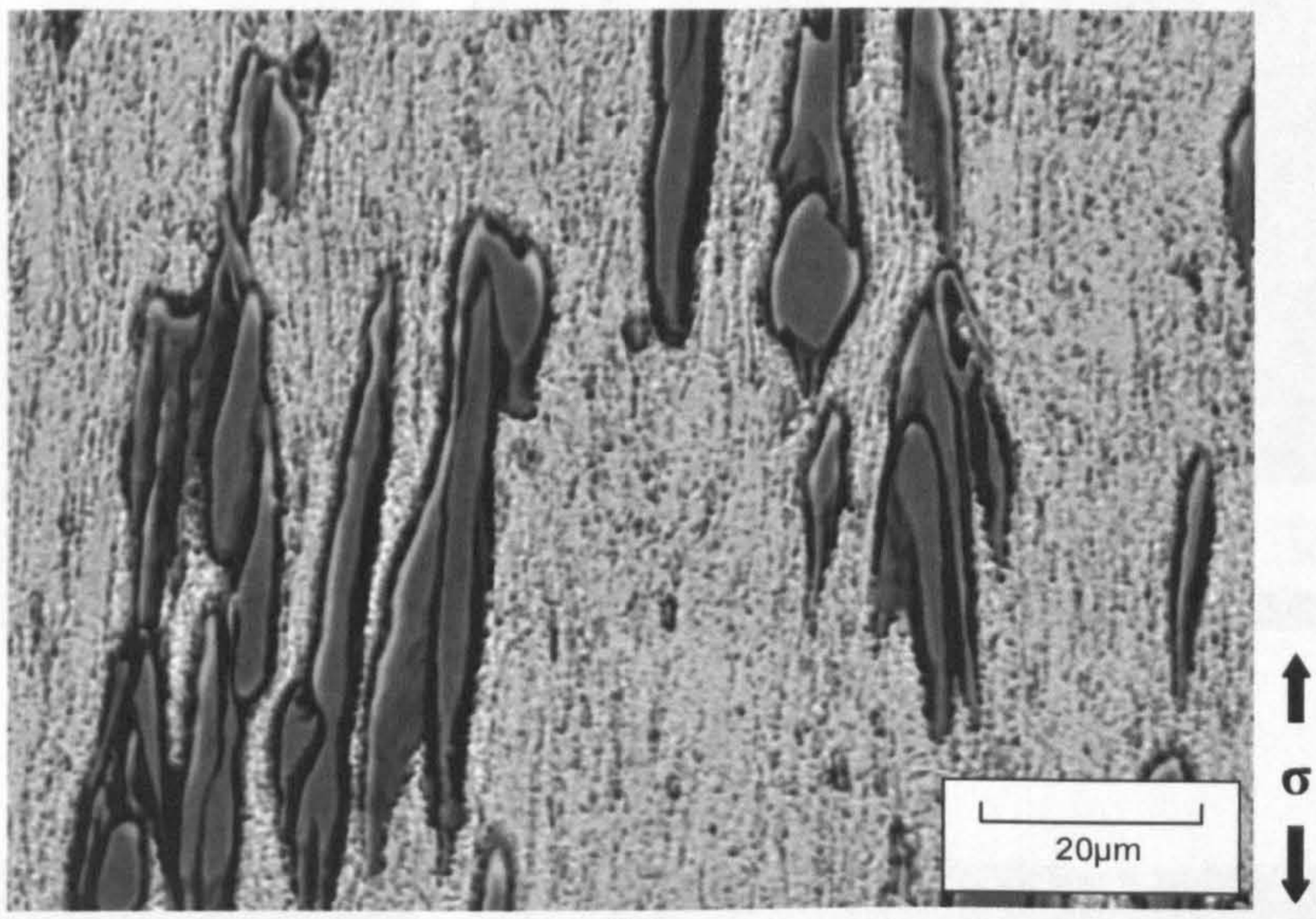

(b)

Figure 5.14 Typical micrographs taken from (a) near the fracture surface and (b) remote from the fracture surface of the composite tested at –70°C: note that damage is localised near the fracture surface in the form of fibre cracking

5.5.2 Room temperature

The fracture surface characteristics of pure Cu (produced using the same method as the composite) and Cu-Cr composites tested at room temperature are shown in figure 5.15 and figure 5.16 respectively. Figure 5.15 shows that the Cu exhibits a large number of dimples, indicating that the sample fractured by a ductile mode.

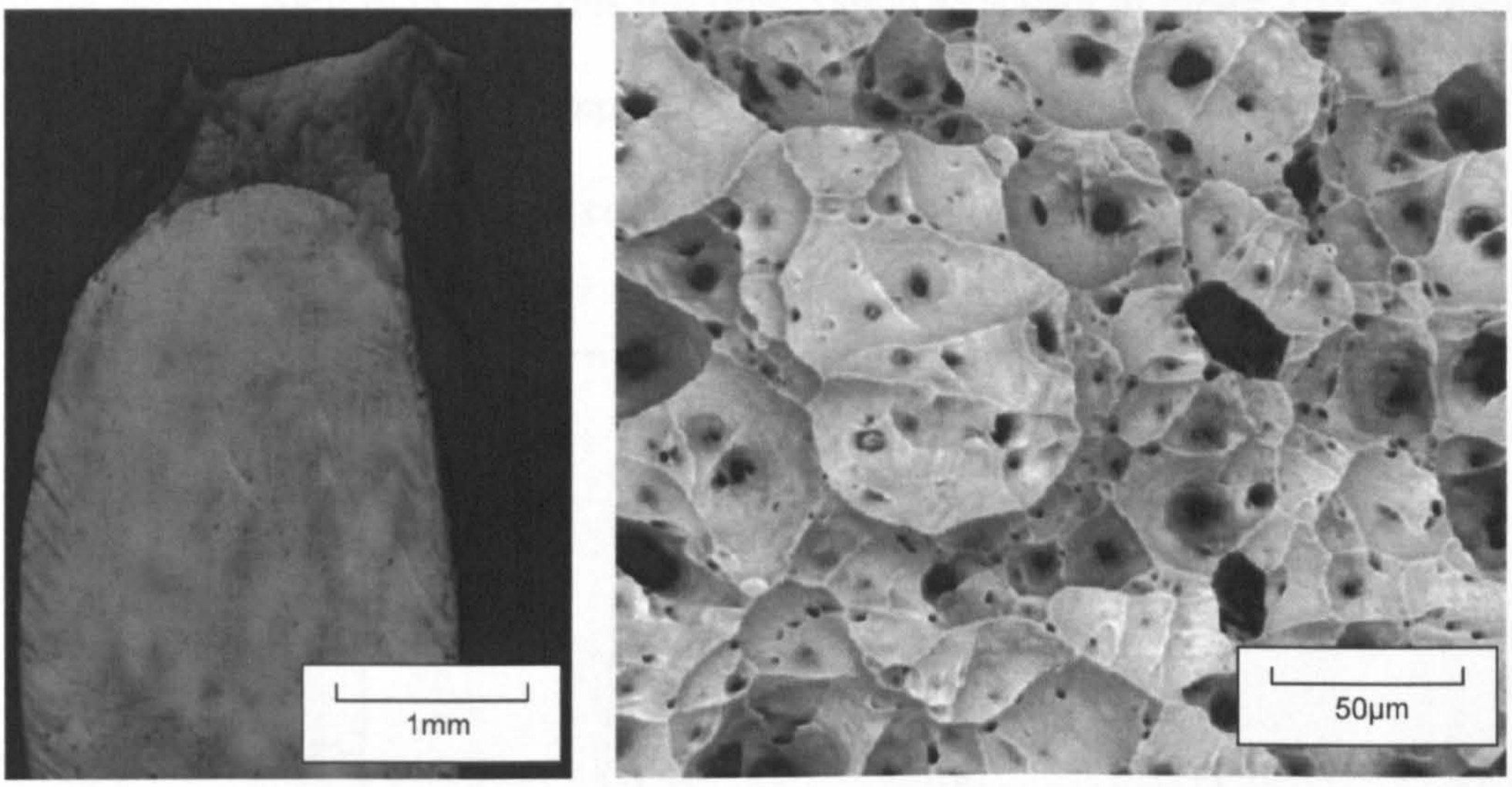

Figure 5.15 SEM images of the fracture surface of pure Cu

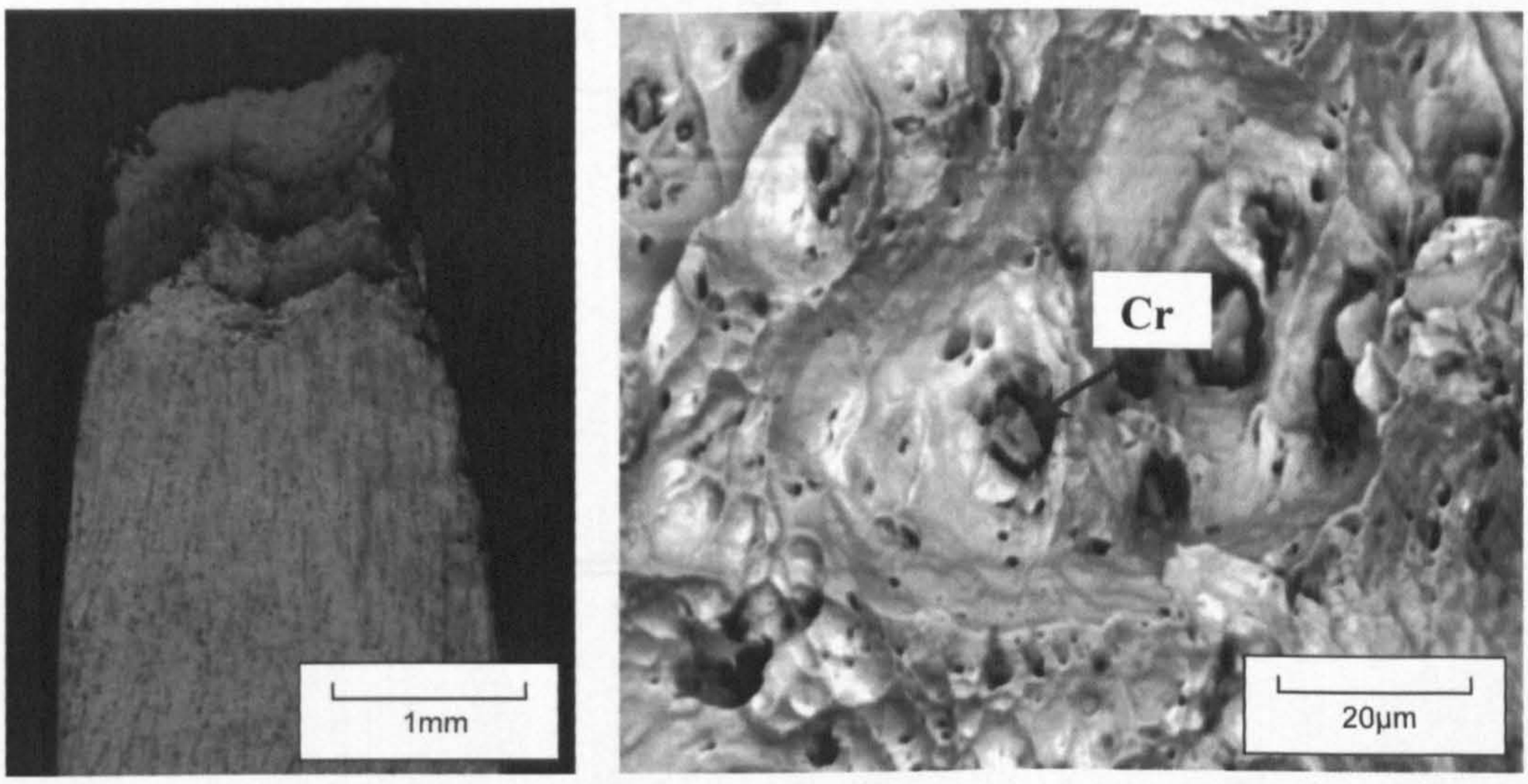

Figure 5.16 SEM images of the fracture surface of the composite

Similar to that of pure Cu sample, the fracture surface of the composite also exhibits a large number of dimples as shown in figure 5.16, indicating that it failed by ductile fracture; no evidence of Cu-Cr separation or early brittle Cr fracture is visible in this micrograph or in the several others taken of this fracture surface. As indicated by the arrow in figure 5.16, the Cr fibre was observed on the bottom of some large dimples on the fracture surface. Microanalysis on figure 5.16 (indicated by the arrow) using EDX confirms this observation as shown in figure 5.17. At high drawing strain ($\eta = 6.8$), the dimples become shallower which indicates that some extent of brittle fracture has also contributed to the failure of the sample [5].

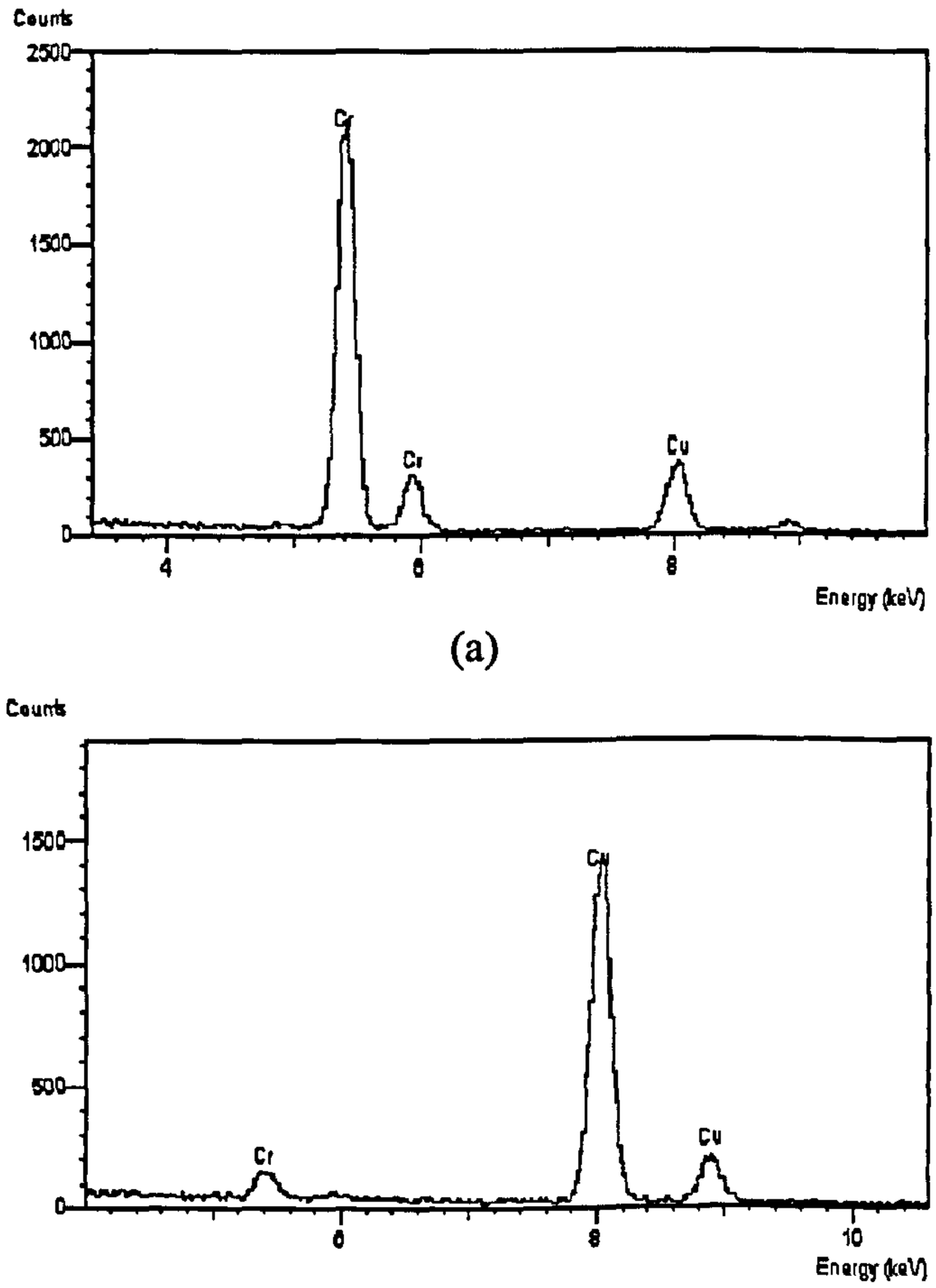

Figure 5.17 (a) EDX spectrum from a Cr fibre at the bottom of a dimple in figure 5.16 as indicated by the arrow; and (b) EDX spectrum from the ligament of the dimples in figure 5.16

The relationship of the Cr fibres with the fracture surface can be seen more clearly by looking at longitudinal sections of the rod just beneath the fracture surfaces of the specimens. Longitudinal cross section SEM images of the tensile sample showed insignificant damage despite its vicinity to the fracture surface (2 mm from the fracture surface) but matrix voids can be seen adjacent to the fibre ends or where fibres might have necked to failure as shown in figure 5.18. Such failure sites were rare even in the immediate vicinity of the fracture surface and were not found at all further from it.

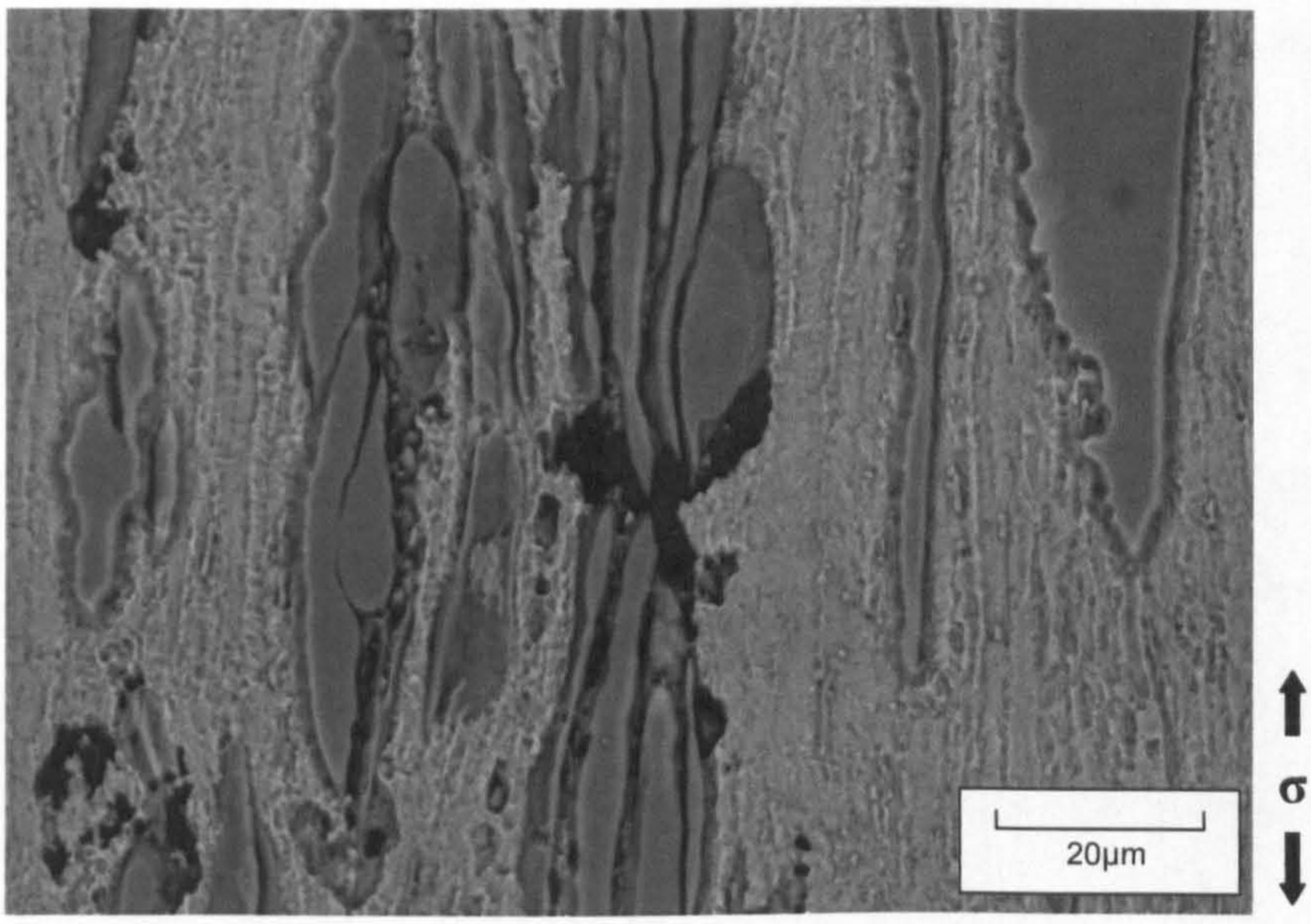

Figure 5.18 Longitudinal section of the fractured composite specimen (2 mm away from the fracture surface (to the top)

5.5.3 Elevated temperatures

One major problem with Cu-based composites is the loss of strength when exposed to high temperatures [1]. The big interphase area within the composites provides a large driving force for the energy minimisation through phase size coarsening. Experimental work has found that the decrease in strength of Cu-20vol.% Nb at temperature above 300°C was due to the Nb fibres coarsening [7,8]. The degree of coarsening increased at a given temperature as the degree of deformation of the wire is increased (fibre thickness decreased). However, as the swaging strain of this composite is relatively low, the morphology of the fibres are unlikely to coarsen. No fibre coarsening was apparent in samples tested even at high temperature during creep testing as will be shown in Chapter 7.

The micrographs shown in figure 5.19, figure 5.20 and figure 5.21 were taken from specimens tested at 300°C, 400°C, and 500°C respectively. Damage is primarily located near the ends of Cr fibres in the form of matrix cavitation. There was also some evidence of matrix cavitation at the interface between the Cu matrix and the Cr reinforcement. In all cases, failure occurred by the coalescence of cavities.

The level of damage was found to increase as the temperature increases. At temperatures up to 300°C, microstructural observation of longitudinal sections of the fractured specimens immediately beneath the fracture surface showed that the damage in the composite was fairly localised. Further from the fracture surface, not much damage was seen as shown in figure 5.19.

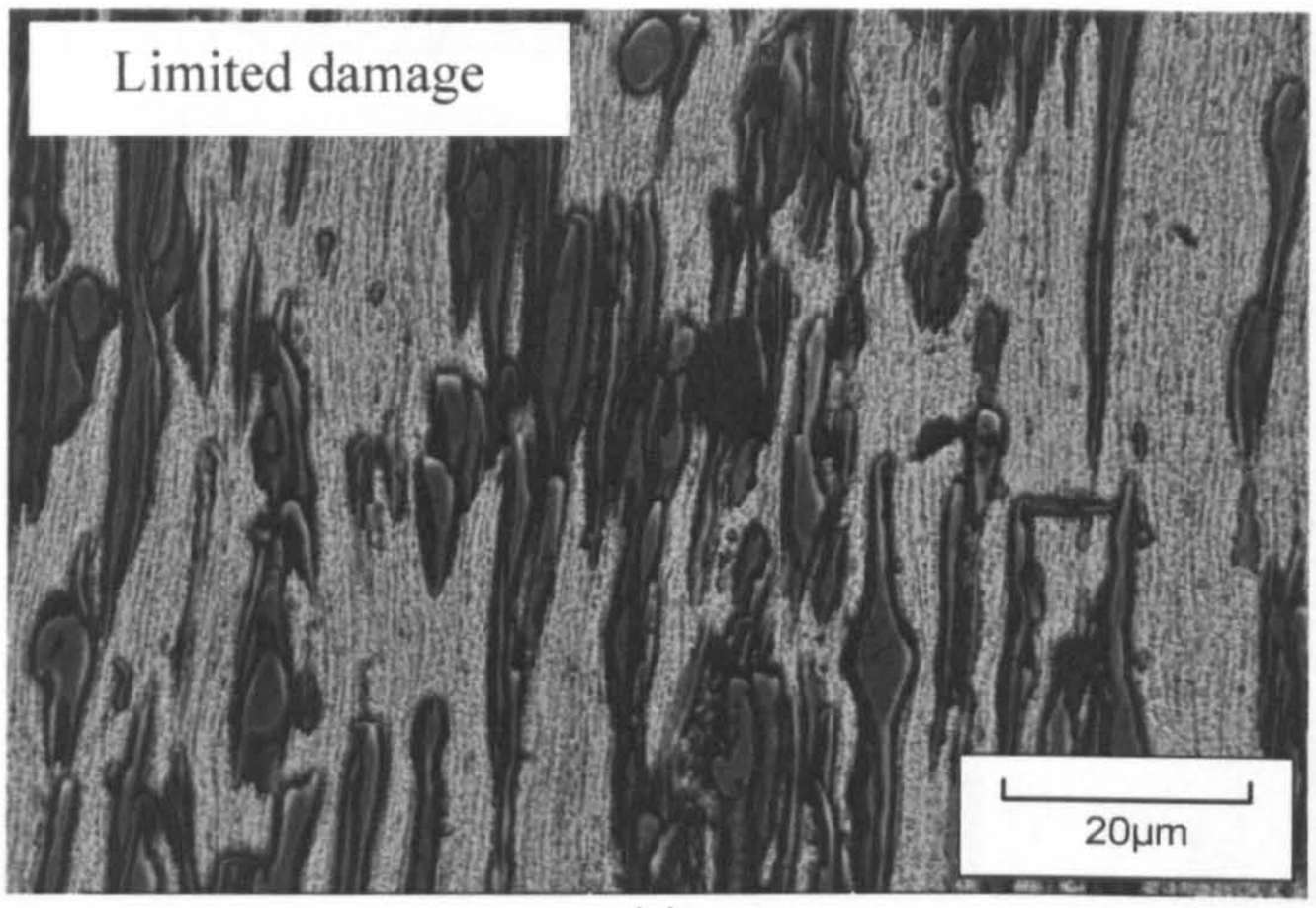

(a)

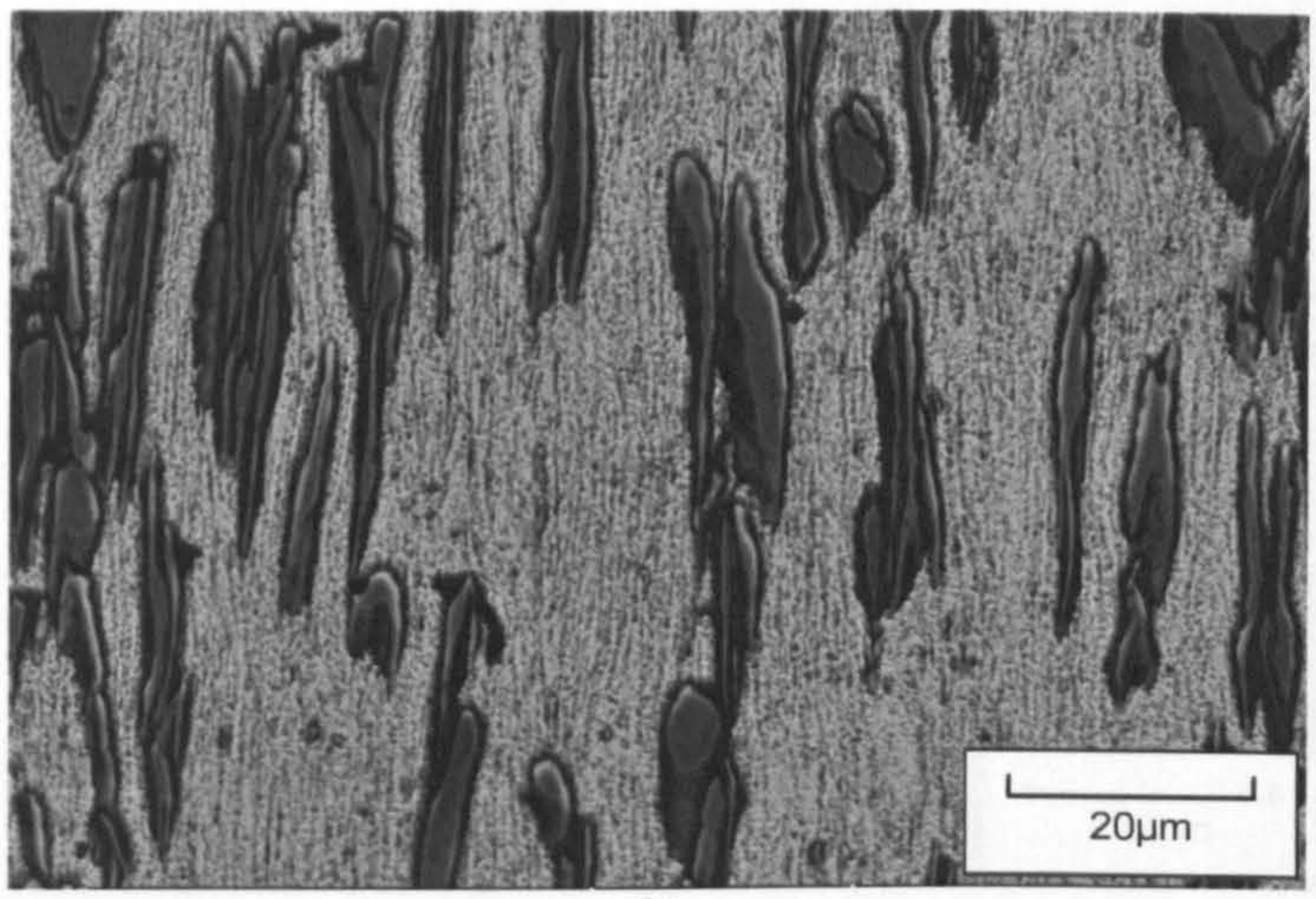

(b)

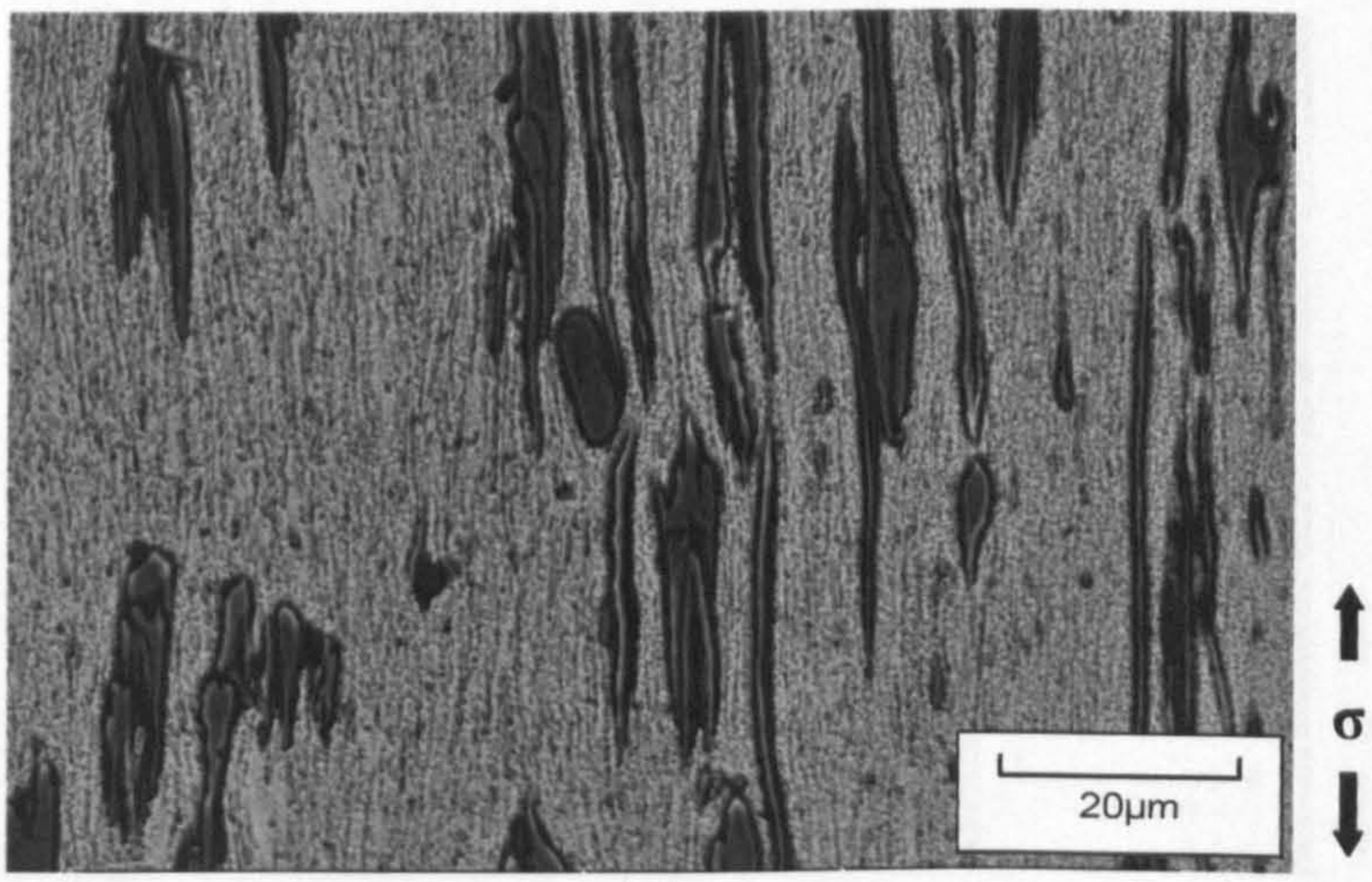

(c)

Figure 5.19 Typical micrographs taken from (a) near the fracture surface and (b) intermediate distance from the fracture surface (c) far from the fracture surface for specimen tested at 300°C

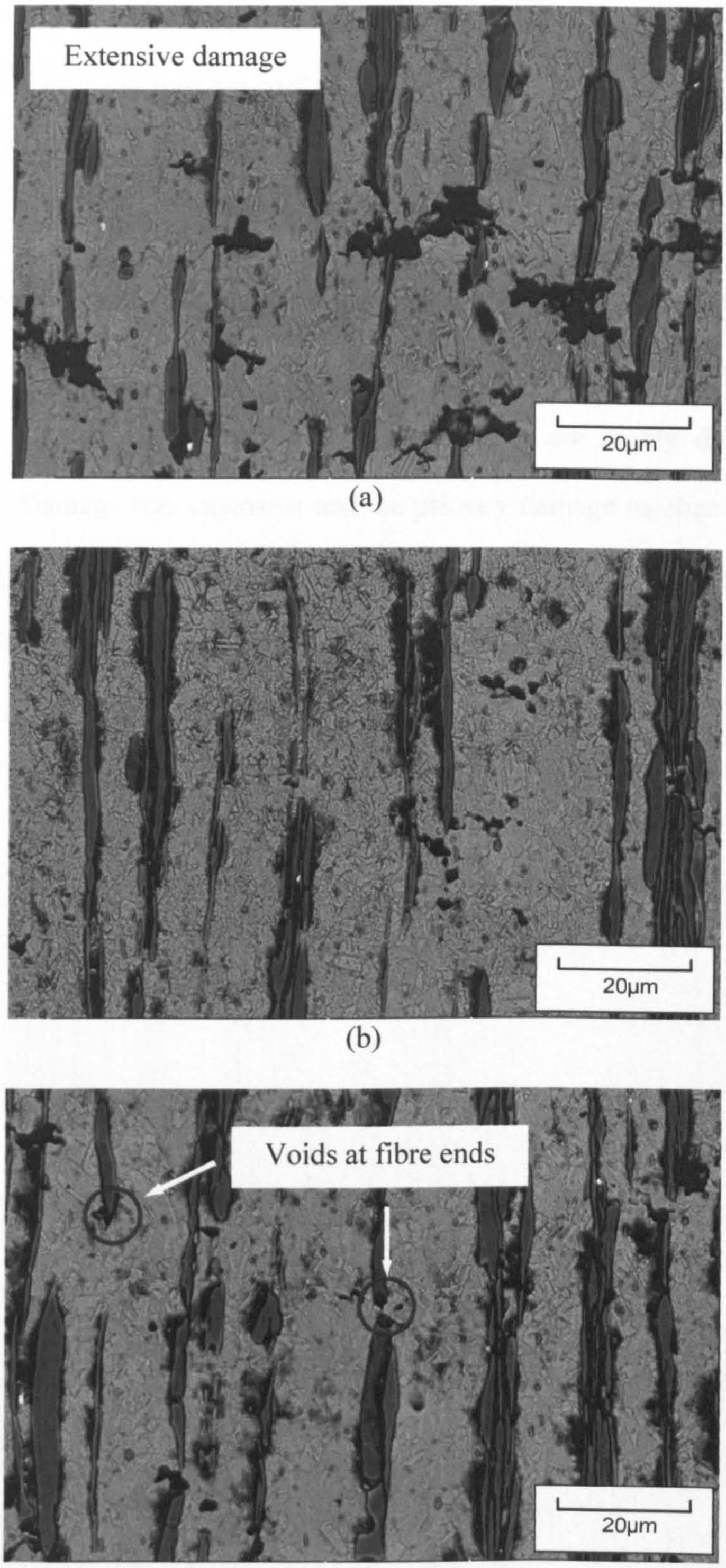

Figure 5.20 Typical micrographs taken from (a) near the fracture surface and (b) intermediate distance from the fracture surface (c) far from the fracture surface for specimen tested at 400˚C

However, for the composite tested at 400°C, the amount of damage was slightly greater near the fracture surface than at 300°C but was also found to extend throughout the gauge section as shown in figure 5.20. The distribution of damage was far more homogeneous in the composite tested at this temperature. One interesting observation is that cracks in the Cr fibres surrounded by intact Cu matrix were rarely observed at high temperature in contrast to the behaviour at low temperatures (figure 5.14), suggesting that Cr fibres are highly ductile at high temperatures. Damage was extensive and the primary damage mechanism was void nucleation at the fibre ends and some reinforcement fracture. These features were accentuated in the sample tested at 500°C so that damage was extensive and spread throughout the gauge length as shown in figure 5.21.

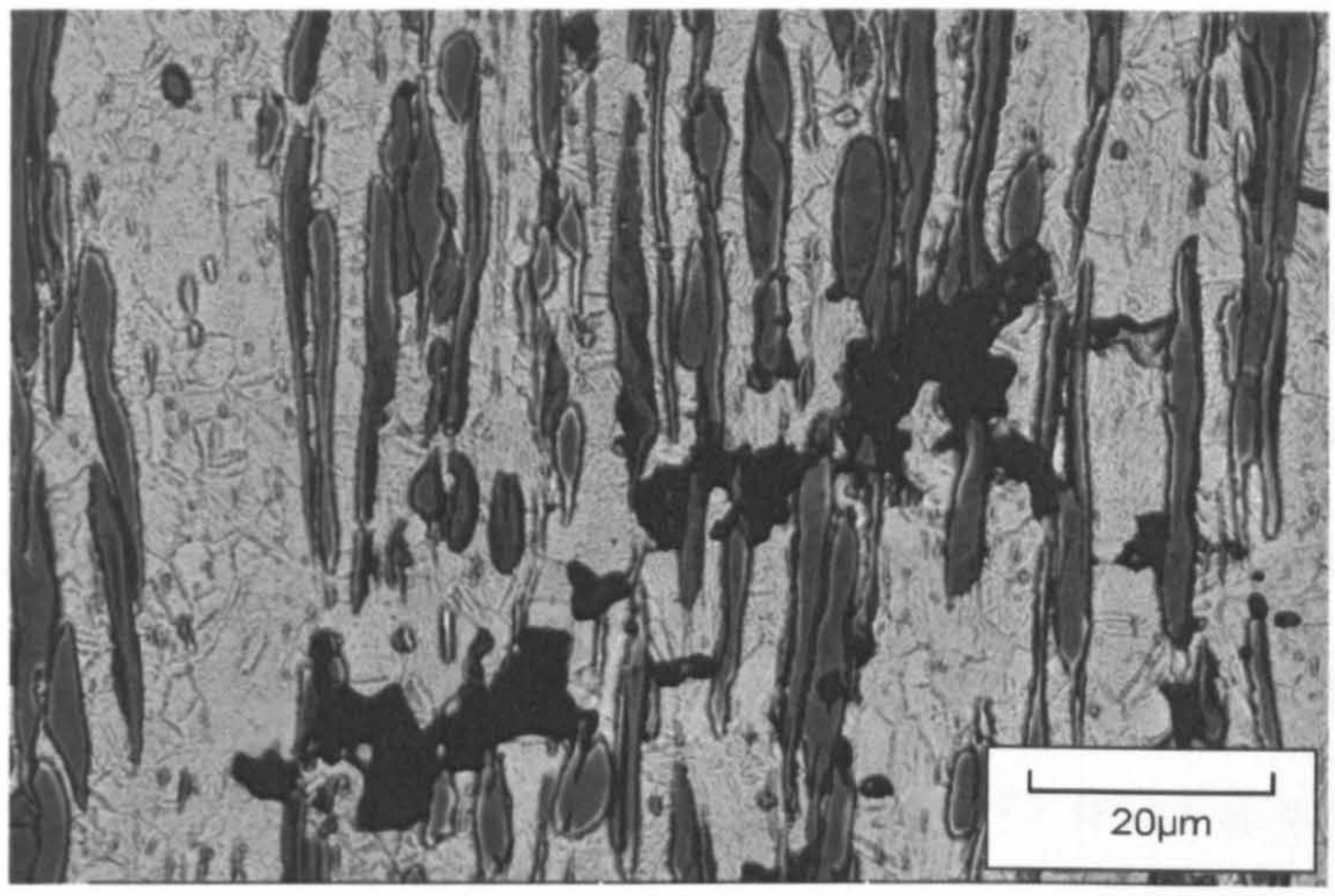

(a)

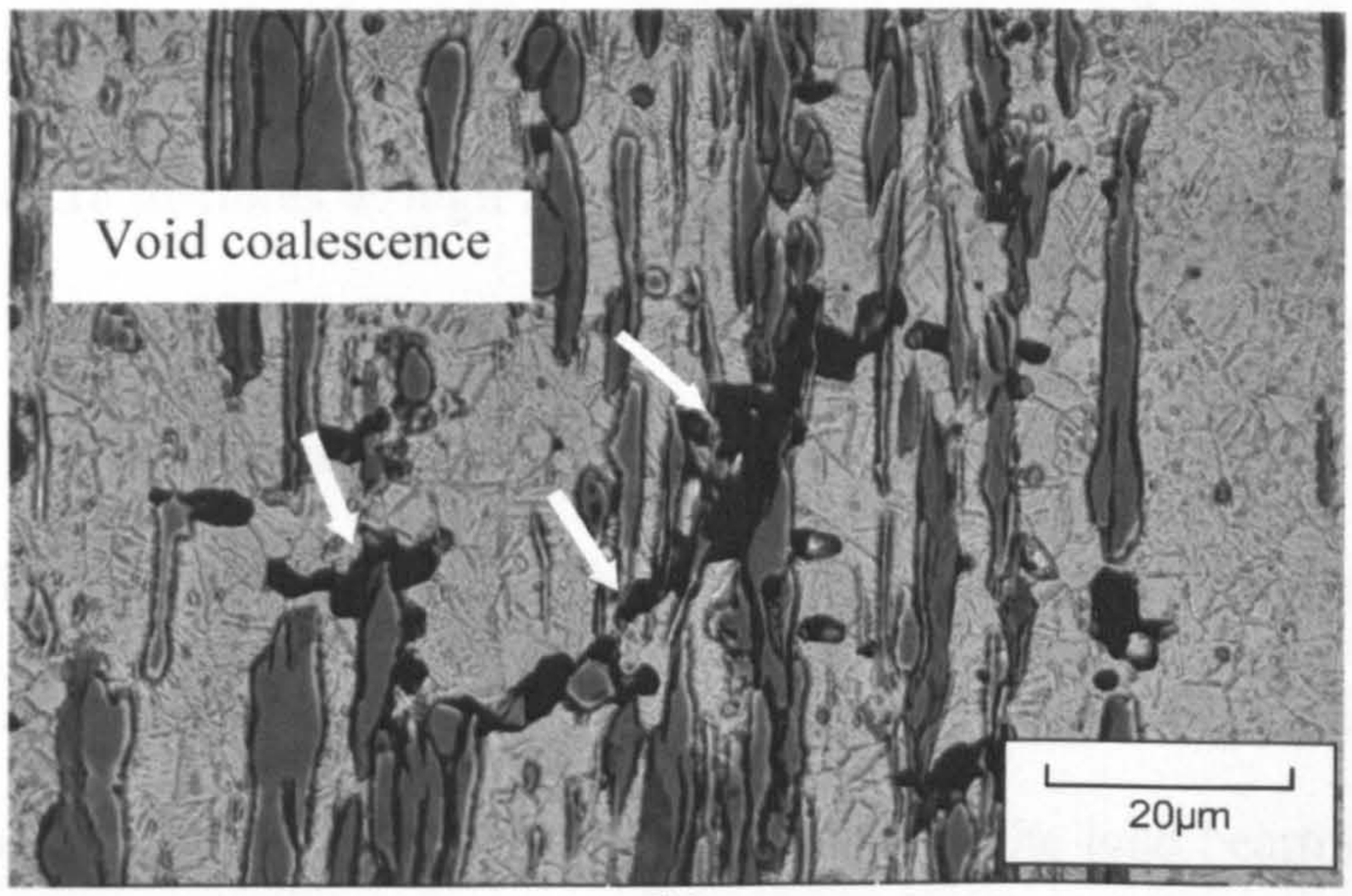

(b)

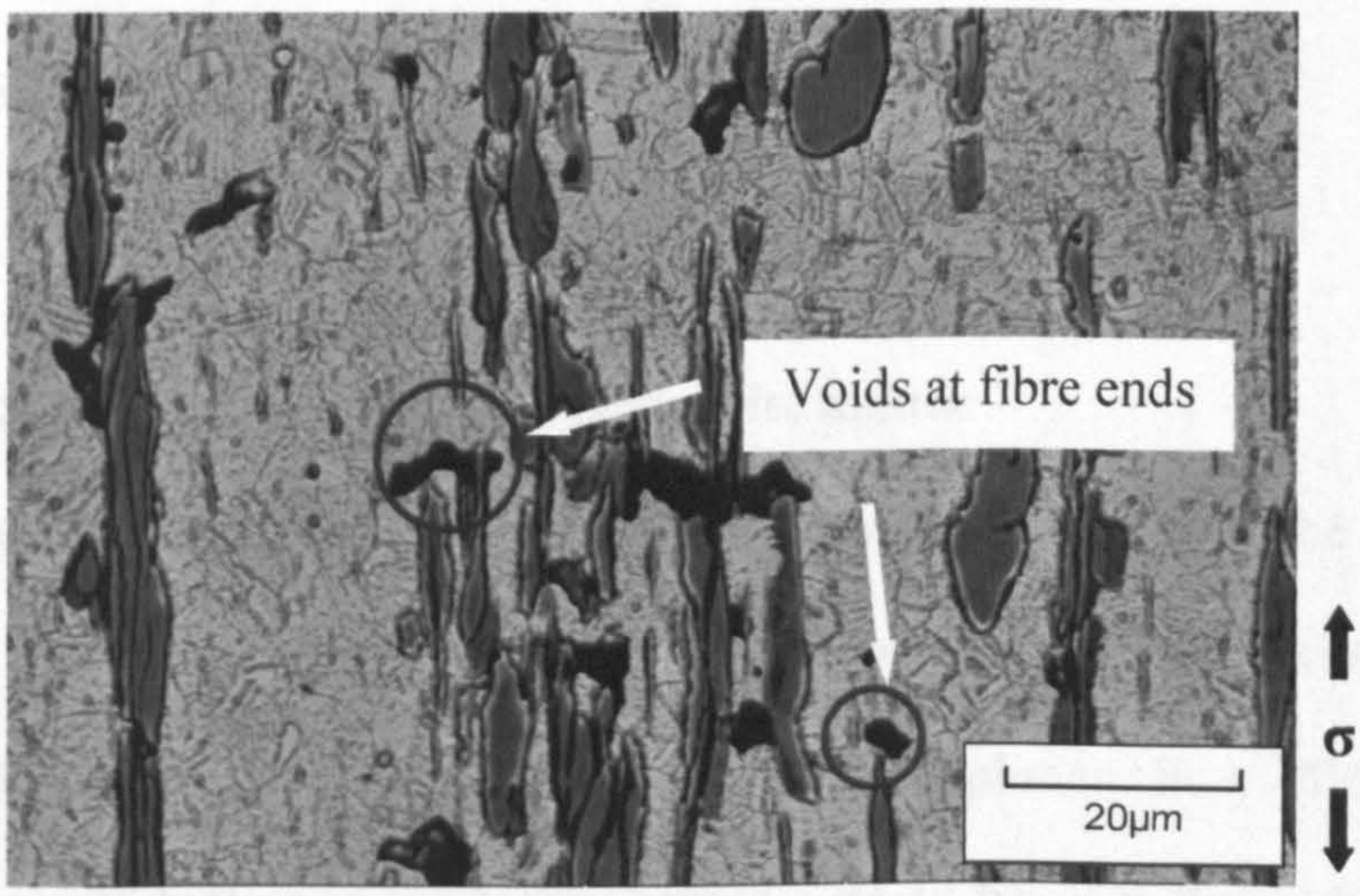

(c)

Figure 5.21 Typical micrographs taken from (a) near the fracture surface and (b) intermediate distance from the fracture surface (c) far from the fracture surface for specimen tested at 500°C

In order to understand the failure mechanism of Cu-Cr composites, it is necessary to understand whether the voids in the Cu matrix precede the failure of Cr fibres or vice versa. The failure sequence can be deduced by observing the damage accumulation with increasing strain. Since the strain is more concentrated near the fracture surface, it may be assumed that the appearance of the damage far away from the fracture surface resembles the initial stage of failure. Voids were also occasionally observed between the ends of two aligned Cr fibres at which the local stress is high [9,10]. A careful examination of the micrographs far from the fracture surfaces (figures 5.20c-5.21c) reveals that voids develop first near the tips of fibres before the failure of fibres at high temperatures. The appearance of major cracks in figure 5.21a also suggests that the crack was formed by a void coalescence and link-up process. The blunt nature of a major crack and the smaller separation between cracked Cr fibres in many cases confirms that the crack propagation arised from void coalescence and link-up at high temperatures. As the composite is stretched further, cracking of more Cr fibres was thought to occur since the load bearing capacity of Cr would drop greatly in the presence of voids or matrix cracks, resulting in the failure of the specimen.

5.5.4 Effect of test temperature on composite failure

The performance of a composite is strongly dependent upon the efficiency with which load is transferred to the reinforcement during deformation. This is determined by the misfit generated between the two phases. In a MMC, elastic and/or plastic deformation in the matrix causes a misfit between the matrix and the reinforcement, which in turn results in load transfer to/from the reinforcement. The resulting high reinforcement stresses, and high local stresses within the matrix near

the reinforcement, may then promote stress relaxation mechanisms. The operation of such stress relaxation mechanisms, which may involve microstructural modification such as dislocation rearrangement near interface regions and phase boundary sliding and microstructural damage such as reinforcement fracture and matrix cavitation, will then act to reduce the misfit and transfer load back to the matrix. Therefore, microstructural observations on the extent of damage in a fractured specimen can provide an indication of whether load transfer has occurred.

At high temperatures, plasticity appears to be uneven (Cu becomes much softer than the Cr) and this would result in high stresses in the Cr fibres which cannot ultimately be borne by the matrix near the fibre ends [11]. This results in the nucleation of many small voids. These remain relatively stable, growing both in size and number until finally void coalescence occurs giving rise to failure. Upon raising the test temperature higher still, a transition was observed from localised damage at the fracture surface to homogeneously distributed damage. The concept of localized and global damage could be introduced to explain the temperature dependency of the damage distribution [12]. When fracture of a fibre leads to significant stress concentration on the neighbouring fibre, then the adjacent fibre could fail and set up a chain of failures leading to the ultimate failure of the composite. This type of damage is termed localised damage. The composite strength is then dominated by the weak fibres; the full fibre bundle strength is never realized. If global damage is dominating the behaviour of the material, then the occurrence of a damage event relaxes the stresses in that area of microstructure. As a result this stress will be distributed throughout the rest of the composite. Therefore the subsequent damage event is more likely to occur in another region of the specimen as the stress in the area of the initial damage was relaxed. This results in a homogeneous distribution of

damage within the composite. Clearly, global damage conditions are desirable for high strength because it utilizes the full strength of the fibres.

In the present study, a clear transition in the distribution of damage occurs from 300°C to 400°C. At higher temperatures deformation is greater in the Cu phase and peak stresses relaxed by increased plasticity and diffusion rates so that local stresses within the Cu matrix are more easily relaxed after a void is formed. As a result, the material strain hardening capacity will increase in order to bear this increase in stress. Therefore the subsequent void event is likely to occur in another region of the sample as the stress in the area of the initial Cu matrix void was relaxed. This results in a homogeneous distribution of voids (damage) within the composite. The decrease in strength of the Cu matrix at high temperature also makes the void nucleation process easier. It can be concluded that as the temperature is increased, there is a distinct change from localised to global damage within the composite.

At low temperature, the phases would be strained equally but the constraint is not sufficient for ductile flow in the Cr phase. Consequently, most of the damage occurs in the form of reinforcement cracking [13] as shown in figure 5.14a. During deformation of the composite, the critical axial stress required for fracture is reached before the critical hydrostatic stress required for cavitation in the matrix due to the brittleness of the Cr phase at this temperature. This damage mechanism in the composite has been modelled by Evensen and Verk [14]. The load was transferred back to the Cu matrix after the reinforcement fractured. This means that at the region of the fractured reinforcement, Cu will deform at a higher local strain rate than the global strain rate. The voids (formed between the Cr fracture points) will grow laterally because there is a plastic zone [17] which extends sideways into the Cu

matrix which is no longer constrained by the reinforcement. Failure will occur when adjacent voids combine. Microstructural observations showed that the damage was concentrated near the fracture surface which suggests that this form of damage is catastrophic, and cannot be accommodated in the composite without rapidly leading to the onset of failure. The ductility of this composite at this temperature is therefore expected to be low which agrees with the low measured failure strain.

5.6 Summary

1 X-ray diffraction had indicated that the Cr fibres had a strong <110> fibre texture; the Cu matrix has both <111> plus <200> texture.

2 The Cu-10vol.% Cr composite has superior yield strength over the pure Cu at room temperature. With increasing strain a monotonic rise in yield stress and a simultaneous decrease in ductility is observed for the composite. The small increase in the resistivity of the composite at room temperature during tensile testing showed that the Cr fibres were behaving in a ductile manner and fracturing or separating from the Cu matrix was not significant as the yield strength was exceeded.

3 Microstructural damage was used as a guide to the degree of load transfer. At low temperature, damage occurred in the form of reinforcement cracking due to its high lattice resistance. At room temperature hardly any damage was observed in the composite, both near and far from the fracture surface. At high temperature, damage occurred near the ends of Cr fibres in the form of matrix cavitation. Some evidence of matrix cavitation was also observed at the interface between the Cu matrix and the Cr reinforcement. In all cases, failure occurred by the coalescence of cavities. At temperatures up to 300°C,

damage was concentrated near the fracture surface, while at 400°C, damage was distributed throughout the specimens. This indicates that a transition from localized to global damage occurred in the composite between 300°C and 400°C.

References

1 A.M. Russell, L.S. Chumbley and T. Yun, Deformation processed metal-metal composites. Advanced Engineering Materials, 2000. 2(1-2): 11-22.

2 C. Biselli and D.G. Morris, Microstructure and strength of Cu-Fe in situ composites obtained from prealloyed Cu-Fe powders. Acta Metallurgica et Materialia, 1994. 42(1): 163-176.

3 Y. Jin, K. Adachi, T. Takeuchi and H.G. Suzuki, Correlation between the cold-working and aging treatments in a Cu-15 wt pct Cr in situ composite. Metallurgical and Materials Transactions A-Physical Metallurgy and Materials Science, 1998. 29(8): 2195-2203.

4 J. Bevk, J.P Harbison and J.L. Bell, Anomalous increase in strength of in situ formed Cu-Nb multifilamentary composites. Journal of Applied Physics, 1978. 49(12): 6031-6038.

5 D.L. Zhang, K. Mihara, E. Takakura and H.G. Suzuki, Effect of the amount of cold working and ageing on the ductility of a Cu-15%Cr-0.2%Ti in-situ composite. Materials Science & Engineering A-Structural Materials Properties Microstructure & Processing, 1999. A266 (1-2): 99-108.

6 http://www.sz-metal.si/rolls/products/table1.htm

7 P.D. Krotz, W.A. Spitzig and F.C. Laabs, High Temperature Properties of Heavily Deformed Cu-20% Nb and Cu-20% Ta Composites, Materials

Science and Engineering A-Structural Materials Properties Microstructure and Processing, 1989. 110: 37-45.

8 J.S. Song and S.I. Hong, Strength and electrical conductivity of Cu-9Fe-1.2Co filamentary microcomposite wires. Journal of Alloys and Compounds, 2000. 311: 265-269.

9 S.R. Nutt and A. Needleman, Void nucleation at fiber ends in Al-SiC composites. Scripta Metallurgica, 1987. 21(5): 705-710.

10 S.R. Nutt and J.M. Duva, A failure mechanism in Al-SiC composites. Scripta Metallurgica, 1986. 20(7): 1055-1058.

11 K.L. Lee, A.F. Whitehouse and A.C.F. Cocks, Thermo-mechanical response of an in-situ copper-based composite, July 1999. Conference on composite materials, ICCM 12, Paris, France.

12 H.E. Carroll and A.F. Whitehouse, Damage and failure during creep of a copper-chromium in-situ composite. Scripta Materialia, 2000. 42: 1133-1137.

13 K.L. Lee, H.E. Carroll and A.F. Whitehouse, Thermo-mechanical behaviour of a copper-chromium in-situ composite. Materials Science and Technology, 2000. 16: 811-816.

14 J.D. Evensen and A.S. Verk, The Influence of Particle Cracking on the Fracture Strain of some Al-Si Alloys. Scripta Metallurgica, 1981. 15: 1131-1133.

Chapter 6

Neutron Diffraction and In-situ Tensile Deformation

6.1 Introduction

The aim of this chapter is to understand the deformation behaviour of the individual phases in a Cu-Cr composite and their interaction through elastic and plastic loading at room temperature. Our approach has been to follow the deformation behaviour of the individual phases by neutron diffraction. The diffraction method is sensitive only to the elastic component of strain and thus the recorded strains can be related to the stress in each phase. From the load partitioning between phases, inferences can be made on the effects of inelastic deformation of individual phases on the macroscopic deformation.

In order to determine the damage mechanisms occurring at the microscale in the composite, in-situ tensile tests were performed at room temperature inside the scanning electron microscope. This technique has been used successfully by many researchers to study the fracture behaviour of metal matrix composites [1-2].

6.2 Neutron sources

Neutrons can be produced by two methods. The first is the steady-state or reactor source, in which a steady flux of monochromatic neutrons from a nuclear reactor is scattered by the sample and the scattered intensity is measured by the detectors as a function of scattering angle 2θ - i.e. wavelength, λ is fixed, θ is varied. The second is the pulsed or time-of-flight (TOF) method, in which a pulsed beam of

polychromatic neutrons is incident upon the sample and the scattered spectra is measured by detectors at fixed angles as a function of wavelength. The wavelength is determined by recording the time-of-flight and thereby the velocity of a detected neutron. So θ is fixed and λ is the variable.

6.2.1 Pulsed neutron diffraction

Neutrons are produced at Rutherford Appleton Laboratory (ISIS) by the spallation process, in which a high-energy proton beam hits a target made of a heavy metal. The collision causes neutrons to be emitted from the metal atom nuclei. The high-energy proton beam is produced in the ISIS accelerator. Protons with energies of 800 MeV-close to the speed of light-are made in three stages.

Firstly, the pre-injector produces H^- ions (protons with 2 electrons) (figure 6.1) from hydrogen gas. These are injected into the linear accelerator (Linac) (figure 6.2), which accelerates the H^- ions to about 9 % of their final energy.

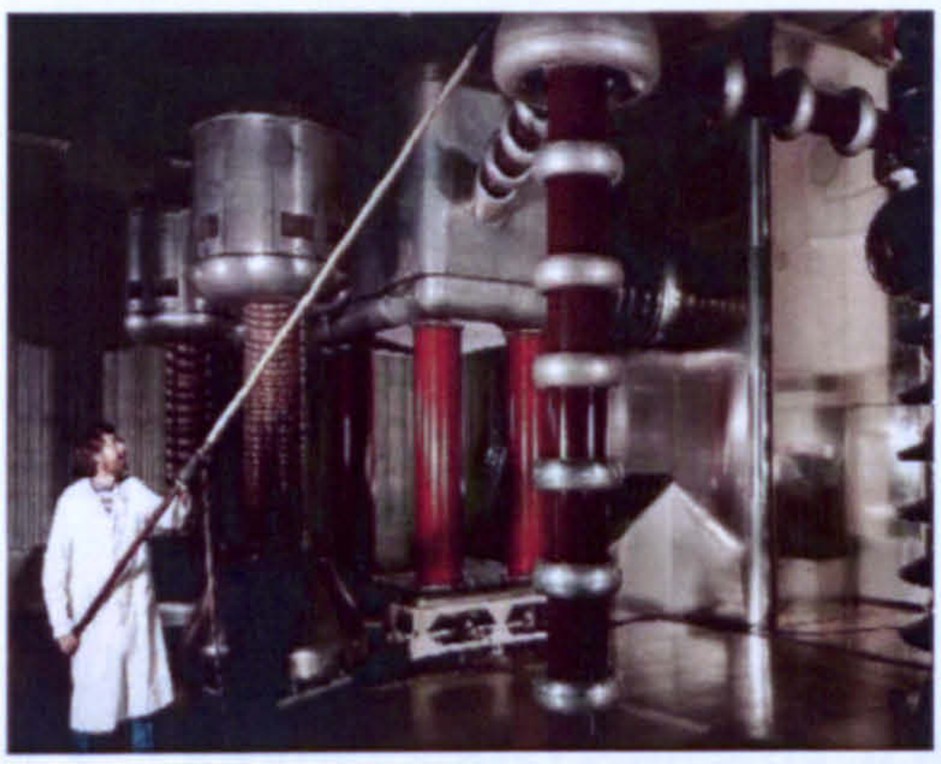

Figure 6.1 The ISIS pre-injector

Figure 6.2 Part of the linear accelerator

Final acceleration of the beam takes place in the synchrotron – a circular accelerator 50 m in diameter as shown in figure 6.3. As they enter the synchrotron, the H^- ions pass through an alumina foil which is about 0.3 μm thick. This removes

the two electrons from each H^- ion to produce a proton beam. The resulting protons travel around the synchrotron many thousands of times, and are accelerated each revolution by pushes from electromagnetic fields generated at points around the ring. When the acceleration is complete, the proton beam is kicked out of the synchrotron into the extracted proton beam line, and transported to the neutron target. This whole process is repeated 50 times a second.

Figure 6.3 The synchrotron accelerator

Neutrons are fired at the sample and are scattered into detectors which not only measure the direction in which the neutrons are scattered but also the time the neutrons take to arrive at the detector. This means that the wavelength or energy of the scattered neutrons can be calculated.

6.3 Fundamental concepts of diffraction methods

The principle behind diffraction techniques is a simple one, i.e. it is based on measurements of interplanar lattice spacings in different directions of the sample. This technique utilize the lattice spacings as a strain gauge. They are obtained from Bragg's Law (figure 6.4):

$$\lambda = 2d_{hkl} \sin\theta \qquad (6.1)$$

where λ = the neutron wavelength

2θ = scattering angle

d_{hkl} = lattice spacing between the (hkl) planes

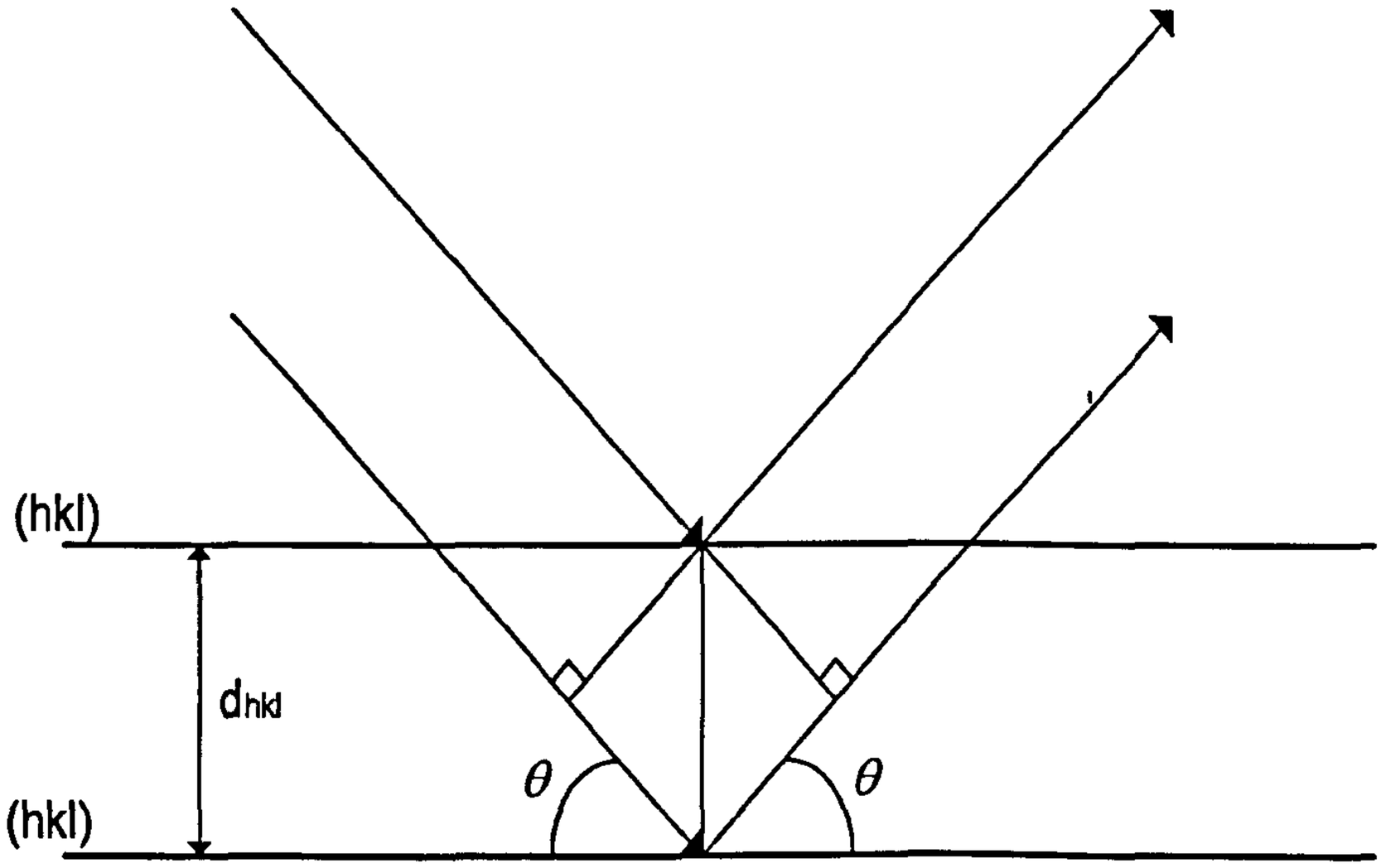

Figure 6.4 Bragg's Law of diffraction

6.4 The neutron diffraction method of strain measurement

The time-of-flight (TOF) neutron diffraction method was used for the strain measurements, in which a pulsed beam of polychromatic neutrons is incident upon the sample and the diffracted spectra are measured by detectors at fixed angles as a function of wavelength. The wavelength is determined by recording the time-of-flight and thereby the velocity of each detected neutron. Our experiments have been carried out on the ENGIN instrument at ISIS, where 2θ is fixed at $\pm 90^\circ$ and λ varies with time. The technique exploits changes in the atomic lattice spacings to

determine strain. Changes in lattice spacings are derived from shifts in the position of diffraction peaks using Bragg's Law:

$$\lambda = 2d_{hkl} \sin\theta_{hkl} \qquad (6.2)$$

where λ is neutron wavelength, 2θ the scattering angle and d_{hkl} the lattice spacing between the (hkl) planes. The wavelengths of the detected neutrons are calculated using the de Broglie equation:

$$\lambda = \frac{h}{m_n v} = \frac{ht}{m_n L} \qquad (6.3)$$

where h is Planck's constant, m_n the neutron mass (1.675×10^{-27} kg), v the neutron speed, L the total length of the flight path of the neutron (source to sample to detector) and t the recorded time of flight of the neutrons, which are produced at a known time. By combining equations (2) and (3), the d-spacing can be expressed in terms of the time of flight as

$$d_{hkl} = \frac{h}{2m_n L \sin\theta_{hkl}} t \qquad (6.4)$$

Elastic strains for individual lattice planes are then calculated using

$$\varepsilon_{hkl} = \frac{\Delta d_{hkl}}{d_{ohkl}} \qquad (6.5)$$

where Δd_{hkl} is the change in the lattice spacing relative to the stress-free lattice spacing $d_{o\,hkl}$.

The use of the time of flight method at a pulsed source is ideal for the study of multi- phase materials such as composites, because it allows many diffraction peaks from both phases to be recorded simultaneously. Since the measurements are made simultaneously, this will guarantee that the loading conditions are the same for all the diffraction peaks to be examined.

6.5 In-situ neutron diffraction loading experiment

A hydraulic tensile testing machine was installed on the diffractometer table at ENGIN. Room temperature tensile tests were performed using incremental step loads in order to maximize the data obtained on a single sample during limited neutron beam time. While the neutron measurements were made the sample was held under load control, after which the load was then raised to the next level of stress. This was done on ENGIN by using a programme which controlled the specimen deformation in terms of applied stress. A standard extensometer for longitudinal strain measurement was used to collect precise values of macroscopic strain.

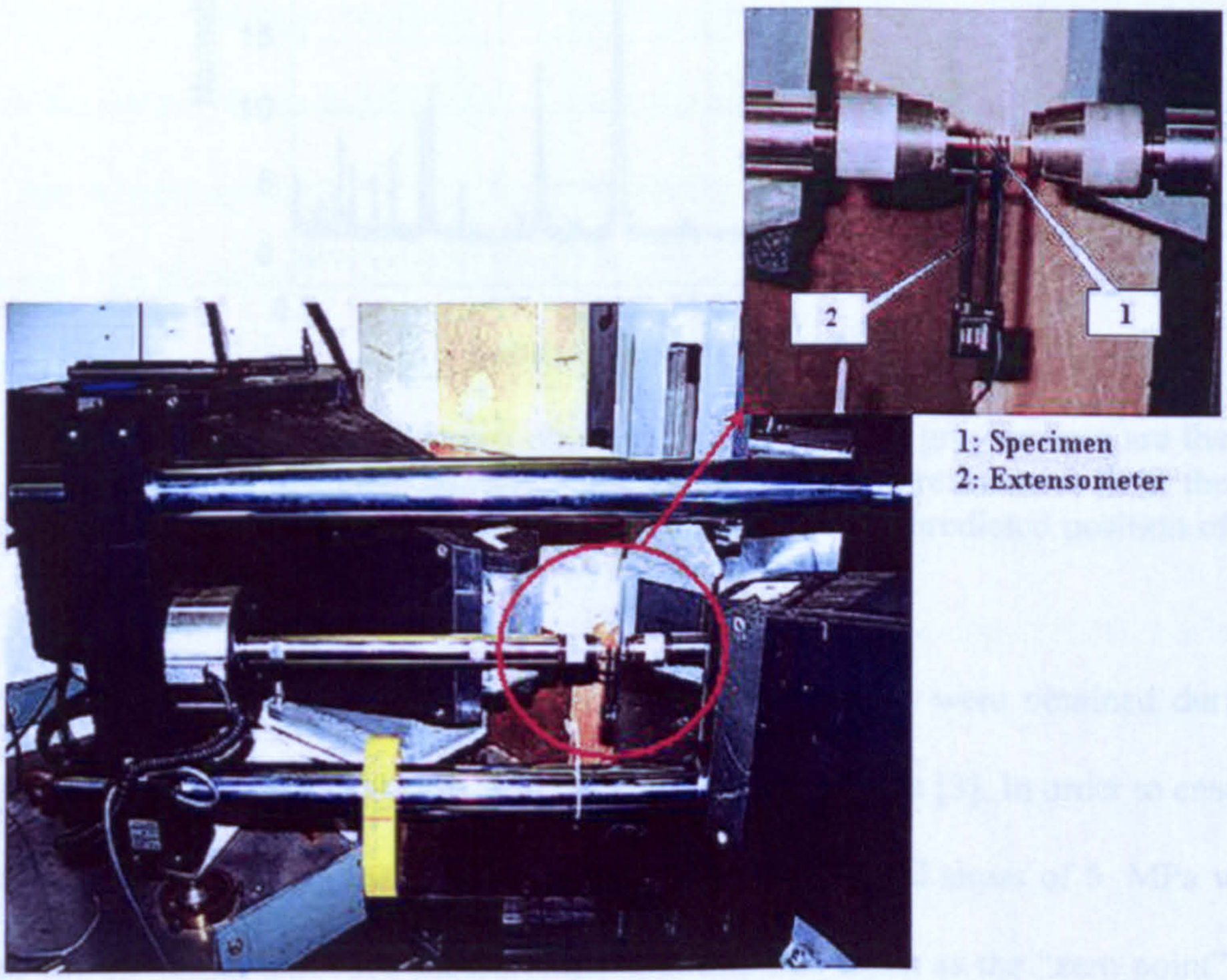

Figure 6.5 Experimental arrangement at ISIS

Tensile test-pieces were 70 mm long with a circular cross section and a diameter of 3.09 mm. The loading axis was horizontal and at 45° to the incoming

beam. This meant that the two 90° detectors were able to measure the lattice plane spacings parallel to and perpendicular to the tensile axis simultaneously. The experimental set-up is shown in figure 6.5. Incident slits 5 mm wide and 3 mm high were used, with the outgoing beam width fixed by radial collimation to be 1.5 mm. The lattice parameter obtained is a phase specific average over this gauge volume. A typical diffraction spectra with fit is shown in figure 6.6.

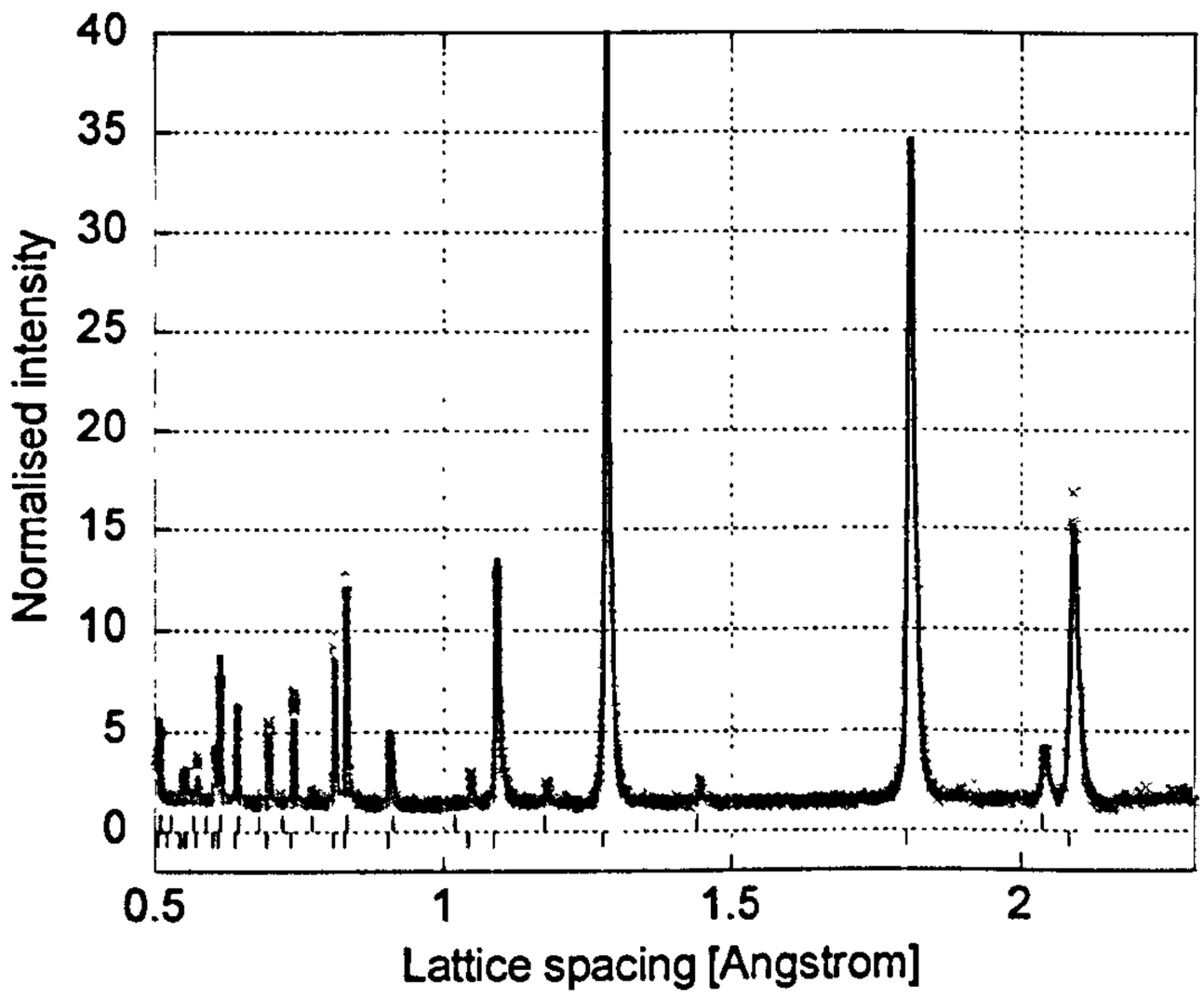

Figure 6.6 Diffraction spectrum obtained at 5 MPa. The grey crosses are the diffraction data obtained, and the black line the Rietveld refinement fit to the data. The tick marks underneath the spectra indicate the predicted position of diffraction peaks for Cu (bottom row) and Cr (top row)

The macroscopic stress levels at which neutron data were obtained during this experiment were 5, 100, 250, 350, 375, 400 and 415 MPa [3]. In order to ensure that the specimen and grips were properly aligned, a nominal stress of 5 MPa was used for the initial unloaded measurement and this was taken as the "zero point" of the experiment. This measurement was taken as the "zero point" of the experiment, for which a reference lattice spacing (d_o) is calculated. The load frame was programmed to step automatically through a pre-set sequence of applied stress. A

count time of approximately 4 hours was needed to give adequate counting statistics in the diffracted spectra for both phases at each stress level. Due to the relatively poor diffraction signal from the small volume fraction of Cr, the uncertainties in strain are much larger than in the Cu phase. A similar experiment was performed by Sinclair [4] to measure the load partitioning between phases in Cu-Cr eutectic alloys during in-situ straining but was unsuccessful in getting any data for the Cr phase due to the low volume fraction of Cr and the high degree of crystallographic texture.

At a time of flight source, pulses of neutrons with a continuous range of velocities and therefore wavelengths, are bombarded at the specimen. Their wavelengths are calculated and diffraction spectra recorded by measuring the flight times of the detected neutrons. As the incident spectra are polychromatic, all possible lattice planes are recorded in each measurement. The scattering vectors for all the reflections collected in one detector lie in the same direction, and thus measure the strain in the same direction. Therefore, each reflection is produced from a different family of grains which are oriented so that the specific plane diffracts to the detector.

Since every measurement at a pulsed source totally captures the whole diffraction pattern, Rietveld refinement [5] is used to fit the spectrum. In this method the predicted diffraction spectrum from the proposed crystal structure is compared with a measured spectrum. From this the idealized structure can be optimized to maximize the agreement between the prediction and measurement. Finally, the atomic positions or lattice parameters are determined by making a least squares fit between the observed and predicted profiles.

6.6 Neutron diffraction results

The macroscopic stress-strain response of the composite recorded during in-situ tensile testing at which the whole neutron measurements were made is shown in figure 6.7. It shows the total strain, measured using a clip gauge type extensometer, as a function of the applied stress. The data points correspond to the positions at which neutron measurements were made (~ 4 hours per point).

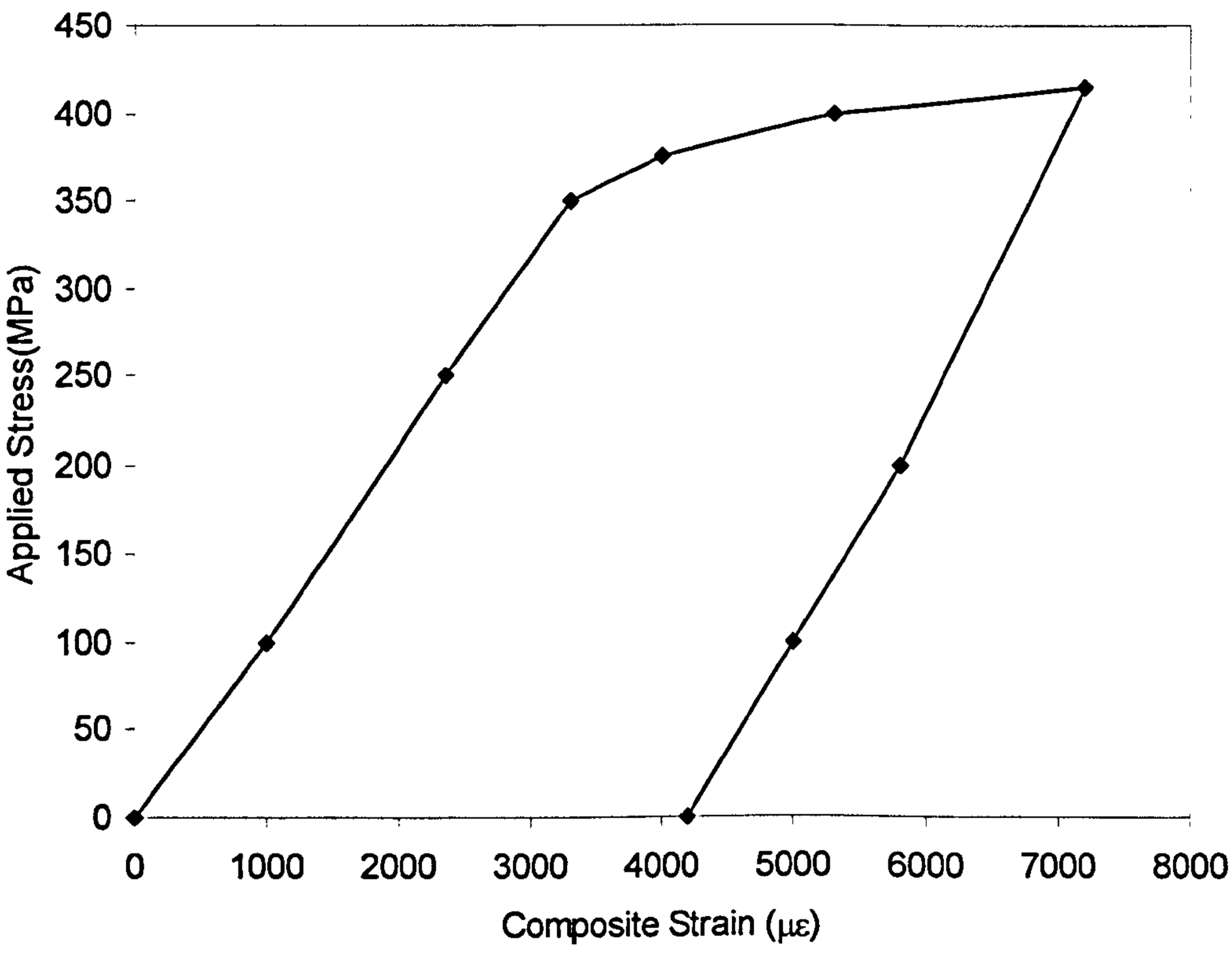

Figure 6.7 Room temperature macroscopic stress-strain response of composite during the tensile test on the neutron diffractometer

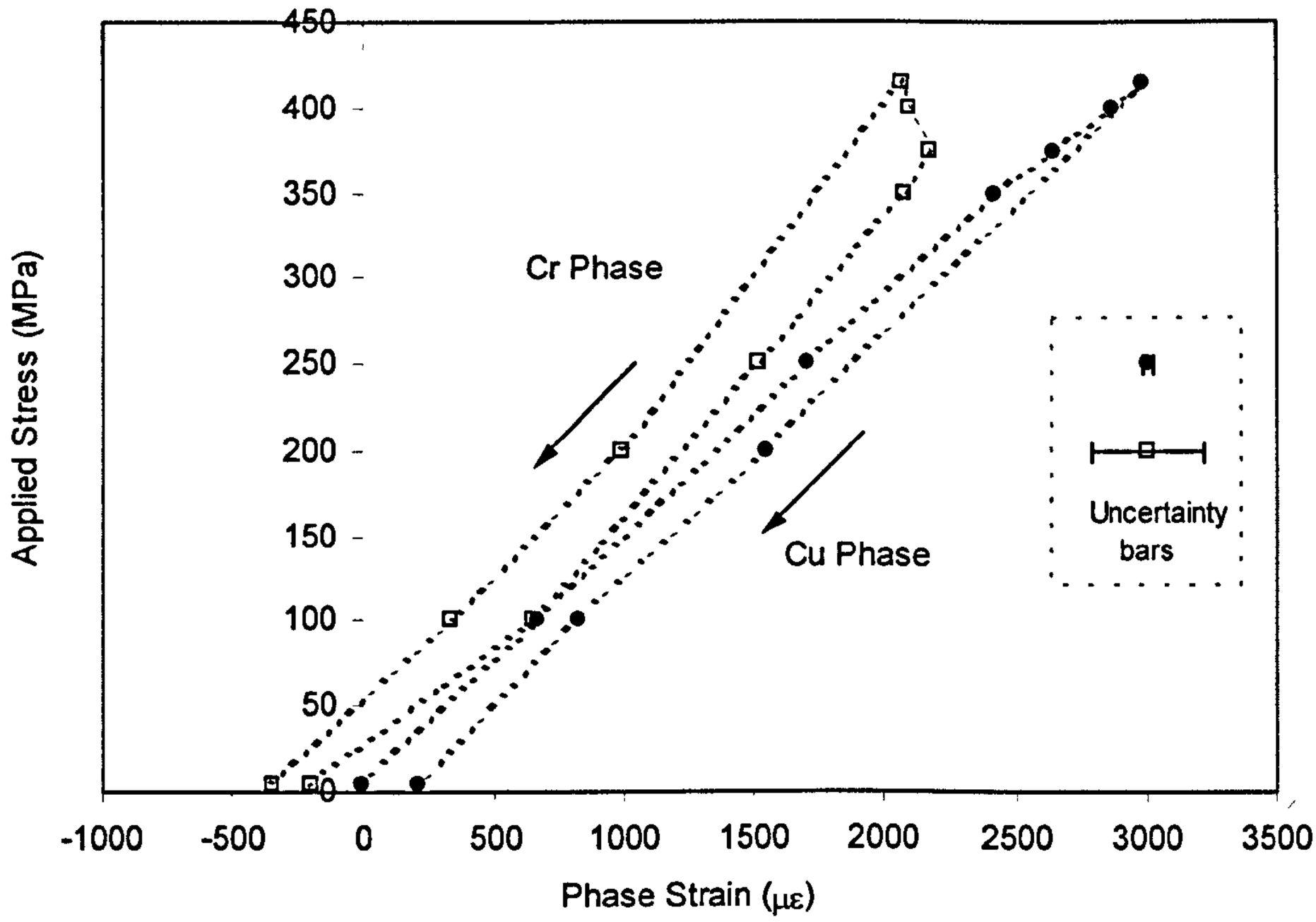

(a)

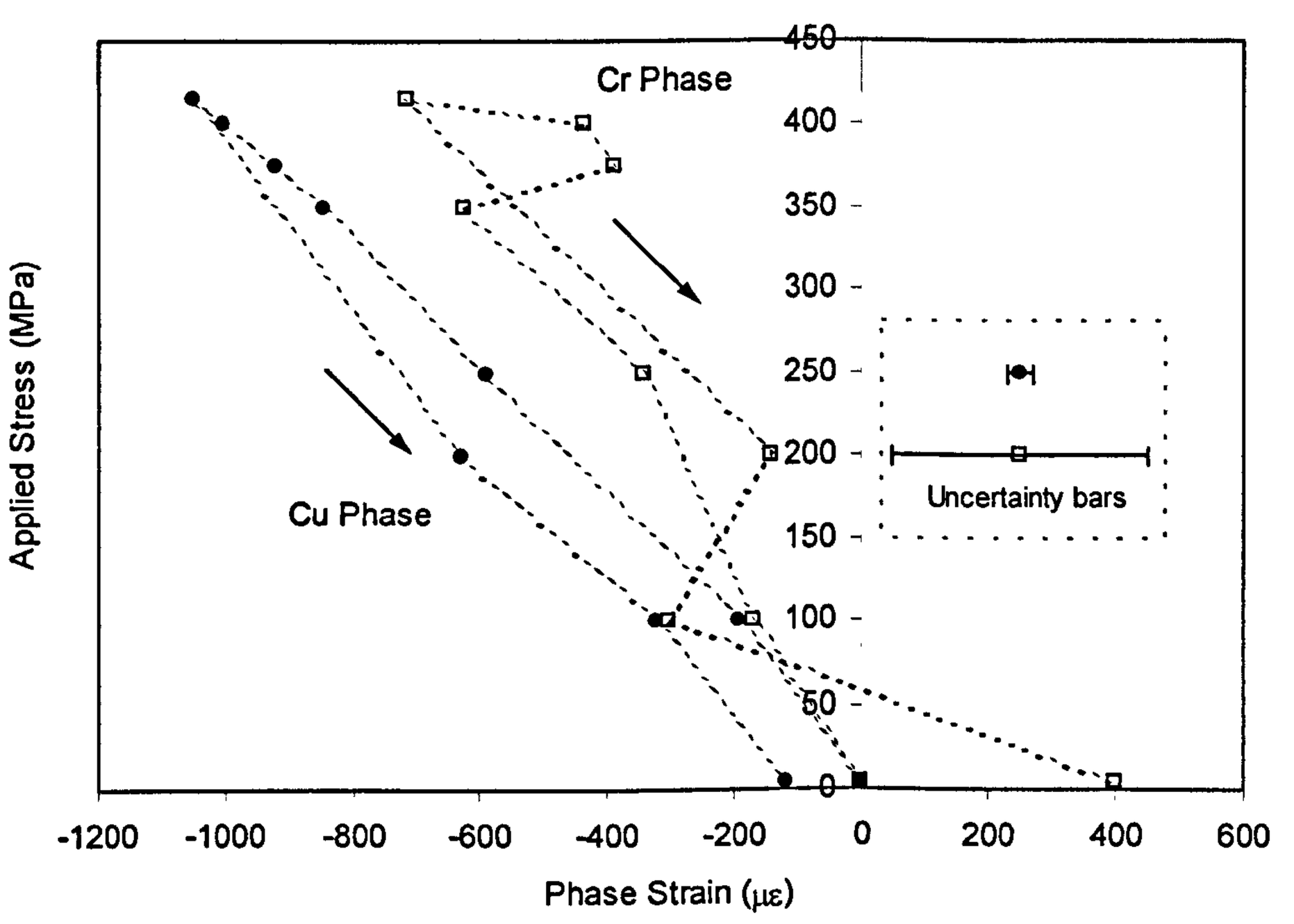

(b)

Figure 6.8 Elastic phase strain as a function of applied stress at room temperature (a) parallel to the loading direction and (b) perpendicular to the loading direction. The arrows indicate the unloading path

Room temperature elastic phase strain parallel and perpendicular to the applied load are shown as a function of applied stress in figure 6.8. The curves show the initial elastic regime of composite deformation, and more importantly, illustrate changes in slope at higher applied stresses (or strains) that must be associated with changes in load partitioning behaviour. The complete load and unload cycles are shown here. Single phase reference samples were not available, thus the strains shown are relative to the initial lattice parameters obtained at 5 MPa. Thus, the presence of thermal or process induced strains have been neglected in the above figures. The experimental scatter shown in the above axial graph ($\pm 20\,\mu\varepsilon$ in the Cu and $\pm 200\ \mu\varepsilon$ in the Cr) was determined from the average error in lattice parameter calculated from the Rietveld analysis. The large uncertainties in the Cr phase are due to the small scattering volume and poor count statistics.

From figure 6.8a, the Cr phase seems to strain to a larger extent than the Cu in the initial stages of straining. Since the aspect ratio of Cr fibres is fairly high and filaments are parallel to the loading axis, a simple equal strain model is sufficient for the elastic region with the result that one would expect both the Cu and Cr phase strains to be equal in the early part of straining. Since the uncertainties in the measurements are quite high for the strain free reference for the Cr phase, it is likely that the measurements are in error. Indeed, an offset of around –200 με (i.e. within the measurement uncertainty) in the strain-free lattice parameter would bring the Cr phase at all times equal or below the elastic strain in the more compliant Cu phase in agreement with expectations. At about 375-415 MPa significant load transfer is indicated by increasing elastic strains in the Cu phase and the sudden decrease in the rate of loading of the Cr. This is indicated by the Cu curve which starts to deflect to the right and the Cr curve deflects in the opposite manner. This result is perhaps

contrary to expectation, given the larger yield stress typical of fine Cr fibres compared with Cu (table 6.1).

The presence of final tensile matrix residual strains and compressive fibre strains are indicative of a positive misfit between the fibres and the matrix, in that the stress free shape of the Cr fibres appears to be longer than the 'holes' in which they sit. Such a plastic misfit causes an inelastic transfer of load from Cr to Cu. Load transfer from fibres to matrix during loading could also occur by matrix voiding (or fibre fracture), but these would not of themselves give rise to residual stresses.

The elastic strains perpendicular to the applied load are shown in figure 6.8b. The magnitude of uncertainty in the strains is almost the same as in the axial direction. The gradients in the transverse direction are much higher, due to the Poisson contraction and constraint effect, and by virtue of the balance of transverse stress, increases in the gradient of one phase are followed by decreases in that of the other.

6.7 Eshelby model

With the above results, a model was developed based on the Eshelby theory to quantify the load transfer under applied loading in the composite which is crucial to the high performance of MMC materials. In this research we have used a development of Eshelby's elastic inclusion model, which is well suited to the study of fibrous composites [6-7]. Eshelby's analysis is suitable for the analysis of diffraction data because the average strain response of the matrix and reinforcements can be easily calculated with the known properties of each phase. The Eshelby

model of the composite response was calculated using a computer program which was made available by Professor P.J. Withers in Manchester Materials Science Centre [7].

Internal stresses arise from misfits which can originate elastically, plastically or thermally. To calculate these, the following material properties were used as input parameters as shown in table 6.1.

	volume fraction	Poissons ratio	Young's modulus (GPa)	CTE (με/K)	UTS (MPa)
Cu matrix	0.90	0.34	135	16.5	350
Cr fibres	0.10	0.21	280	6.5	650

Table 6.1 Typical materials properties [8]

To conserve volume, the retained plastic misfit strain vector $\underline{\varepsilon}^{P*}$ between the phases was taken to have the form $\varepsilon^{P*}(-½, -½, 1)$ with the 3-axis parallel to the loading direction, with a positive ε^{P*} indicative of a greater axial tensile strain in the Cr than the Cu. The elastic response was calculated based just on the elastic properties of the two phases and the fibre aspect ratio (25). The variation in the retained matrix-fibre misfit generated during plastic straining was chosen so as to follow the axial Cu matrix strain response. When this misfit has been established, the transverse Cu and longitudinal and transverse Cr strain will be generated automatically and are shown in figure 6.9.

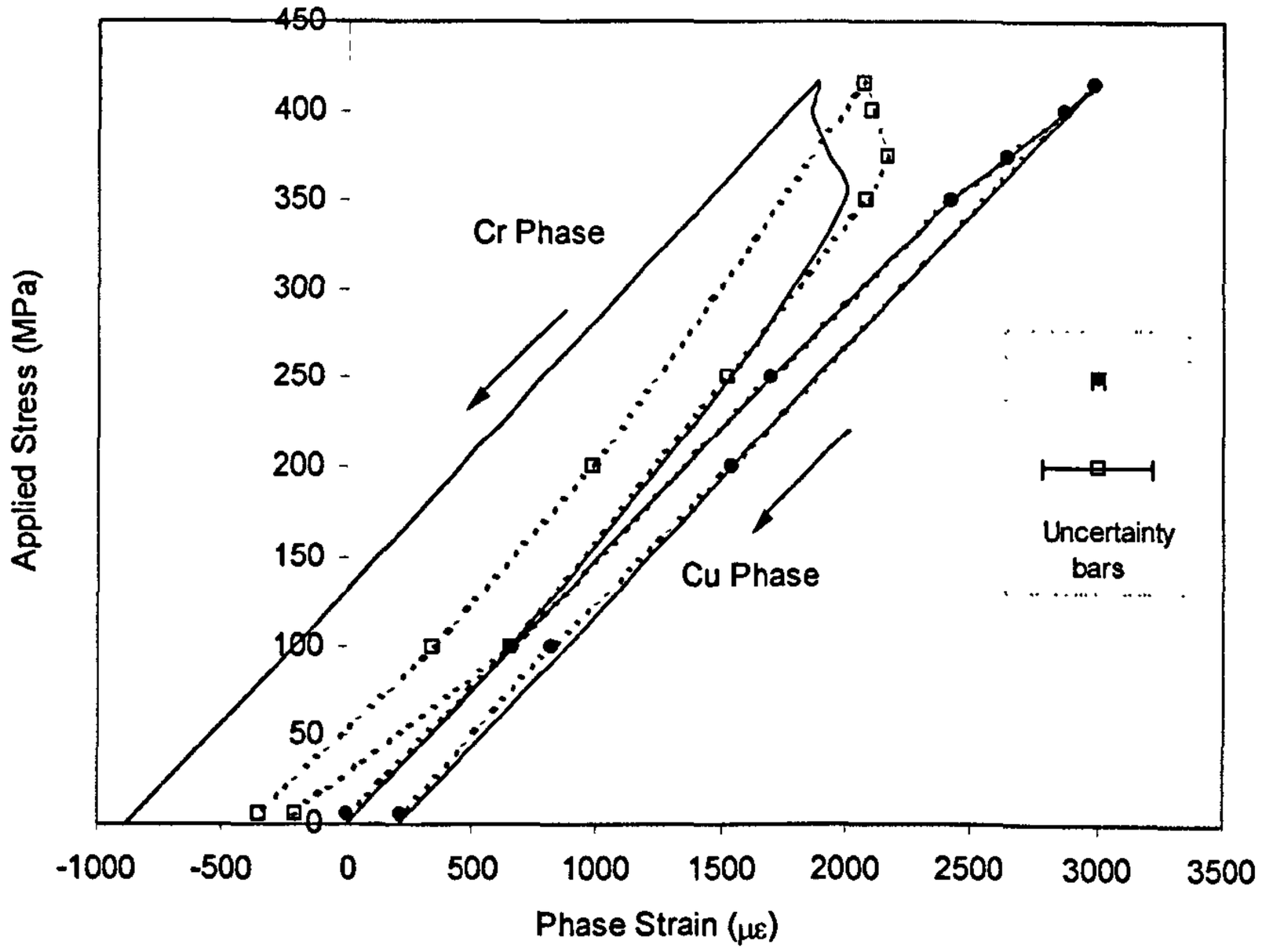

(a)

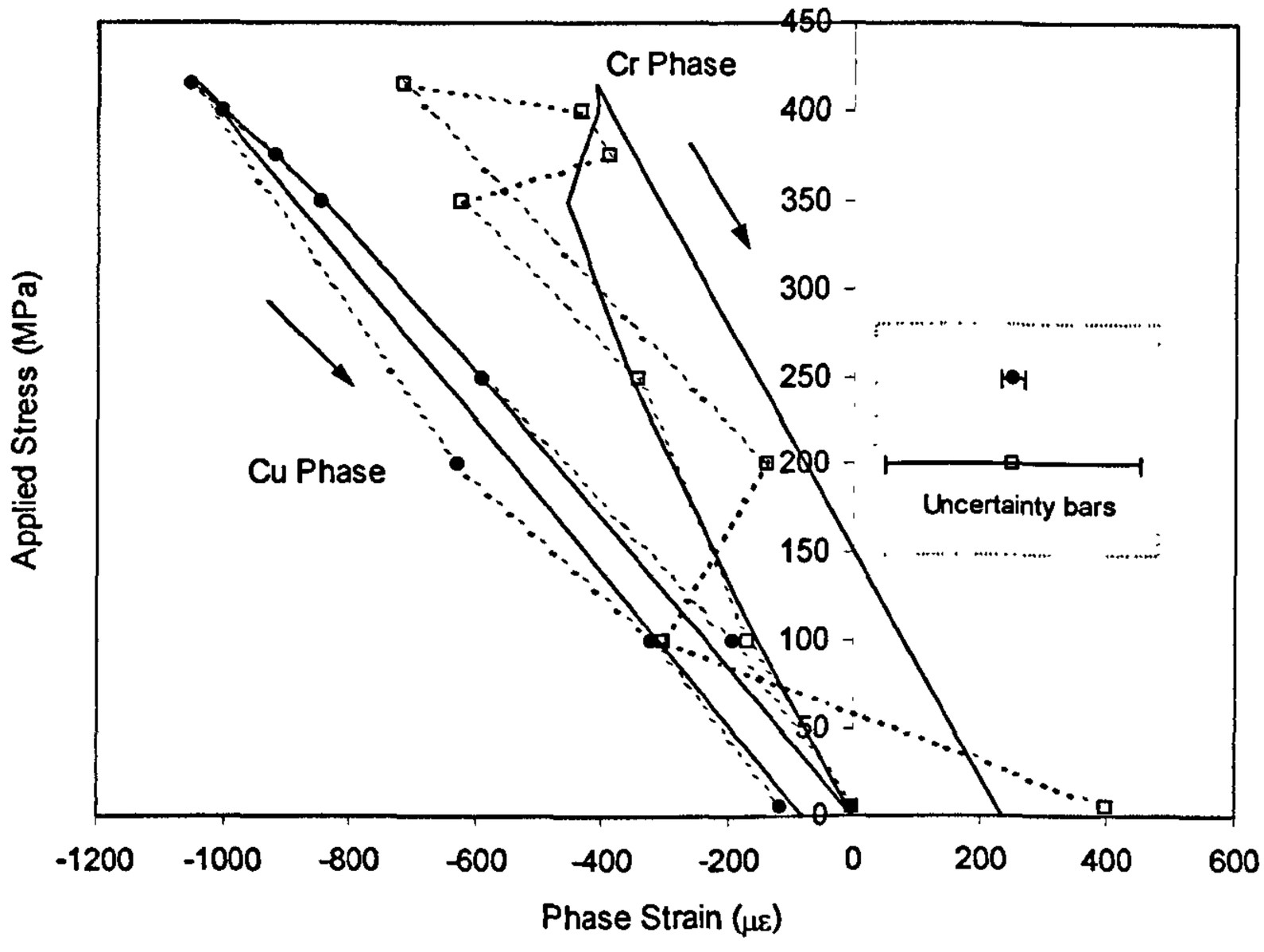

(b)

Figure 6.9 Cu matrix and Cr fibre elastic lattice strains measured by neutron diffraction and as predicted by the Eshelby model (solid line) in the (a) axial and (b) transverse directions using the misfits shown in figure 6.10. In (a) the Cr strains have been offset by -200 με (less than the measurement error). The arrows indicate the unloading path

The misfit strains are shown in figure 6.10 and indicate that the Cr is extending plastically to a larger amount than the Cu. As the composite strains

plastically, the rate of misfit generation increases at a decreasing rate. Since the volume fraction of the Cr phase is relatively low in this composite, these strains are at no stage enough to bring about the observed plastic strain without some plastic strain in the Cu.

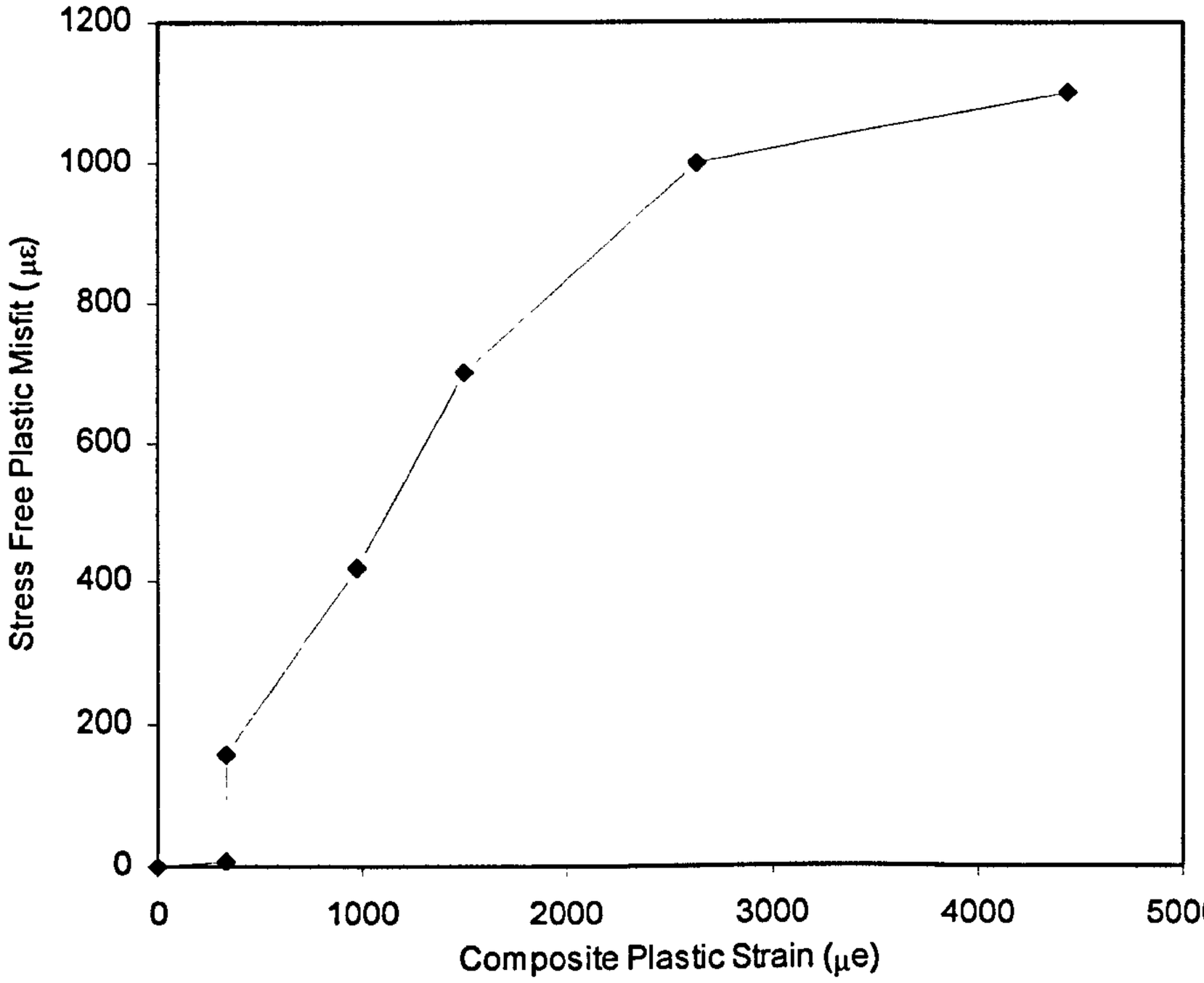

Figure 6.10 The stress free fibre-matrix misfit (a positive strain indicates the Cr to be strained more than the Cu) inferred from the axial inelastic lattice strain response of the Cu phase

The decreasing gradient in figure 6.10 indicates that at the higher plastic strains the two phases deform more and more similarly. Alternatively, the misfit may be being relaxed either plastically (unlikely given the large aspect ratio) or through the occurrence of damage, however the latter mechanism alone would not justify the observed residual strains.

The axial and transverse phase strains calculated based on the misfit plotted in figure 6.10 are shown in figure 6.9. As it is forced to be, the modelled axial Cu response is in good agreement with the experimental data. Despite the final

compressive misfit is overestimated for the axial Cr response (this is probably due to an overestimation of the Cr ribbon Young's Modulus, but could also be due to the influence of limited damage), the overall shape is well predicted. In the transverse direction, agreement with the measured data is within the uncertainties of the measurements, with the compressive Cu and tensile Cr residual strains well predicted. In order to illustrate the stress in each phase during the composite deformation, all the strains value are converted into stresses. Figure 6.11 shows the stresses carried by each individual phase relative to the applied composite stress.

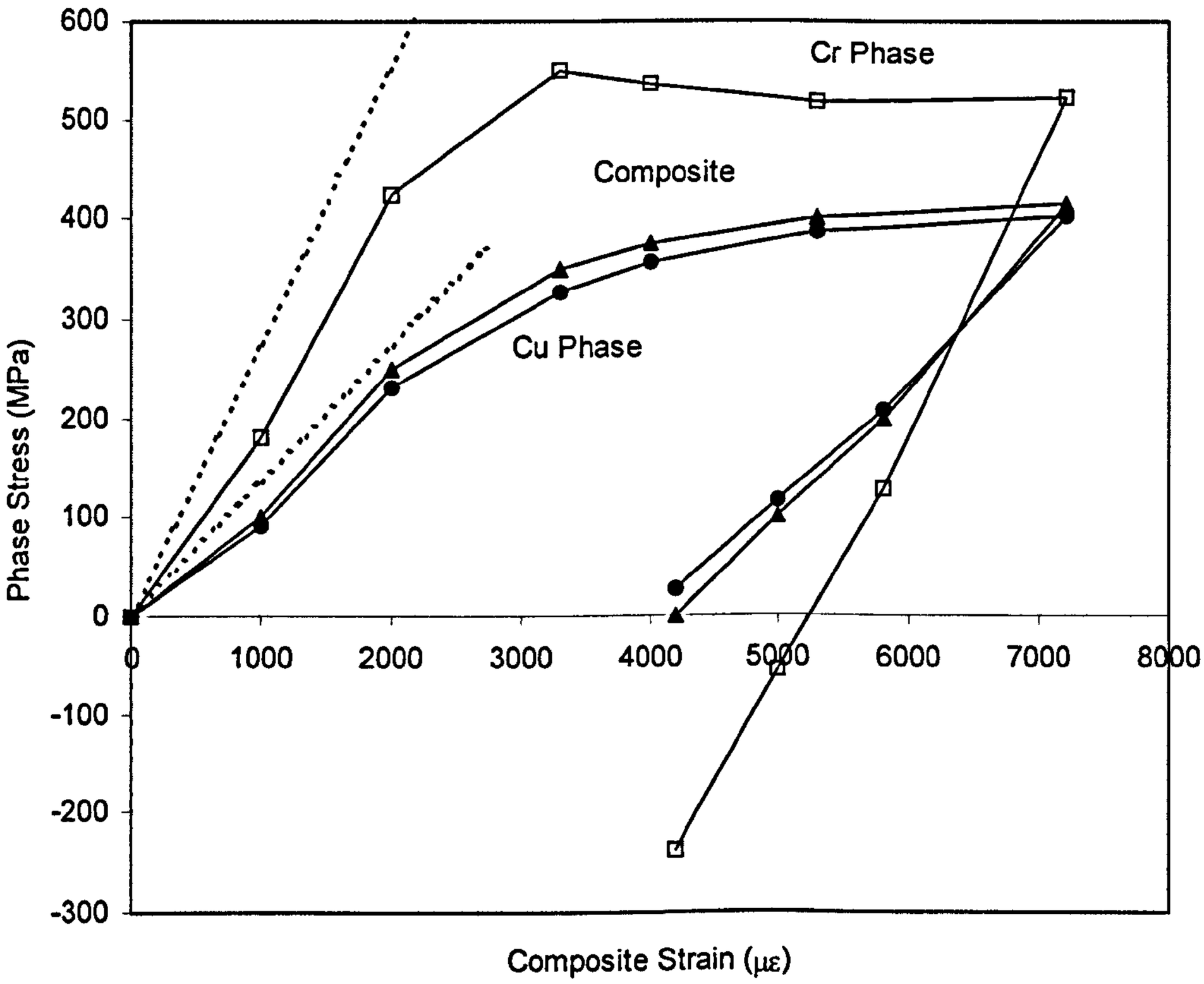

Figure 6.11 The individual Cu (circles) and Cr (squares)(axial phase stress responses compared to the bulk composite (triangles) response. The stiffness of single phase Cu and Cr are shown by the dashed lines

Since it was not possible to perform a loading experiment on pure Cu and pure Cr the stiffness was taken to be 135 GPa and 280 GPa respectively [8]. The elastic curves lie below the expected elastic response. This was probably caused by an overestimation of the composite strain caused by a small amount of bending of the specimen recorded by the clip gauge during the early stages of loading. The use of clip gauges on both sides of the sample might have solved this uncertainty, but this would have interfered with the neutron beam access to the sample.

The above phase stresses are the changes relative to the initially unloaded state, and therefore do not include pre-existing residual stresses. It is clear from figure 6.11 that the stresses increase in the Cr phase to about 500 MPa and then saturate while the Cu phase begins to plastically deform when the stresses have increased to about 300 MPa, saturating at around 400 MPa. It is unusual that the Cr fibres deformed preferentially in the view of its high load bearing capacity. However, when considering these results it is important to take into account that the composite was heavily co-deformed prior to tensile testing. This has increased the fibre aspect ratio, introduced significant plastic strain into both phases and possibly generated considerable residual strains.

Dunand et al. [9] used the synchrotron X-ray transmission technique to study the internal load transfer and micromechanical damage in Cu matrix composites with nominal contents of 7.5 or 15 vol.% molybdenum particles at room temperature. They found that at small applied strains, load was transferred from the yielding matrix to the elastic reinforcements. At larger strains, the load fraction carried by molybdenum reached a maximum and then decreased continuously. This was due to the disintegration of the molybdenum particulates, which consisted of fine, sintered molybdenum particles infiltrated by Cu.

Sun [10] reported that a tensile residual stress of ~140 MPa was generated in the Cr fibres at a drawing strain of 3.1 for the Cu-15vol.% Cr composite. Using this measured residual stress on our composite will give a tensile stress of Cr of approximately 700 MPa. This value is fairly close to the tensile strength value obtained from the hardness test.

6.8 In-situ tensile tests inside the scanning electron microscope

In order to understand the damage mechanism of the composite, in-situ tensile tests were performed at room temperature using a tensile stage coupled to the scanning electron microscope. A crosshead displacement rate of 0.1mm/min was chosen. It was not possible to collect load or extension data.

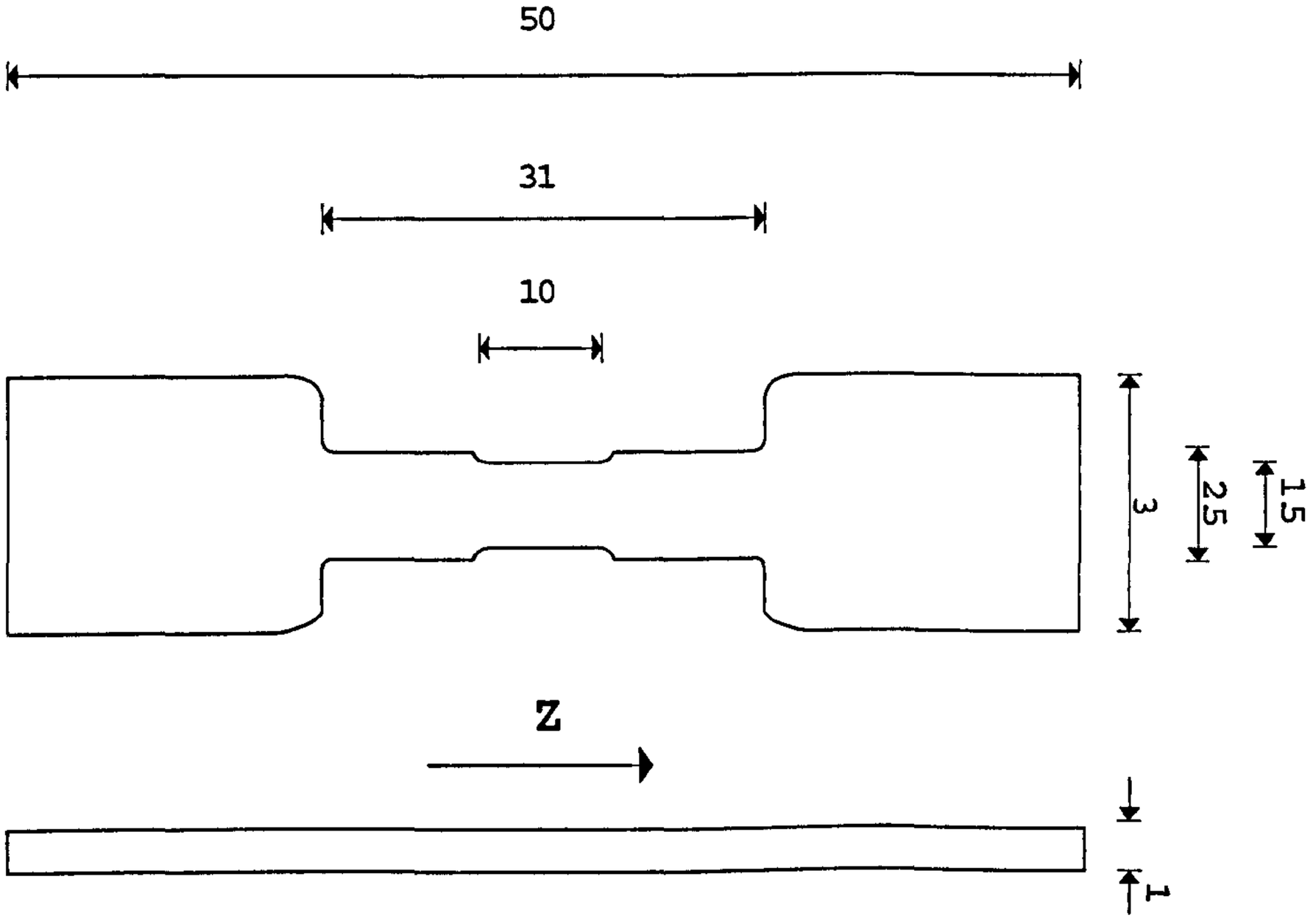

Figure 6.12 Shape and dimensions of a specimen for "in-situ tensile test in SEM"; the dimensions are in millimetres

Flat tensile specimens were produced by electroerosive machining. They had a cross section of 1 x 1.5 mm^2 and a gauge length of 10 mm. They were polished down to 1 μm abrasive size. Specimens with the dimensions shown in figure 6.12 were used for the testing. After failure, specimens were polished and observed under the SEM again to examine the damage behaviour of the bulk.

At low strain (before yielding), no modifications to the structure were observed. As plastic strain progressed close to the onset of necking, the first cracks appeared in the Cr fibres (figure 6.13a). While some cracks were observed far from the ultimate failure location, most occurred in a narrow band (imaged in figure 6.13). The sample was deformed further in-situ to follow the continued deformation of the Cr fibres. Prior to this point, deformation had been fairly uniform, but as is clear from the sequence in figure 6.13, at this deformation broke up into a series of $\pm 45^\circ$ shear bands having a periodicity of the order of 10-15 μm. It is particularly striking that these bands appear undisturbed by the crossing Cr fibres. This implies that these bands have origin in the bulk. Both 0° and 45° fibre fractures can be seen. The crack orientations might be due to a crystallographic effect or could simply be a reflection of whether the fibre lies on a single 45° shear band or where two contrary bands cross. Voids can also be seen at the ends of Cr fibres. These are particularly evident in cluster of fibres, when fibre ends are separated by only a thin Cu region as shown in figure 6.14(a).

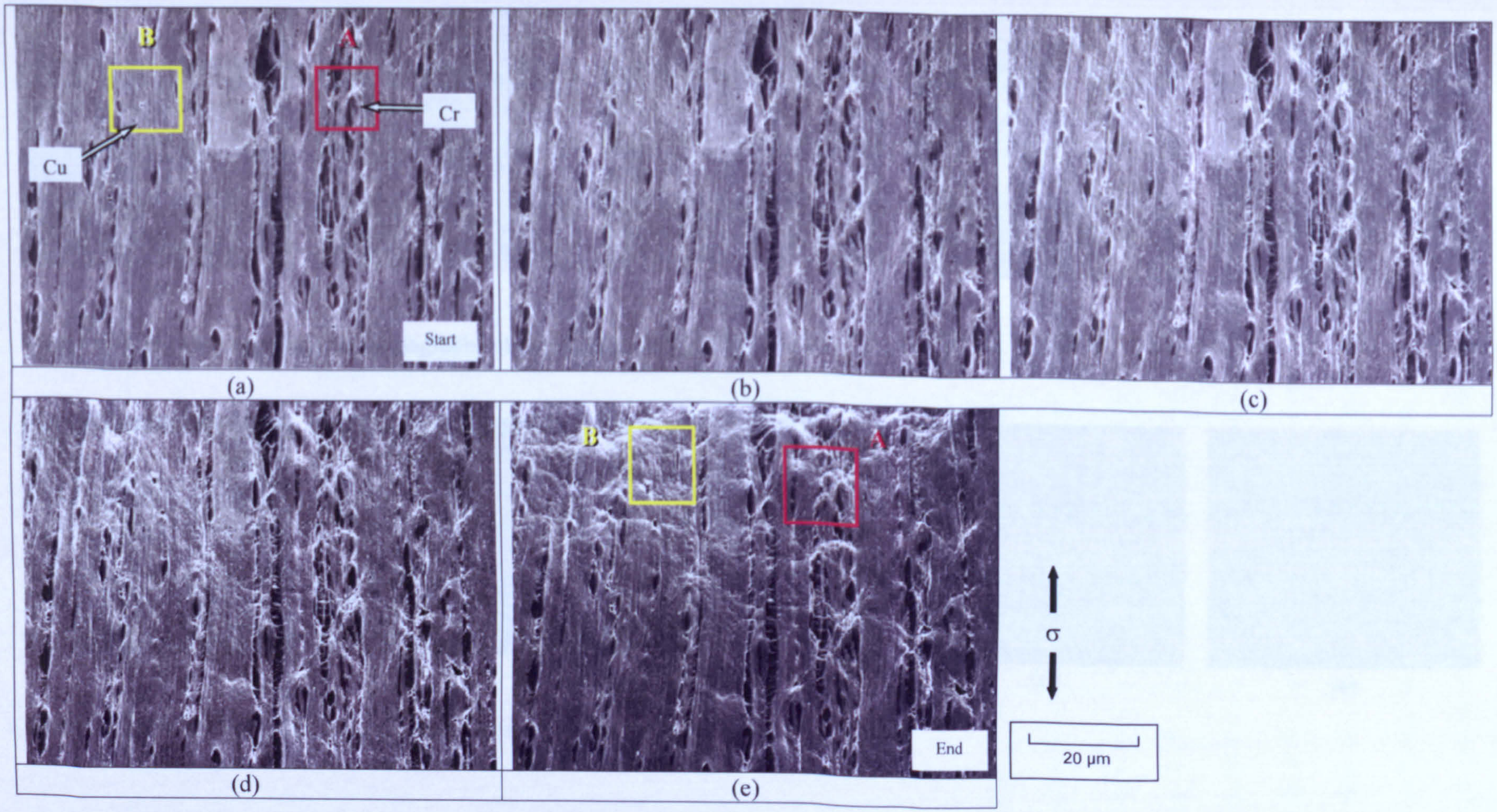

Figure 6.13 Series of sequential SEM images taken at low magnification during in-situ straining of the composite. Strain increases from (a) to (e). Regions A and B are shown magnified in Figure 6.14 and Figure 6.15 respectively

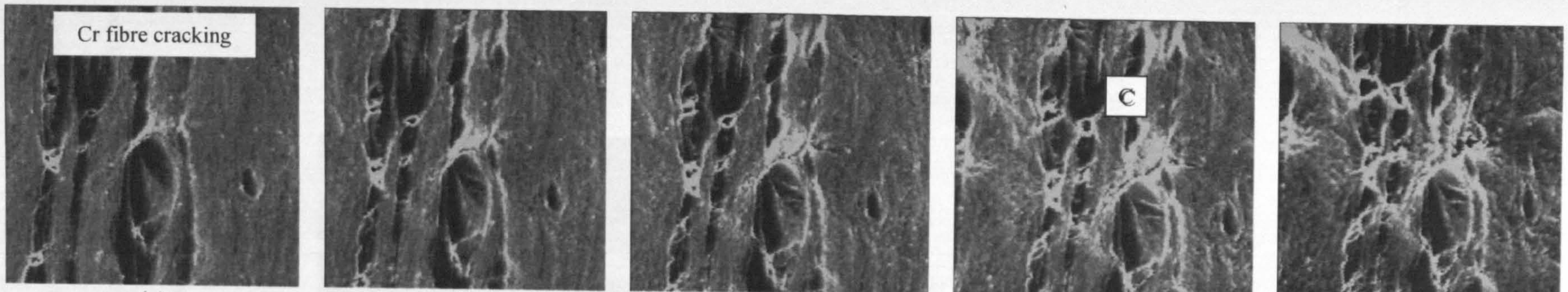

(a) (b) (c) (d) (e)

Figure 6.14 Higher magnification micrographs of region A shown in Figure 6.13

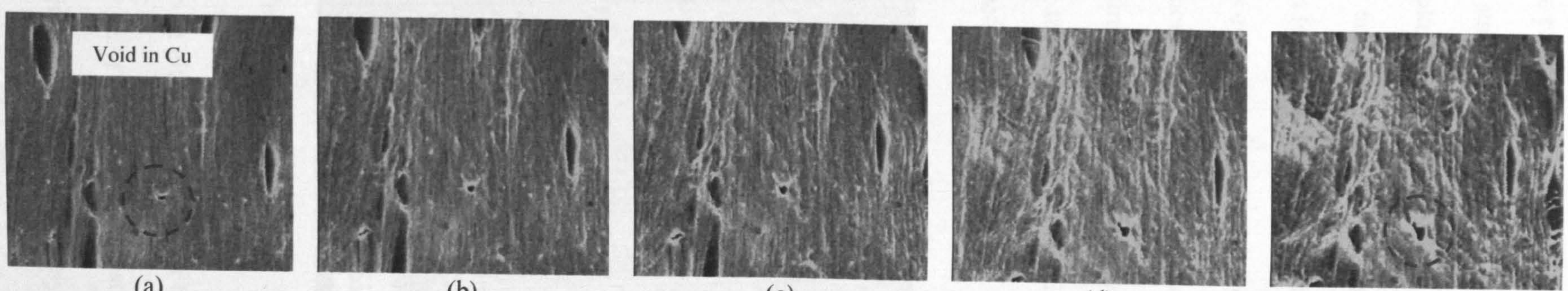

(a) (b) (c) (d) (e)

Figure 6.15 Higher magnification micrographs of region B shown in Figure 6.13

Figure 6.14 and 6.15 show the progressive damage of a group of Cr fibres near the surface and a region free from surface breaking fibres respectively at a higher magnification. These images were taken at the same location as those taken at low magnification (figure 6.13: region A and B). In figure 6.14, small shear style cracks are apparent within the fibres even in (a). These grow across the sequence and by (e) coalescence of neighbouring cracks is evident at the point labelled C where +45° and -45° meet. In figure 6.15, the area is mostly free of voiding defects from (a) to (d), but under the intense local straining occurring in the final increment in figure 6.13(e), a surface breaking void can be seen at the point of highest local strain formed during this increment. The final fracture trajectory is shown in figure 6.16.

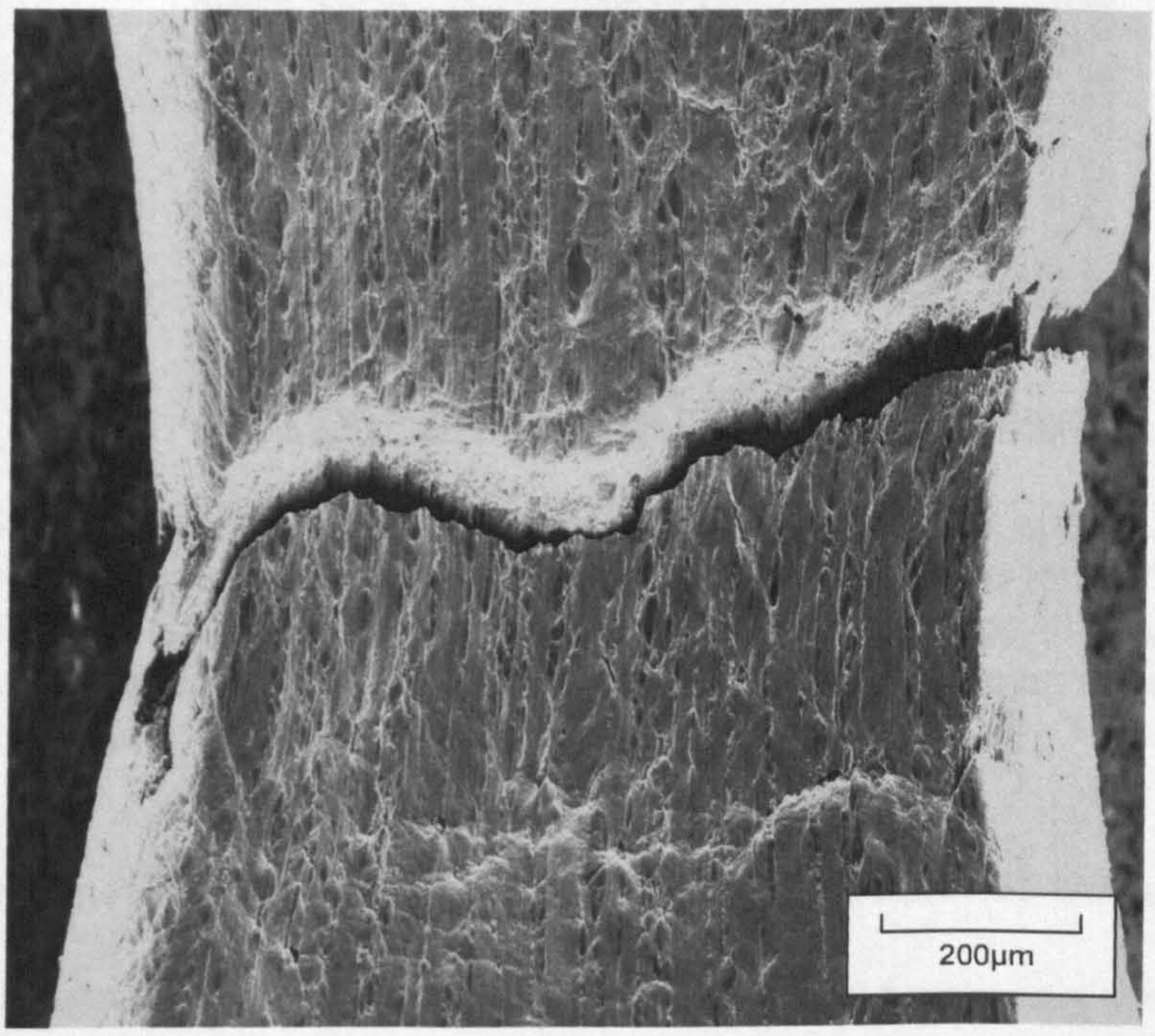

Figure 6.16 Final fracture trajectory

Since the surface behaviour can be different from that of the bulk, the material below the surface was examined in the SEM after the tensile testing ended. This sub-surface was exposed by removing a thin layer of approximately 0.6 mm of surface

material with abrasive paper and then re-polishing the newly exposed surface. As shown in figure 6.17, almost no cracks were observed in the material below the surface. It is evident that Cr fibres cracked readily near surface regions, but extensive Cr fibre cracking was not the bulk behaviour.

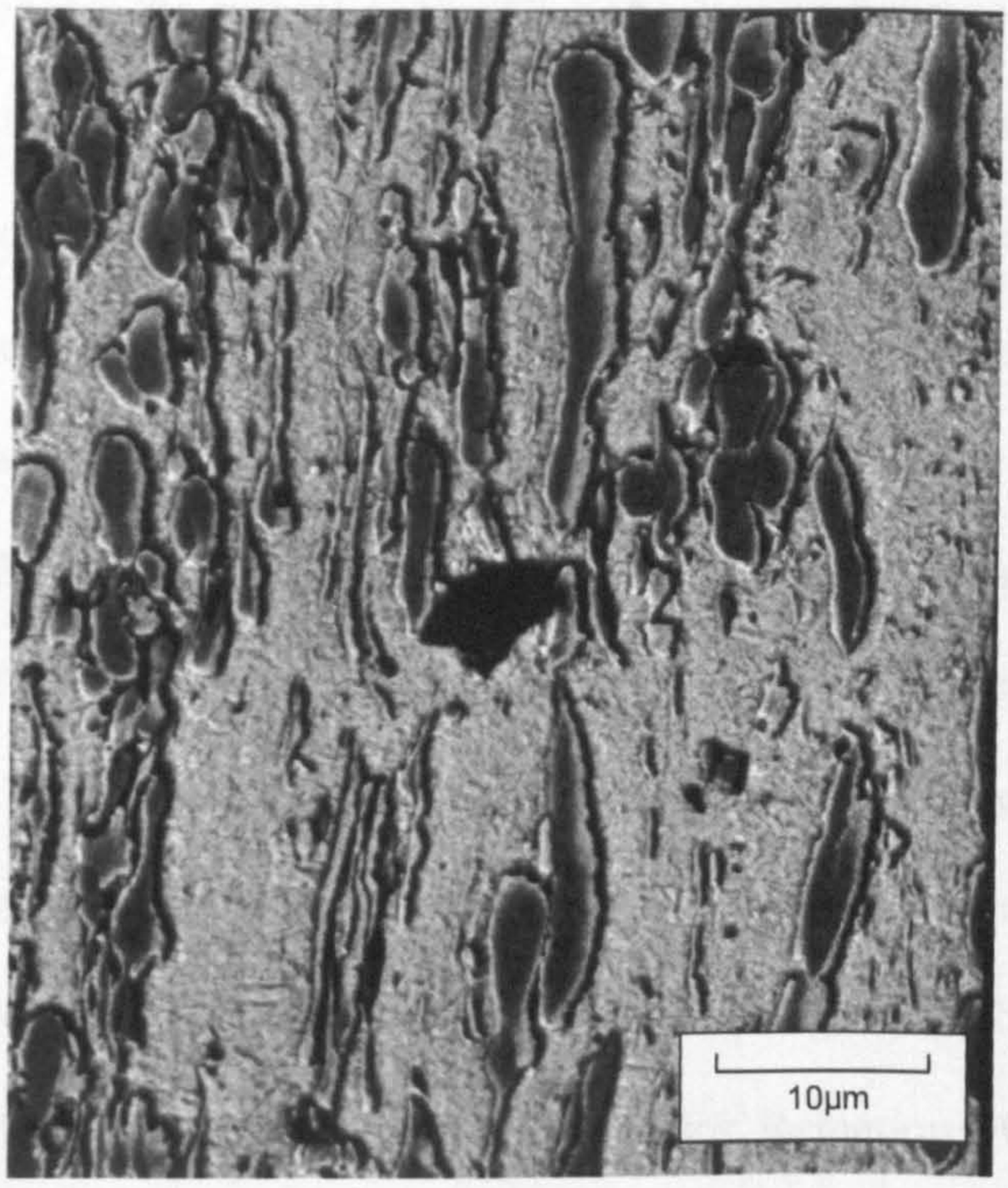

Figure 6.17 Micrograph of the composite that lay below the surface during the tensile tests. This surface was revealed by abrading away ~0.6 mm of the surface seen in Figures 6.13-6.14, then repolishing. Note the absence of cracks in both phases, which indicates that the cracks were a surface phenomenon only, and no cracking occurred in the bulk material of the composite

Many investigators have suggested that the mechanical behaviour of the surface is different from that of the bulk. There has been controversy concerning the so-called "hard" or "soft" surface behaviour. Fourie et al. [11] suggested a soft surface in uniaxially deformed metals on the basis of direct mechanical testing and observation of a low dislocation density near the surface. On the other hand, Klamer et al. [12] suggested a hard surface on the basis of the flow stress changes during continuous polishing experiments. However, regardless of whether the surface is soft

or hard, the small increase or decrease of the surface strength would be insufficient to cause the drastic increase of the number of cracks on the surface of the Cu-Cr composite specimens during in-situ tensile testing.

The severe localization of damage close to the fracture surface and the absence of cracks beneath the surface suggest that the damage behaviour in the bulk differs from that at the surface. The most obvious explanation for this difference is the extreme notch sensitivity of Cr at room temperature. The critical size crack for Cr is very small, and the material at the surface is vulnerable to formation of flaws that can initiate cracks. However, the difference in the stress state between the surface and the bulk may also contribute to the observed behaviour. This arises because the lack of constraint at the free surface. In the bulk, the stress state is triaxial, because the flow of the material in the bulk is resisted by the surrounding materials. Indeed it is the large level of triaxiality that is generated by co-deformation that produces the long Cr fibres in the first place. This constraint increases the ductility of the Cr phase and inhibits crack formation. At the surface this mechanism is less effective, and there is a tendency for the fibres to crack and for defects to form at fibre ends. The in-situ experiments have shown that plastic deformation in the composite occurs by shearing at persistent slip bands. As a result plastic deformation is unstable which limits the elongation and leads to failure of the composite. The absence of cracks in the bulk was also seen after normal tensile testing (Chapter 5). The surface cracks did not penetrate into the matrix because of the high ductility of the Cu matrix.

6.9 Summary

1 To summarise, the penetrative property of the neutron beam is useful because the whole body of a specimen can be examined and not merely its surface. The internal stresses of the Cu-Cr composite during tensile deformation were successfully evaluated by using the neutron diffraction technique. The scatter in the neutron diffraction experiment can be reduced considerably if a longer count time was available to generate more data at each stress level.

2 As expected given the large aspect ratio of the fibres, the two phases strain almost equally in the axial direction. Somewhat surprisingly however, the onset of plasticity results in a strain misfit between the phases which acts to transfer load *from* the nominally reinforcing Cr phase to the Cu phase. Microstructural observations showed that the damage in the Cr phase was not significant, it must be concluded that the Cr phase deforms more than the Cu phase. This suprising result was borne out by the final residual strains.

3 This is because co-deformation prior to testing had meant that the Cr phase reaches the yield locus at approximately the same strain as the Cu phase. This is due to a combination of its higher stiffness and the probable presence of swaging induced residual stresses. A flatter work hardening rate for the Cr phase relative to the Cu phase means that although the two phases deform approximately equally, the Cr phase has the larger plastic component resulting in load transfer from Cr to Cu with increased straining. This is shown in table 6.2 which shows that the Cr phase is effectively carrying a higher proportion of the applied load in the elastic region, this benefit decreases with increased plastic straining.

Applied stress (MPa)	Relative Stress in Cu (MPa)	Relative Stress in Cr (MPa)	Stress ratio Cu : Cr
100	90	181	1 : 2.0
250	230	423	1 : 1.8
350	327	550	1 : 1.7
375	357	535	1 : 1.5
400	387	516	1 : 1.3
415	403	522	1 : 1.2

Table 6.2 Stresses in the individual phase during deformation

4 The Eshelby method was seen as a powerful tool for the study of phase stresses because of its computational efficiency, flexibility and the capability to reduce most internal stress problems to some matrix/reinforcement misfit without needing details knowledge of the complex matrix/reinforcement stress field. This method has been used extensively in neutron diffraction studies of metal matrix composites phase strain data. For the composite, a fairly good agreement is observed in the phase strains predicted by the Eshelby theory and measured by neutron diffraction despite the large scatter in the experimental data.

5 The in-situ tensile test in SEM showed that the composite damage mechanism behaviour of the surface was different from that of the bulk. Cr fibres were found to crack easily at the surface but extensive fibre cracking was not found in the bulk. The different damage behaviour of the surface and the bulk can be explained in terms of the extreme notch sensitivity of Cr and the difference of the stress state in the surface and the bulk.

References

1 P.M. Mummery and B. Derby, In situ scanning electron microscope studies of fracture in particulate-reinforced metal-matrix composites. Journal of Materials Science, 1994. 29(21): 5615-5624.

2 M. Besterci, J. Ivan, L. Kovac, T. Weissgaerber and C. Sauer, Strain and fracture mechanism of Cu-TiC. Materials Letters, 1999. 38(4): 270-274.

3 K.L. Lee, A.F. Whitehouse, P.J. Withers and M.R. Daymond, Neutron Diffraction Study of the Deformation Behaviour of Deformation Processed Copper-Chromium Composites. Materials Science and Engineering A, 2003. A348: 208-213.

4 C. Sinclair, Co-deformation of a two-phase FCC/BCC material, PhD thesis, McMaster University, 2001.

5 H.M. Rietveld, Line profiles of neutron powder-diffraction peaks for structure refinement. Acta Crystallography, 1967. 22: 151-158.

6 P.J. Withers, W.M. Stobbs and O.B. Pedersen, The Application of the Eshelby Method of Internal Stress Determination for Short Fibre Metal Matrix Composites. Acta Metallurgica, 1989. 37: 3061-3084.

7 T.W. Clyne and P.J. Withers, An Introduction to Metal Matrix Composites. Cambridge Solid State Series. 1993, Cambridge: Cambridge University Press (Also in Chinese). 509.

8 Smithells Metals Reference Book, 7th edition, Editor: E.A. Brandes and G.B. Brook.

9 A. Wanner and D.C. Dunand, Synchrotron x-ray study of bulk lattice strains in externally loaded Cu-Mo composites. Metallurgical and materials transaction A, 2000. 31: 2949-2962.

10 S. Sun, Structures & Residual Stresses of Cr Fibers in Cu-15Cr In-Situ Composites. Metallurgical Transactions A-Physical Metallurgy & Materials Science, 2001. 32: 1225-1232.

11 J.T. Fourie and N.C.G. Dent, The soft surface effect in deformed ∝-phase Cu-5.8 at.% Al. Acta Metallurgica, 1972. 20: 1291-1296.

12 I.R. Klamer, Effect of the surface on the activation energy and activated volume for plastic deformation of fcc metals. Trans AIME, 1964. 230: 991-1000.

Chapter 7

Creep Deformation of Cu-Cr composites

7.1 Introduction

Since the thermal conductivity of Cu-based composites is high, they have potential use in future space and energy technologies such as aerospace propulsion systems [1]. These materials require not only high thermal conductivity but also adequate creep resistance to ensure reliable performance in service. Since potential applications for Cu-Cr composites include high temperature service, it is important to characterize their creep and creep fracture behaviours.

Although Cu possesses corrosion resistance in ambient temperature environments, it weakens rapidly in oxidizing environments at high temperatures due to formation of an unprotective oxide [2]. Reaction with oxygen is the most common cause of deterioration. Research has shown that at above 400°C, Cu oxidizes rapidly because of oxide decohesion and flaking leaving the surface exposed for further oxidation [2]. Oxidation is normally undesirable since it causes both thinning of the sample and also promotes premature failure during creep testing due to oxide particles acting as cavity nucleation sites.

To investigate the effect of oxidation on this composite, creep tests were performed in air and in vacuum (10^{-5} Pa) at temperatures between 200°C-650°C (0.35 to 0.68 T_m, where T_m is based on the 1358 K melting temperature of pure Cu) and stresses ranging from 18 to 270 MPa. To provide data for comparison with the composite material, pure Cu specimens manufactured by the same method as the composite were tested whenever possible. A total of 50 creep tests were carried out in this research.

7.2 General creep characteristics

The test conditions and the results of the creep tests of the composites tested in air are summarized in Table 7.1. The failure strains are the total strain tested at failure. For comparison, the creep behaviour of pure Cu tested in air and composite tested both in air and vacuum are shown in Table 7.2.

Temperature (°C)	Applied stress (MPa)	Minimum strain rate (s^{-1})	Failure strain	Failure time (Minutes)
200	270	2.33E-06	0.057	252
200	260	1.99E-07	0.048	2148
200	250	7.77E-07	0.072	1050
200	240	1.32E-07	0.066	4542
200	230	4.19E-08	0.062	10080
200	220	4.30E-09	0.037	40800
300	180	2.14E-06	0.060	229
300	170	2.32E-06	0.057	235
300	160	2.22E-08	0.054	1870
300	140	1.77E-07	0.068	2225
300	130	9.86E-08	0.056	3815
300	120	8.24E-09	0.042	18360
400	110	2.57E-07	0.061	775
400	100	2.90E-07	0.081	1250
400	90	1.20E-07	0.085	2445
400	60	8.39E-08	0.076	4260
450	90	1.41E-06	0.110	345
450	60	6.84E-07	0.130	1055
500	60	3.53E-06	0.144	325
500	55	2.71E-06	0.141	425
500	50	9.64E-07	0.136	1200
500	40	3.84E-07	0.114	2875
500	30	9.25E-08	0.096	9315
550	60	2.76E-05	0.171	70
550	50	1.59E-05	0.147	110
550	40	2.34E-06	0.114	485
550	30	1.89E-07	0.100	4695
600	50	3.33E-05	0.209	50
600	40	1.81E-05	0.183	125
600	30	4.71E-06	0.174	500
600	25	9.01E-07	0.143	1970
650	25	1.17E-05	0.227	210
650	20	5.06E-06	0.254	570
650	18	1.75E-05	0.189	1120

Table 7.1 Summary of all creep tests for the composite tested in air between 200-650°C

		Vacuum			Air					
		Composite			Composite			Pure copper		
Temperatures (^{0}C)	Applied stress (MPa)	Failure strain	Failure time (min)	Minimum creep rate (s^{-1})	Failure strain	Failure time (min)	Minimum creep rate (s^{-1})	Failure strain	Failure time (min)	Minimum creep rate (s^{-1})
400	110	0.073	2460	1.54E-07	0.061	775	2.57E-07	—	—	—
	90	0.102	5965	6.63E-08	0.085	2445	1.20E-07	—	—	—
	60	0.135	33175	2.36E-08	0.077	4260	8.39E-08	0.221	170	1.83E-05
450	90	0.097	565	1.45E-06	0.110	345	1.41E-06	—	—	—
	60	0.096	11210	6.81E-08	0.130	1055	6.84E-07	—	—	—
500	50	0.145	7505	1.22E-07	0.136	1200	9.64E-07	—	—	—
	40	0.110	24075	1.83E-08	0.114	2875	3.84E-07	0.21	100	2.33E-05
550	60	0.230	430	5.64E-06	0.171	70	2.76E-05	—	—	—
	50	0.153	920	1.58E-06	0.147	110	1.59E-05	—	—	—
	40	0.112	7000	1.13E-07	0.114	485	2.34E-06	—	—	—
600	60	0.187	70	2.90E-05	—	—	—	—	—	—
	50	0.133	240	6.46E-06	0.174	50	3.33E-05	—	—	—
	40	0.147	755	1.91E-06	0.183	125	1.81E-05	—	—	—
650	40	0.181	625	3.02E-06	—	—	—	—	—	—
	25	—	—	—	0.227	210	1.17E-05	—	—	—
	20	—	—	—	0.254	570	5.06E-06	—	—	—
	18	—	—	—	0.189	1120	1.75E-05	—	—	—

—: No test was performed

Table 7.2 Comparison of creep properties of pure Cu tested in air and composite tested both in air and in vacuum

Figure 7.1a shows the typical creep curves at 200°C for the composite tested in air under different values of applied stress. Inspection suggests that the composite exhibits a minimum creep rate at the higher applied stress, while at a lower applied stress it shows the normal three stages of creep behaviour: a short primary stage, a steady-state region where the creep rate is reasonably constant, and then an abrupt tertiary stage and failure. However, when the data from figure 7.1a are replotted in the form of log instantaneous strain rate versus strain as shown in figure 7.1b and it is apparent that the steady state region (of the order of 15-35 % of the whole creep life as a function of time) is reasonably well defined for both the applied stresses. This behaviour was also observed in specimens tested at 300°C at all applied stresses.

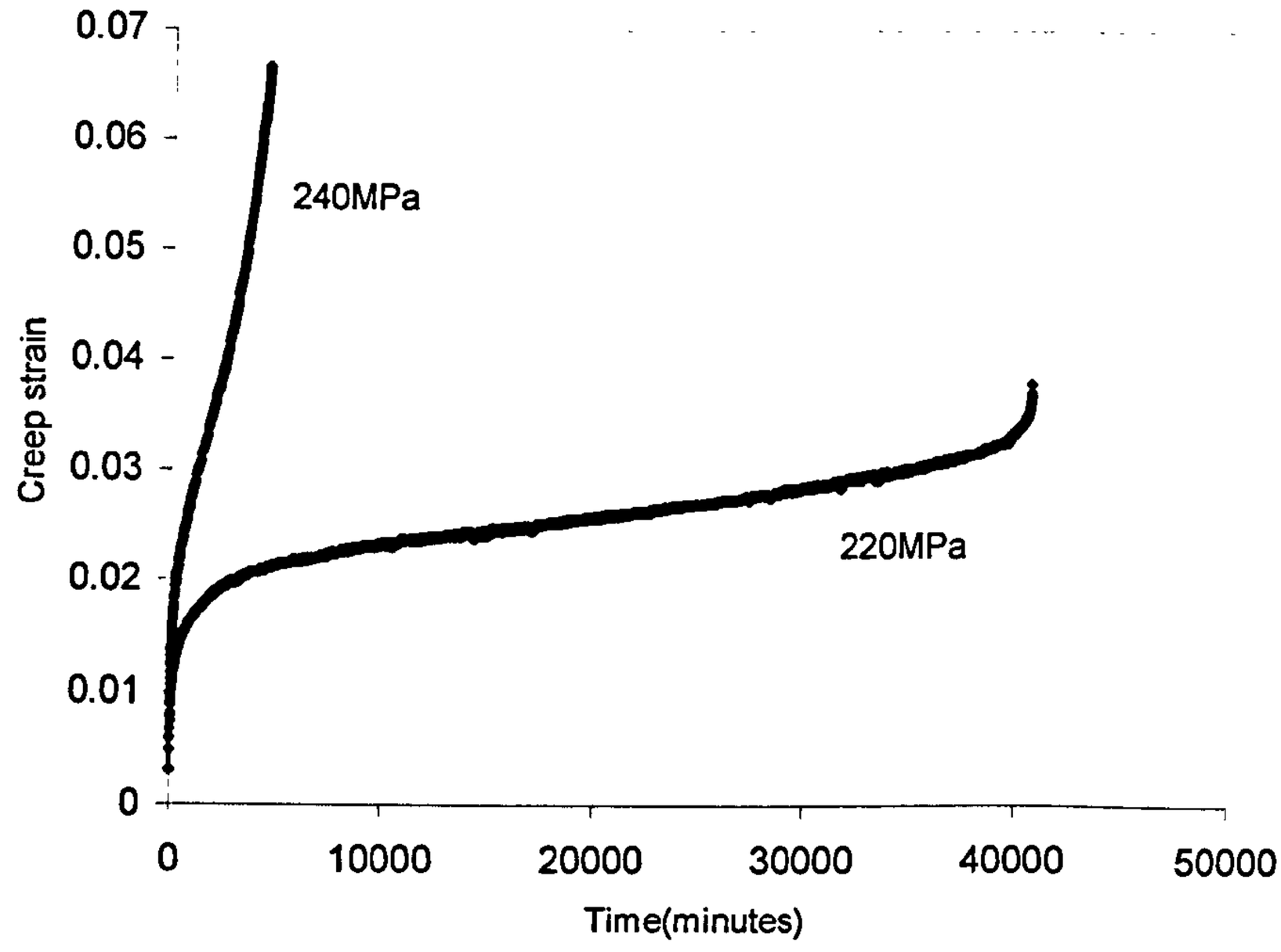

(a)

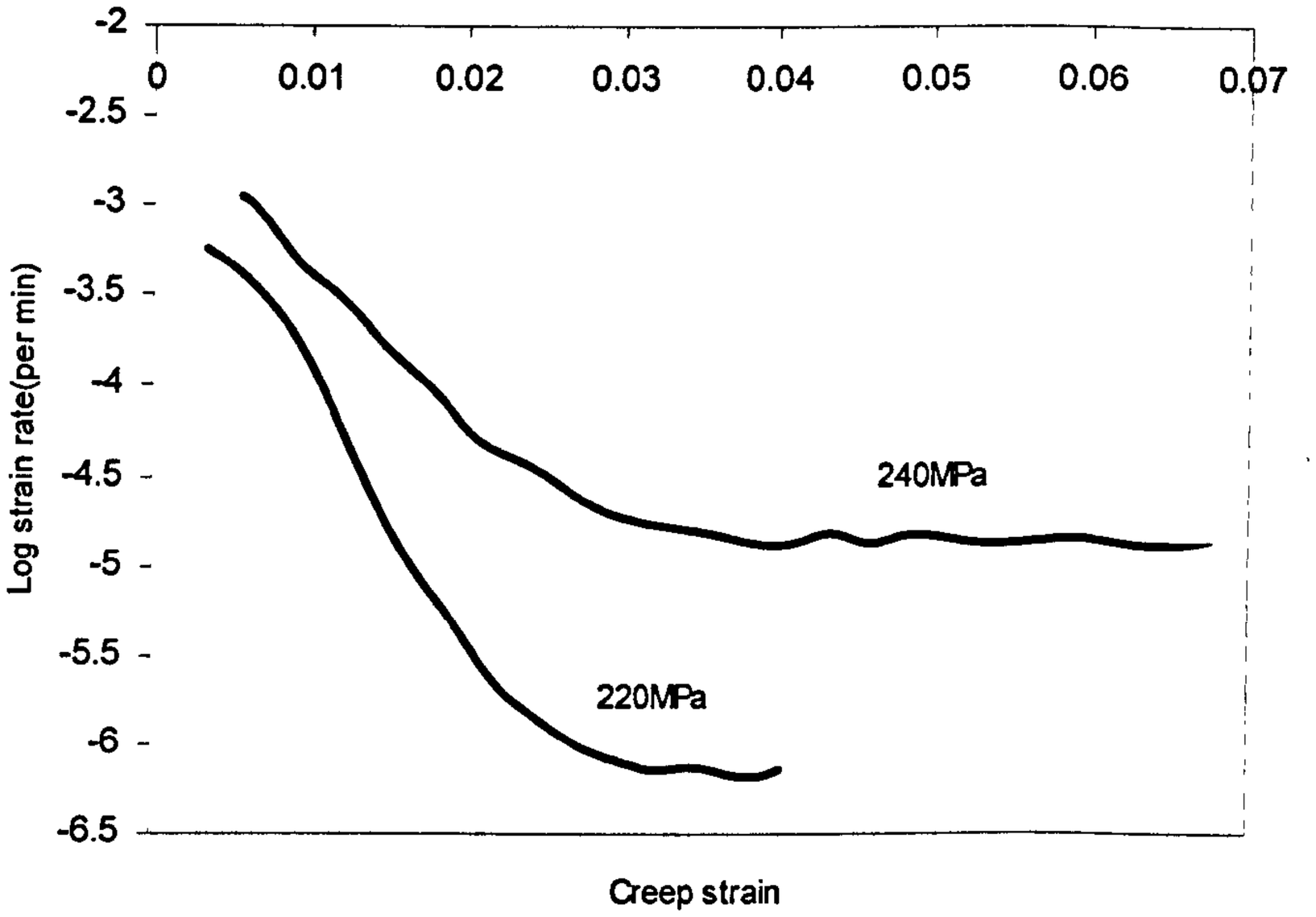

(b)

Figure 7.1 (a) Typical creep curves for the composite at 200°C at different applied stresses (b) Plot of log of instantaneous creep rate versus creep strain shown in (a)

By contrast, the composite exhibited different creep curves at higher testing temperatures (above 400°C) in comparison to those at low temperatures. Typical creep curves at 500°C for the composite tested in air are shown in figure 7.2a.

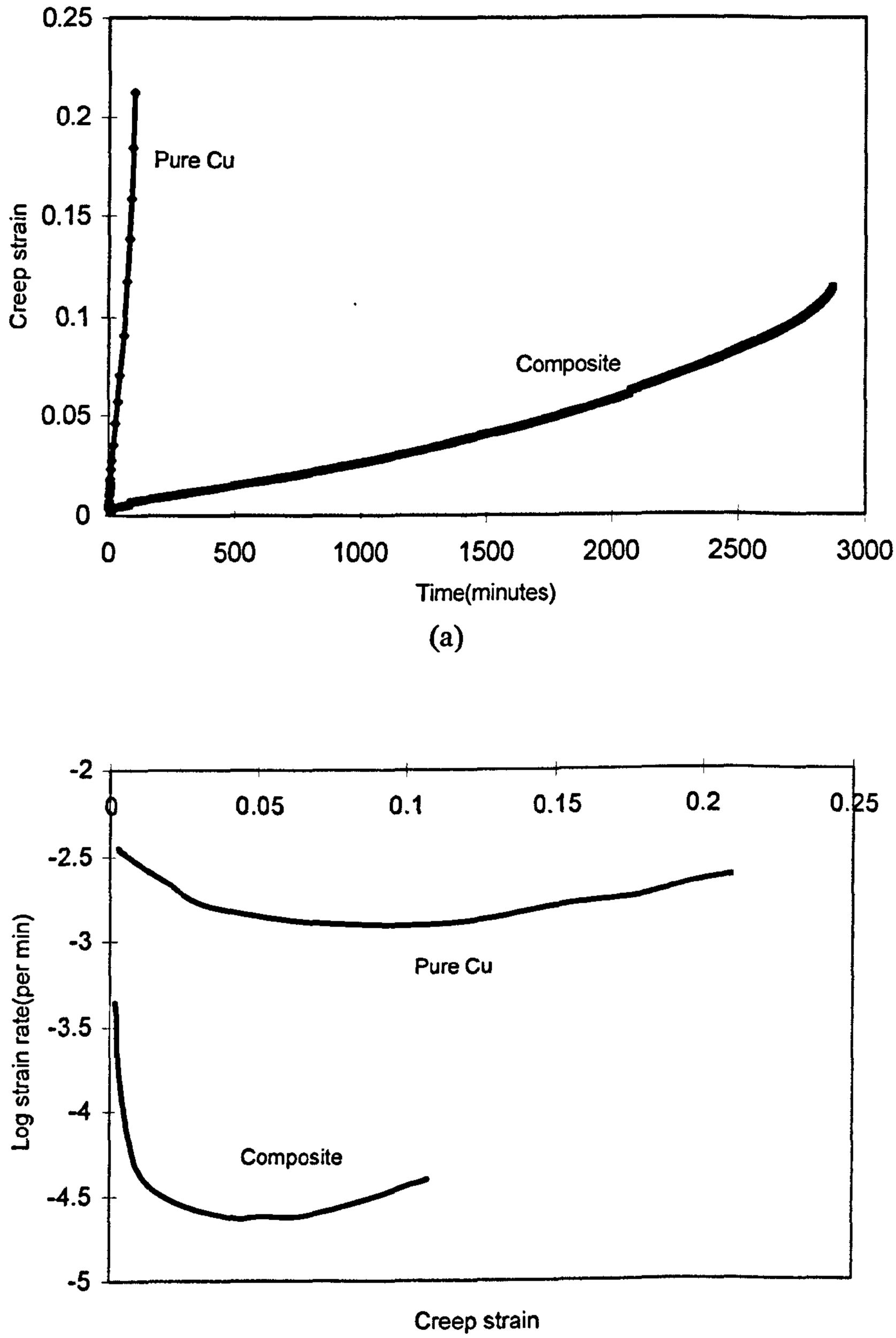

Figure 7.2 (a) Typical creep curves for the composite and pure Cu tested in air at 500°C under an applied stress of 40 MPa (b) Plot of log of instantaneous creep rate versus creep strain shown in (a)

The primary stage is again very short, but there is no well-defined steady state region and instead the creep rate passes through a minimum and then gradually increases through a fairly long tertiary stage. The same behaviour is also exhibited by the pure Cu tested in air at the same temperature and stress level as shown in figure 7.2a. Figure 7.2b shows the corresponding plot of the log instantaneous strain rate versus strain for these two materials, and it is clear that the steady state region is not well defined for both materials.

Figure 7.3 show typical creep curves of the composite tested in air and in vacuum (10^{-5} Pa) at 600°C. The results showed that the composite tested in air led to an increase in minimum creep rate and a reduction in time to rupture. It may be noticed that the effect of the environment on the rupture time of the composite was reduced as the applied stress increased. This effect is attributed to the reduced oxide thickness that forms during the shorter rupture time at a higher stress.

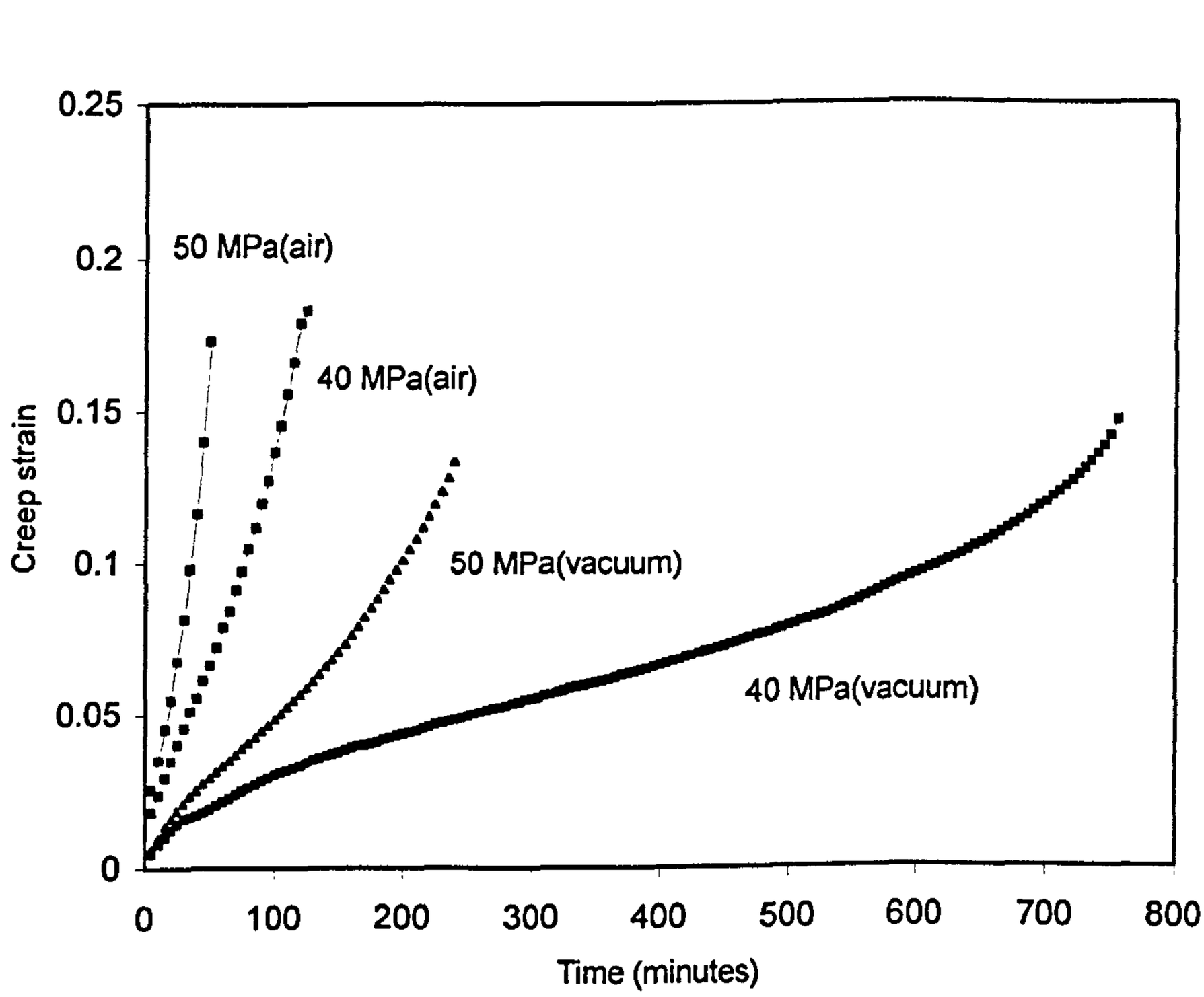

Figure 7.3 Typical creep curves for the composite at 600°C tested in air and in vacuum at different applied stresses

Examination of this figure along with others obtained at various strain rates and temperatures (400-650°C) indicates the duration of the minimum creep rate of the composite is small (of the order of 5-20 % of the total creep life as a function of time). The minimum strain rate is thought to be the result of a balance between a decreasing strain rate caused by the dislocation generation and the load transfer to the fibers and an increasing strain rate caused by the recovery and the accumulation of damage in the composite. Damage in the composite may occur in the form of fracture of the fibre network, void formation at the ends of the fibres or debonding of the fibre-matrix interface. The long tertiary creep stage for this composite suggests that damage occurs early during creep deformation and the tolerance to damage before the final fracture is high at high temperatures.

In many experiments on MMCs, the secondary stage is of a sufficiently short duration that it is more appropriately termed a minimum creep rate [3-7]. Research by Pandey et al. [7] showed that a well defined steady-state creep rate can be obtained in compression but not in tensile creep. This behaviour can be explained in terms of damage mechanisms. Damage can occur very early during tensile deformation, as a result this behaviour will never reach a true steady state. The damage is not normally catastrophic and will build up throughout the deformation without leading immediately to failure. These damage mechanisms do not operate in compression, and therefore a true steady-state behaviour can be achieved. On the other hand, there are some composites where reports have demonstrated that the steady-state is fairly extensive during tensile creep testing, thereby demonstrating that an abrupt and possibly poorly defined minimum creep rate is not an intrinsic property of all metal matrix composites [8].

From the results shown in Table 7.2, a number of observations can be made. There is significant difference between the rupture times exhibited by pure Cu and by the composite even in the same environment. Under the same testing condition, the introduction of Cr fibres into Cu produces a large increase (more than 25 times) in the creep rupture time over that obtained for pure Cu. Similar to the creep rupture data, the minimum creep rate of the composite tested in air are about two to three orders of magnitude less than that of the pure Cu. Such a difference can arise when significant load transfer partitions the external load between the matrix and reinforcement [9]. In the presence of load transfer, the creep data can be reconciled by putting, for the same creep loading condition, the ratio of the minimum creep rates of the composite and the matrix alloy equal to a factor given by $(1-\alpha)^n$ where α is a load transfer coefficient having values between the range from 0 (no load transfer) to 1 (full load transfer) and n is the stress exponent. For the present Cu-Cr composite, the values of α inferred from the data in Table 7.2 are within the range of ~0.5-0.6. This means that approximately 50-60 % of the external load is transferred to the reinforcement during creep of the composite. Thus, incorporation of Cr fibres into the Cu matrix greatly increases the creep resistance.

Hong et al. [10] examined the microstructural stability of Cu-based composites after high temperature annealing. They observed the break-up and spheroidzation of fibres and recrystallization of Cu matrix at high temperatures, which resulted in the decrease of the mechanical strength. Spitzig et al. [11] have shown that even for the as-cast state (η=0), the incorporation of the Nb phase into the Cu matrix results in a significant increase in the creep rupture time over that obtained for pure Cu. However, the increase in the creep rupture strength did not continue with increasing draw ratio, unlike room temperature strengthening, probably due to the

microstructural instability of heavily deformed Nb fibres. Spitzig et al. [11] also observed that an increase in draw ratio to above 6.9 did not show any significant improvement in creep resistance. Hong et al. [12] suggested that the microstructural scale of the Cu matrix is limited by Nb fibres and the strengthening due to fine Nb fibres plays an important role at high drawing strains (> 5.5). Since these fine fibres are unstable at high temperatures because of high stored cold work energy and high interfacial energy, they are not likely to provide an improved creep resistance at high temperatures.

7.3 Creep exponent

Theoretically, $n_{composite} \approx n_{matrix}$ if the creep mechanism of the matrix is not severely affected by the introduction of the reinforcement. The relationship between ln (strain rate) versus ln (applied stress) for the composite tested in air at six test temperatures is shown in figure 7.4a. If the simplest power-law creep equation, relating strain rate $\dot{\varepsilon}$ to applied stress σ of

$$\frac{\dot{\varepsilon}}{D} = A(\frac{\sigma}{E})^n \qquad (7.1)$$

is used, where A is a constant and n is a stress exponent, the stress exponents are 26.6, 12.4, 5.2, 5.3, 5.7 and 5.8 at 200°C, 300°C, 400°C, 500°C, 600°C and 650°C respectively by best linear approximation.

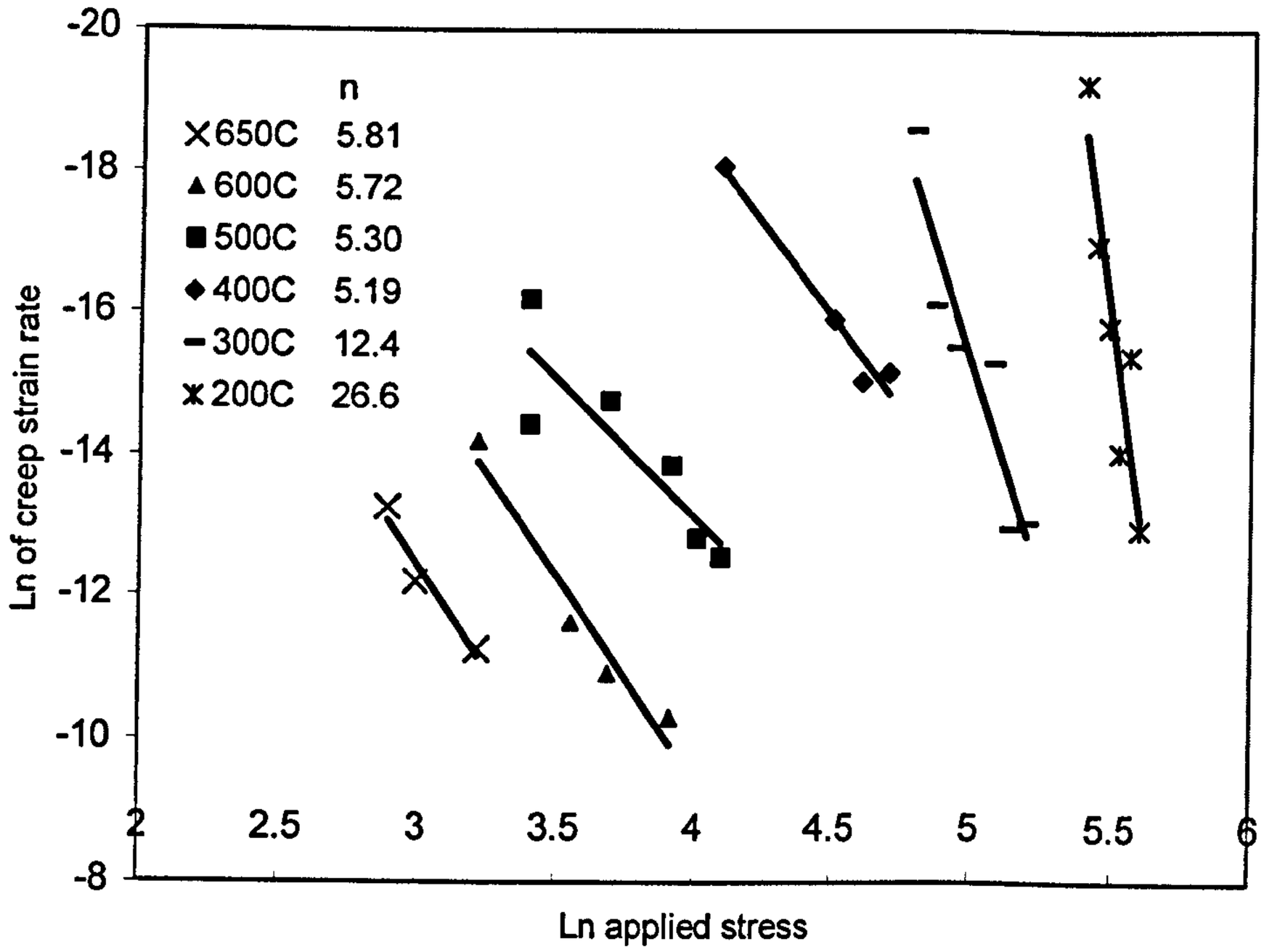

(a)

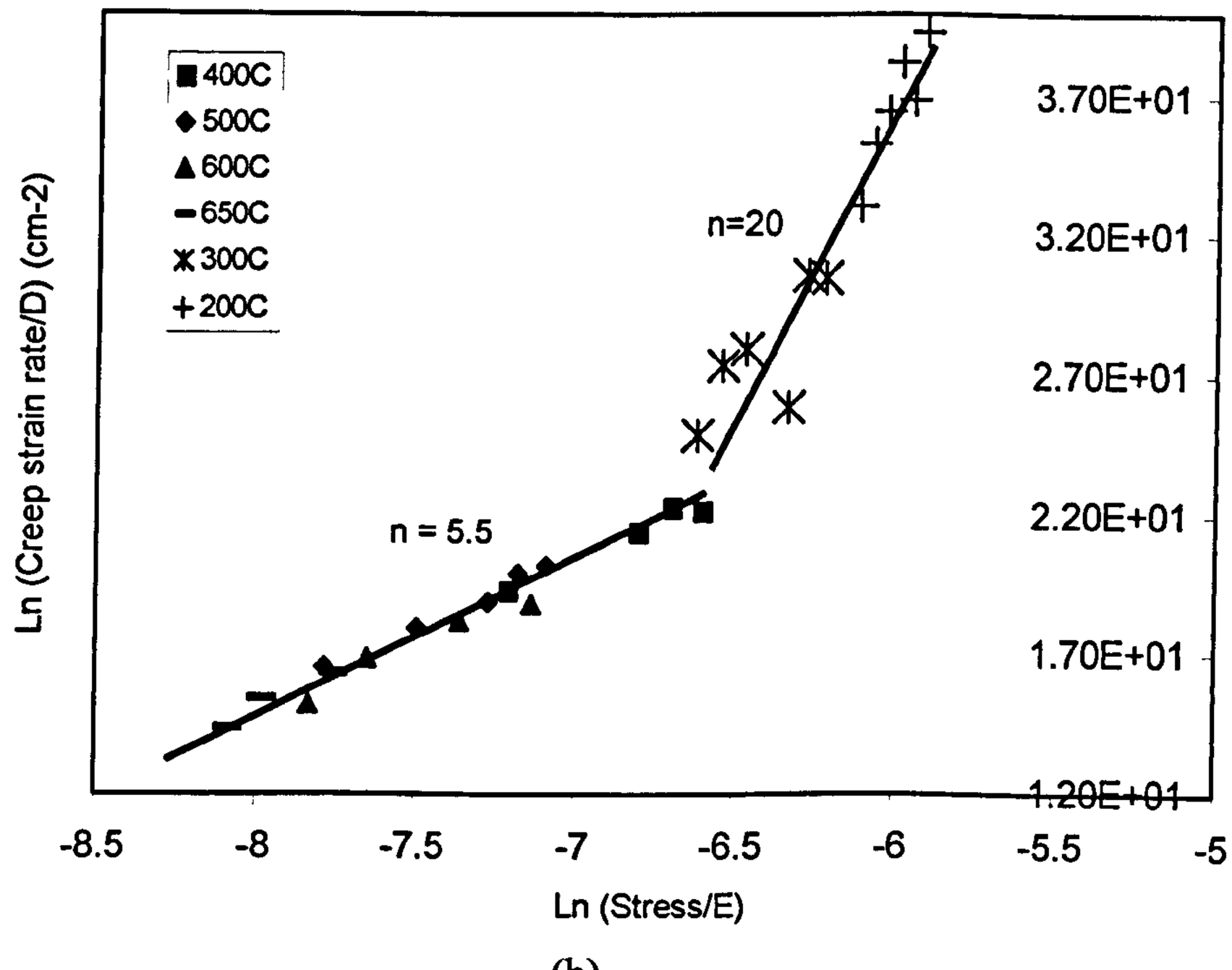

(b)

Figure 7.4 (a) Ln of creep strain rate against ln of applied stress for the composite tested in air and (b) Plot of the minimum creep rate normalized to the coefficient of matrix lattice diffusion against the stress compensated by the Young's modulus for the composites tested in air

In figure 7.4b, the minimum creep rate of the composite normalized to the coefficient of matrix lattice diffusion is plotted against the stress compensated by the Young's modulus. In the creep data calculation, values of the coefficient of lattice self diffusion, D, for pure Cu were obtained from the relationship [13]

$$D = A_1 \exp\left(-\frac{Q_1}{RT}\right) + A_2 \exp\left(-\frac{Q_2}{RT}\right) \qquad (7.2)$$

where $A_1 = 0.13$ cm^2/sec, $Q_1 = 197.8$ kJ/mole and $A_2 = 4.5$ cm^2/sec, $Q_2 = 237.4$ kJ/mole, R= 8.314 Jmol^{-1}K^{-1} and T is temperature in Kelvin. The activation energy for diffusion in materials is known to increase with increasing temperature [13] and the diffusion coefficient of pure Cu is well described by the equation (7.2) over a wide range of temperature. Since the creep tests of the present study were performed over a wide range of temperature (200-650°C), the diffusion coefficient data with two activation energies was used to reflect the change of activation energy for diffusion at various temperatures.

Values of the pure Cu Young's modulus were obtained from the equation [10]

$$E = 142 - 0.0905T \qquad (7.3)$$

It can be seen that the data points at high temperatures (≥ 400°C) are well fitted on a single straight line with a slope of 5.5. The stress exponents for the composite tested in vacuum at 400°C and 600°C are 4.6 and 5.9 respectively as shown in figure 7.5. The stress exponents for the composite tested in vacuum are very similar to those of the composite tested in air. Therefore, the controlling deformation mechanism must be the same for specimens tested in air and in vacuum. Frost and Ashby [14] reported that the stress exponent for creep of pure Cu is 4.8 under power law creep condition. It should be noted that the stress exponents above 400°C are fairly close to 5 and

those at lower temperatures (200°C and 300°C) are quite high (> 12). The close agreement between the stress exponents for the composite and for pure Cu at temperature between 400-650°C suggests that the creep deformation mechanism of Cu-Cr composites at high temperatures may be quite similar to that of pure Cu. The sharp increase of stress exponent from 5.5 (400-650°C) to 12-30 at lower temperatures (200-300°C) is most likely indicative of a change in the deformation mechanism from diffusion controlled to a non-diffusion controlled process with an increase in stress and a decrease in temperature.

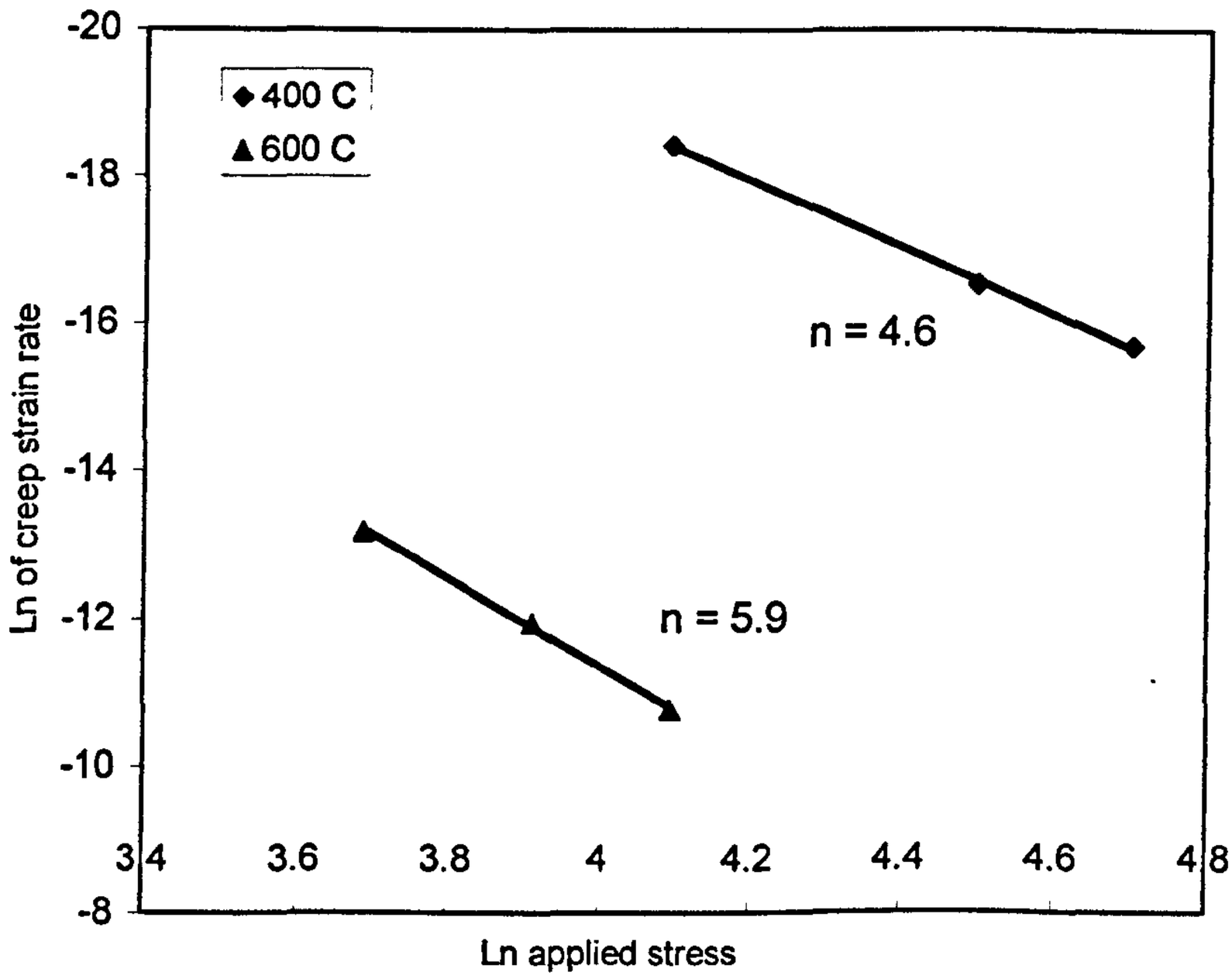

Figure 7.5 Graph of ln of creep strain rate against ln of applied stress for the composite tested in vacuum

To investigate the reason for the sharp increase of the stress exponents at low temperatures (200°C and 300°C), the dislocation substructures after creep deformation in air were examined at 200°C and 600°C. Figure 7.6 shows the dislocation substructures after creep deformation at 200°C and 600°C. As shown in figure 7.6a, the initial as-processed microstructure was not appreciably modified at

200°C. The elongated dislocation cells and subgrains parallel to the swaging axis appear to be stable at low temperatures and act as obstacles to dislocation movement.

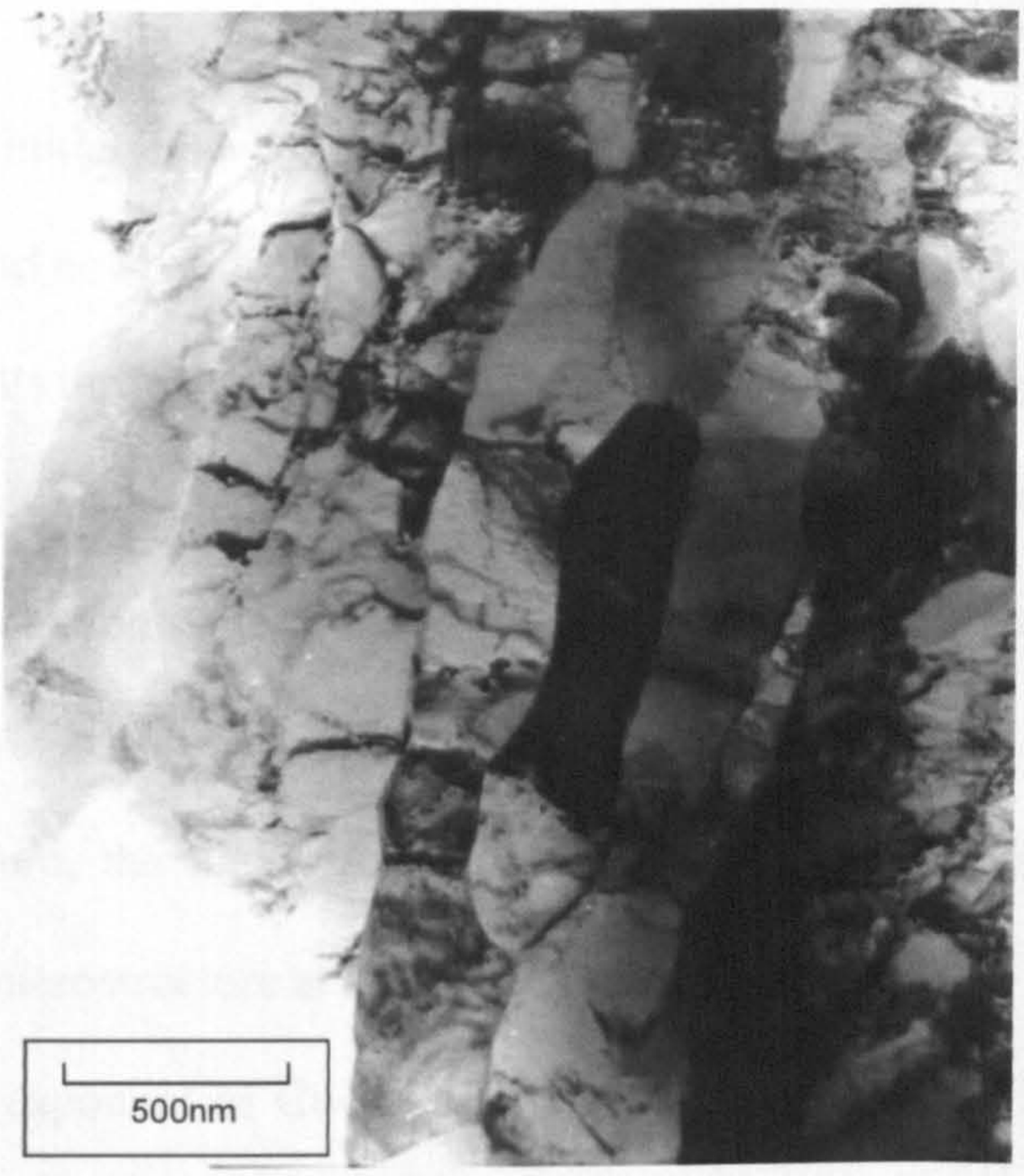

(a)

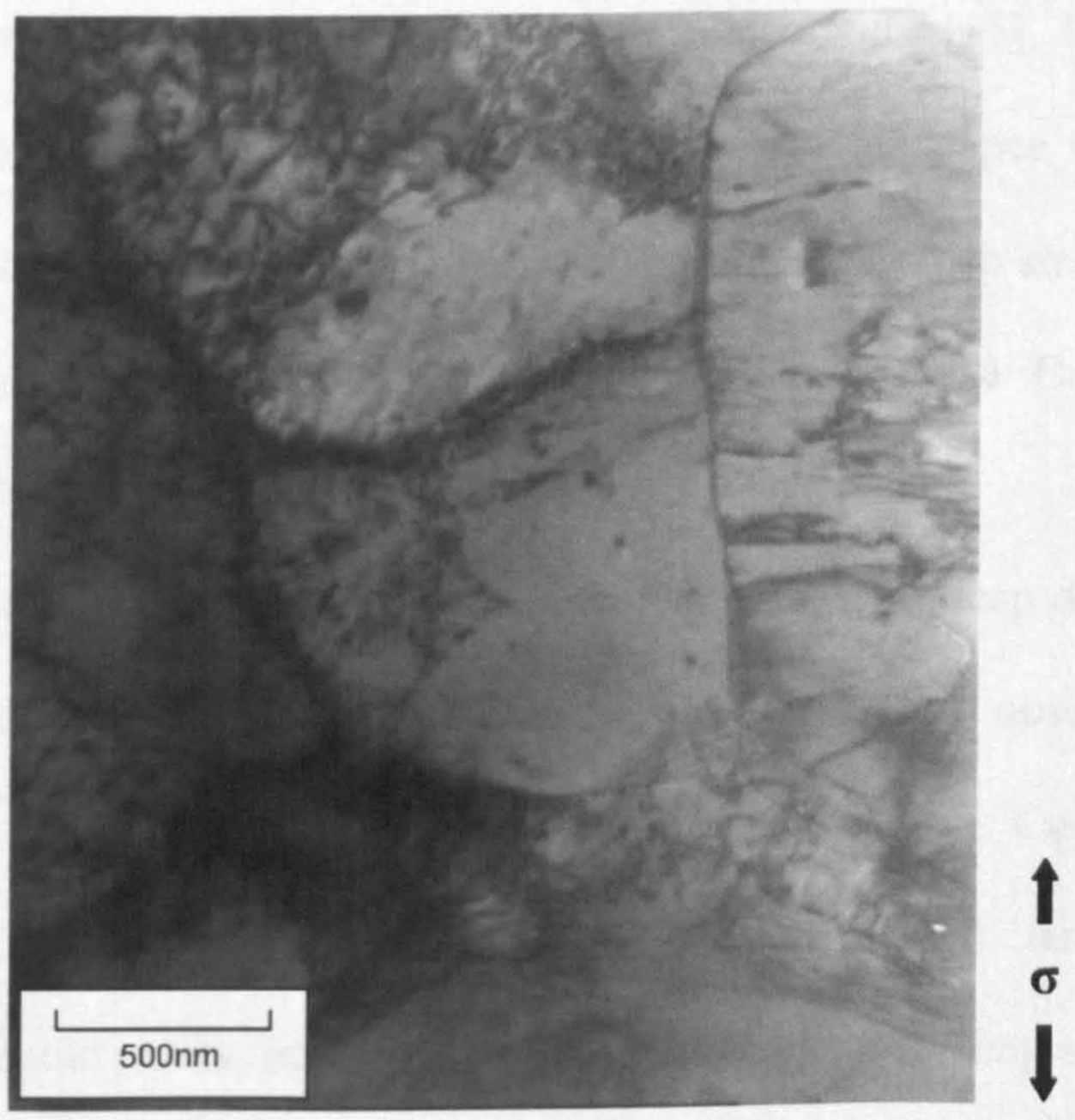

(b)

Figure 7.6 TEM images of typical dislocation substructures after creep deformation of 7 and 15 % at (a) 200°C and (b) 600°C respectively

At high temperatures, however, the initial as-swaged microstructure was not stable, and equi-axed dislocation cells and substructures, a typical microstructure after high temperature creep deformation of pure metals, was observed. At high temperatures, the initial as-swaged microstructure was completely replaced through recrystallization and newly generated dislocations during creep may have transformed into dislocation cells through glide, cross slip and climb. In this case, climb could be a rate controlling process as mentioned above. For low temperature creep deformation, the elongated dislocation cells and subgrains can be considered as strong athermal obstacles which may impose the threshold stress below which no creep deformation can occur. Therefore, the high stress exponent is likely to be associated with the stable as-swaged microstructure at low temperatures.

The stress exponent of Cu-10vol.% Cr composites at 500°C observed in the present study is in sharp contrast with high stress exponent (n= 14.8) observed in Cu-30vol.% Cr composites at the same creep testing temperature [15]. However, it is important to note that the creep data range reported in this paper was relatively narrow, covering only two to three orders of magnitude of the creep strain. Thus, it is difficult to elucidate the operative creep mechanisms in these Cu-30vol.% Cr composites unambiguously.

Spitzig et al. [11] observed that the stress exponents in creep deformation of Cu-Nb with higher drawing strains (4.8-8.2) were 6.5-8.1. They observed that the stress exponent increased with increasing drawing strain in Cu-20vol.% Nb composites. They tried to associate the larger stress exponents (i.e. larger than pure Cu) with the threshold stress, but found no correlation. Instead, they suggested that the increase in creep strength in Cu-20vol.% Nb composites was associated with the

reduction in the power law creep damage, due to the constraint introduced on the matrix creep flow by the Nb phase.

7.4 Activation energy

The temperature dependence of the creep rate for the composite tested in air at high temperatures (≥ 400°C) is shown in figure 7.7. The apparent activation energy for creep in the high stress region at 60 MPa is approximately 180 kJ/mol, while the value estimated in the low stress region at 30 MPa is about 216 kJ/mol.

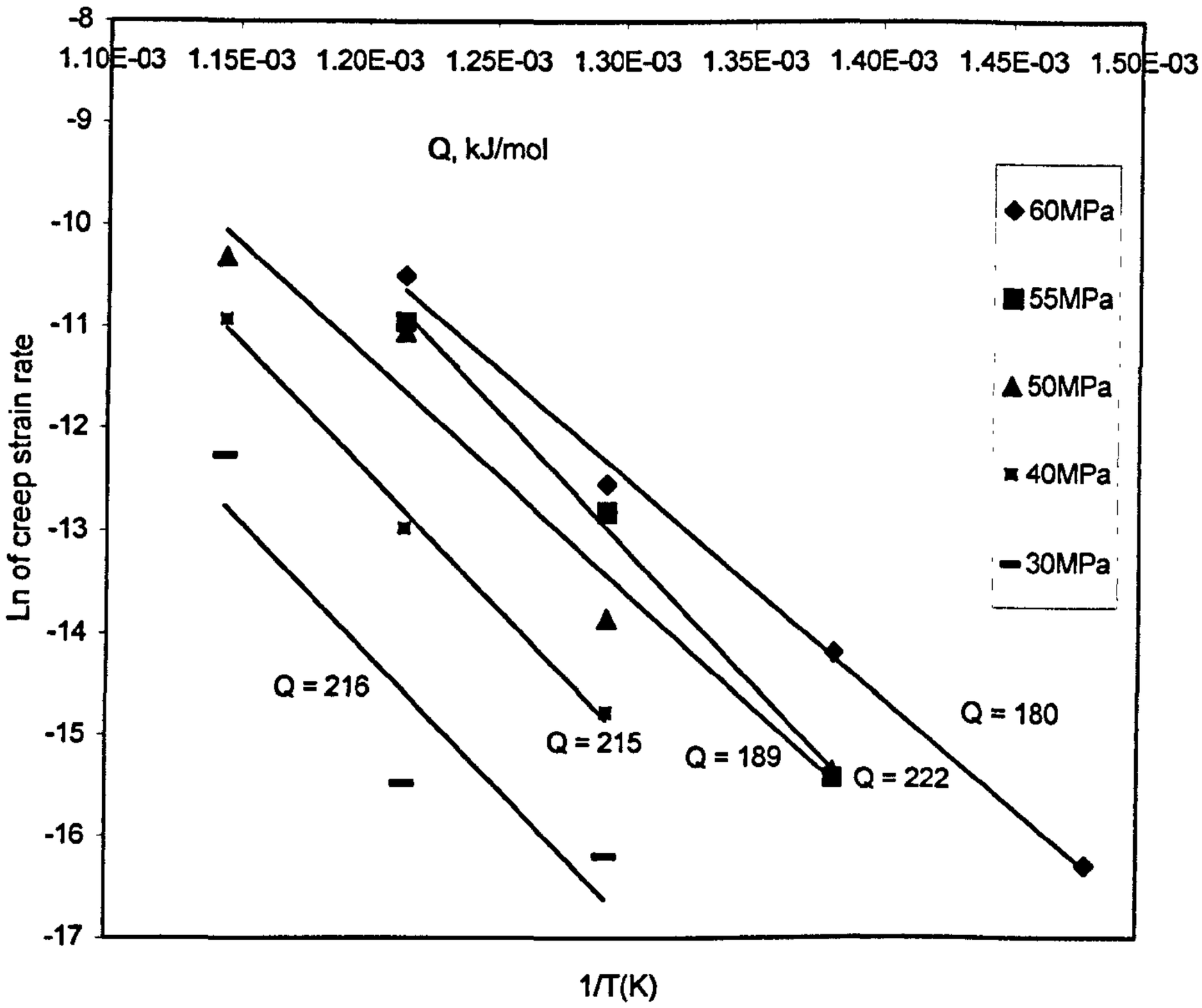

Figure 7.7 Graph of ln strain rate against 1/temperature for the composite tested in air

The activation energy for creep over the temperature and stress range of this investigation is nearly constant as shown by the lines of different stresses that are almost parallel to one another. Assuming that the small difference in these values is associated with normal scatter in the data, the average activation energy for the

composite is approximately 203 kJ/mol, which is close to that for lattice diffusion of Cu (197 kJ/mol) [14], again supporting the argument that the creep behaviour of the composite is dominated by the deformation of the matrix, and that continuum mechanics apply. The activation energy for the composite tested in vacuum are very similar to the composite tested in air as shown in figure 7.8.

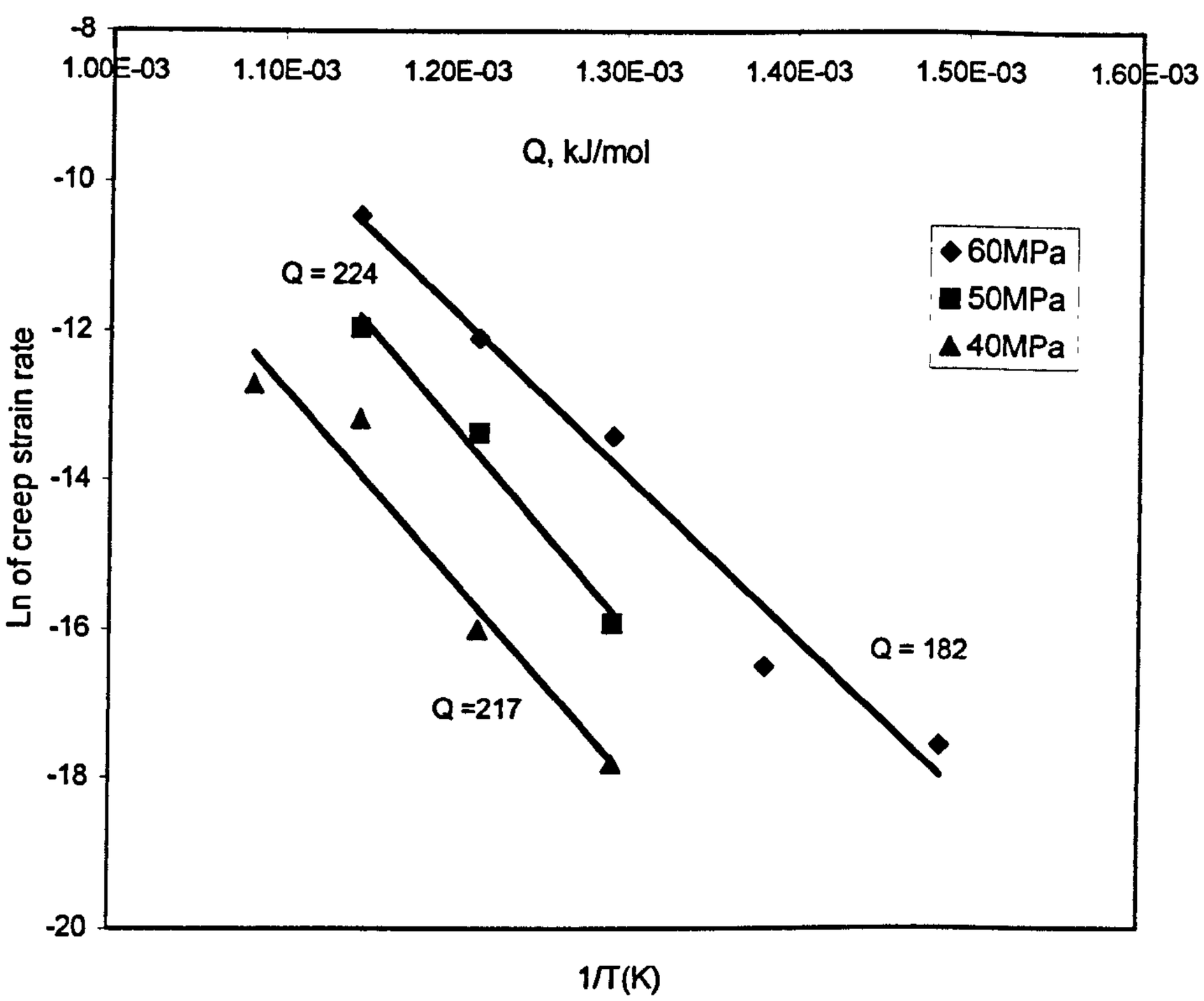

Figure 7.8 Graph of ln strain rate against 1/temperature for composite tested in vacuum

This shows that the nature of the rate controlling mechanism was not greatly affected by the oxidation. As will be discussed in the "Damage evolution and fracture" section, the oxide scale in the composite cracked and spalled as it thickened because of the volume expansion and did not affect the deformation mechanism. The interpretation of rate controlling mechanism(s) during creep is usually based on the activation energy and stress exponent. The observation that the stress exponent and the activation energy for creep of Cu-Cr composites at high temperatures in air and in

vacuum (≥ 400°C) are close to those of pure Cu suggests that the creep deformation of Cu-Cr composites is rate-controlled by climb of dislocations as in pure Cu. In the present study, Cr phases act as athermal obstacles and increase the athermal strengthening component, which would increase the creep resistance greatly. Since the creep deformation proceeds by overcoming thermal obstacles in the Cu matrix, the stress exponent and the activation energy are not appreciably modified by the presence of relatively big Cr fibres.

The similarity of the activation energy and the stress exponent of Cu-Cr composites at high temperatures to those of pure Cu suggest that the contribution of deformation of Cr fibre to the creep deformation is negligible. This suggests that the elongation of Cr fibres is not significant for high temperature creep, which is compatible with the observation of the similarity of creep activation energy and the stress exponent in Cu-Cr and pure Cu. At high temperatures, the misfit strain between the Cu and Cr during creep can be relieved by the dynamic recovery and recrystallization of Cu matrix. Similar behaviour was also observed in some Al alloy matrix composites reinforced with relatively big ceramic particles [16]. The deformation mechanism of Al matrix composites is controlled by the matrix microstructure and not greatly modified by the presence of big ceramic particles.

Many creep experiments [7,8,17-19] on MMCs have shown that the values of the apparent stress exponent and apparent activation energy are often exceptionally high and variable. These values provide little or no useful information on the nature of the rate controlling process during creep. When a threshold stress is incorporated into the analyses, these high values of true stress exponent and true activation energy are reduced to much lower values. These lower values are often similar in magnitude to those anticipated from the creep of pure metals.

7.5 Damage evolution and fracture

The effect of temperature on the failure strain of the composite is shown in figure 7.9. The fracture strain was not greatly affected by the environment in the tested temperature range. This observation may indicate that the overall failure mode is not greatly affected by the presence of oxide scale in Cu-Cr composites tested in air.

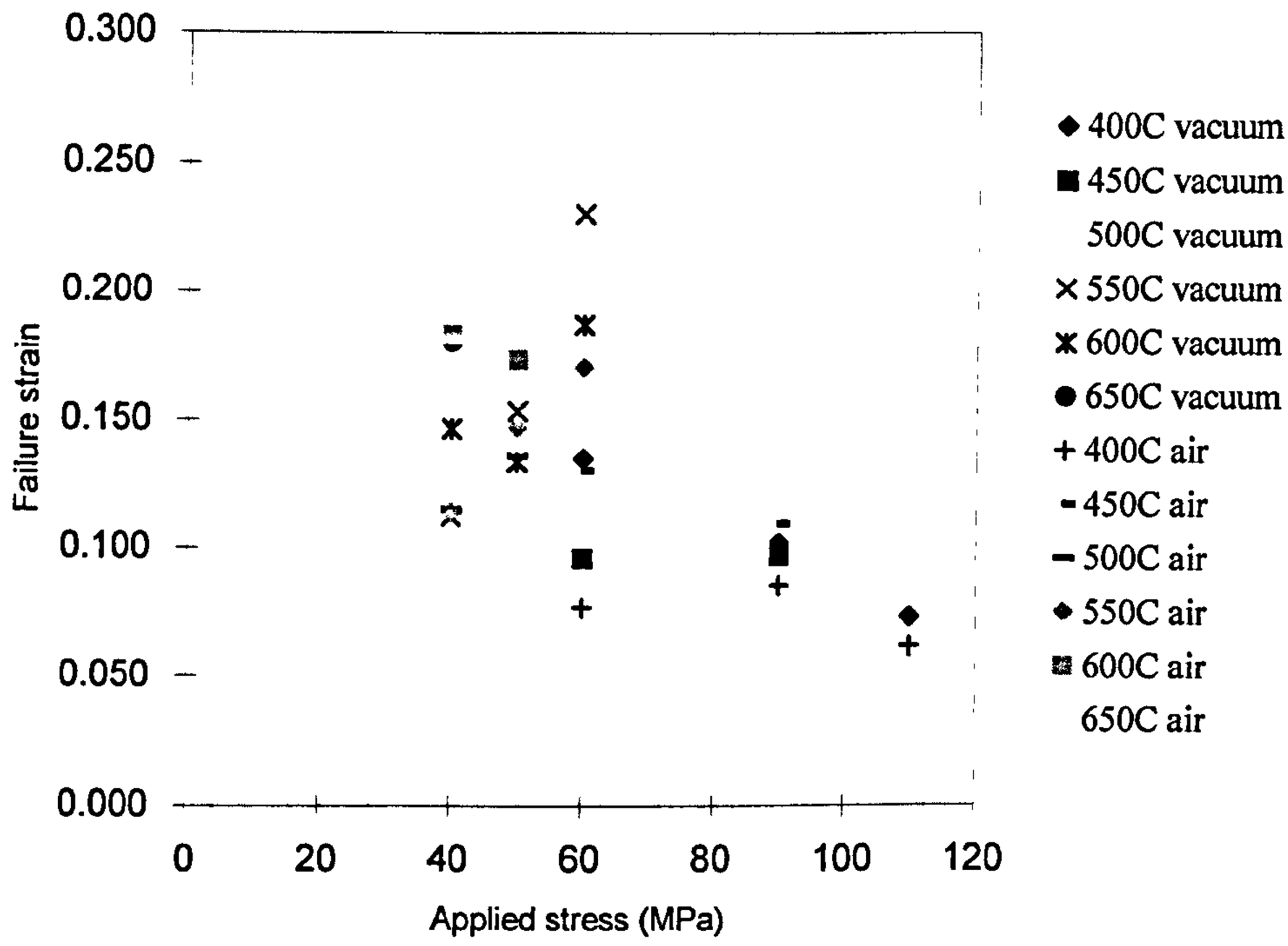

Figure 7.9 Effect of temperature on the failure strain of the composite

For each stress value, the failure strain has been found to increase with increasing temperature. This increase has been accompanied by an increase in the number of damage sites observed, as well as by an increase in the distance from the fracture surface at which damage is observed. This is presumably because of a greater extent of internal void growth before final failure.

The fracture surfaces of the crept samples were examined in the scanning electron microscope. No significant differences were found on the fracture surfaces

tested in air and vacuum at the investigated temperatures. One example is shown in figure 7.10 for a specimen tested at 600°C.

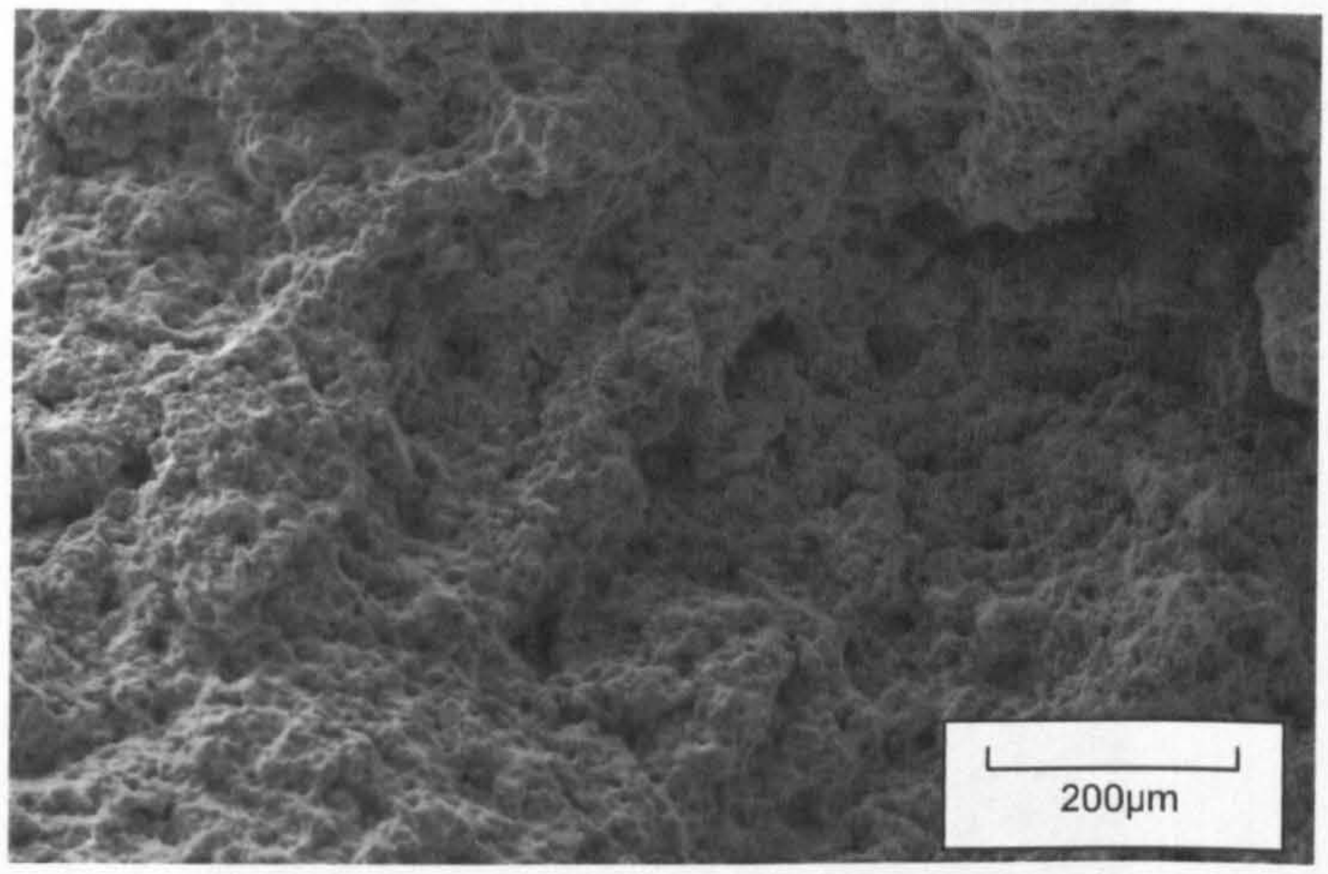

(a)

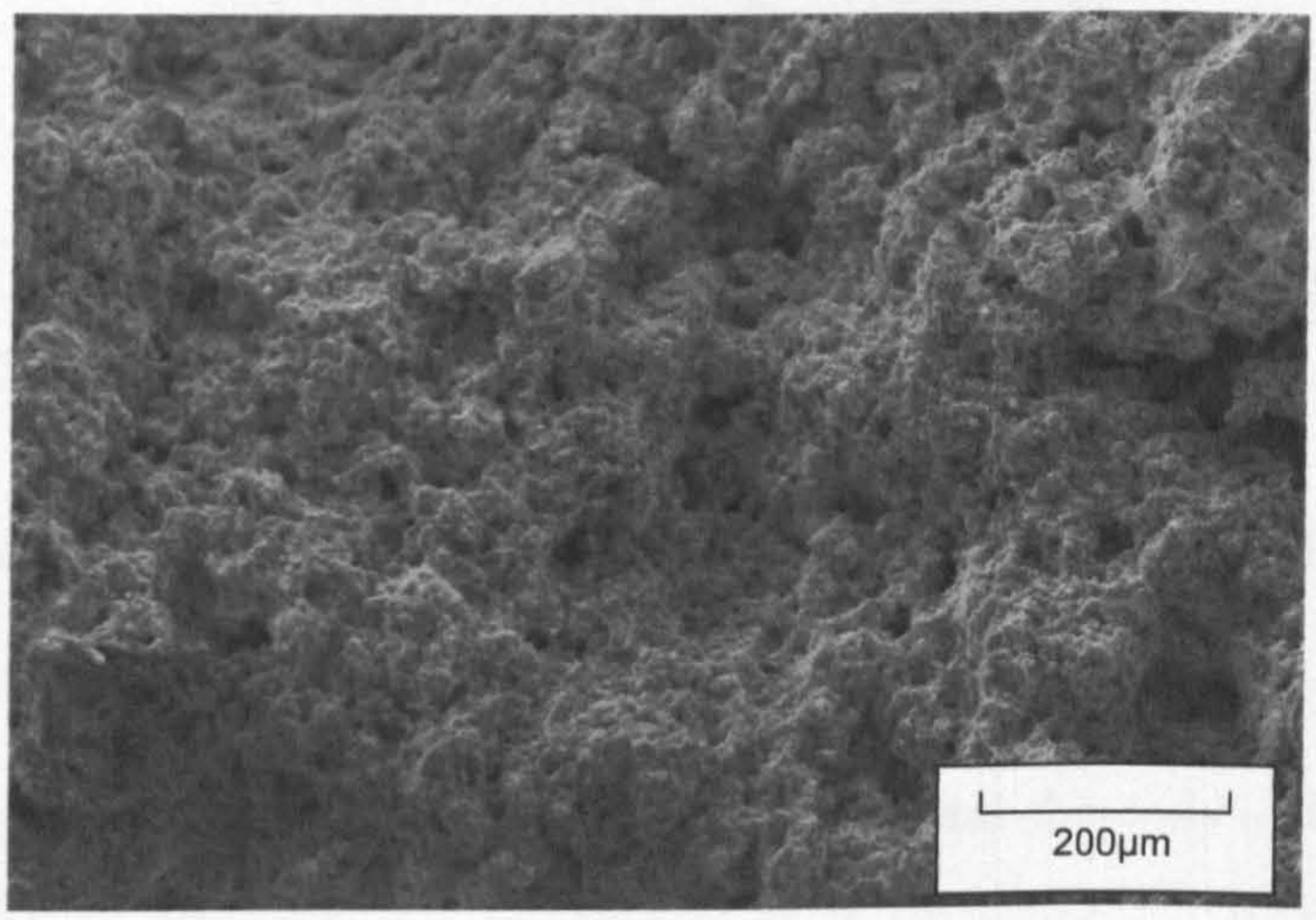

(b)

Figure 7.10 Appearance of fracture surface at 600°C using 50 MPa of applied stress (a) air and (b) vacuum

It is difficult to determine the damage mechanism because of the very fine characteristics of the microstructure and also the difficulty in distinguishing Cr fibres on the fracture surface. The examination of the longitudinal section of the crept samples usually reveals useful information on the creep mechanism that leads to failure during creep testing.

The pure Cu crept specimen at 400°C in air shows intergranular surface cracking as shown in figure 7.11.

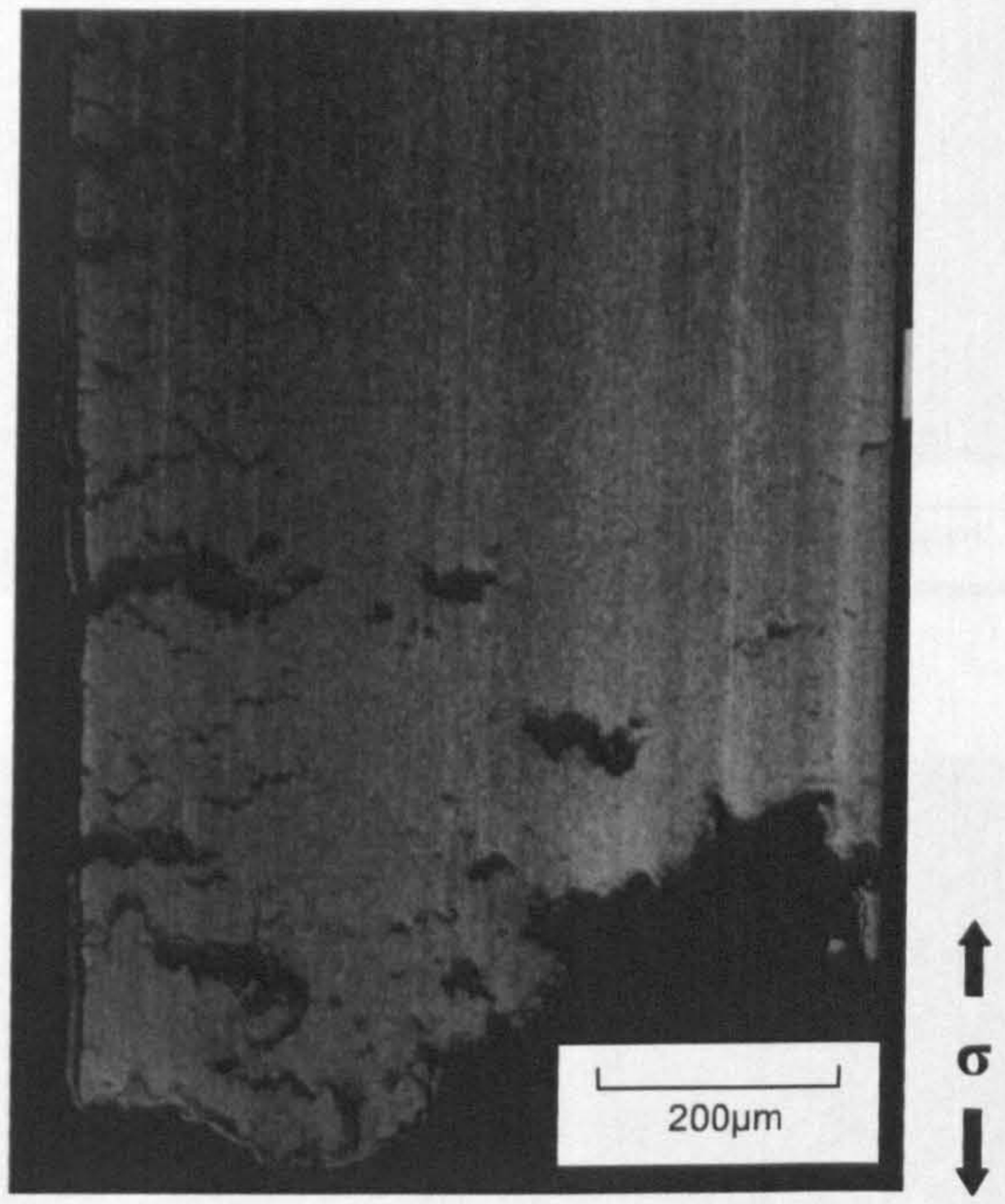

Figure 7.11 Longitudinal section of fracture surface for pure Cu tested at 400°C under an applied stress of 60 MPa

The mechanism of damage was found to be quite similar for all the creep tests performed, but the distribution and extent of damage was found to be very sensitive to the test temperature. Damage was primarily found near the ends of Cr fibres in the form of matrix cavitation. There was also some evidence of matrix cavitation at the interface between the Cu matrix and the reinforcement. The micrographs shown in figure 7.12 were taken from a specimen tested in air at 300°C. The level of damage was found to increase as the temperature increases. The microstructures of the creep ruptured specimens are very similar to those observed on tension tested specimens. At temperatures up to 300°C, microstructural observation of longitudinal sections of the creep specimens immediately beneath the fracture surface revealed that the damage in the composite was fairly localized. The rather short tertiary stage is consistent with the observation that damage accumulation was not extensive.

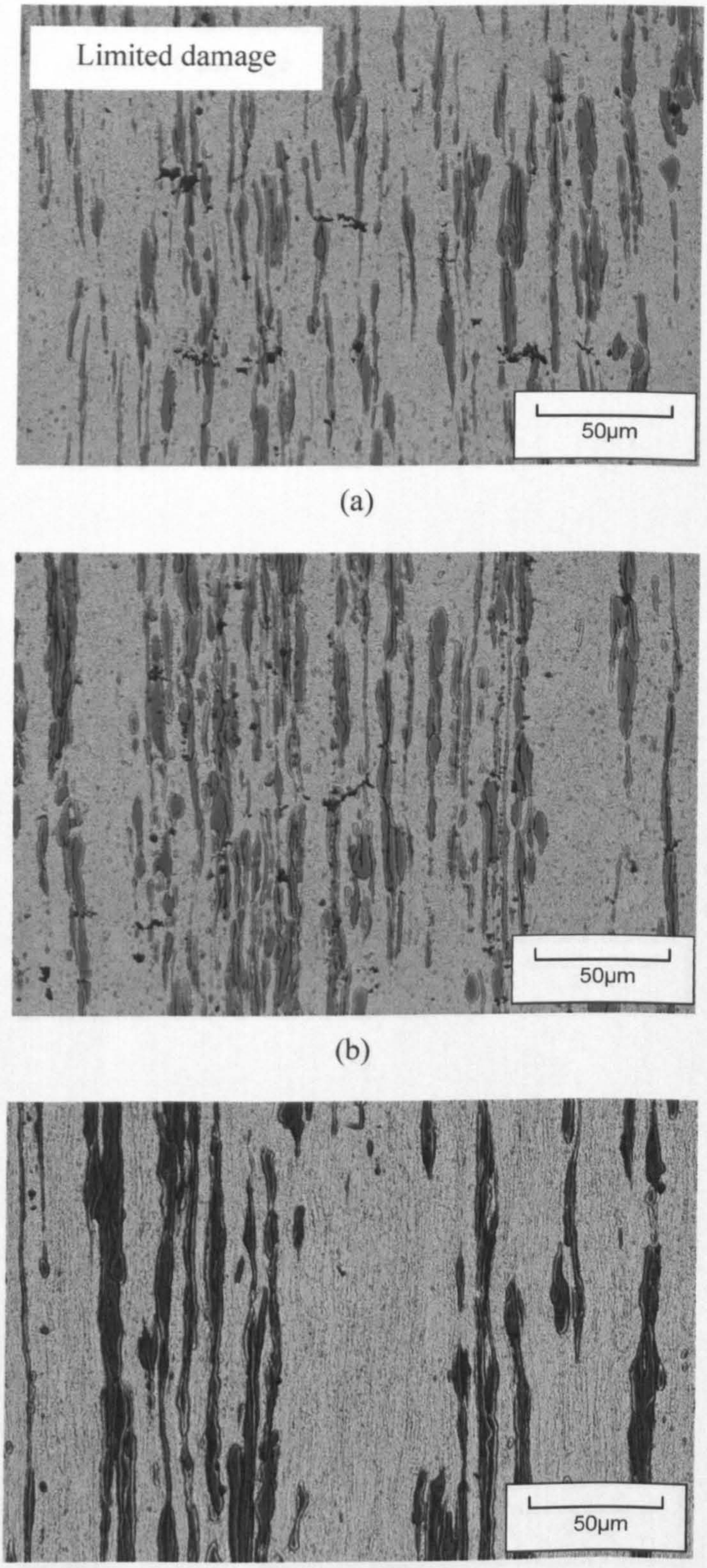

Figure 7.12 Typical micrographs taken from (a) near the fracture surface and (b) intermediate distance from the fracture surface (c) far from the fracture surface for a specimen tested at 300°C under an applied stress of 160 MPa in air

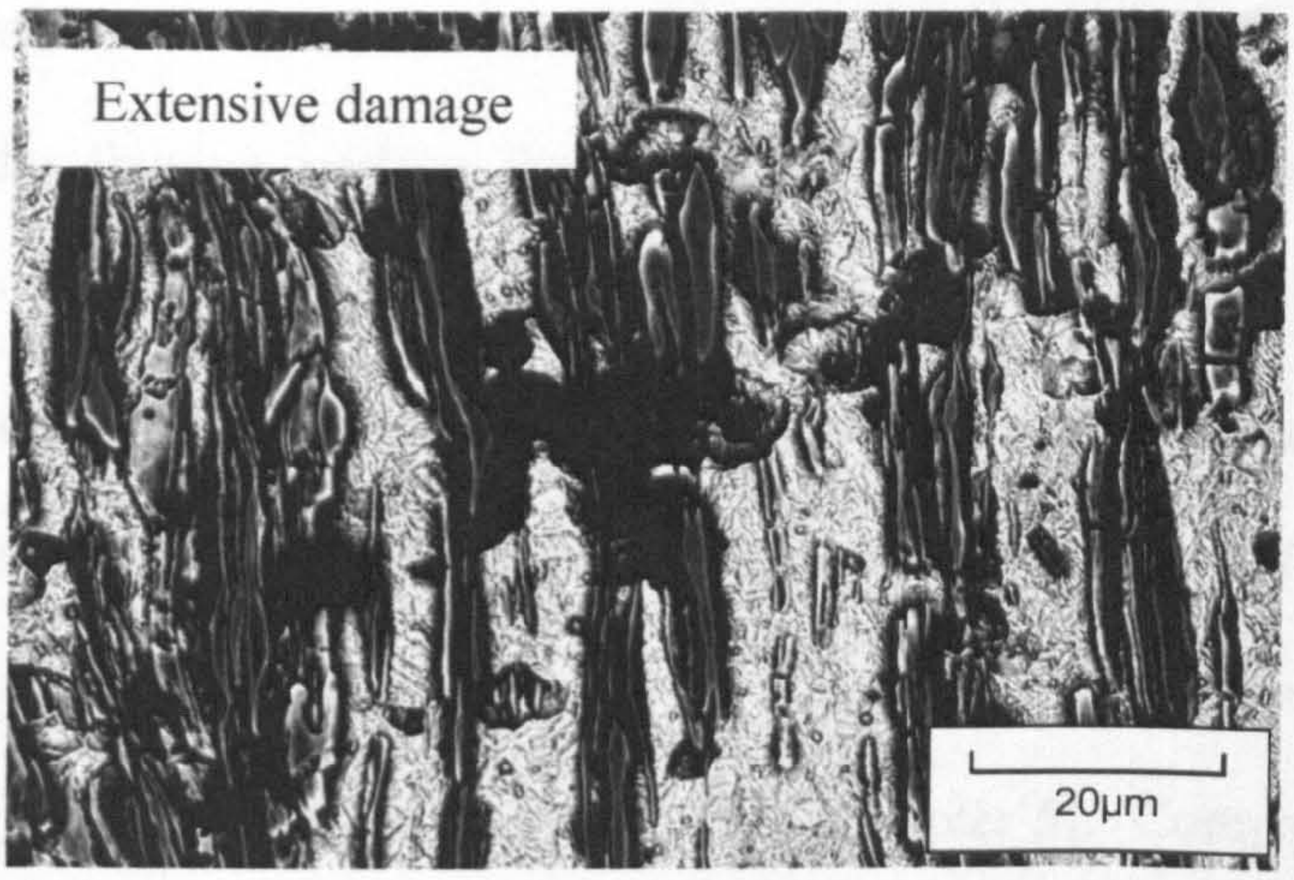

(a)

(b)

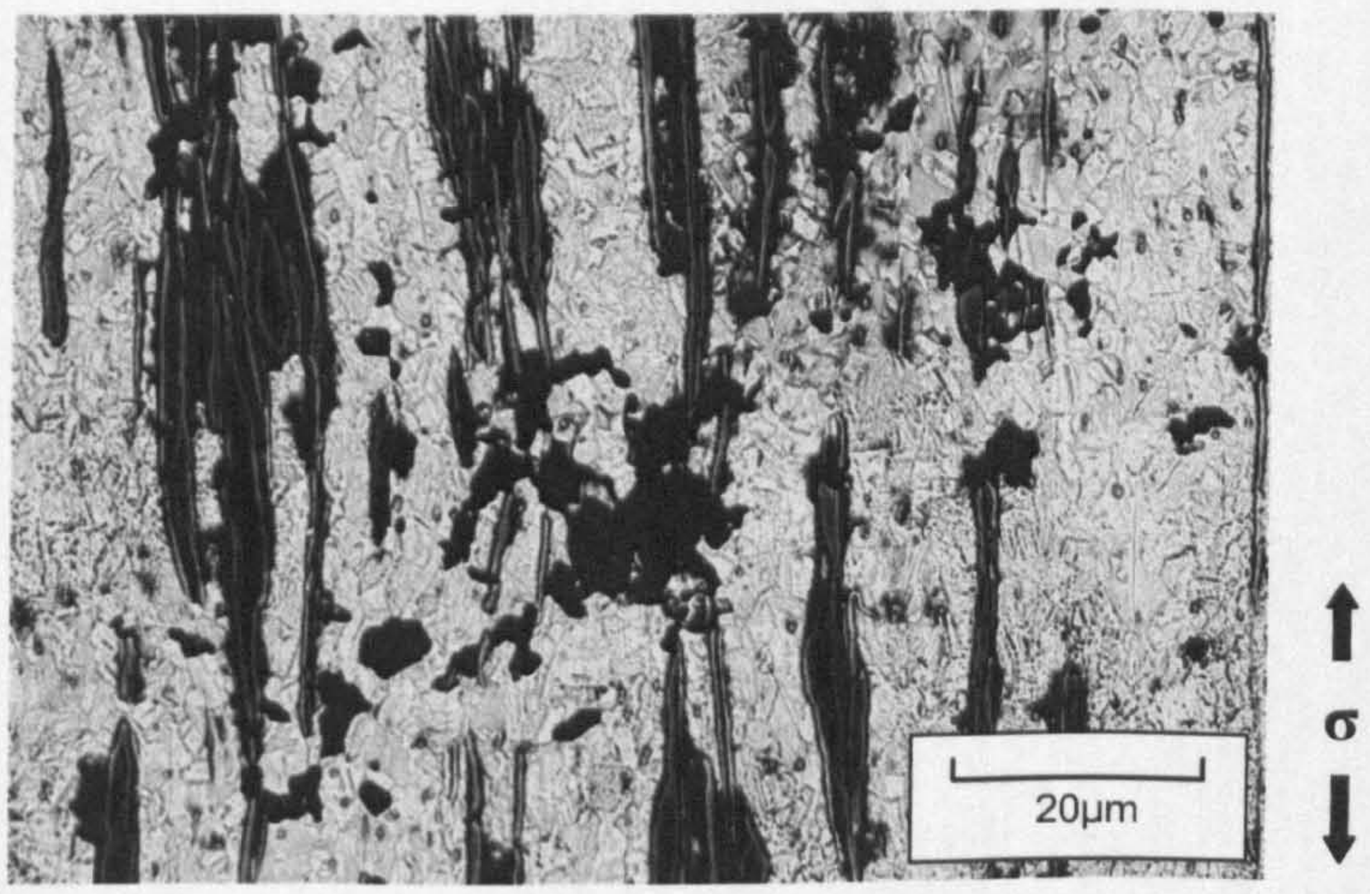

(c)

Figure 7.13 Typical micrographs taken from (a) near the fracture surface and (b) intermediate distance from the fracture surface (c) far from the fracture surface for a specimen tested at 400°C under an applied stress of 110 MPa in air

However, for the specimen tested at 400°C in air, the amount of damage was greater near the fracture surface than at 300°C but was also found to extend throughout the gauge section as shown in figure 7.13. This behaviour was also observed in composites tested in vacuum at the same temperature as shown in figure 7.14. Therefore, increasing the testing temperature from 300°C to 400°C results in a change in the distribution of damage in the composite. This behaviour was also consistent with the high temperature tensile tests [Chapter 5]. Comparing the extent of damage observed under creep and tensile deformation shows that the creep specimens exhibit a higher level of damage both in air and in vacuum than material subjected to tensile testing. This shows that under similar testing condition (same temperature), more voids are allowed to nucleate and grow, without immediately leading to failure, during creep than during tensile tests. This is consistent with the higher strains at failure seen during creep deformation vis-à-vis tensile testing. The higher ductility in creep is thought to be due to low strain rate deformation, which allows more extensive strain from diffusion-controlled damage processes such as void formation.

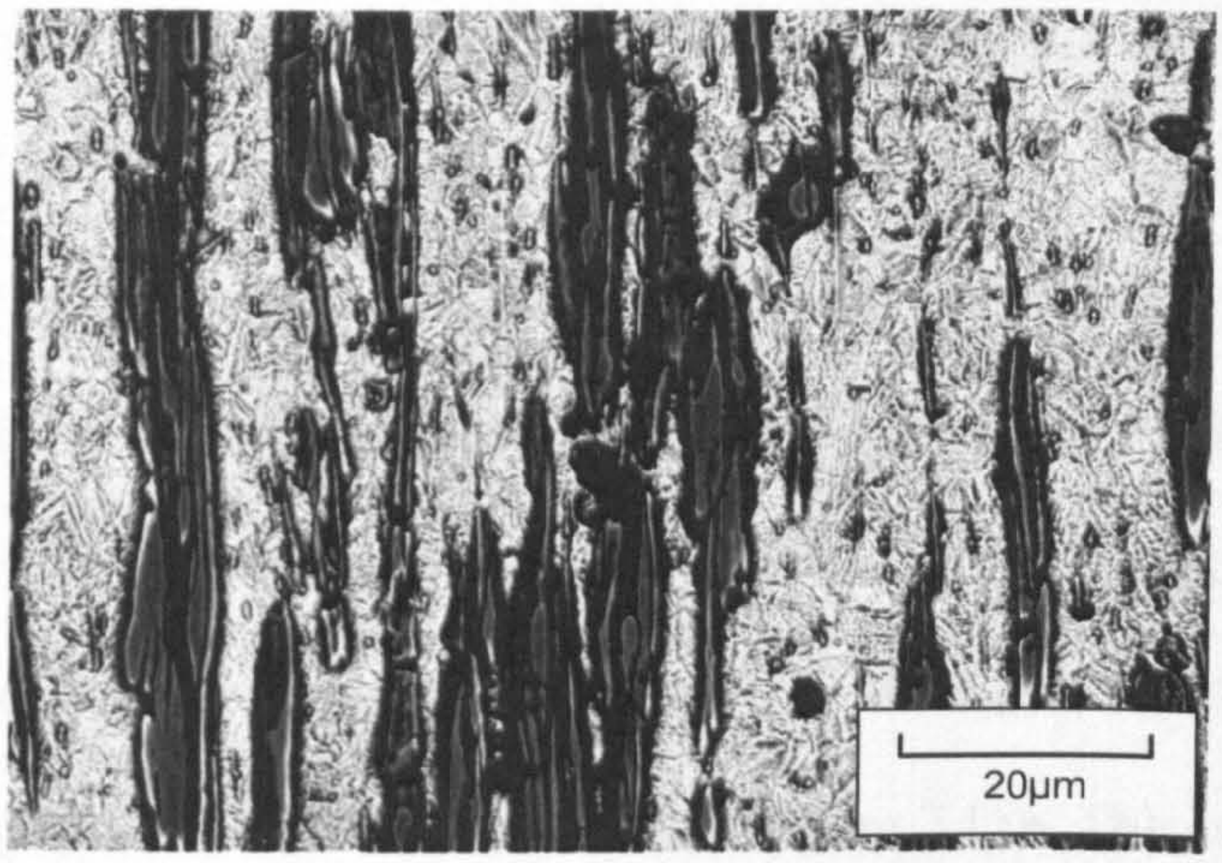

(a)

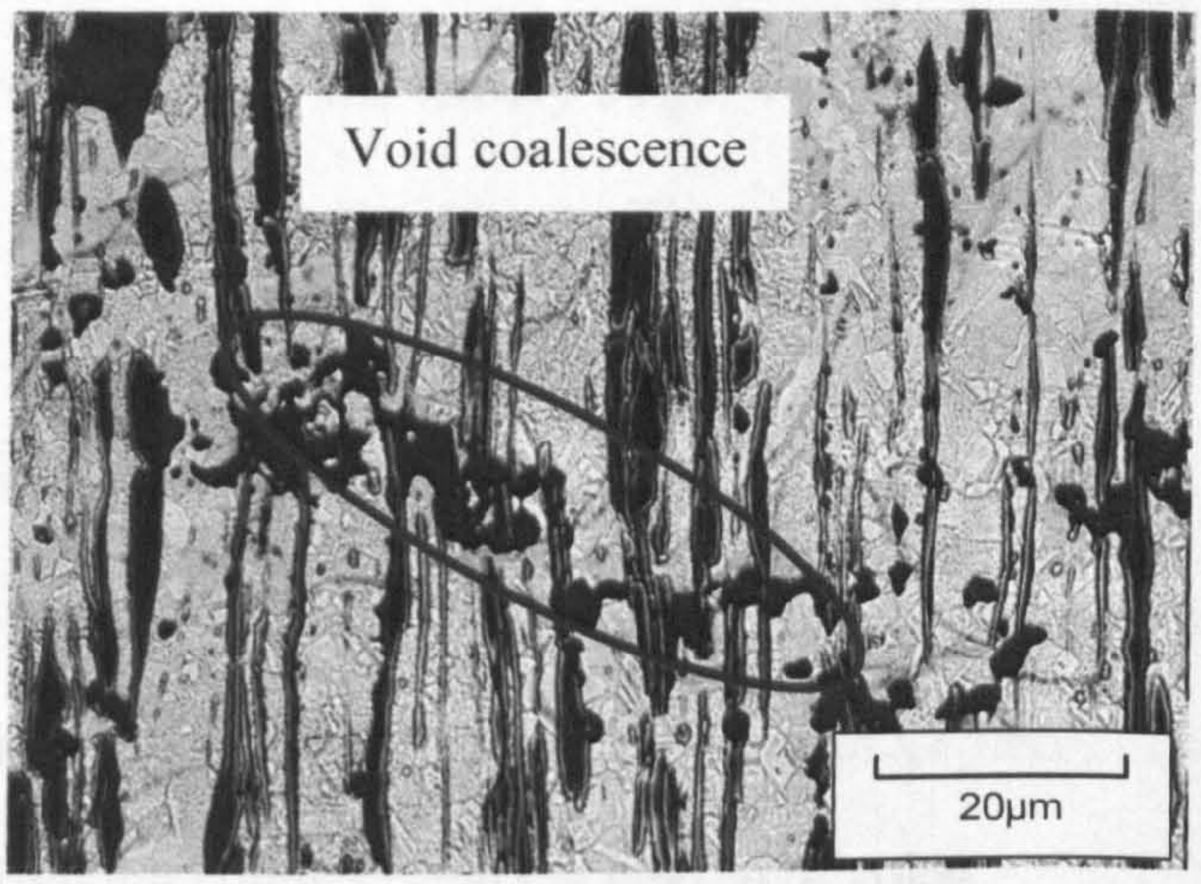

(b)

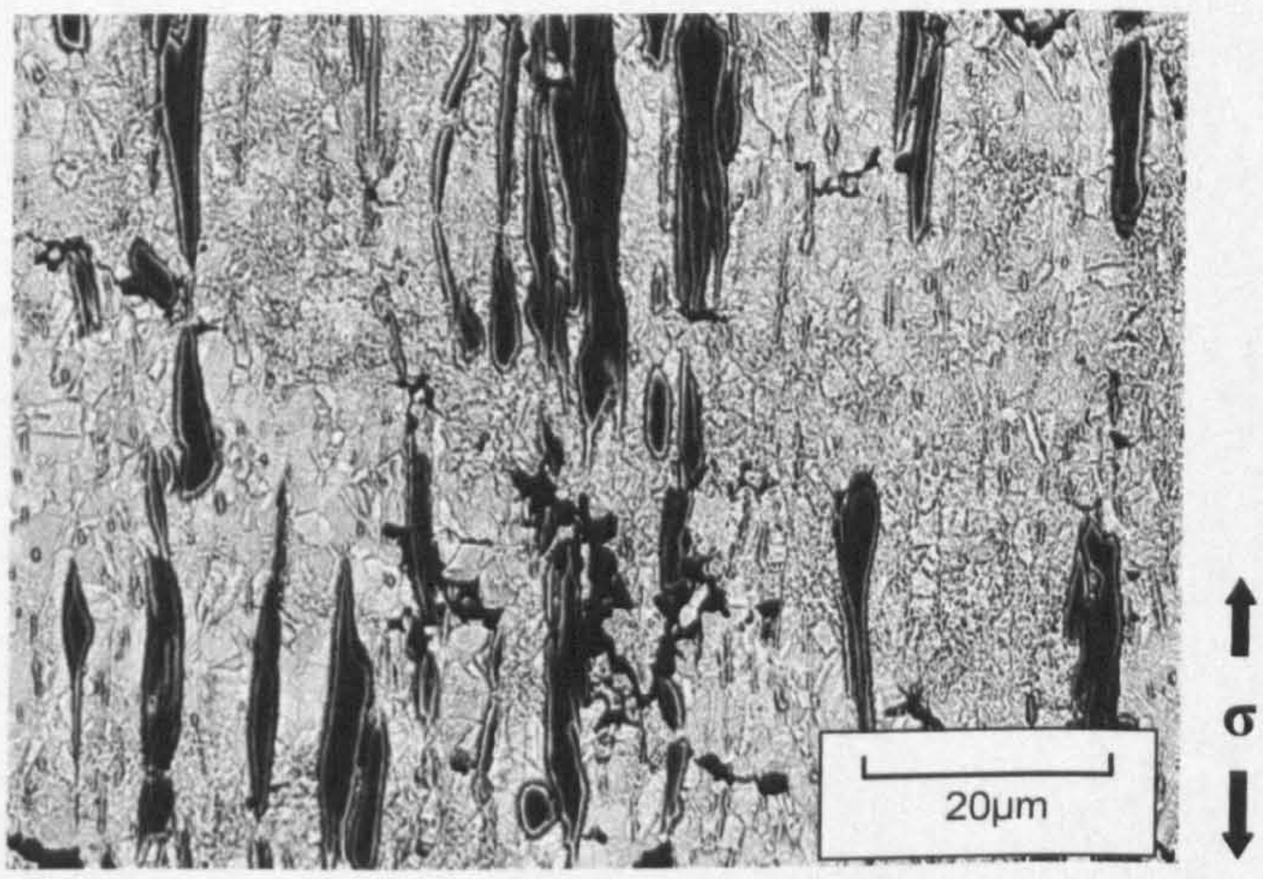

(c)

Figure 7.14 Typical micrographs taken from (a) near the fracture surface and (b) intermediate distance from the fracture surface (c) far from the fracture surface for a specimen tested at 400°C under an applied stress of 110 MPa in vacuum

The creep fracture of the composite was preceded by a coalescence of voids initiated mostly at the Cu-Cr interfaces; this fracture process is schematically shown in figure 7.15. According to the numerical analysis of stress distribution in composites [20], the stress concentrates at interfaces normal to the loading axis, and those interfaces are the preferred sites for void nucleation. Since this composite includes a considerably large area of interface, thus the composite is more likely to nucleate the cavities at the interfaces as shown in figure 7.15b. This was shown by the microstructure image in figure 7.16. This image was taken from a specimen interrupted before the start of the tertiary stage. Voids can clearly be seen at the tips of the Cr fibres, as shown by the arrows. The growth and link up of the nucleated voids lead to the failure of the composite. Figure 7.17 shows the longitudinal section of the fractured specimen at 500°C tested in air. The fibre pull-out is readily visible on the fracture surface. A close examination of figure 7.13c suggests that the fibre pull-out results from void formation around the tips of Cr fibres. The fractured fibres appear to result from the failure during the link-up of voids.

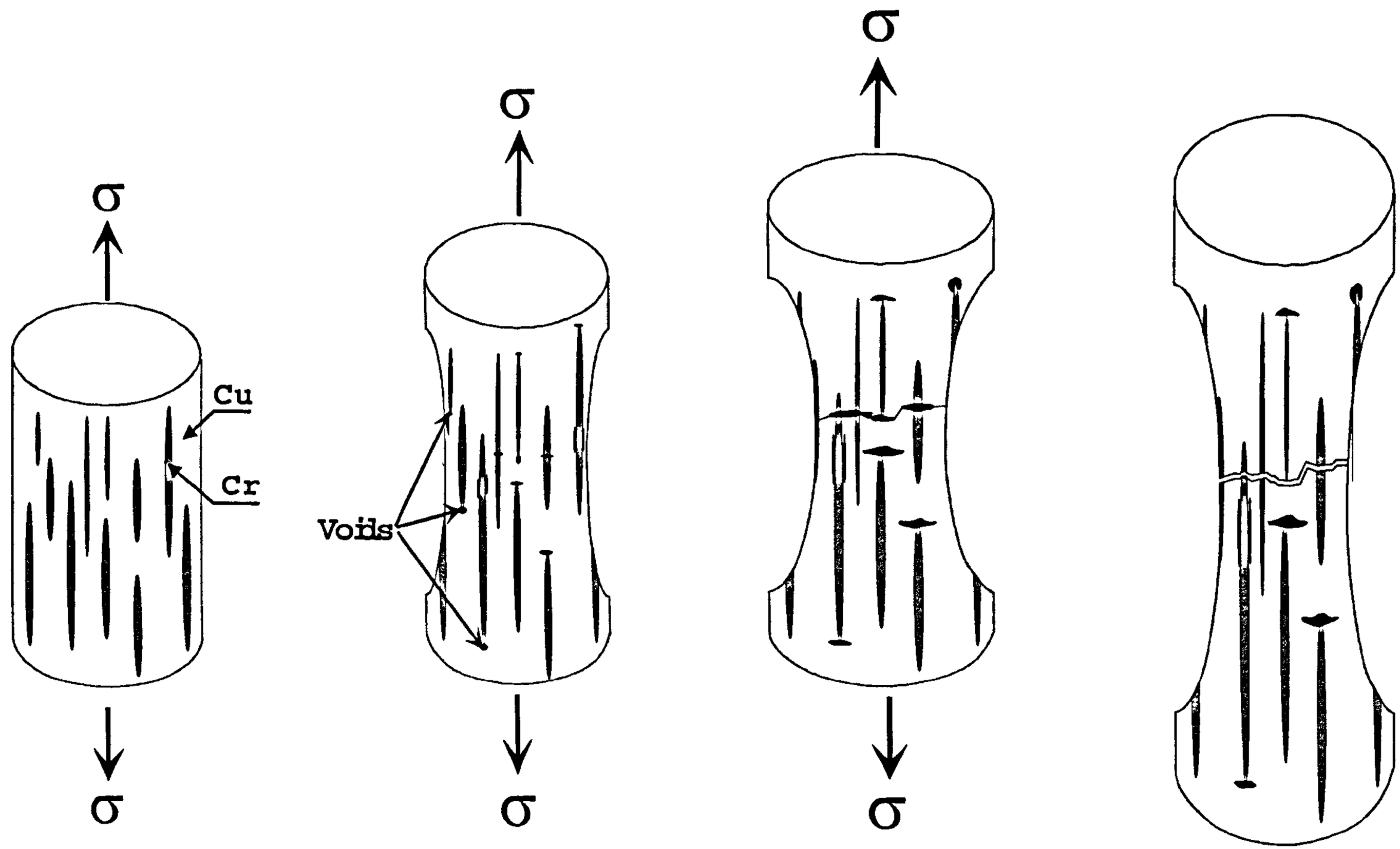

(a) (b) (c) (d)

Figure 7.15 Schematic diagram of creep fracture process of the composite (a) Initial stage (b) Nucleation of void (c) Growth and coalescence of voids (d) Failure of composite

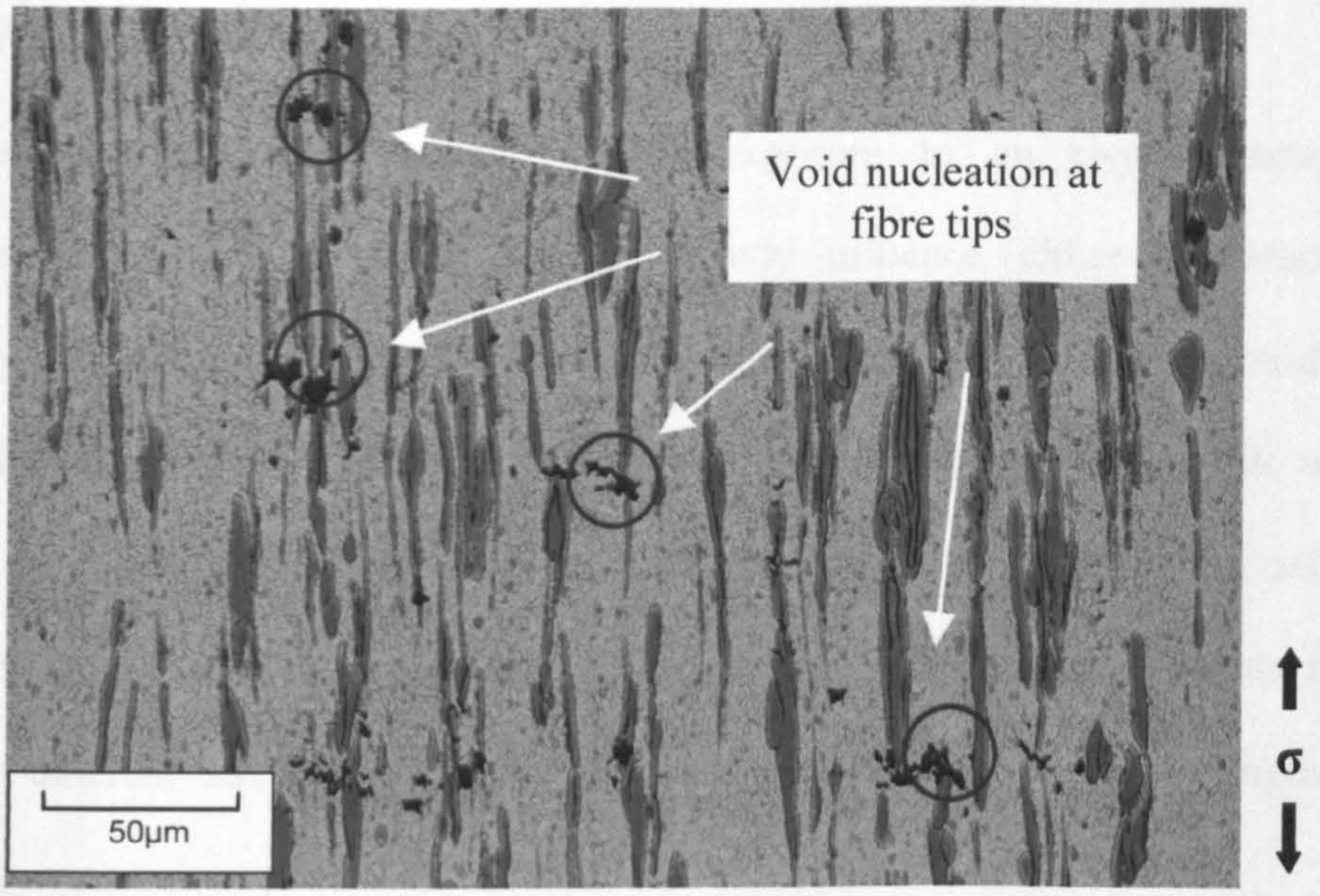

Figure 7.16 Microstructure showing void nucleation at the tip of the Cr fibres from an interrupted creep test before the start of the tertiary stage at 400°C under an applied stress of 90 MPa for composite tested in air

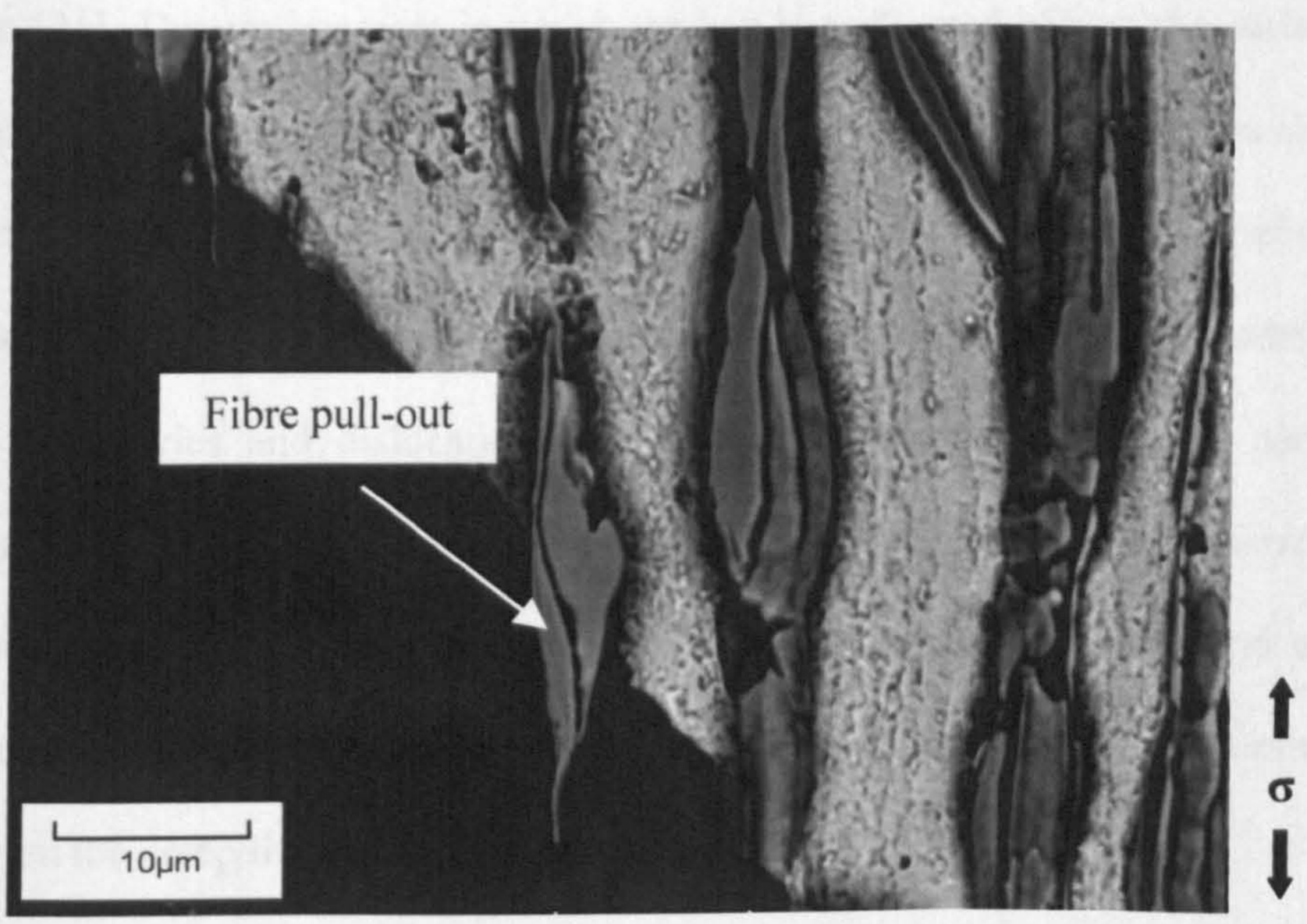

Figure 7.17 Micrograph showing typical fibre pull-out

7.6 Effect of the environment on creep behaviour

It has long been recognized that exposure to an oxygen-containing environment during creep testing can significantly influence (either beneficially or adversely), the creep properties of metals and alloys [21]. When creep and oxidation occur simultaneously, it becomes difficult to unambiguously distinguish which changes are attributable to oxidation and which to fracture [21]. When the oxide is strong and firmly adherent to the metal, it can improve creep strength, but if the oxide had low inherent strength or spalls away from the surface, creep strength can decrease.

Stresses that develop during scale growth at high temperature can lead to scale fracture, buckling, and spallation, subjecting the underlying metal to renewed oxidation [21]. The environment in which the test is performed affects the surface of the composite. It is well known that Cu is inclined to easy oxidation, and its surface should be quickly covered by an oxide layer when exposed to air at elevated temperature. Diffusion of oxygen in Cu, especially along high diffusivity paths such as grain boundaries and dislocations, can result in formation of oxide particles decorating these paths. For example such particles could influence the deformation and damage process by acting as nucleation sites for microcrack formation at the grain boundaries. Growth of these cracks could increase the tertiary creep rate and thus shorten the creep life.

The oxidation behaviour of pure Cu and Cu-Cr composites between 400-600°C, without any applied stress, has been investigated in collaboration with University of Oslo. Figure 7.18 shows the weight gain during oxidation of the pure Cu and Cu-Cr composites, as a function of time at 500°C and 600°C.

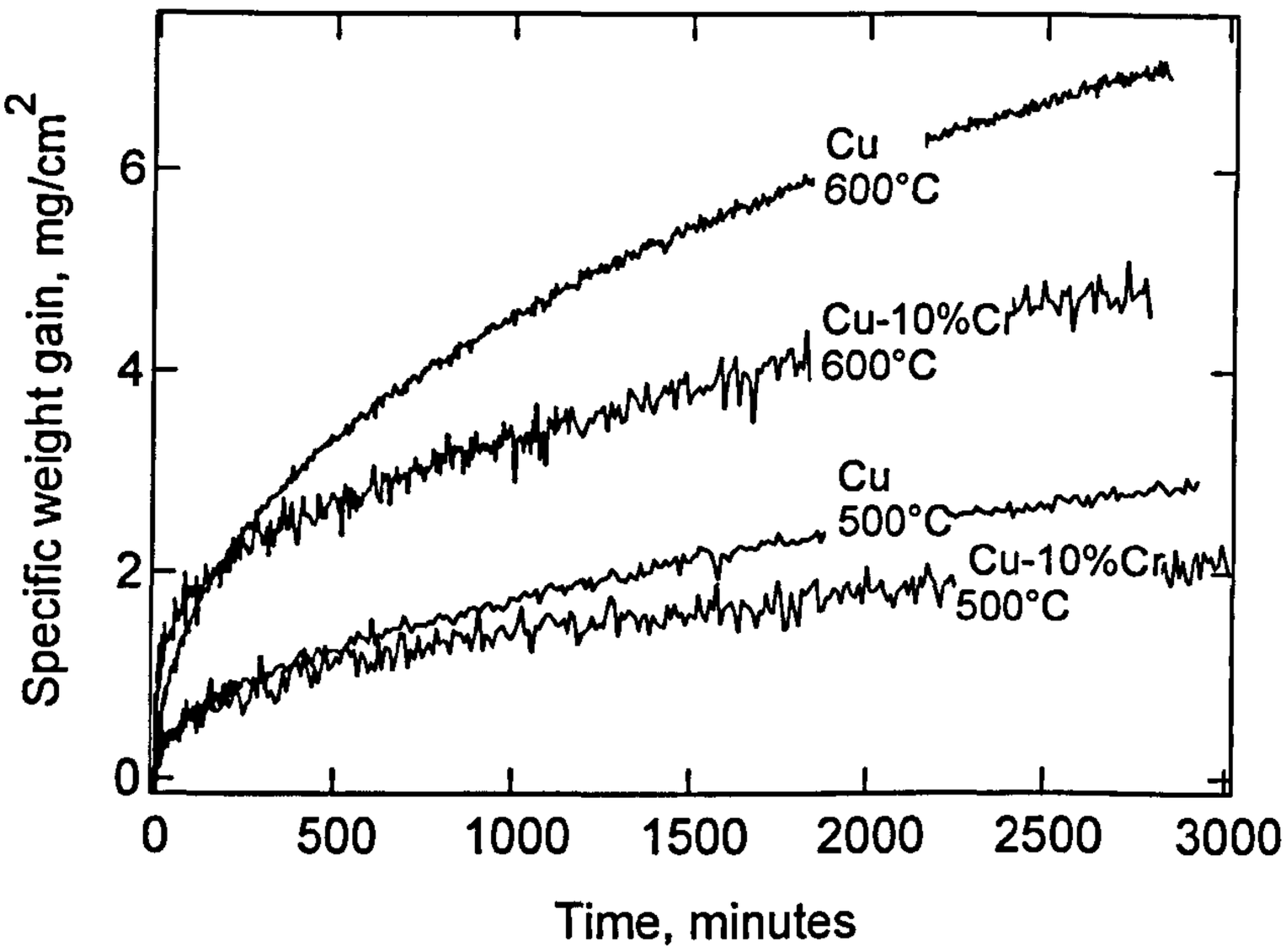

Figure 7.18 Weight gain during oxidation for pure Cu and Cu-Cr composites at 500°C and 600°C

Comparison of the rates at 500°C and 600°C showed the rate of oxidation of the composite was slower than that of Cu. It can be seen that the oxidation kinetics were essentially parabolic for the composite. This indicates that the scale growth is governed by diffusion of one of the reactants through the scale [22]. High temperature diffusional growth of Cu oxides is predominated by outward diffusion of Cu through Cu_2O [22]. The oxidation of Cu_2O into CuO is slow and as long as there is a continuous flux of CuO through the Cu_2O scale, only a relatively thin, outer fraction of the scale consists of CuO. The slower oxidation rates observed for the Cu-Cr composites, compared to those of Cu were due to the Cr fibres blocking a fraction of the diffusion cross-section through the Cu_2O scale [22]. It was also found that the Cu-Cr composites oxidized in Ar containing 10ppm O_2 was about 2 orders of magnitude lower than for the specimen oxidized in air, as shown in figure 7.19. These differences are due to the variations in the protective ability of the Cu oxides. It was

also found that the oxide scales formed under vacuum are thinner than those formed in air [22].

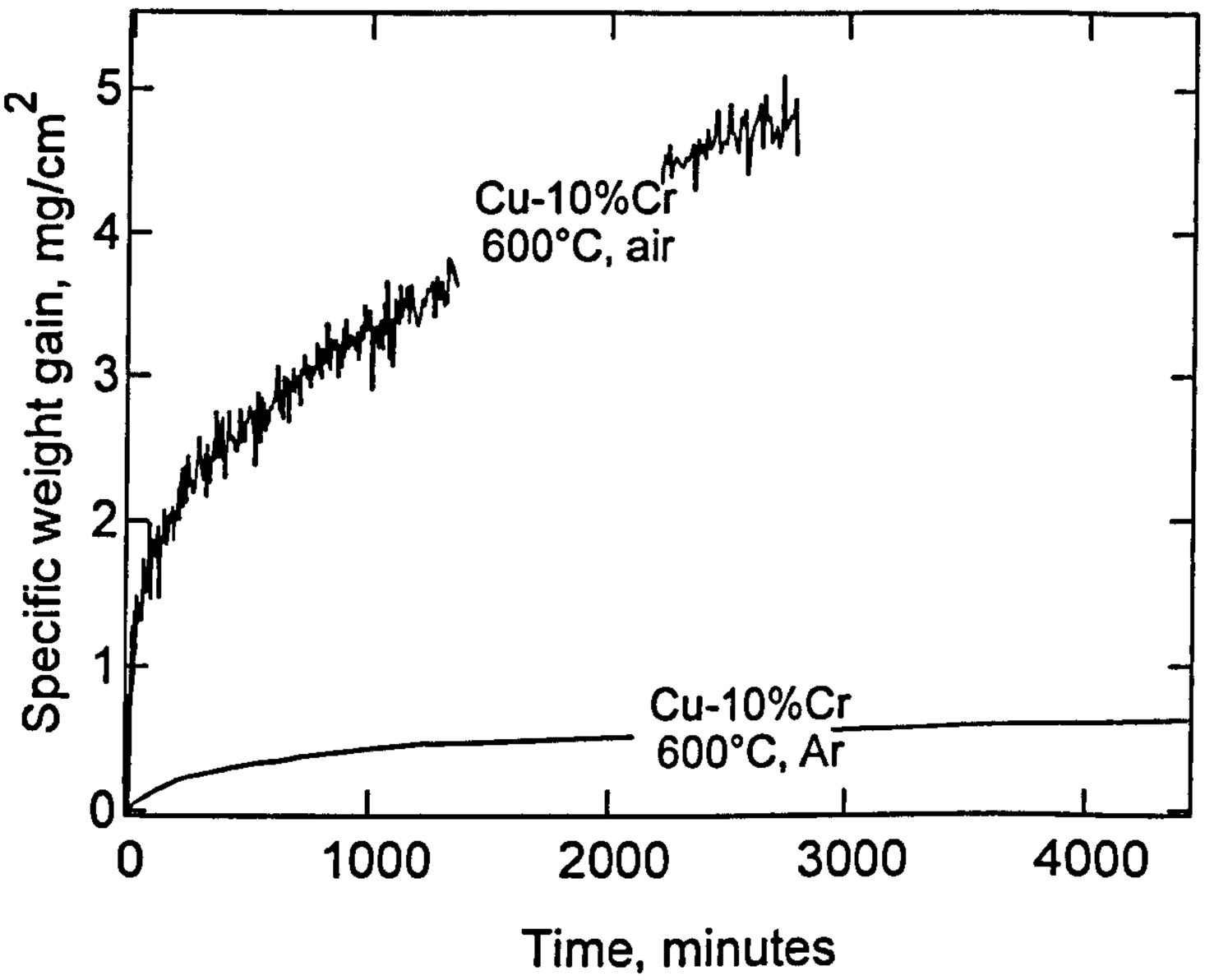

Figure 7.19 Weight gain during oxidation for the composite in air and in Ar containing 10ppm O_2 at 600°C

In this study, a detailed analysis at the surface of the composite tested at 400°C in air showed the presence of surface cracking while the specimen tested in vacuum showed a smooth edge (figure 7.20). It has been observed by Ohnami et al. [23] that a nonprotective film of CuO was preferentially formed in air, and it is easily cracked and spalled, whereas a more protective scale of Cu_2O was formed under high vacuum conditions.

A careful observation of the sub-surface oxide scale revealed that the oxide cracks did not penetrate into the matrix because the oxide scale usually flaked off and spalled (figure 7.20a) in Cu-Cr composites. It appears that the boundary between the matrix and the oxide scale is sharp and clear. Since the subgrains (and grains) and Cr fibres are heavily elongated along the swaging direction (parallel to the surface in figure 7.20), the easy diffusion paths into the matrix such as the grain boundary and

interface boundary are quite limited and almost parallel to the surface. Therefore, the direct effect of oxygen on the deformation and the damage in the matrix is likely to be quite limited.

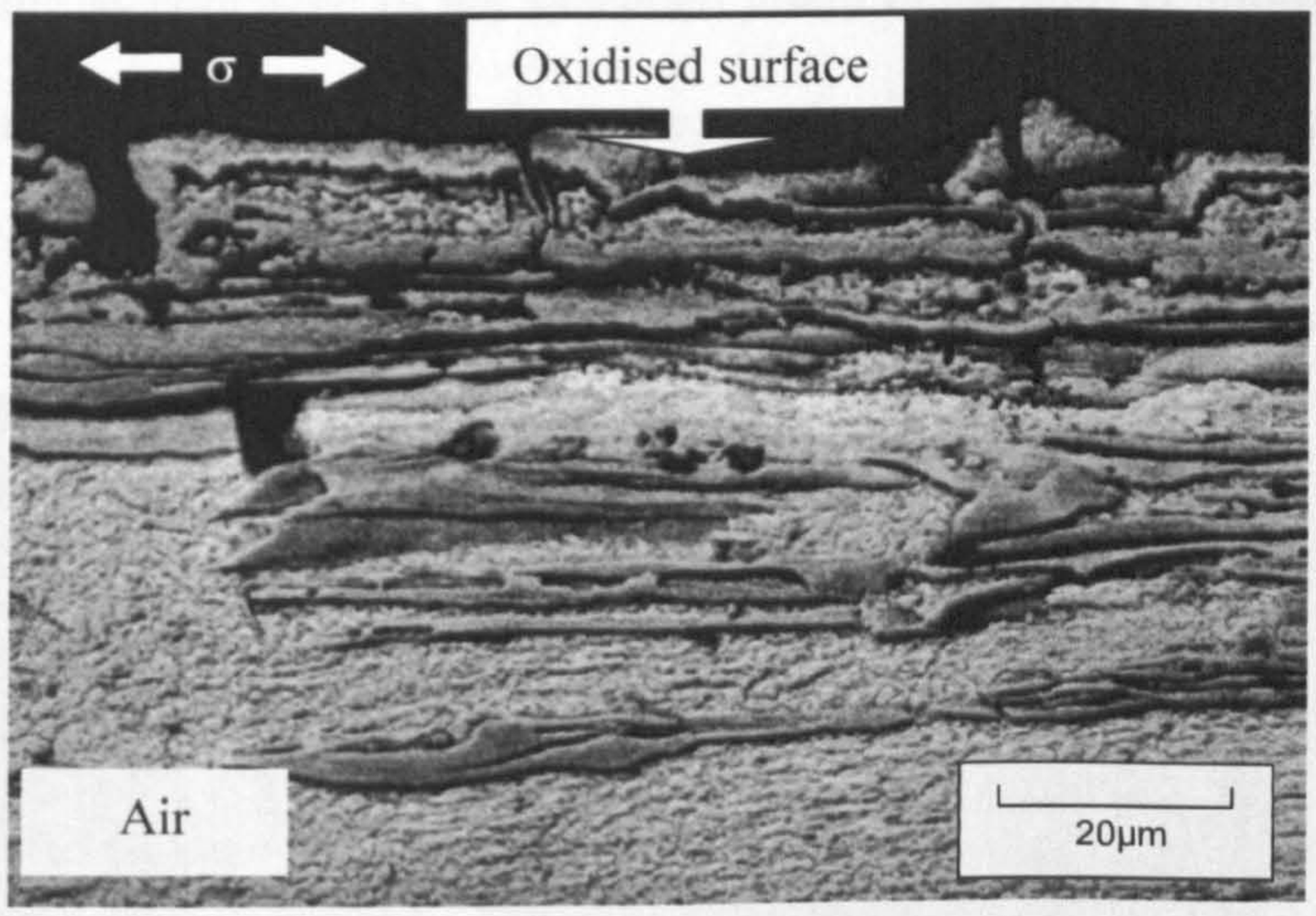

(a)

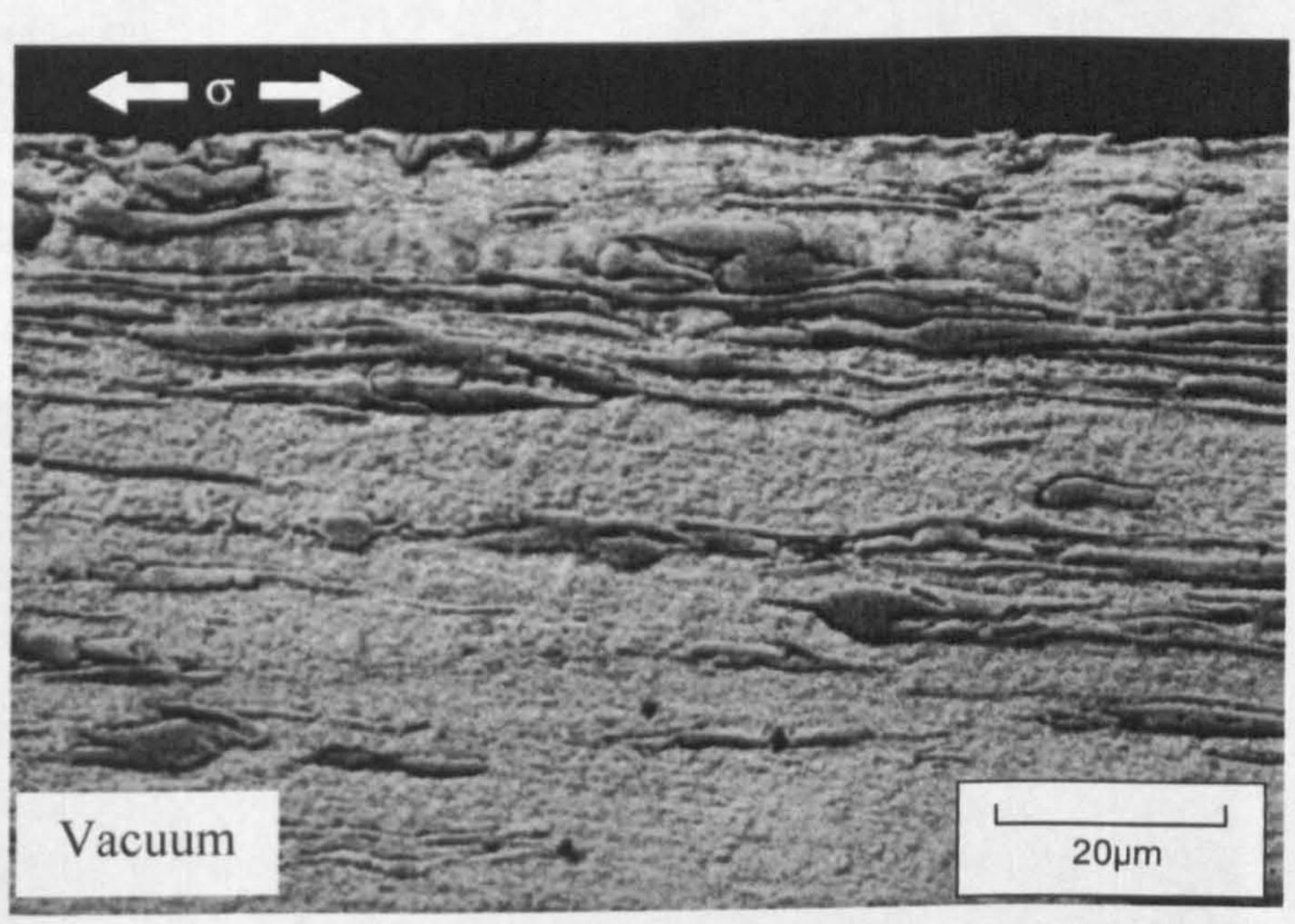

(b)

Figure 7.20 Edge of the composite tested at 400˚C using 110 MPa in (a) air and (b) vacuum

At 600˚C, the damage in the specimen tested in air was much greater than at 400˚C, and the amount of damage increased at 600˚C in the region farther from the fracture surface. While the incidence of damage also increases in specimens tested in

vacuum at 600°C, it is less than the specimen tested in air. No preferential oxidation along the Cr fibres was observed at any of the test temperatures. Microstructural observations conducted at the specimen deformed in air at 600°C, revealed extensive surface cracking as compared to the specimen tested in vacuum as shown in figure 7.21. The energy spectra of the edge from the sample tested in air indicate a dominant presence of Cu oxide.

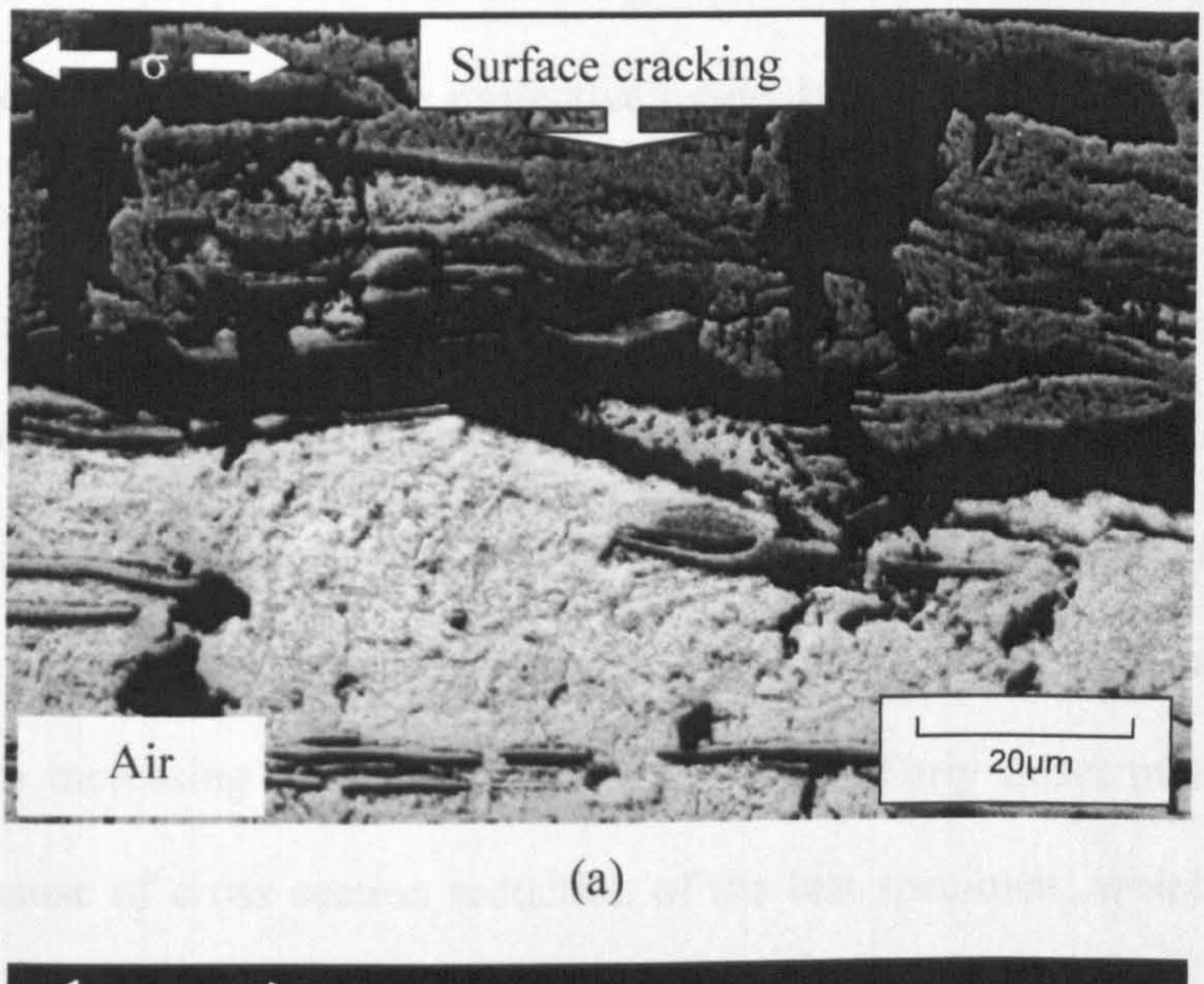

(a)

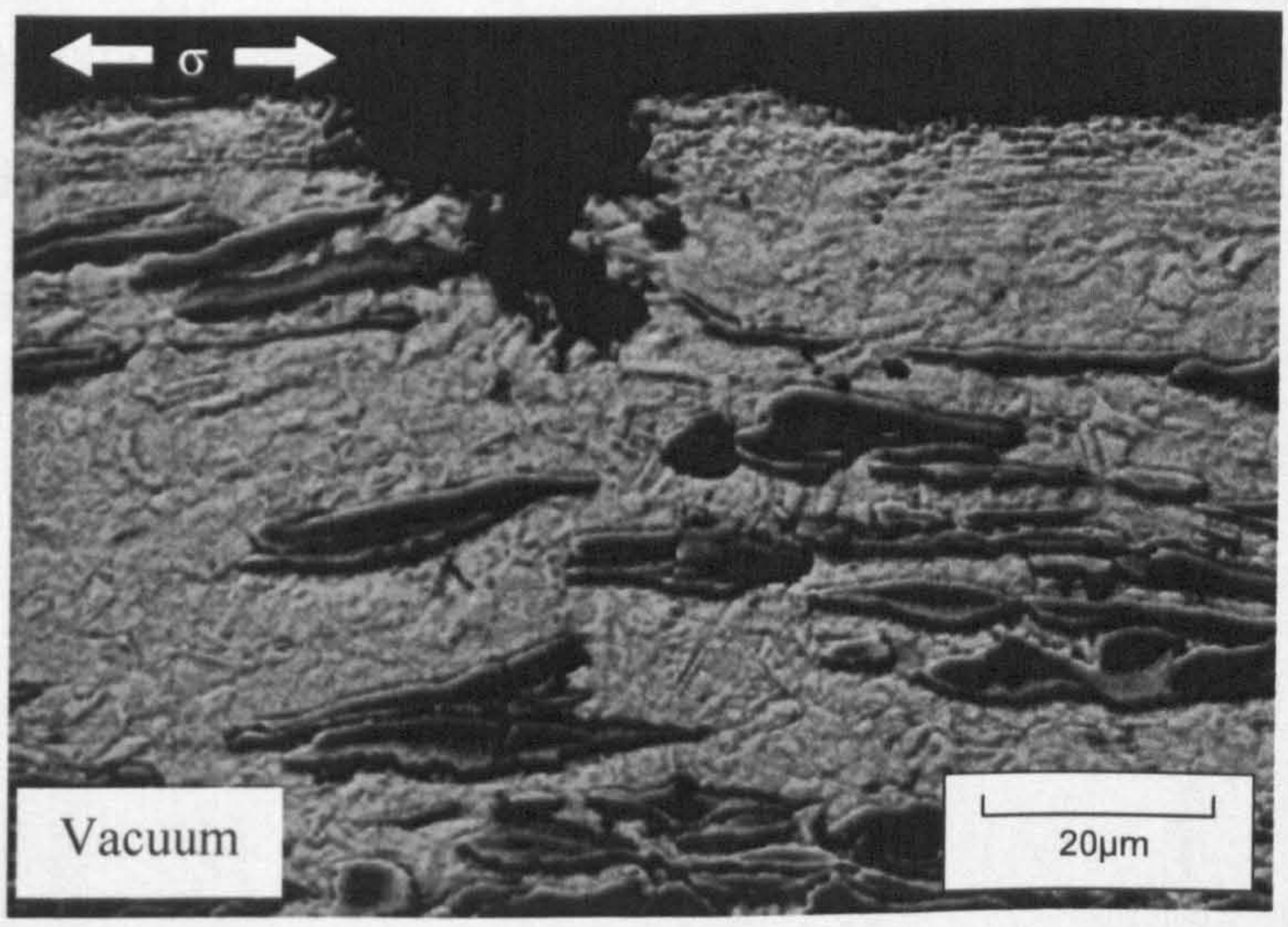

(b)

Figure 7.21 Edge of the composite tested at 600°C using 50 MPa in (a) air and (b) vacuum

Protection of metallic components against high temperature oxidation requires a dense slow growing oxide [21]. To retard oxidation of the composite, it is desirable to form a continuous layer of the slower growing oxide. This requires that the concentration of the metallic component forming the most protective surface oxide is sufficient to really form such a layer. The actual amount required depends on a complex balance between the thermodynamic and kinetic parameters between both the composite and the oxide phases for the given oxidation conditions. In the case of Cu-Cr composites, Cr is the more protective oxide, but since the concentration of Cr in the composite is low, most of the scale consists of Cu oxides only.

Overall, the similarities of the activation energy and the stress exponent in air and in vacuum strongly suggest that the oxygen and/or the oxide have no direct effect on the deformation mechanism of Cu-Cr composites. Rather, the acceleration of creep rate in air can be explained by the gradual decrease of the cross sectional area of the matrix due to increasing thickness of the oxide layer. Early onset of tertiary stage occurred because of cross section reduction of the test specimen, which for the test conducted at 500°C amounted to about 30 % cross section reduction at the point of failure. As the load bearing cross-sectional area was reduced due to spalling/cracking of the oxide scale, this would accelerate the minimum creep rate.

7.7 Summary

Mechanisms of tensile creep deformation and damage were studied for Cu-Cr composites both in air and in vacuum at temperatures ranging from 200-650°C and stresses ranging from 18-270 MPa. The following conclusions were drawn:

1 Creep resistance increases greatly with the introduction of Cr fibres into Cu. Under the same test conditions (same stress and temperature), the creep life increased more than 25 times in Cu-Cr composites over pure Cu. The higher creep rate of the composite in air than in vacuum seems likely to be due to the gradual decrease of the cross-sectional area of the matrix due to increasing thickness of the oxide layer.

2 The closeness of the stress exponent and activation energy in air and in vacuum for creep of Cu-Cr composites at high temperatures (≥ 400°C) strongly indicates that the oxygen and/or the oxide have no direct effect on the deformation mechanism. The stress exponent and the activation energy for creep of Cu-Cr composites at high temperatures (≥ 400°C) were observed to be between 4.6-5.9 and 179-217 kJ/mol. The observation that the stress exponent and the activation energy for creep of Cu-Cr composites at high temperatures (≥ 400°C) are close to those of pure Cu suggests that the creep deformation of Cu-Cr composites is dominated by the deformation of the Cu matrix. The increase of creep rate for composite tested in air can be explained by the gradual decrease of the cross sectional area of the matrix due to increasing thickness of the oxide layer.

3 The high stress exponent at low temperatures (200°C and 300°C) is thought to be associated with the as-swaged microstructure which contains elongated dislocation cells and subgrains that are stable and act as strong athermal obstacles at low temperatures.

4 The mechanism of damage was found to be similar for tensile and creep tests. Damage is primarily found near the ends and at the interfaces of Cr fibres in the form of matrix cavitation. The creep fracture of the composite was preceded by a coalescence of voids initiated mostly at the tips and the interfaces of Cu-Cr.

References

1 Z.Y. Ma and S.C. Tjong, High temperature creep behaviour of in-situ TiB_2 particulate reinforced Cu-based composite. Materials Science & Engineering A-Structural Materials Properties Microstructure & Processing, 2000. A284: 70-76.

2 H. Leidheiser, The corrosion of Cu, Tin and their Alloys, Krieger Publishing Company, Melbourne, FL, 1979.

3 T.G. Nieh, Creep rupture of a silicon carbide reinforced aluminium composite. Metallurgical Transactions A-Physical Metallurgy & Materials Science, 1984. 15A(10): 39-46.

4 F.A. Mohamed, K.T. Park and E.J. Lavernia, Creep behaviour of discontinuous SiC-Al composites. Materials Science & Engineering A-Structural Materials Properties Microstructure & Processing, 1992. A150(1): 21-35.

5 T. Morimoto, T. Yamaoka, H. Lilholt and M. Taya, Second stage creep of SiC whisker/6061 aluminium composite at 573 K. Journal of Engineering Materials & Technology-Transactions of the ASME, 1988. 110(2): 70-76.

6 K.T. Park, E.J. Lavernia and F.A. Mohamed, High temperature creep of silicon carbide particulate reinforced aluminium. Acta Metallurgica et Materialia, 1990. 38(11): 2149-2159.

7 A.B. Pandey, R.S. Mishra and Y.R. Mahajan, Creep behaviour of an aluminium-silicon carbide particulate composite. Scripta Metallurgica et Materialia, 1990. 24(8): 1565-1570.

8 T.L. Dragone and W.D. Nix, Steady state and transient creep properties of an aluminium alloy reinforced with alumina fibers. Acta Metallurgica et Materialia, 1992. 40(10): 2781-2791.

9 K. Park, F.A. Mohamed, Creep Strengthening in a Discontinuous SiC-Al Composite. Metallurgical & Materials Transactions A-Physical Metallurgy & Materials Science, 1995. 26A: 3119-3129.

10 S.I. Hong and M.A. Hill, Microstructural stability and mechanical response of Cu-Ag microcomposite wires. Acta Materialia, 1998. 46(12): 4111-4122.

11 S.B. Biner and W.A. Spitzig, Creep characteristics of wire-drawn Cu-20% Nb. Materials Science & Engineering A-Structural Materials Properties Microstructure & Processing, 1992. A150(2): 213-220.

12 S.I. Hong and M.A. Hill, Mechanical properties of Cu-Nb microcomposites fabricated by the bundling and drawing process. Scripta Materialia, 2000. 42(8): 737-742.

13 Smithells Metals Reference Book, 7th edition, Editor: E.A. Brandes and G.B. Brook.

14 H.J. Frost and M.F. Ashby, Deformation Mechanism Maps: The Plasticity and Creep of Metals and Ceramics, Pergamon Press, Oxford, UK, 1982.

15 H.E. Carroll and A.F. Whitehouse, Damage and failure during creep of a copper-chromium in-situ composite. Scripta Materialia, 2000. 42: 1133-1137

16 S.I. Hong, G.T. Gray and J.J. Lewandowski, Dynamic deformation behaviour of Al-Zn-Mg-Cu alloy matrix composites reinforced with 20 vol.% SiC. Acta Metallurgica et Materialia, 1993. 41(8): 2337-2342.

17 K.T. Park, F.A. Mohamed, Creep strengthening in a discontinuous SiC-Al composite. Metallurgical & Materials Transactions A-Physical Metallurgy & Materials Science, 1995. 26A(12): 3119-29.

18 A.F. Whitehouse, H.M.A. Winand and T.W. Clyne, The effect of processing route and reinforcement geometry on isothermal creep behaviour of particulate and short fibre MMCs. Materials Science & Engineering A-Structural Materials Properties Microstructure & Processing, 1998. A242: 57-69.

19 A.F. Whitehouse and H.M.A. Winand, The tensile creep response of Al-SiC particulate and whisker composites. Scripta Materialia, 1999. 41(8): 817-822.

20 S.B. Biner, The role of interfaces and matrix void nucleation mechanism on the ductile fracture process of discontinuous fibre-reinforced composites. Journal of Materials Science, 1994.29: 2893-2902.

21 B. Burton, The interaction of oxidation with creep processes. Single crystal properties, 1982.B1: 1-48.

22 K.T. Chiang, C.H. Meier and F.S. Pettit, Oxidation behaviour of Cu-Cr composites, S.B. Newcomb, J.A. Little (Eds), Microscopy of oxidation-3, Institute of Materials, London, 1997. 453-461.

23 M. Ohnami and R. Imamura, A study on the effect of vacuum environments on creep rupture property of a commercial pure Cu at elevated temperature, Proceedings of the Japan congress on materials research 1980. 132-137.

Chapter 8

Conclusions and Future Work

Work is the greatest thing in the world, so we should always save some of it for tomorrow.

-Don Herald

8.1 Introduction

This final chapter will summarize the work presented in this thesis, draw conclusions, as well as some suggestions for further work.

8.2 Conclusions

8.2.1 Microstructure and tensile behaviour

A Cu-10vol.% Cr composite was produced by melt processing and deformed by swaging to form rods with a total deformation true strain of 3.15. Scanning electron microscopy showed that the composite microstructure consisted of Cr fibres aligned with their long axes parallel to the rod axis. Transmission electron microscopy found a relatively large number of dislocations both in the Cu and Cr phase. X-ray diffraction indicated that the Cr fibres had a strong <110> fibre texture; the Cu matrix had a mixed <111> plus <200> texture.

The mechanical properties of the composite were measured by tensile testing over the temperature range -70 to 600°C. The presence of the Cr fibres increases the room temperature yield strength of the material by 77 % and the ultimate tensile strength of the material by 43 % compared to those of pure Cu. The ductility of the material is relatively low at all temperatures and decreases as the temperature decreases. The small increase in the resistivity of the composite at room temperature

during tensile testing showed that the Cr fibres were behaving in a ductile manner and fracturing or separating from the Cu matrix was not significant as the yield strength was exceeded.

It has now been established that the failure mechanisms of the Cu-10vol.% Cr composites fell into distinct regimes. At cryogenic temperature, damage occurred in the form of reinforcement cracking. At room temperature, very little damage was observed in the composite. As the temperature is increased, damage occurred mostly at the ends of Cr fibres in the form of matrix cavitation. Failure of the composite occurred by the coalescence of cavities. With increasing temperature a transition from localized to global damage occurred between 300°C and 400°C.

8.2.2 Neutron diffraction and in-situ tensile test in SEM

The high level of penetration of neutrons was used to follow the deformation behaviour of the individual phases in Cu-Cr composite and their interaction through elastic and plastic loading at room temperature. The onset of plasticity results in a strain misfit between the phases which acts to transfer load towards the Cu phase. This surprising result was borne out by final residual strains. The co-deformation processing prior to testing had meant that the Cr phase reached the yield locus at roughly the same strain as the Cu phase due to a combination of its high stiffness and the probable presence of swaging induced residual stresses. A higher stiffness for the Cr phase relative to the Cu phase meant that although the two phases deformed approximately equally, the Cr phase had the larger plastic component resulting in load transfer from Cr to Cu with increased straining. The Cr phase is effectively carrying a higher proportion of the applied load in the elastic region but this benefit decreases with increased plastic straining. A better tensile performance might be expected if the

damaging tensile residual stresses could be relieved prior to tensile testing without softening the Cu and Cr phase considerably. Fairly good agreement is observed in the phase strains predicted by the Eshelby theory and measured by neutron diffraction despite the large scatter in the experimental data.

The in-situ SEM tensile test showed that the composite damage mechanism behaviour of the surface was different from that of the bulk. Cr fibres were found to crack easily at the surface but extensive fibre cracking was not found in the bulk. The different damage behaviour of the surface and the bulk can be explained in terms of the extreme notch sensitivity of Cr and the difference of the stress state in the surface and the bulk.

8.2.3 Creep

A systematic study of creep deformation and fracture behaviour was carried out for Cu-10vol.% Cr composites both in air and in vacuum over a temperature range of 200-650°C. It was found that the creep resistance increases significantly with the introduction of Cr fibres into Cu. The similarities of the stress exponent and activation energy in air and in vacuum for creep of the composite at high temperatures (≥ 400°C) shows that the nature of the rate controlling mechanism was not greatly affected by the oxidation.

The acceleration of creep rate of the composite in air can be explained by the gradual decrease of the cross sectional area of the matrix due to increasing thickness of the oxide layer. The observation that the stress exponent and the activation energy for creep of Cu-10vol.% Cr composites at high temperatures (≥ 400°C) are close to those of pure Cu shows that the creep deformation of Cu-10vol.% Cr composites is dominated by the deformation of the Cu matrix. The high stress exponent at low

temperatures (200°C and 300°C) is thought to be related with the as-swaged microstructure such as elongated dislocation cells and subgrains which are stable and act as strong athermal obstacles at low temperatures. The mechanism and distribution of damage for Cu-10vol.% Cr composites were found to be similar during tensile and creep testing.

8.3 Future work

The work described in this thesis branches out into some interesting avenues for further exploration. This section describes five main directions of future work that are worth pursuing.

The use of neutron diffraction offers many new and exciting opportunities. In relation to the work here, further measurements should be carried out at high temperature. At high temperature, the Cu matrix is going to be much more plastic (softer) than the Cr reinforcement and hence load transfer would occur from the matrix to the reinforcement. The neutron diffraction data obtained from this high temperature test will provide a measure of efficiency of load transfer within the composite. From this, a better understanding of the internal stresses generated during loading would be obtained for the composite at different temperatures. It would also be useful to determine the deformation behaviour of the individual phases and their interaction through elastic and plastic loading for higher drawing strains of Cu-Cr composites. At high drawing strains, the high yield strength of the Cr fibre would be expected to carry a much higher load than the Cu matrix during tensile deformation and significant load transfer might occurred from the Cu phase to the Cr phase and hence give a better performance composite material.

At room temperature, Cu-Cr composite has shown to have superior tensile strength over similarly processed unreinforced Cu. Limited research (Chapter 3, reference 35) has shown that at very high temperatures (above 300°C), the strength of Cu-Nb composites showed pronounced deterioration, and at 600°C, it was not much better than pure Cu. The degree of coarsening increased at a given temperature as the fibre thickness decreased, that is, as the degree of deformation processing of the material increased. Because the drawing strain of the current composite was relatively low, no fibre coarsening was observed even at high temperatures. It would therefore be interesting to compare the current strength of the composite with pure Cu drawn at the same drawing strain tested at high temperatures.

Since more than 75 % of failures in engineering components are due to fatigue failure, and as the performance from engineering materials is continually increased, the need to understand the failure of materials becomes increasingly important. Therefore to ensure the long-term reliability of this composite, it is important to understand the mechanical and thermal fatigue of this composite.

Creep rupture of composite material depends on both load transfer to the reinforcement to reduce the creep rate and the onset of damage. A greater understanding of the damage processes occurring within the composite can be achieved by monitoring the Poison's ratio during creep deformation. One of the advantages of this technique is that the test does not have to be interrupted.

The present study has focused on one drawing strain of composite. Since the damage and creep characteristics have not yet been investigated for higher drawing strains of Cu-Cr composites, the logical step would be to extend the study to characterise the effect of drawing strain on these properties. Obtaining an

understanding of the damage and creep behaviour over a range of drawing strain would render a more complete picture of the composite response.

Appendix

All creep curves

(a) Pure Cu tested in air

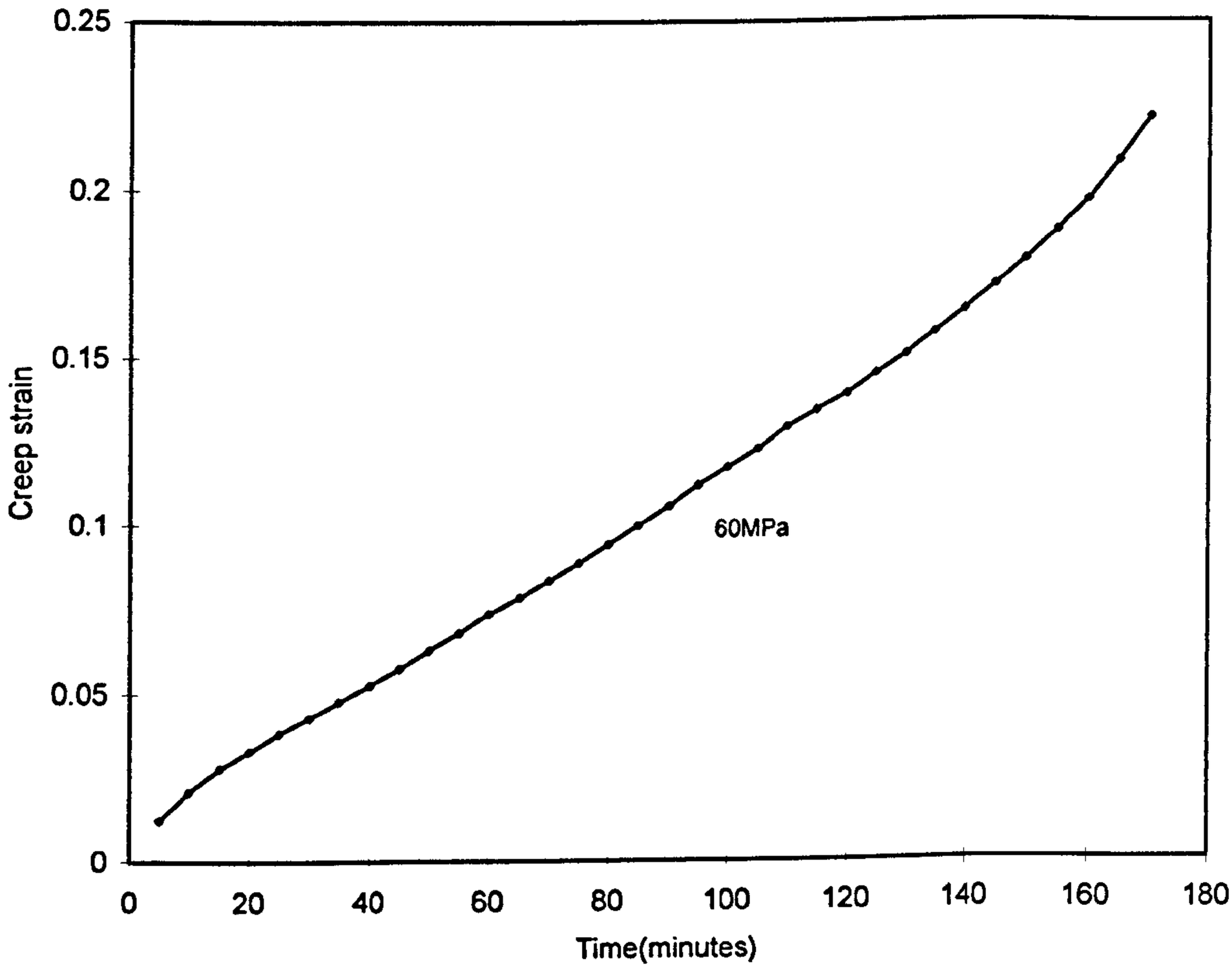

Figure 1 Graph of creep strain against time at 400°C with 60MPa of stress

(b) Composite tested in air

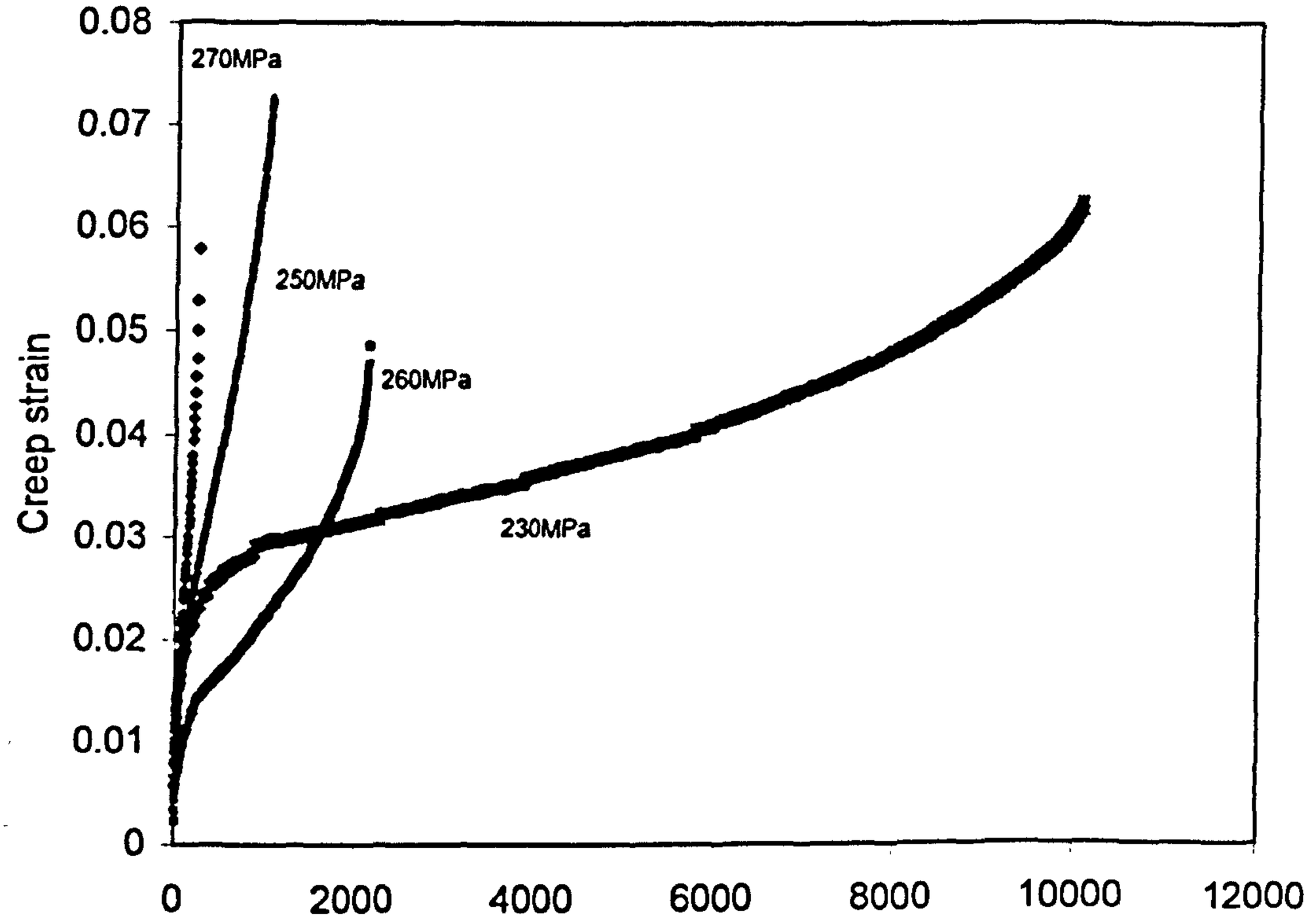

Figure 2 Graph of creep strain against time at 200°C with stresses range from 230-270 MPa

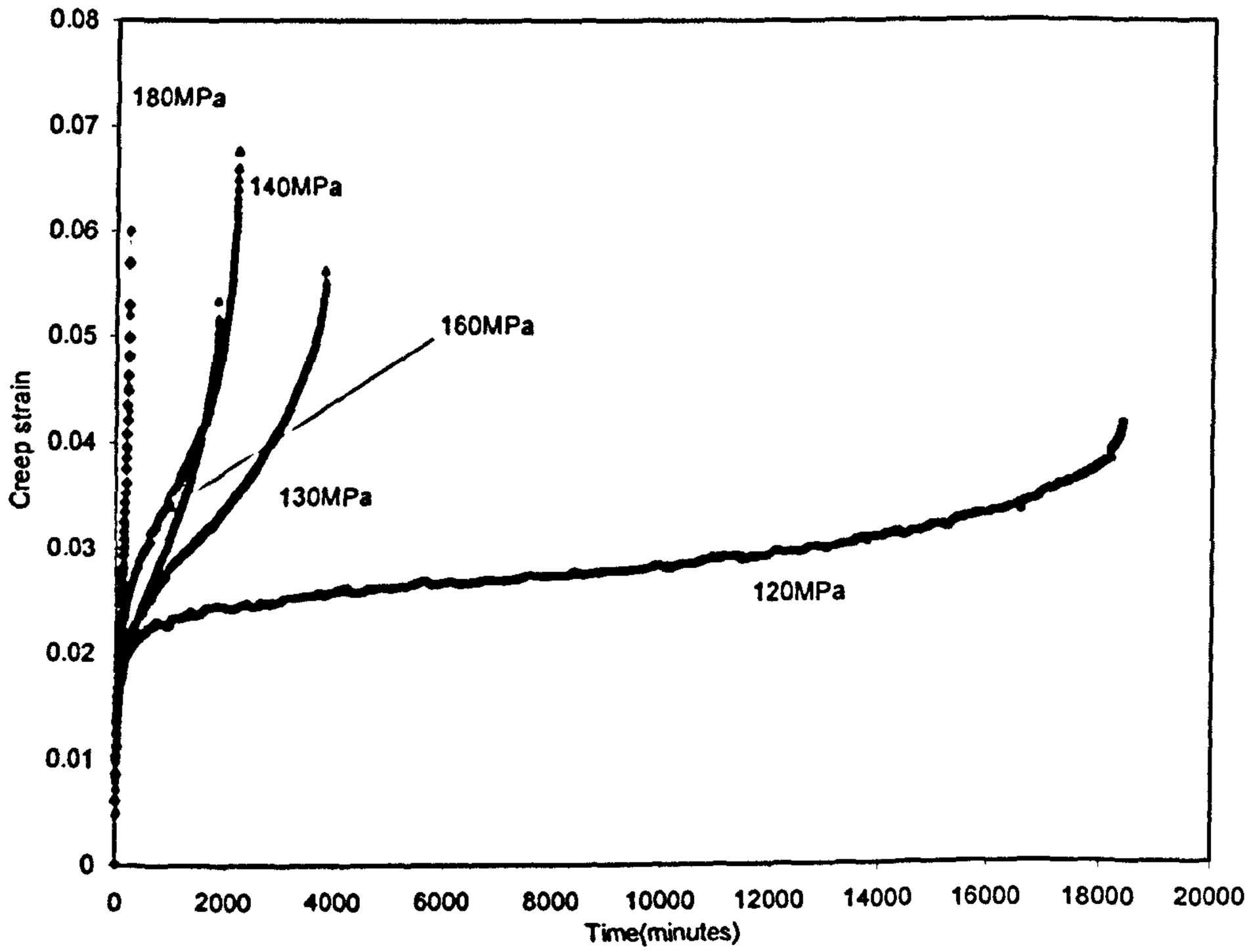

Figure 3 Graph of creep strain against time at 300°C with stresses range from 120-180 MPa

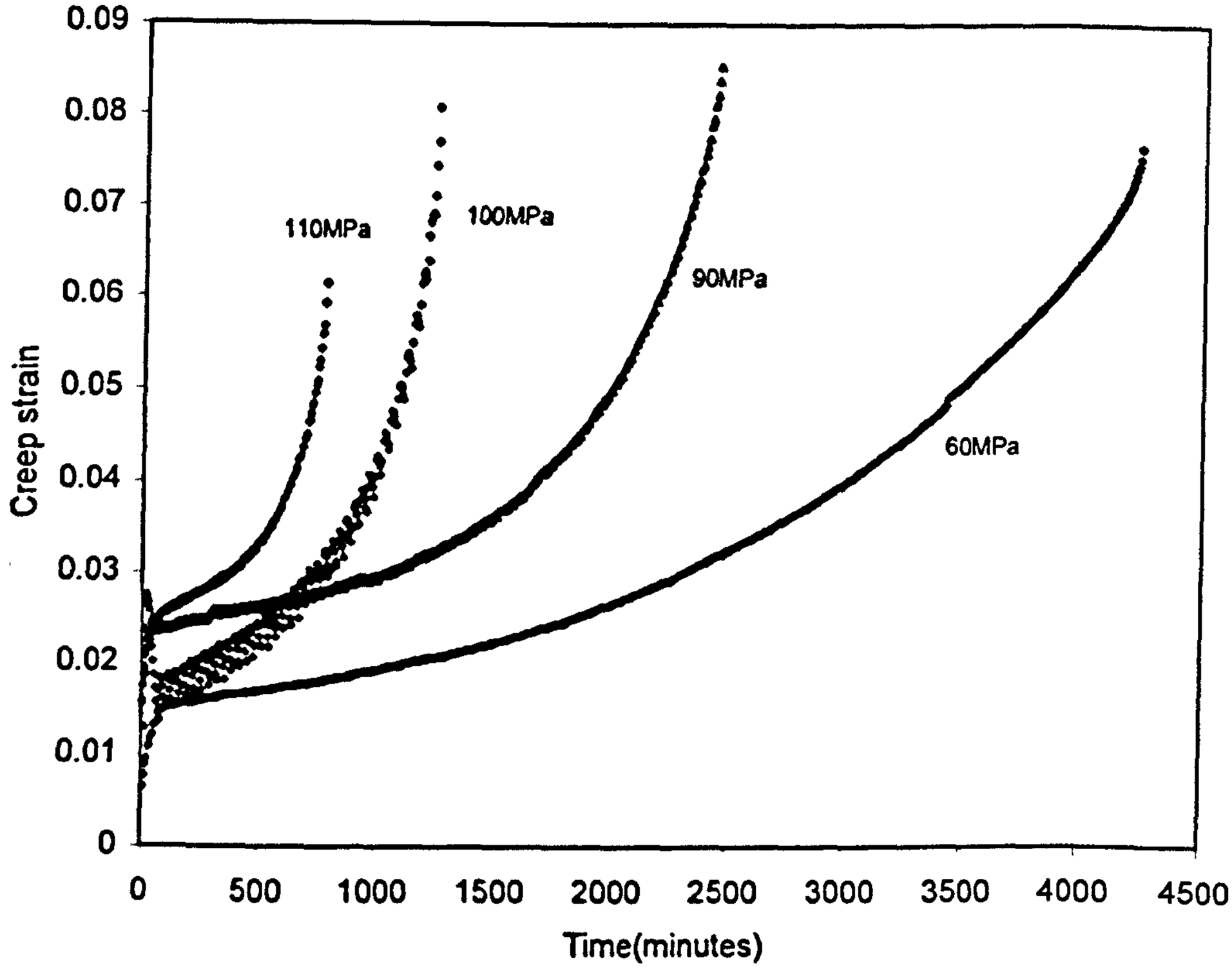

Figure 4 Graph of creep strain against time at 400°C with stresses range from 60-110 MPa

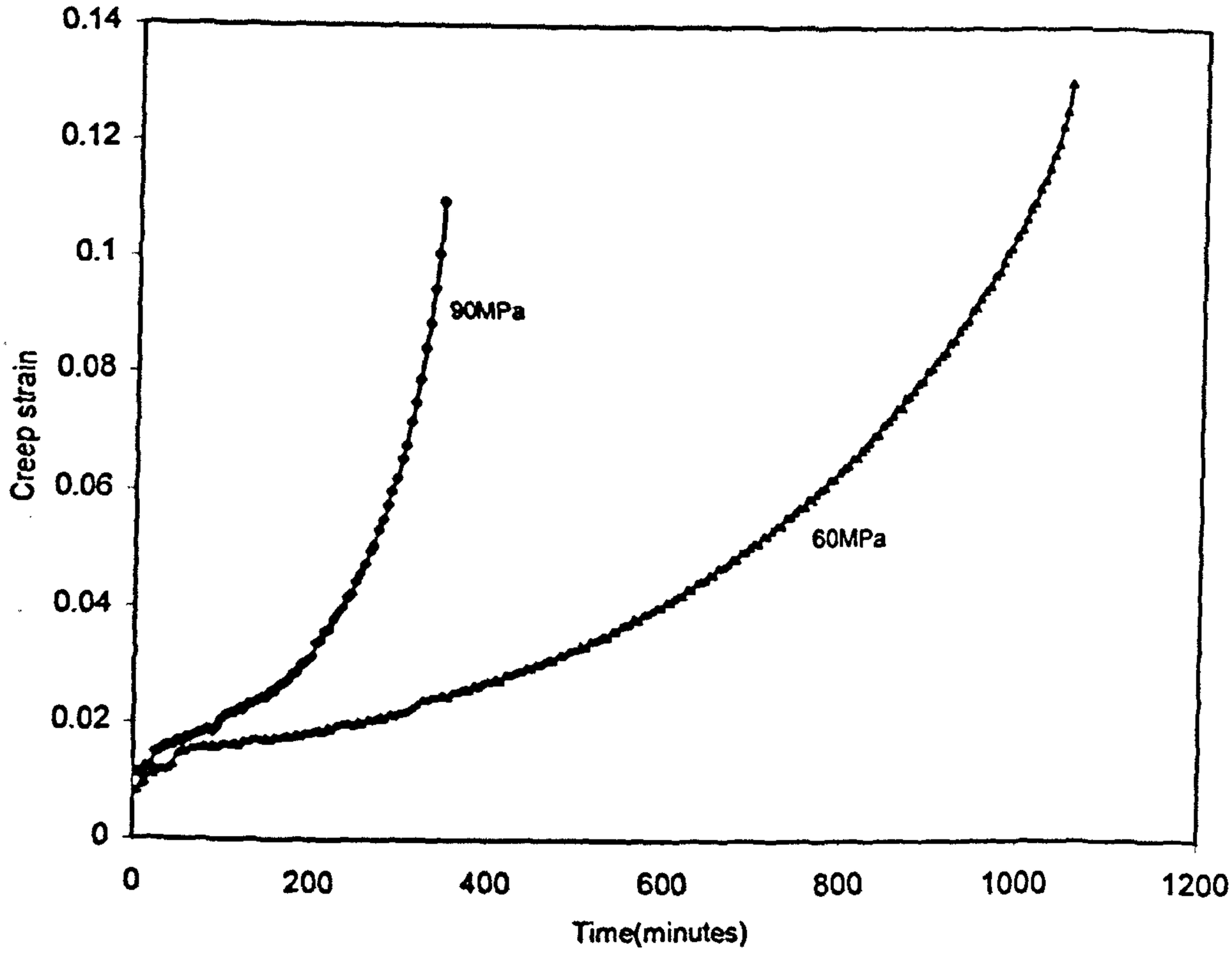

Figure 5 Graph of creep strain against time at 450°C with stresses range from 60-90 MPa

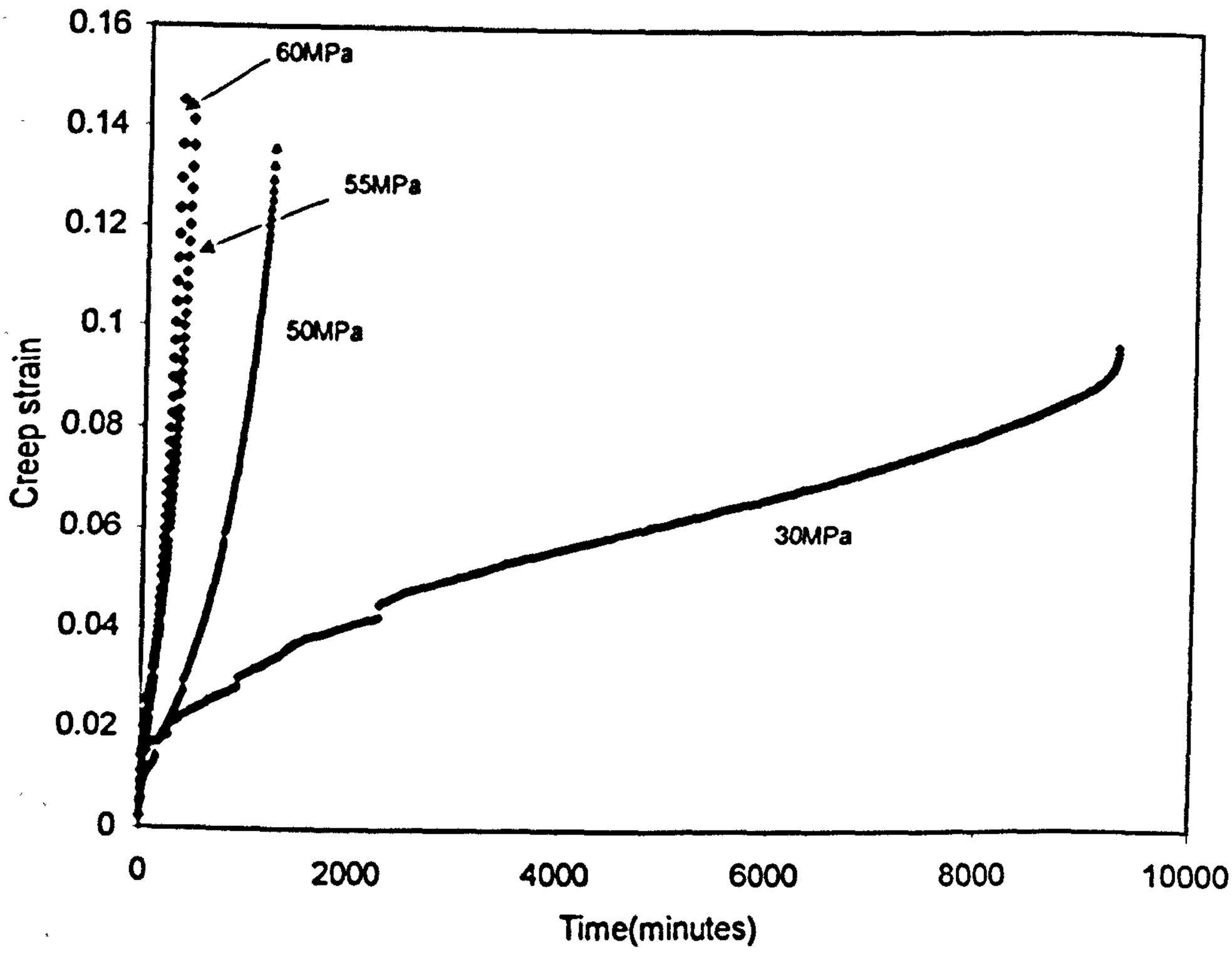

Figure 6 Graph of creep strain against time at 500°C with stresses range from 30-60 MPa

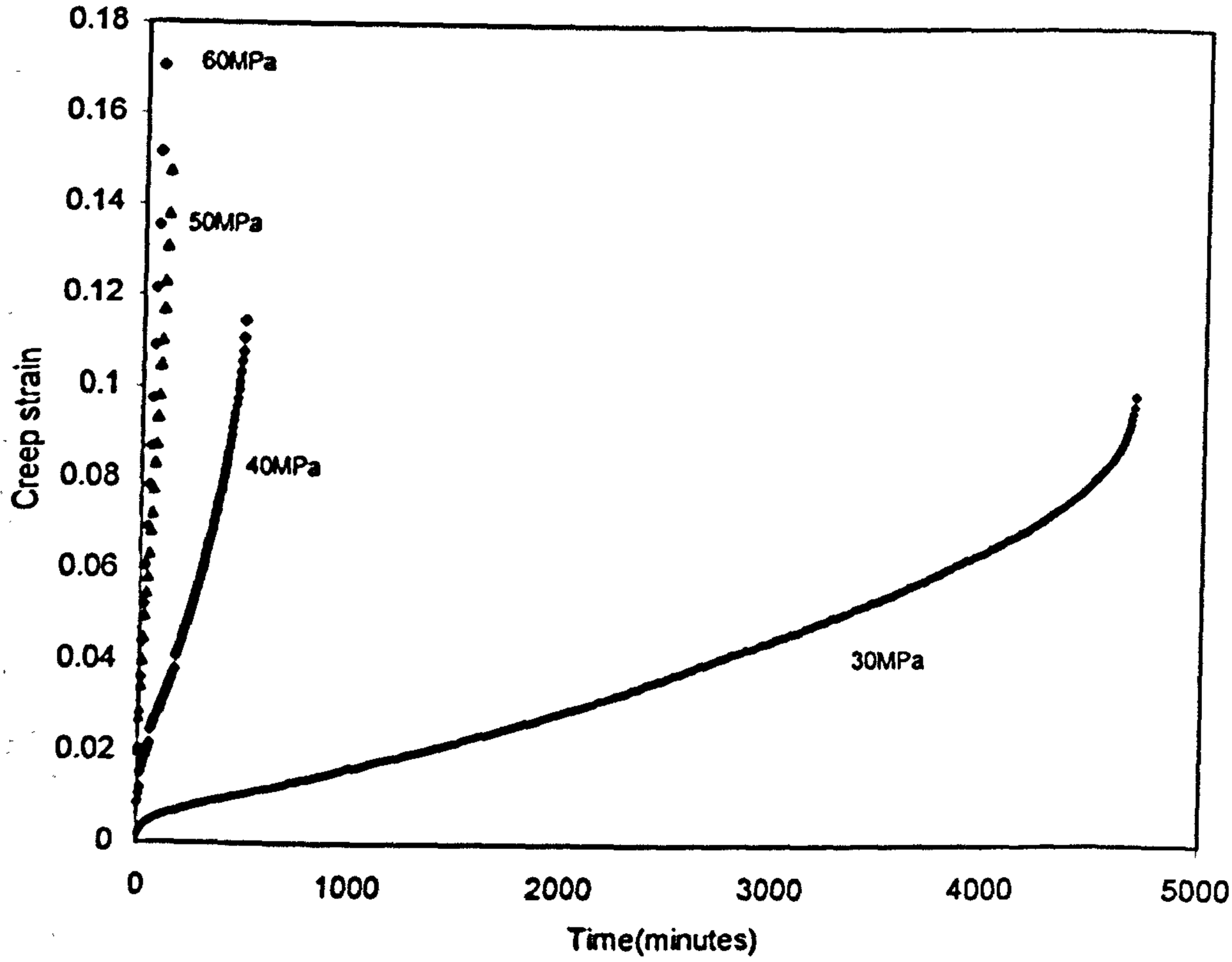

Figure 7 Graph of creep strain against time at 550°C with stresses range from 30-60 MPa

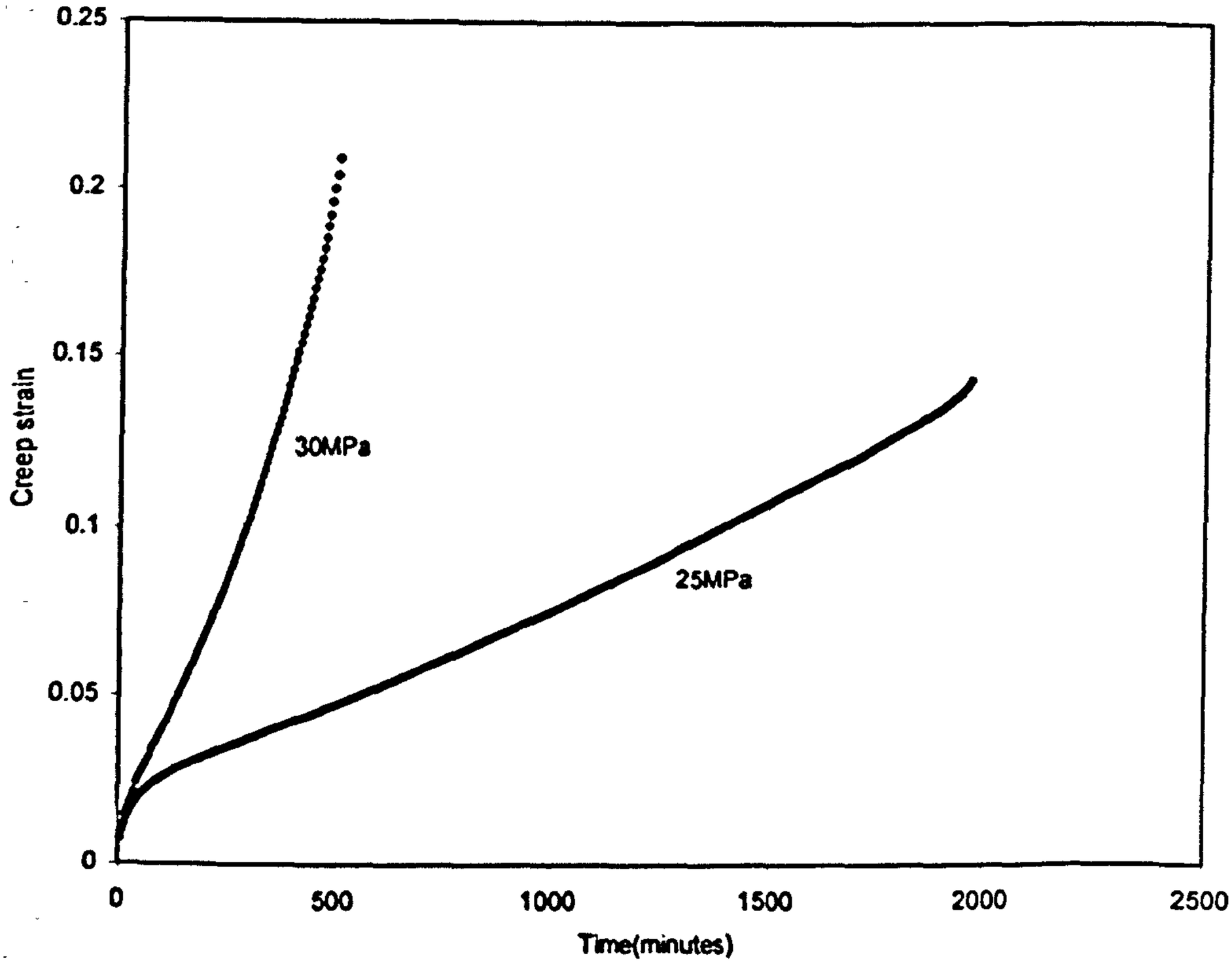

Figure 8 Graph of creep strain against time at 600°C with stresses range from 25-30 MPa

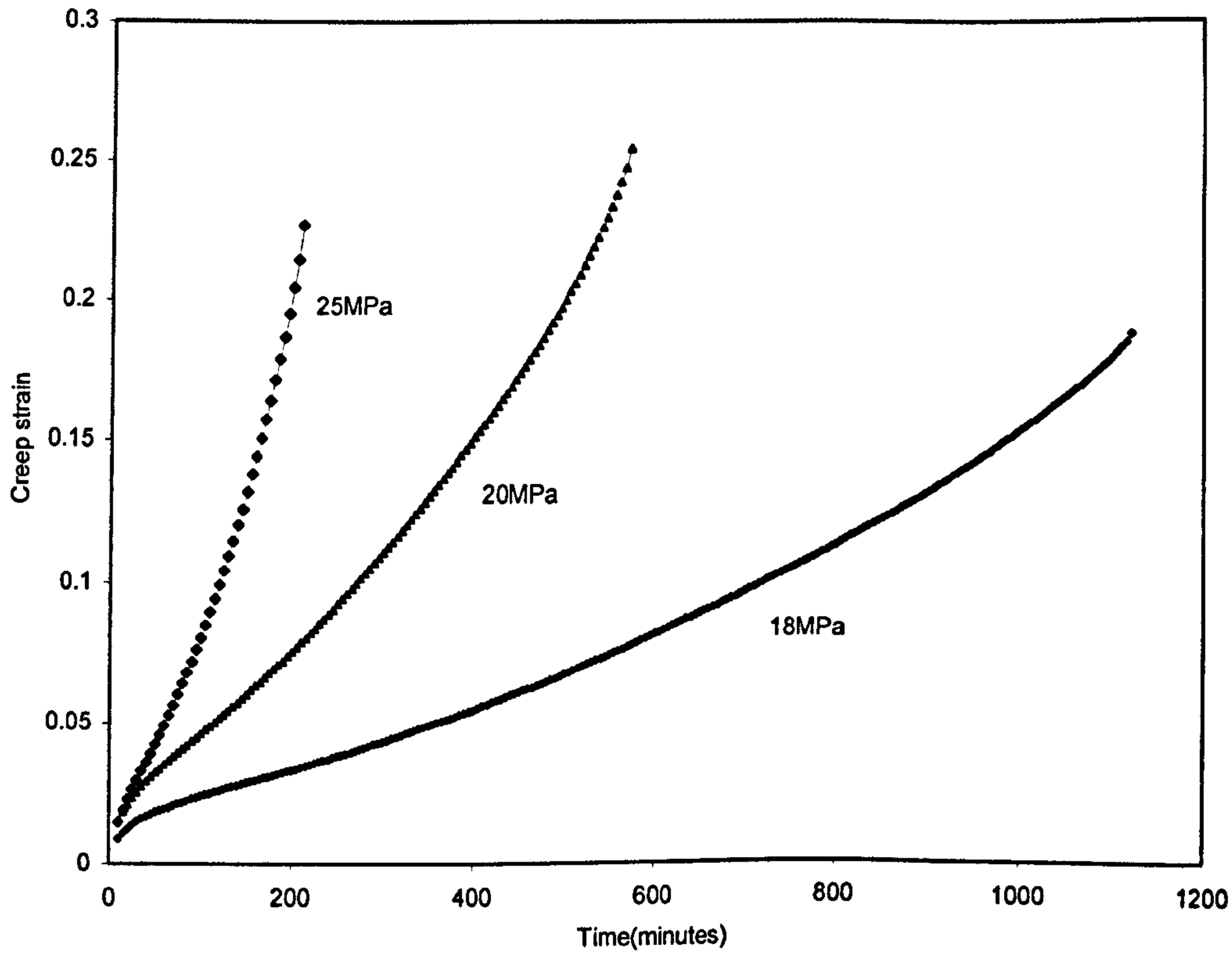

Figure 9 Graph of creep strain against time at 650°C with stresses range from 18-25 MPa

(c) Composite tested in vacuum

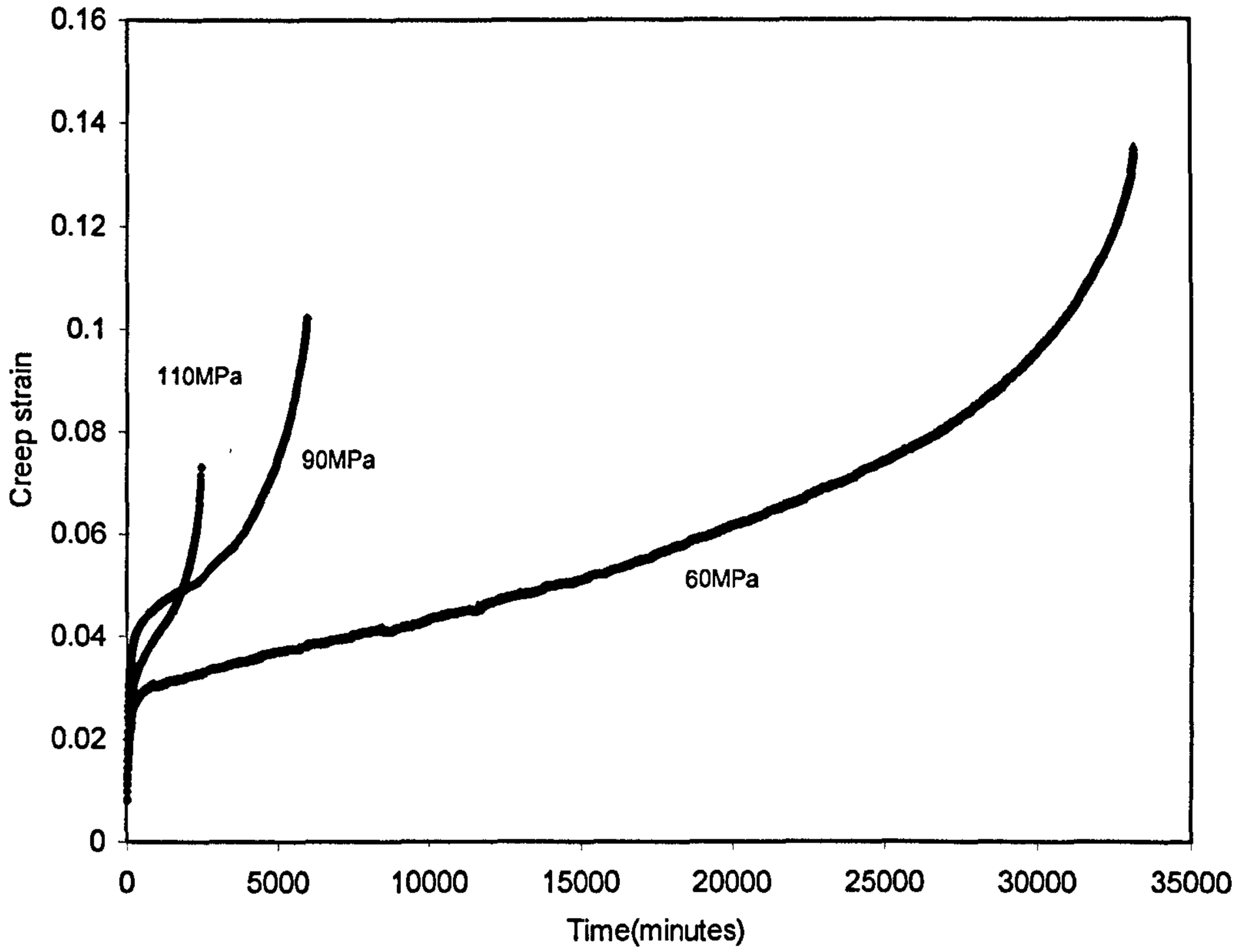

Figure 10 Graph of creep strain against time at 400°C with stresses range from 60-110 MPa

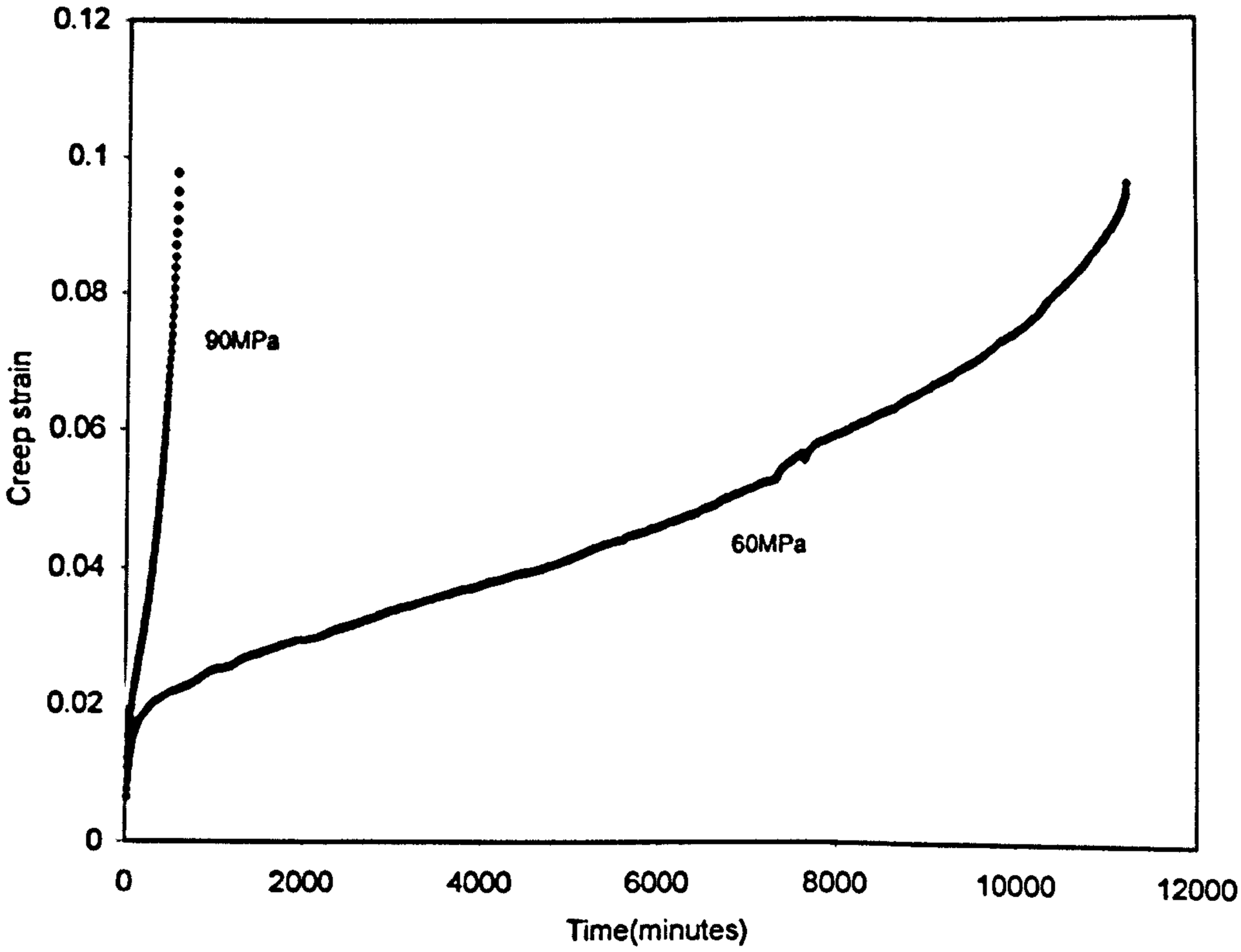

Figure 11 Graph of creep strain against time at 450°C with stresses range from 60-90 MPa

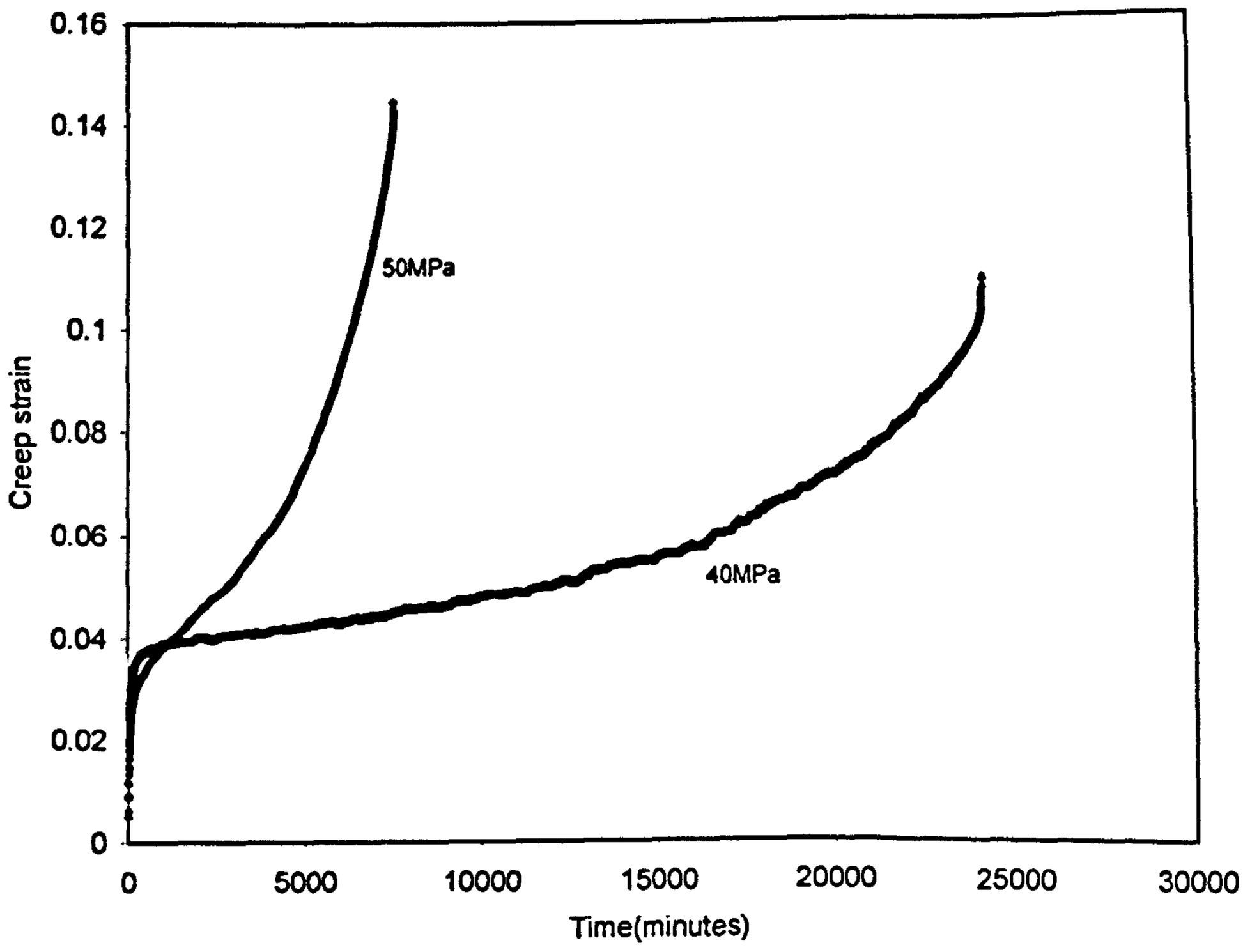

Figure 12 Graph of creep strain against time at 500°C with stresses range from 40-50 MPa

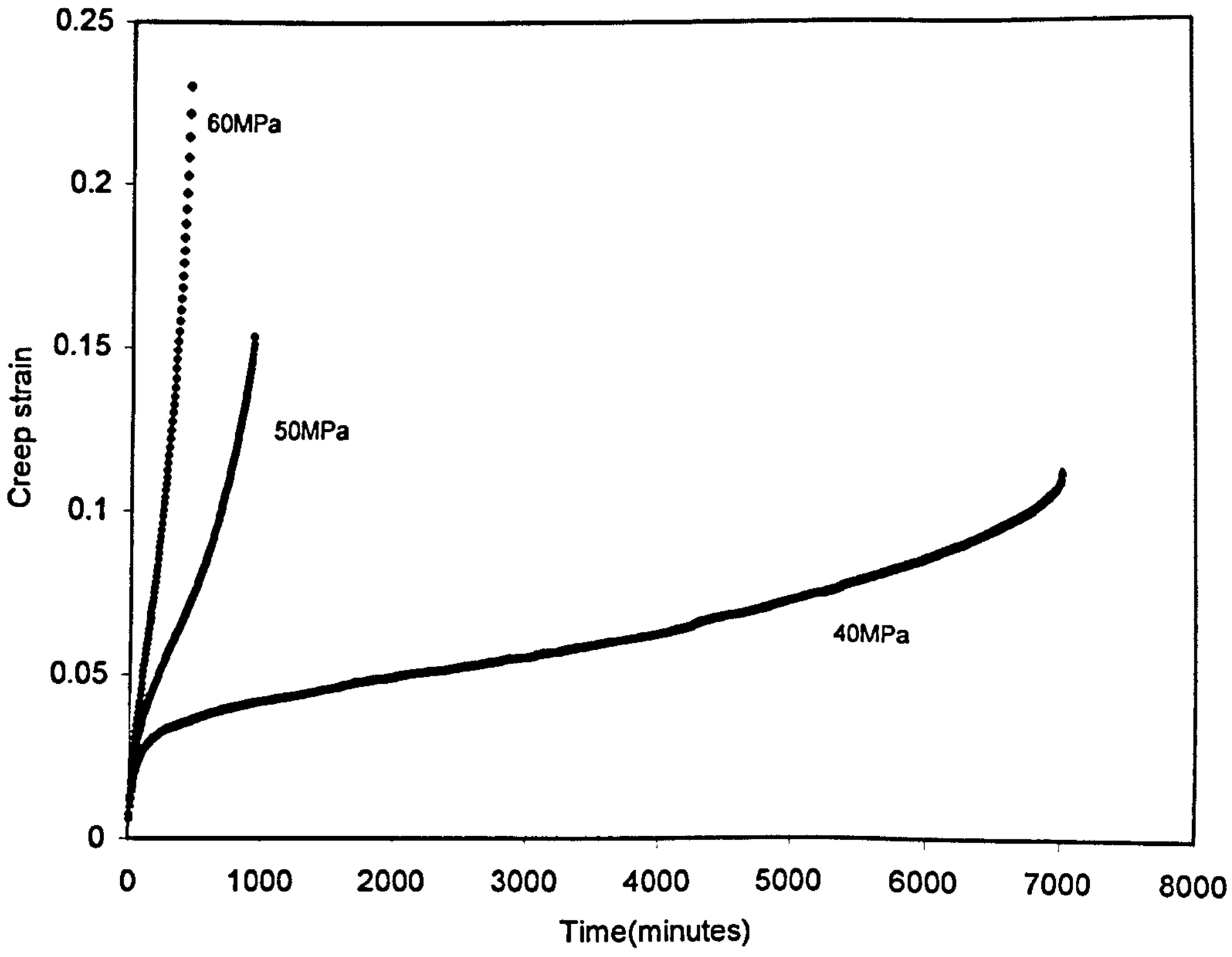

Figure 13 Graph of creep strain against time at 550°C with stresses range from 40-60 MPa

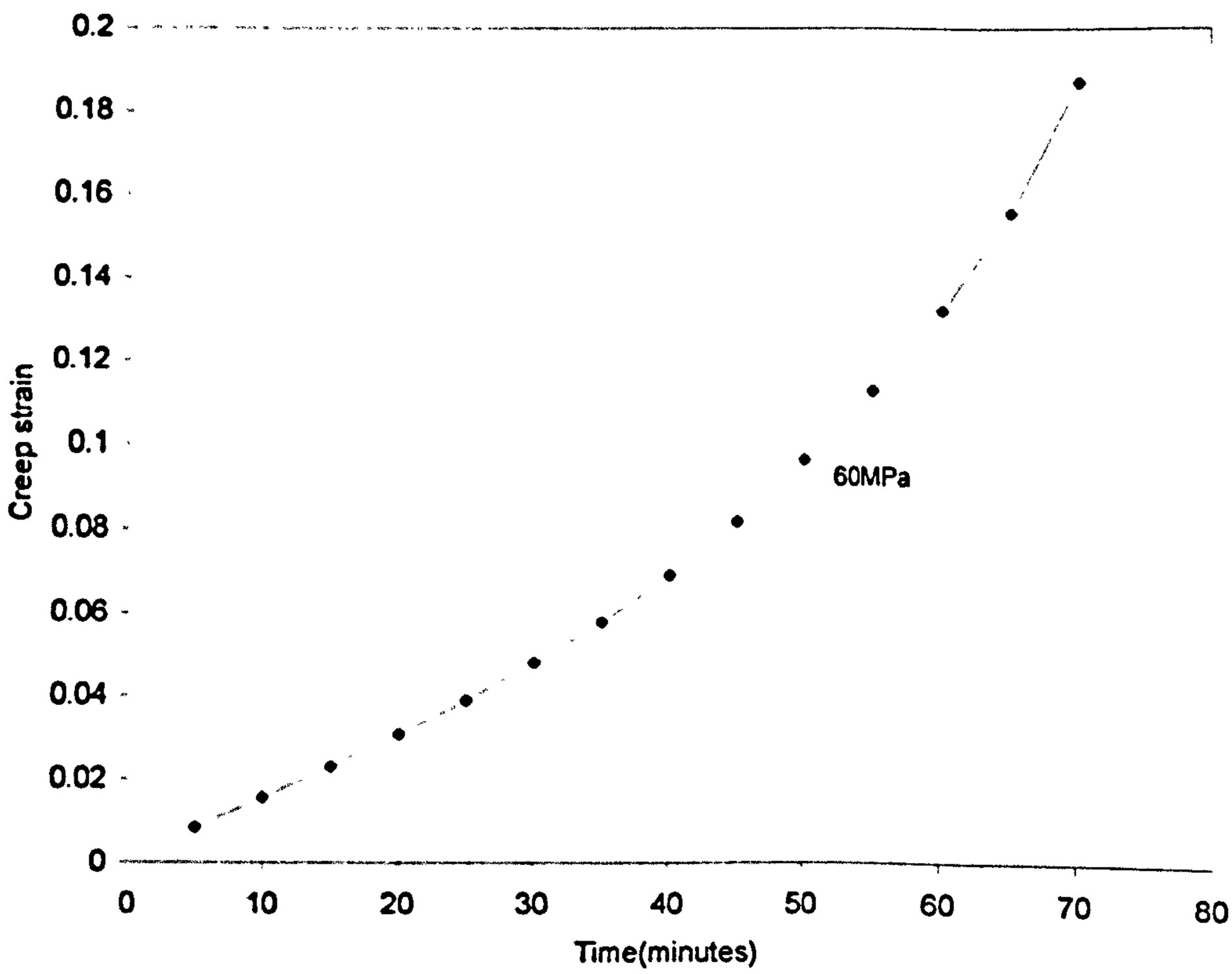

Figure 14 Graph of creep strain against time at 600°C with 60MPa of stress

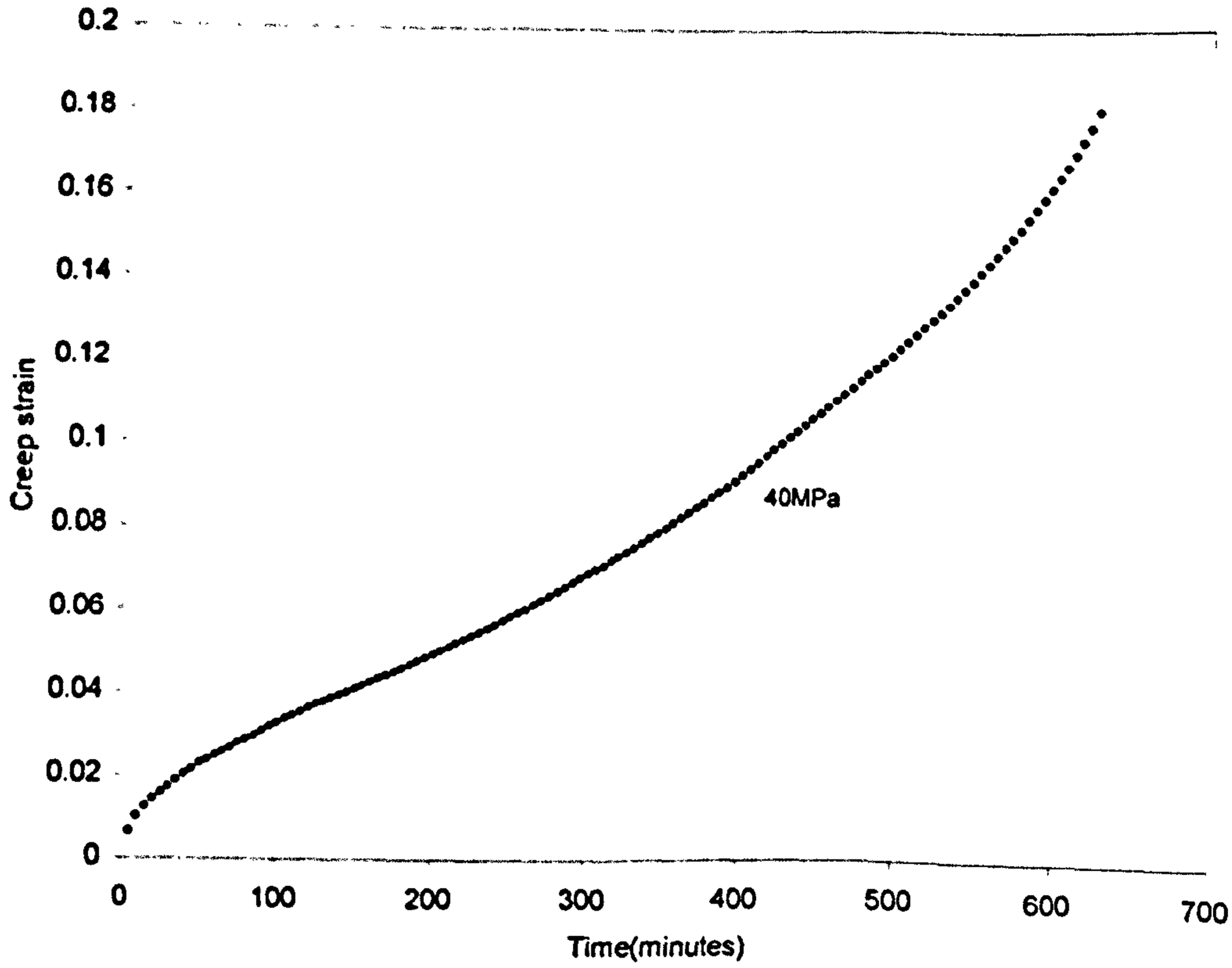

Figure 15 Graph of creep strain against time at 650°C with 40MPa of stress

Due to third party copyright restrictions the published articles have been removed from the appendix of the electronic version of this thesis. The unabridged version can be consulted, on request, at the University of Leicester's David Wilson Library.